POLITECNICO DI MILANO

School of Industrial and Information Engineering

Master of Science in
Energy Engineering

Experimental analysis of an air-to-air heat pump equipped with digital scroll compressor and evaluation of the pulsing flow influence on the refrigerant/air side and on the overall performances

Advisor: Prof. Luca MOLINAROLI

Co-advisor: Prof. Lorenzo CREMASCHI

MSc thesis of:

Gabriele CORTI Matr. 763503

Stefano MARELLI Matr. 765270

Academic Year 2012 - 2013

Ringraziamenti

Desideriamo esprimere la nostra gratitudine e riconoscenza verso tutte le persone che a vario titolo hanno contribuito alla buona riuscita di questo progetto.
Innanzitutto vogliamo ringraziare il correlatore della tesi professor Lorenzo Cremaschi, responsabile della camera psicrometrica del dipartimento ATRC dell'Oklahoma State University presso cui abbiamo realizzato la nostra ricerca, per la grande professionalità e dedizione profuse nella supervisione del progetto e per la straordinaria possibilità che ci ha offerto di fare una così importante e significativa esperienza formativa.
Un ringraziamento va inoltre ai nostri colleghi di laboratorio Pratik, Jeremy, Ardi, Shanshan, Xiao, Jimmy e Andrea: nonostante non fossero coinvolti direttamente nel progetto sono stati sempre disponibili a fornire il loro prezioso aiuto, facendoci familiarizzare con le attrezzature e condividendo con noi i "trucchi del mestiere".
Ringraziamo anche AAON, Inc., principale sponsor del progetto, nella persona dell'ing. John Gall, nostro referente e tramite con l'azienda, per il supporto tecnico alla realizzazione dell'apparato sperimentale.
Ultimo ma non in ordine di importanza esprimiamo la più sentita e sincera gratitudine al nostro relatore ing. Luca Molinaroli. È stato per noi un privilegio avvalersi della sua consulenza attenta e meticolosa e dell'infinita disponibilità che abbiamo potuto apprezzare anche come suoi allievi durante il nostro corso di studi.

Table of Contents

List of Tables

List of Figures

Abstract

Techniques of compressor capacity control are increasingly common in energy efficient direct expansion HVAC equipment. Compressor short cycling is one such technique that increases system efficiencies at part loads by continued heat transfer in the heat exchangers during the compressor off cycle. In particular, the digital scroll compressor is a device that is outfitted with a unique clutching mechanism designed to initiate short cycling behaviour while minimizing compressor wear due to startup/shutdown. In this thesis an investigation into the behaviour of the digital scroll compressor and its capacity control mechanism is presented. For these purposes, a 15ton (52,7 kW) nominal capacity heat pump unit was retrofitted with digital scroll compressors and a new control module. The operating conditions of the unit were varied in a parametric fashion using a large scale climate controlled psychrometric chamber. Instantaneous suction and discharge flow rates were measured to determine the flow cycling characteristics and their effect on the capacity and efficiency. Pressures, temperatures, and compressor absorbed power were measured in-line and in real time during compressor short cycling operating conditions. The new data serve to validate the modeling method proposed in this thesis. A detailed R-410A digital scroll compressor model is also developed using Modelica, a dynamic simulation environment, to support the experimental campaign. A novel experimental testbed apparatus is developed.
In the second stage of tests, a further investigation was made on the behaviour of the compressor at very low load (below 25%). Then another set of tests was conducted in order to evaluate the unit performances, to see the influence of the pulsing flow on the overall system (air properties included). A heat balance was built across the evaporator coil, air side and refrigerant side, in order to demonstrate that since they are similar (difference below 5%) the collected are reliable.
Finally, an electric heater was installed right before the evaporator coil to see a preliminary shape of a settle transitory of the unit, with the final goal of looking for the optimal control strategy.

Keywords: scroll compressor, dynamic simulation, short cycling, capacity control, compressor modeling, heat balance.

Sommario

Le tecniche di controllo del potere frigorifero dei compressori sono sempre più frequenti in un contesto di efficienza energetica dei sistemi a espansione diretta. La gestione del compressore in *short-cycling* è una delle tecniche che aumentano l'efficienza del sistema a carico parziale attraverso uno scambio di calore continuo negli scambiatori, anche durante il periodo *off* del compressore stesso. In particolare, i compressori Digital Scroll sono caratterizzati dell'essere equipaggiati con un peculiare meccanismo di accoppiamento per lavorare in short-cycling.
In questa tesi viene presentata un'indagine sul comportamento del compressore digital scroll e sui suoi effetti sul sistema unità-ambiente. Questo è stato fatto realizzando un apparato sperimentale costituito da una pompa di calore aria-aria di 52,7 kW di potenza frigorifera nominale, modificata tramite l'installazione di due nuovi compressori digital scroll e un nuovo modulo di controllo. Le condizioni operative dell'unità sono state variate utilizzando una camera psicrometrica di dimensioni adeguate alla potenzialità dell'apparato e ne sono state valutate le prestazioni a carico totale e parziale. Sono state misurate le portate istantanee in aspirazione e scarico al compressore per determinare le caratteristiche dei cicli e il loro effetto sulle prestazioni e sull'efficienza del sistema. Pressioni, temperature, surriscaldamento, potenza elettrica assorbita sono state misurate real time. I dati sperimentali ricavati servono a validare il modello di simulazione di un compressore digital scroll ad R-410A sviluppato in Modelica, un simulatore dinamico.
Nel secondo stage di test, un'ulteriore investigazione è stata condotta sul comportamento del compressore a carico molto basso, sotto il 25%. Una serie di nuovi test è stata poi condotta al fine di determinare le prestazioni dell'unità funzionante in modalità raffrescamento per capire l'influenza della portata pulsante, e soprattutto dimostrare che i dati raccolti sono affidabili effettuando un bilancio termico a cavallo dell'evaporatore, lato aria e lato refrigerante, mostrando che questi coincidono a meno di una tolleranza prefissata (5%).
Infine, è stato installato un riscaldatore elettrico a monte della batteria di evaporazione per cercare di osservare un tempo di assestamento dell'unità tra le condizioni stazionarie di partenza e quelle di arrivo, attraverso l'introduzione di una variazione a gradino della temperatura di ritorno dell'aria.

Parole chiave: compressore digital scroll, simulazione dinamica, short-cycling, potere frigorifero, modellazione, bilancio termico.

Chapter 1

Project overview and objectives

1.1 Overview of objectives of the research and of this thesis work

The **ultimate goal** of this three-years project, sponsored by Oklahoma State University and AAON, Inc., and named *"Optimally Controlled Air-Conditioning Equipment for Sustainable Building Systems"*, is to develop and experimentally validate optimal supervisory and process control algorithms for air-to-air heat pumps with digital scroll compressors. In other words, one of the objectives is to look for the optimal strategy to operate HVAC systems in order to achieve the same performances that guarantee the desired internal ambient comfort conditions with the lowest expense possible.
Optimal control needs first of all an optimal model, but it needs to be considered that the optimality may vary with time and operating conditions. The objective of a real-time optimization is to find the optimal input for an unknown or time varying output map. The drawbacks are the system inertia between input and output and the variations due to the system on the input.
It's now clear how it's not that easy to achieve the project's objectives, since a great effort in the modeling needs to be made before any kind of experimental test campaign on the optimal control of the system is made.
The goal has to be reached step by step, with simple step variations at first, in order to validate the simulation data and evaluate the time response of the system. After this, it will be possible to implement the real dither function in the controller.

That's the reason of the work done: first of all, the experimental testbed had to be built by equipping a conventional air-to-air 15ton (53 kW) heat pump with all the new components needed for this kind of research; then, a static map of the only compressor had to be developed, in order to **validate the simulation data** that was looked up in the literature and developed for the project purposes. After this, it was necessary to build an operational map of the whole unit, by evaluating its performances. This had to be done first demonstrating that the sensors were reliable by building a **heat balance** across the evaporator. After this, some punctual kinds of tests had to be done focusing on the influence that the **pulsing flow** imposed by the digital scroll compressor has on both the refrigerant and the air side of the unit.

In the next stages, the project will keep running focusing on the research of the best way to build an optimal model of this particular equipment when operating at part loads, because it is difficult, so it takes time, to define the dynamically varying states associated with this condition, even in steady-state operating conditions. After the model is developed it is possible to implement the **optimal control strategy** on the controller, which requires work in defining the right amplitude, frequency and phase of the dither signal to be put into it. One of the control purpose options that still have to be chosen is the ESC - Extremum Seeking Control strategy, that will be explained in the next sub-section.

In chapter 2, a general description of the digital scroll compressor and the mathematical model to be developed is done.
In chapter 3 are described the experimental facilities, as the psychrometric chamber, the data acquisition system and the air-to-air heat pump that were used during the experiments.
In chapter 4, the outputs of a first compressor-oriented investigation are reported with a description of the experimental methodology, the results and what concerned the model validation.
In chapter 5 are reported the outcomes of the tests that were conducted in the second stage on the upgraded unit, with an investigation on the performances and on the effects that the pulsing flow imposed by the compressor had on the behavior of the system. Preliminary results on a temptative dynamic operation are reported, too.
In chapter 6 are described the conclusions and the future developments for the project.

1.2 The control purposes: Extremum Seeking Control

Extremum seeking is a non-model based real-time optimization approach for dynamic problems where only limited knowledge of a system is available, such as when the system has a nonlinear equilibrium map which has a local minimum or maximum [1]. It is possible to use extremum seeking to tune a set point to achieve an optimal value of the output (the value that minimizes or maximizes the output), or the parameters of a feedback law [2].
This method is based on a gradient search: after the plant is perturbated with a *dithering signal*, $d_2(t)$, a gradient-proportional signal is extracted through a demodulation and filtering process.
Driving the gradient to zero (this means optimality) closes the loop.

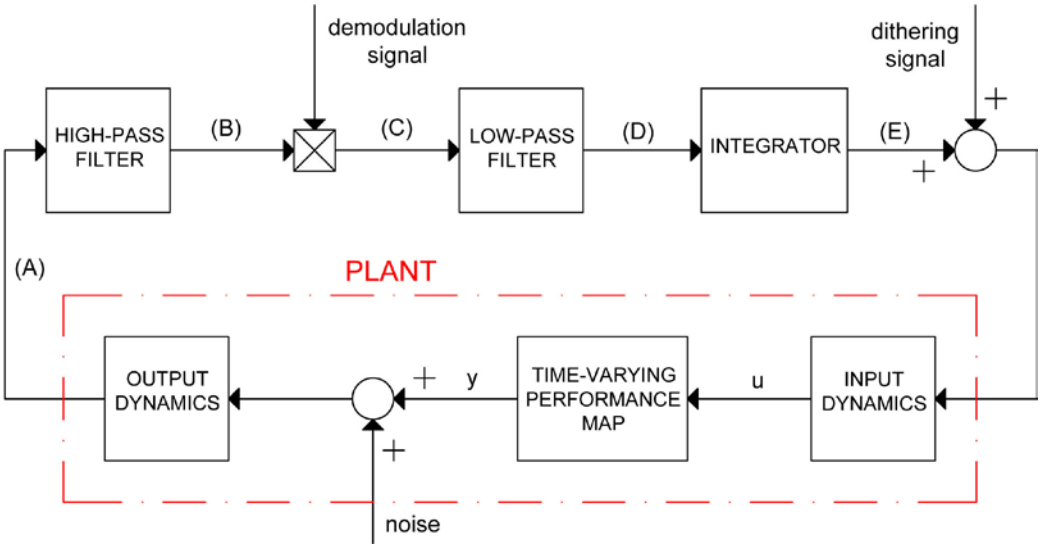

Figure 1.1. Block diagram showing the ESC control loop.

A simplified scheme of the ESC control loop is shown in figure 1.1 where:

- (A) represents the overall plant signal $l(u + a\sin(\omega t))$ and is made of:
  - INPUT DYNAMICS (F_1), which means for example the time between when the flow rate is set to increase and when this happens;
  - TIME-VARYING PERFORMANCE MAP ($l\,(t,u)$);
  - OUTPUT DYNAMICS ($F_0\,(s)$), which is for example the speed at which a sensor settles.

By expanding the signal with a Taylor series, we obtain (F_1 and F_0 will be neglected, which is a good approximation if the dithering signal $d_2(t)$ frequencies are not too high):

$$l(u + a\sin(\omega t))) = l(u) + a\sin(\omega t)\frac{dl}{du} + (\dots) \qquad (1)$$

- (B) is the signal modified by the HIGH-PASS FILTER, which has a $\frac{s}{s+\omega}$ shape, and removes the $l(u)$ component since what is really interesting is just the gradient, and retains the high-frequency component;
- (C) is the DEMODULATION SIGNAL, which has a $d_1(t) = sin(\omega t)$ shape, so that we obtain, by using trigonometric properties:

$$d_1(t)\, y_{hp} = \sin(\omega t)\left[a\sin(\omega t)\frac{dl}{du} + (\dots)\right] = \frac{a}{2}\frac{dl}{du} - \frac{a}{2}\frac{dl}{du}cos(2\omega t) \quad (2)$$

- (D) is the signal passing through a LOW-PASS FILTER, which has a $\frac{\omega}{s+\omega}$ shape, and retains the *dc* component proportional to the gradient. That allows us to get rid of the $cos(\dots)$ term, because the goal is to converge to steady-state while this term keeps perturbing the system.

- (E) allows to close the loop by getting a gradient-proportional signal $\frac{a}{2}\frac{dl}{du}$ that needs to be sent to zero, after having the signal increased so that no noise is left.

In order to implement the ESC kind of strategy into the controller, the input dynamics needs to be determined, so that it is possible to determine the characteristics of the dithering signal:

$$d_2(t) = a \cdot \sin(\omega t + \phi) \quad (3)$$

where
ω is the dither frequency;
a is the dither amplitude;
ϕ is the dither phase.

The dither frequency ω is suggested by the input dynamics, and means how fast the system has to be perturbed.
The dither amplitude a is also important because it can both cause a phase shift in the dynamics and if it is too small it can be mistaken as noise, as the dithered signal itself cannot be discriminated from the noise.
It also has to be determined how much phase shift ϕ is accumulated in the system because it has to be compensated: in fact, the more the phase angle reaches the 90°, the more it seems to the solution gets closer because the gradient search approaches zero, but the goal is to have a 0° phase shift. This depends on the knowledge the user has on the system and its dynamics.

Chapter 2

The digital scroll compressor

2.1 Overall Information

The scroll compressor has become widely adopted in HVAC equipment due to its high efficiency, reliability, and low noise [3]. More recently, adaptations to standard on/off scroll compressors such as speed and capacity control mechanisms have facilitated increases in cooling cycle efficiency at part load conditions. The so-called digital scroll or rapid cycling scroll compressor (figure 2.1) is one such mechanism that operates by cycling the compressor on and off rapidly (with cycle period ≤ 30 seconds).

Figure 2.1. Picture of a digital scroll compressor (left) and picture of a digital scroll compressor mounted in the experimental set-up (right).

The rapid cycle period is composed of an “on” or loaded state, and an “off” or unloaded state (see figure 2.4). During the loaded state, the fixed scroll is held in place by an axial compliance mechanism. This standard feature of many scroll compressors minimizes tip leakage by maintaining a tight seal between the

orbiting and fixed scroll [4], shown in figure 2.2. During the unloaded state, a valve is opened to relieve the back pressure chamber to the suction pressure, reducing the load on the fixed scroll. The fixed scroll is lifted, and compression no longer occurs, though roughly constant power is drawn, as the motor continues to spin the orbiting scroll freely [5]. The capacity modulation is achieved by varying the fractional "on" time of the compressor (loaded state) on the total cycle time. This sort of capacity control is chosen for its reliability, efficiency gains over conventional scroll compressors [6], and to approach the performance capabilities of the variable speed system without the costly inverter technology [7].

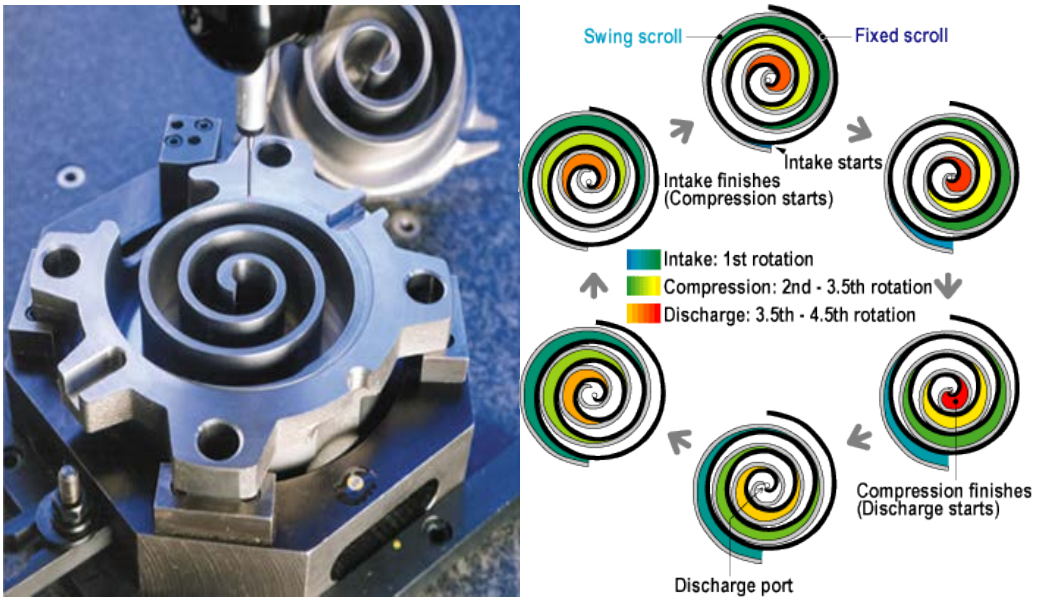

Figure 2.2. View of the two scrolls (left) and simplified representation of the compression phases of a scroll compressor (right).

This kind of compressor is being used mainly for these three potential reasons, which occur stronger than in a conventional scroll compressor:

a) Tight temperature and humidity control through load matching
b) Compressor reliability (so its lifespan) increase when it is left on, and there are fewer transient on/off cycles
c) Energy savings through modulating power.

The variation of the thermal power delivered by the digital scroll compressor is obtained by the separation in the axial direction of the two spirals. This mechanism, which is called axial compliance, allows the fixed scroll to lift, and the scrolls to unmate stopping compression and eliminating mass flow of refrigerant at discharge.

By using a solenoid valve, in fact, it is possible, by filling a back pressure chamber, to make the discharge chamber of the compressor, which is located at high pressure, communicate with its inlet section that instead is at a lower pressure (see figure 2.3). This determines a pressure difference on both sides of a piston (modulating piston) which is connected to the movable scroll and allows a translational motion in the vertical direction of the orbiting scroll and the consequent decoupling from the fixed scroll.

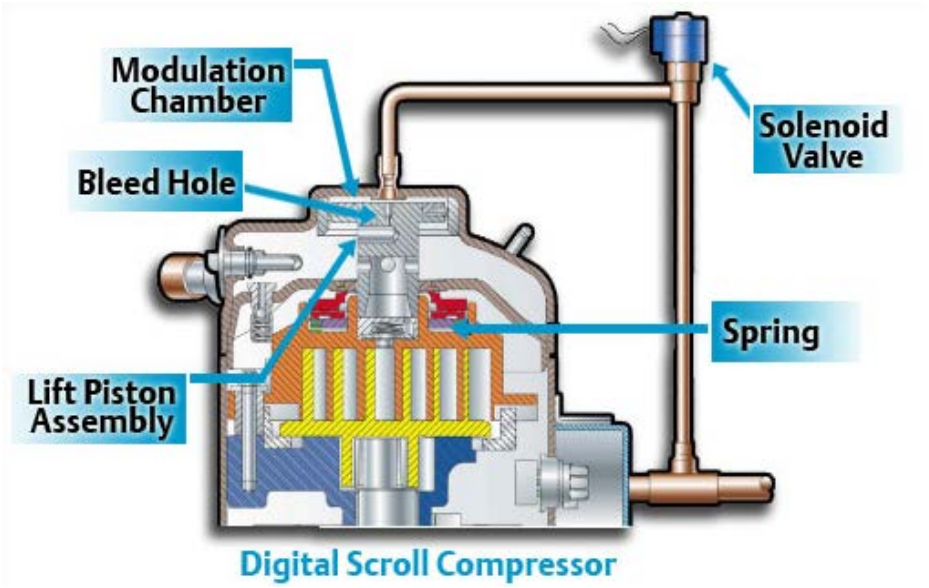

Figure 2.3. Vertical section of the top of the digital scroll compressor.

In this phase (unloaded state, shown in figure 2.4), the fluid between the two spirals, which is separated by the fluid located in the discharge chamber through a non-return valve, is put into motion by the movable scroll, however without undergoing any compression, and such a no-load operation determines a power consumption of approximately 10% of rated power input. Note that through the "bleed hole" that connects the discharge chamber with the modulation chamber there is a fluid flow, but this is not a real by-pass because it does not involve compressed fluid flow.

During the compression phase (loaded state, shown in figure 2.4), the solenoid valve is not energized, and this interrupts the connection between the modulation chamber and the intake section. Consequently, the high-pressure fluid in the discharge chamber, through the bleed hole, causes the rapid pressure increase in the modulation chamber, the balance of the forces acting on the piston and its lowering to the "natural" position. So the spirals are coupled and consequently the system delivers maximum thermal power. The modulation of the thermal power occurs then by pulsing flow, which means using a suitable succession of compression (maximum thermal power) and non-

compression/decoupling (zero-thermal capacity), while there are no intermediate stages of coupling. In particular, when the valve is opened, the modulation chamber back pressure is relieved to suction, lifting the fixed scroll by approximately 1 mm, so that compression and mass flow are suspended. So during this unloaded state, the motor spins freely.

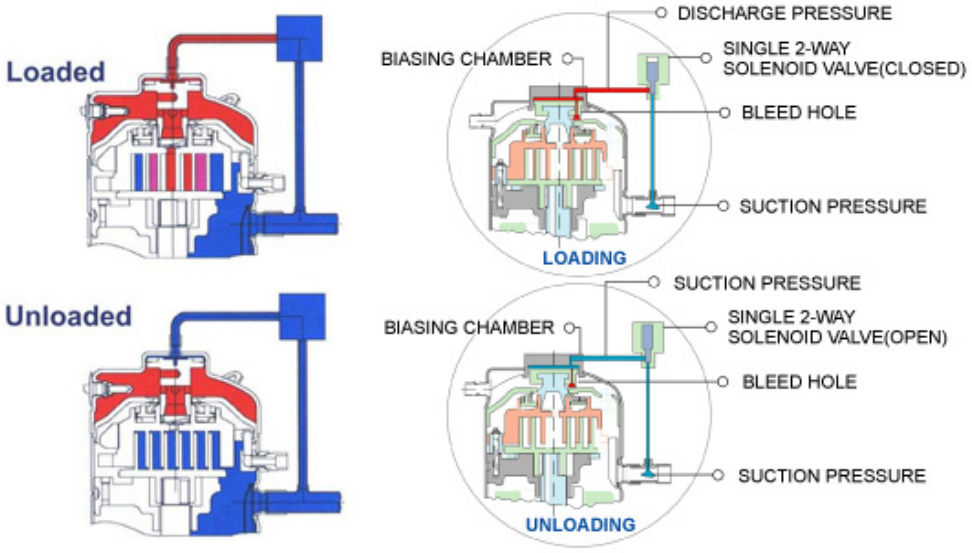

Figure 2.4. Loaded and unloaded state and operation of the solenoid valve.

The fractional on time, or the duration of the loaded state of the cycle is based on the load ratio (see figure 2.5), and optimal cycle time can vary with load ratio. It's important to get to know the optimal cycle time and this is why a sharp modeling of the compressor starts to get crucial.
The trend of the electric power absorbed by the compressor is very similar to the trend of the provided thermal power. The difference is that during the non-compression phase the compressor absorbs an electric power that is about 10% of the nominal power, which is necessary to keep the two spirals rotating, but causes energy dissipation (see figure 4.12). The absorption of electric inrush current is the same as a conventional scroll compressor fixed speed.

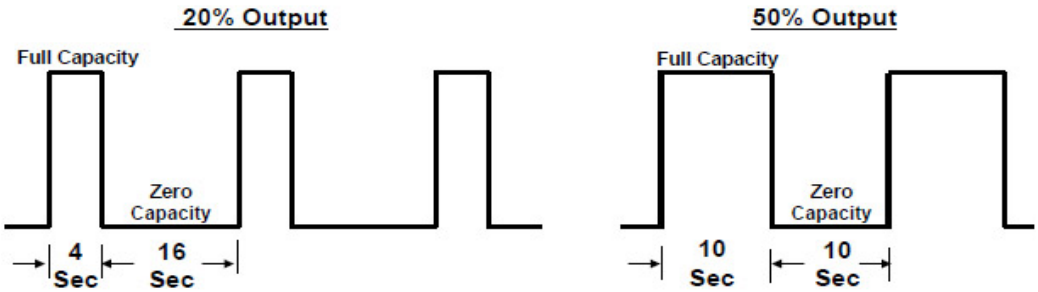

Figure 2.5. Examples of modulation (20% and 50% load) of a digital scroll compressor with a time cycle of 20 s.

The two parameters that have to be established for the compressor operation are therefore the regulation of the ratio between the time of the non-compression phase and the time of the compression phase (in the range 10% to 100%) and the total cycle time, i.e. the sum of the time interval during which the spirals are coupled and the time interval during which the spirals are decoupled.
The recommended total cycle time is in the range 15 s to 30 s, longer times may influence the proper cooling of the engine, and therefore its operational life, while shorter times have effects the entire system efficiency but not on the heating of the motor. The duration of every single phase must not be less than 2 s, for a correct decoupling of the spirals. Still, it's commonly assumed that the optimal total cycle time depends on the application.

2.2 Digital scroll compressors' performance enhancements over the inverter technology

Wide Capacity Range
The digital scroll compressor is characterized by an extended operating range, (from 10% to 100% of the nominal heat output), wider than the operating range that it is possible to obtain, with the same thermal power output, with compressors equipped with inverters, where capacity outputs can only be achieved in steps. In fact these compressors' operating frequency range is from 30 Hz to 100 Hz, so they can deliver a minimum thermal capacity which is equal to 40% of the nominal thermal capacity, while further reductions are reachable only by by-pass mechanisms of the compressed vapor which, on the other hand, introduce additional energy dissipation, or by an on-off succession of the compressor, in analogy to a fixed speed compressor. Digital scroll capacity output is continuous and seamless; the seamless delivery of capacity also ensures that there is a very tight control on room air temperature. A wide capacity output also contributes to a high seasonal energy efficiency (ESEER) of

the system. Start-stops of the compressor consume more energy. The wider capacity output of the Digital Scroll reduces the number of start- stops.

Rapid pull down
Quick pull down of room temperature and quick adjustment to demands are essential for indoor comfort. Digital scroll, because it can slide from 100% capacity to 10% capacity or vice versa instantaneously by changing the loaded and unloaded cycle time, can react to the changes in system demand much faster without having to pass through intermediate speed changes, which is necessary in the inverter systems.

Oil return
Oil return is a major issue in variable capacity multiple evaporator systems. Current technologies use an oil separator and/or complicated oil return cycle to ensure oil return after some period of operation. The digital scroll is a unique compressor – it does not require an oil separator or an oil return cycle.
Unlike a scroll compressor equipped with an inverter, the oil return is not a problem since it leaves the compressor only at the end of the compression phase (that has limited duration at minimum loads) and is carried by vapour that has enough speed. There are 2 factors that make the oil return easy. Firstly, the oil leaves the compressor only during the loaded cycle. So at low capacities, very little oil leaves the compressor. Secondly, as explained before, the compressor operates at full capacity during the loaded cycle. The gas velocity in the loaded cycle is sufficient to return oil back to the compressor.
For this project, oil separators have been installed anyway, in order to prevent any potential problems of oil return.

Dehumidification
Dehumidification is necessary to ensure customer comfort and this becomes more important during low modulation operation. In the inverter system, at low modulation, the compressor operates at a lower frequency. This reduces the mass flow of refrigerant and results in a higher suction pressure. This results in a higher Sensible Heat Factor (SHF). The digital scroll compressor provides very good dehumidification because it operates at a lower suction pressure than the inverter. As mentioned before, during any modulation output, the compressor operates at full capacity during the loaded part of the cycle. This full capacity operation results in a lower average suction pressure that leads to a lower SHF.

Electromagnetic Interference
Electromagnetic interference is a major issue in inverter driven systems. In many countries, particularly Europe, there are strict regulations on the amount of electromagnetic interference that any device can emit. The digital scroll system generates negligible electromagnetic interference because the loading and

unloading of the scrolls is a mechanical operation. This unique feature not only eliminates the need for expensive electromagnetic suppression electronics, it also adds to the reliability and simplicity of a Digital system.

Reliability
In an inverter system, the electronics is typically complicated and exposing this complicated electronics to the uncertainties in installation and the extremes of weather, results in reliability issue. The situation is made further complex by the usage of various bypasses (hot gas bypass and liquid bypass). The evident bottom-line is that complex systems have a higher probability of failure. The digital scroll system is fundamentally simple.

Refrigerant Bypass Circuits
Hot gas bypass and liquid bypass is used in most of the present technology options. These protection devices are required because the compressor is not able to go down to very low capacities. The digital scroll is able to go down to as low as 10% capacity and so these bypasses are not required, resulting in cost savings and system simplicity.

2.3 Literature review

Digital scroll compressors are relatively new in the HVAC field, but some studies were already made on its behavior and, in general, on how a system reacts when cycling the compressor faster than a common on/off compressor does.
Ilic, Bullard, Hrnjak [8] studied the effects of on/off cycle times shorter than a typical heat exchanger, with a varying from 10 to 80 seconds cycle period and found that the performances were little worse than a continuous (simulating variable speed) operation of the compressor.
Poort, Bullard [7] presented a study on the applications/control of air conditioning systems using rapid cycling to modulate capacity which was focused on the evaporator side and how the refrigerant properties in the evaporator itself are affected by the short-cycling.
Hu, Yang [9] reported the results from the development and performance testing of a cost effective, energy efficient, multi-type air conditioner that connected five indoor units (evaporators) to one outdoor unit (condenser) with a digital scroll compressor and considered this technology as 20% less costly than a comparable system with an AC inverter.
Tu, Dong, Zou, Lin [10] made a comparison between a 13 kW multi-split air conditioner with a digital scroll compressor and a standard compressor and developed a control model that can be used to solve the frequent on-off

phenomenon of the standard compressor and oscillation of the operation parameters.
Zhang W., Zhang C. [5] developed a transient model of a multi-split air conditioner with a digital scroll compressor for predicting the system transients under performance modulations.
Huang et alii [6] conducted an experimental study on operation characteristics with variable air volume under refrigerating and heating condition of ducted air conditioning (AC) unit with digital scroll compressor and conventional scroll compressor and showed that the system is good for the economical and reliable operation of the unit.
Joppolo, Molinaroli [11] developed an experimental testbed of an AC system equipped with digital scroll compressor and studied its performance, that show that they are better than a fixed speed air conditioner, both at full load and part load conditions, but worse than a variable speed (equipped with inverter) air conditioner.

2.4 Technical specifications

In this sub-section are reported the technical specs of the Copeland 7,5 ton ZPD83KCE digital scroll compressor provided by Emerson. Table 2.1 shows the specs about nominal capacity, nominal COP, pressure limits, geometric size, weight, oil quantity and so on. More detailed specs about cooling capacity and electrical power are displayed in table 2.2. In figure 2.6 it is possible to see the standard operating envelope for the compressor (the blue one) which encloses all the possible operating points changing both the condensing temperature and the evaporating one.
Further info about performance, mechanical and electrical features are available in figure 2.7.

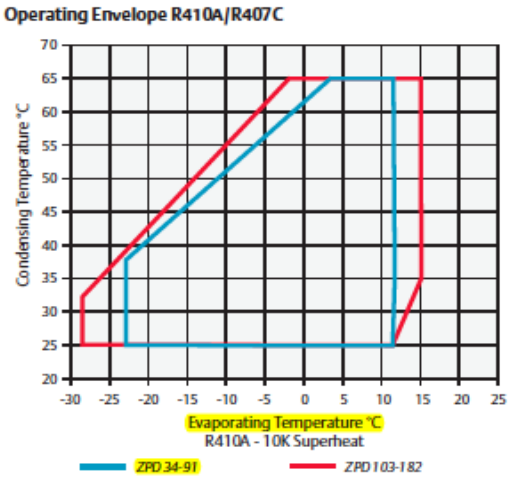

Figure 2.6. Envelope of the possible operating points of the ZPD digital scroll compressor.

Table 2.1. Main specifications of the ZPD83KCE digital scroll compressor

MODEL		ZPD83KCE
Nominal hp		6,00
Capacity (kW)		17,70
COP		3,00
Displacement (mc/h)		13,40
Oil q.ty (l)		1,77
Length/Width/Heigth (mm)		241/246/484
Net Weight (kg)		40,00
Max Operating Current (A)		16,00
Sound pressure @1m (dBA)		64,00
Max allowable Pressure Suction (bar)		28,00
Max allowable Pressure Discharge (bar)		43,00

Table 2.2. Cooling capacity and power input at different evaporating and condensing temperature of the ZPD83KCE digital scroll compressor.

	Condensing Temperature +40°C						
	Cooling Capacity (kW)/Power Input (kW)						
MODEL	**-15**	**-10**	**-5**	**0**	**5**	**10**	
ZPD83KCE	9,7/4,5	11,9/4,6	14,4/4,7	17,2/4,7	20,5/4,8	24,1/4,9	

	Condensing Temperature (°C)	Evaporating Temperature (°C)								
		-20	**-15**	**-10**	**-5**	**0**	**5**	**7**	**10**	**12,5**
Capacity (kW)	**30**	9,10	11,10	13,50	16,30	19,45	23,00	24,55	27,00	29,10
	40	7,90	9,70	11,85	14,35	17,20	20,50	21,90	24,15	26,10
	50			10,10	12,30	14,80	17,70	19,00	21,00	22,80
Power input (kW) -	**30**	3,54	3,63	3,70	3,76	3,82	3,89	3,93	3,99	4,05
	40	4,32	4,48	4,59	4,68	4,74	4,80	4,82	4,86	4,89
	50			5,61	5,77	5,89	5,98	6,01	6,04	6,07
Operating Conditions: 10K Suction Superheat, 0K Liquid Subcooling										

ZPD83KCE-TFD

HFC, R-410A, 60Hz, 3- Phase, 460 V
Air Conditioning

Production Status: Available for sale to all U.S. customers. Please check with your local Emerson Climate Technologies Representative for international availability.

Performance

Evap(°C)/Cond(°C)	7.2 / 54.4	7.2 / 37.8
RG(°C)/Liq(°C)	18.3 / 46.1	18.3 / 29.4
Capacity (Watts)	24300	29600
Power (Watts):	8000	5800
Current (Amps):	12.30	10.00
EER (COP):	3.05	5.10
Mass Flow (g/s):	154	157
Sound Power (dBA):	78 Avg	83 Max
Vibration (mm(peak-	0.051 Avg	0.076 Max
Record Date:	2006-03-17	

Mechanical

Number of Cylinders:	0	Displ(cm^3/Rev):	77.20
Bore Size(mm):	0.00	Displ(meters^3/hr):	16.21
Stroke(mm):	0.00		
Overall Length (mm):	240.7	Mounting Length (mm):	190.50
Overall Width (mm):	246.3	Mounting Width (mm):	190.50
Overall Height (mm):	494.2	Mounting Height (mm):	500.6 *

Suction Size (mm):	22 7/32 Stub
Discharge Size (mm):	12 11/16 Stub
Oil Recharge (ml):	1656
Initial Oil Charge (ml):	1774
Net Weight (kg):	40.78
Internal Free Volume (cm^3):	
Horse Power:	

*Overall compressor height on Copeland Brand Product's specified mounting grommets.

Electrical

LRA-High*:	100.0	MCC (Amps):	19.7	UL File No:
LRA-Half Winding:		RPM:		UL File Date:
LRA Low*:		Max Operating Current:	16.5	
RLA(=MCC/1.4;use for contactor selection):		14.1		
RLA(=MCC/1.56;use for breaker & wire size		12.6		

*Low and High refer to the low and high nominal voltage ranges for which the motor is approved.

Alternate Applications

Refrigerant	Freq (Hz)	Phase	Voltage	Application
R-410A HFC	60	3	460	A/C, 50% Load Of Compressor
R-410A HFC	50	3	380/420	A/C, 50% Load Of Compressor
R-410A HFC	50	3	380/420	Air Conditioning

Figure 2.7. ZPD83KCE rating.

2.5 Mathematical model

A large number of scroll compressor models have been developed building upon early work in the 1980's [12],[13]. A detailed model of the hermetic scroll compressor using R-22 [3] and R-410A [14] has been developed, incorporating a number of subsystem models that detail the compression process to determine temperature, mass flow rate and pressure of the discharge refrigerant. The detailed model includes development of the scroll geometry, the compression process model, suction and discharge process models, flank and radial leakage models, and heat transfer to and from the refrigerant. Also included is the mechanical/motor loss model due to friction, used to determine compressor shaft power, and motor electrical input power. This type of model is complex, but comprehensive and verified experimentally.
Another approach to scroll compressor modeling that has been taken is to construct a simplified model with the purpose of reducing the computational effort in order to incorporate the model in the larger simulation of an HVAC system [15]. This type of model is offered for situations when a limited number of compressor parameters are known, and simplifies the compression process model, heat transfer model, and electromechanical loss model. The model was constructed for R-22, but when adapted to study various other refrigerants [16,17] an inability to accurately predict discharge temperature was observed.

While scroll compressor modeling is fairly mature, there has been little in the way of digital scroll compressor modeling. One study incorporated a model of a digital scroll compressor into a larger vapor compression cycle model [5], but did not attempt to account for the physics of the model, but instead incorporated the ARI (*Air-conditioning and Refrigeration Institute*) standard n-term polynomial approximation as a stand-in for the compression process. During the off-cycle portion of the rapid cycle, the compressor was treated as off, but with a small constant (or nearly constant) power input to keep the motor driving the orbiting scroll spinning freely (idle cycle). Another study [18] did in fact produce a model of the digital scroll that treats the problem as an energy balance on four chambers developed by the compression process, but the model details are vague and it is difficult to determine the reasoning behind its development.

Anyway, the compressor model will be one of the key aspects of all the project, because it deals a lot with the prediction of the unit’s performances, and this allows the simulation to get close to a realistic operation of the system. From the experimental point of view, the model will be considered as validated if the compressor map that we are going to build is matching what the numerical simulation provides as output.

As a general overview of the modeling process, the project's goals are to feed the simulation with two main parameters: the **refrigerant inlet state** and the **inlet mass flow rate**. The corresponding outputs the model is wanted to provide are the **outlet mass flow rate**, the **refrigerant outlet state** (*h, T, p*) and the **power absorbed by the compressor**.

By considering some important aspects of the compressor such as geometry, compression process, leakages, axial compliance, heat transfer and motor, which all have to be modeled, it should be able to reach a satisfying look of the model, which has the goal to be validated by the experimental evidence.

2.5.1 Volume model

The physical geometry model for an asymmetric scroll chamber presented by Chen [3] is adapted, [18] that develops the scroll wrap geometry via the involute of a circle, with the orbiting scroll being offset by 180° and through a distance such that the involutes are in conjugacy defined by:

$$\varphi_k = \varphi_e - \theta - (k-1)2\pi \tag{4}$$

where:
θ is the orbiting angle defined so that at θ = 0 and k = 1 the tip of the orbiting scroll is in conjugacy with the fixed scroll,
φ_e is the ending angle of the orbiting scroll, and
φ_k is the point of conjugacy.

These angles are defined with respect to the fixed scroll, not the orbiting scroll, that is offset through radians. The distinction is important for the development of scroll chamber volumes. The suction chamber volumes are defined by:

$$V_{s1} = h\left(\frac{1}{2}\int_{\varphi_k-\pi}^{\varphi_e-\pi} L_{io}^2 d\varphi - \frac{1}{2}\int_{\varphi_k-2\pi}^{\varphi_e-2\pi} L_{of}^2 d\varphi\right) \tag{5}$$

$$V_{s2} = h\left(\frac{1}{2}\int_{\varphi_k}^{\varphi_e} L_{if}^2 d\varphi - \frac{1}{2}\int_{\varphi_k-\pi}^{\varphi_e-\pi} L_{oo}^2 d\varphi\right) \tag{6}$$

There is a distinct difference between the angle of conjugacy in equation (5) and that in equation (6). The angle of conjugacy in equation (5) is for the mating of the inner involute of the orbiting scroll and the outer involute of the fixed scroll. The angle of conjugacy in equation (6) is for the mating of the outer involute of the orbiting scroll and the inner involute of the fixed scroll. These two angles are

not the same, and in fact are π radians different. This is a critical distinction to make when computing the volumes of the chambers.
Then,

$$V_{s1} = \frac{1}{2} h r_b r_o \left(2\vartheta\varphi_e - \theta^2 - \frac{3}{2}\theta\pi \right) \tag{7}$$

$$V_{s2} = \begin{cases} \frac{1}{2} h r_b r_o \left(2\theta\varphi_e - \theta^2 - \frac{3}{2}\theta\pi + 2\pi\varphi_e - \frac{\pi^2}{2} \right) & \text{for } 0 \le \theta \le \pi \\ \pi h r_b r_o \left(2\varphi_e - 2\theta + \frac{1}{2}\pi \right) & \text{for } \pi \le \theta \le 2\pi \end{cases} \tag{8}$$

where
V_{s1} is the Suction Chamber 1 volume
V_{s2} is the Suction Chamber 2 volume
h is the height of the scroll
L_{io} is the length of the inner involute of the orbiting scroll = $r_b(\varphi - \varphi_{i0o})$
L_{of} is the length of the outer involute of the fixed scroll = $r_b(\varphi - \varphi_{o0f})$
L_{if} is the length of the inner involute of the fixed scroll = $r_b(\varphi - \varphi_{i0f})$
L_{oo} is the length of the outer involute of the orbiting scroll = $r_b(\varphi - \varphi_{o0o})$
r_b is the radius of the base circle
φ_0 is the initial angle of the involute of the circle
r_o is the orbiting radius = $r_b\pi - t$
t is the orbiting wrap thickness = $r_b(\varphi_{i0} - \varphi_{o0})$

A correction was applied for the offset distance associated with the motion of the orbital scroll, adjusting equations (5) and (6). The inclusion of the offset gives the equations:

$$V_{s1} = \frac{1}{2} h r_b r_o \left(2\theta\varphi_e - \theta^2 - \frac{3}{2}\theta\pi + 2(1 - cos\theta) - 2(\varphi_e - \pi)sin\theta - \frac{\pi}{4} sin(2\theta) \right) \tag{9}$$

$$V_{s2} = \frac{h}{2} r_b r_o \left(2\theta\varphi_e - \theta^2 - \frac{3}{2}\theta\pi + 2\pi\varphi_e - \frac{\pi^2}{2} + 2(1 + cos\theta) + 2(\varphi_e) sin\theta - \frac{\pi}{4} sin(2\theta) \right) \quad (10)$$

when $0 \leq \theta \leq \pi$ and

$$V_{s2} = \pi h r_b r_o \left(2\varphi_e - 2\theta + \frac{1}{2}\pi \right) \quad (11)$$

when $\pi \leq \theta \leq 2\pi$

For modeling purposes, the wish is to know the derivative terms with respect to the orbiting angle θ,

$$\frac{dV_{s1}}{d\theta} = \frac{1}{2} h r_b r_o \left(2\varphi_e - 2\theta - \frac{3}{2}\pi - 2(\varphi_e - \pi) cos\theta - \frac{\pi}{2} cos(2\theta) + 2sin\theta \right) \quad (12)$$

$$\frac{dV_{s2}}{d\theta} = \frac{1}{2} h r_b r_o \left(2\varphi_e - 2\theta - \frac{3}{2}\pi - 2sin\theta + 2\varphi_e cos\theta - \frac{\pi}{2} cos(2\theta) \right) \quad (13)$$

for $0 \leq \theta \leq \pi$ and

$$\frac{dV_{s2}}{d\theta} = -2\pi h r_b r_o \text{ for } \pi \leq \theta \leq 2\pi \quad (14)$$

for $\pi \leq \theta \leq 2\pi$

It is important to note that the volume equations 5-14 are valid only over a range from $0 \leq \theta \leq 2\pi$. After orbiting angle 2π is reached, the volume of refrigerant vapor transitions to the compression chambers of the scroll compressor. The compression process largely takes place in the compression chamber by reduction of the volume of the compression pockets as the refrigerant vapor transitions from suction to discharge regions of the scroll mechanism.
The suction chambers define the openings that draw the refrigerant volume into the compression process, but as the orbiting scroll seals the chambers, compression chambers 1 and 2 develop. The volumes of these chambers is defined in a fashion similar to that of the suction chambers.

$$V_{c1} = h\left(\frac{1}{2}\int_{\varphi_k-3\pi}^{\varphi_k-\pi} L_{io}^2 d\varphi - \frac{1}{2}\int_{\varphi_k-4\pi}^{\varphi_k-2\pi} L_{of}^2 d\varphi\right) \tag{15}$$

$$V_{c2} = h\left(\frac{1}{2}\int_{\varphi_k-3\pi}^{\varphi_k} L_{io}^2 d\varphi - \frac{1}{2}\int_{\varphi_k-3\pi}^{\varphi_k-\pi} L_{of}^2 d\varphi\right) \tag{16}$$

In the evaluation of the compression chamber volume, there is a difference between the angle of conjugacy used in equation (15), and that in equation (16). Equation (15) describes the mating between the inner involute of the orbiting scroll and the outer involute of the fixed scroll, while compression chamber 2 describes the mating between the inner involute of the fixed scroll and the outer involute of the orbiting scroll.
Solving for the values of the compression volumes in terms of orbiting angle θ gives the following expressions

$$V_{c1} = V_{c2} = 2\pi h r_b r_o \left(2\varphi_e - 2\theta - \frac{7}{2}\pi\right) \tag{17}$$

$$\frac{dV_{c1}}{d\theta} = \frac{dV_{c2}}{d\theta} = -2\pi h r_b r_o \tag{18}$$

These equations are valid in a specific range of orbital angle where the compression pockets exist, for $0 \leq \theta \leq \varphi_d$ where φ_d is the discharge angle and is defined as:

$$\varphi_d = \varphi_e - 3\pi - \varphi_{os} \tag{19}$$

φ_{os} is the outer starting angle of the scroll involute, and in [19] is given as a geometric parameter. At φ_d, the refrigerant vapor enters the discharge process. The discharge volume in [3], [19] behaves according to

$$V_{d1} = 2h\left(\frac{1}{2}\int_{\varphi_{os}+\pi}^{\varphi_k} L_i^2 d\varphi - \frac{1}{2}\int_{\varphi_{os}}^{\varphi_k} L_o^2 d\varphi\right) + V_{cl} \tag{20}$$

where

$$\varphi_k = \begin{cases} \varphi_e - 2\pi - \theta & \text{if } 0 \leq \theta \leq \varphi_d \\ \varphi_e - \theta & \text{if } \varphi_d \leq \theta \leq 2\pi \end{cases} \tag{21}$$

so

$$V_{d1} = hr_b r_o \left({\varphi_k}^2 - (\varphi_{os} + \pi)^2 - \frac{3\pi}{2}\left(\varphi_k - (\varphi_{os} + \pi)\right) \right) + V_{cl} \qquad (22)$$

where

$$V_{cl} = h{r_c}^2 \left(\pi - sin^{-1}\left(\frac{2r_b}{r_c}\right) - \frac{2r_b}{r_c} \right) \qquad (23)$$

giving

$$\frac{dV_{d1}}{d\theta} = hr_b r_o \left(-2\varphi_k + \frac{3\pi}{2} \right) \qquad (24)$$

The term r_c is given only as a parameter in this model, but a relationship for r_c is developed in [15], and will not be repeated here.
The equations for V_{d1} are again valid only for $0 \leq \theta \leq 2\pi$. To examine a volume of refrigerant as if flows from suction to discharge, one must carefully examine the orbital angle using this method. For increasing angles of orbital angle during the compression process for example, one must use $\theta - 2\pi$ in place of θ, and for determining φ_k with (20) use $\theta - 2\pi$ in place of θ when $\varphi_d \leq \theta \leq 2\pi$, and use $\theta - 4\pi$ in place of θ when $0 \leq \theta \leq \varphi_d$.

2.5.2 Leakage model

Leakage between the scroll chambers occurs due to small gaps between the contacting surfaces, and is included in the compressor model because it can result in a significant decrease in compressor efficiency. While theoretically the scrolls mate ideally, realistic tolerances mean that there is finite spacing at the interfaces, forming a leakage path. The driving force for the leakage flow is the difference in fluid pressure between the chambers, with refrigerant flowing from a region of higher pressure to lower pressure. This requires the volume that leaks to be compressed again, and thus constituting the efficiency loss. In terms of mathematics, a leakage model is defined by an expression for the area through which the leakage occurs, and an expression for the mass flow rate of leakage. We adapt the leakage model from Wang et al [20].
In this model two types of leakage are simultaneously in existence, that between scroll flanks, and that between scroll tips. Tip leakage occurs due to nonzero clearances between the base of a scroll plate and the tip of the involute scroll wrap. Flank leakage occurs due to nonzero clearances between mating scrolls at points of conjugacy. The driving force for the leakage mechanism is the pressure

difference across the leakage gap. The model uses an assumption of isentropic mass flow rate through an orifice to characterize the leakage flow, excepting the no flow and choked flow scenarios. The no-flow scenario occurs when upstream and downstream pressures are equal.

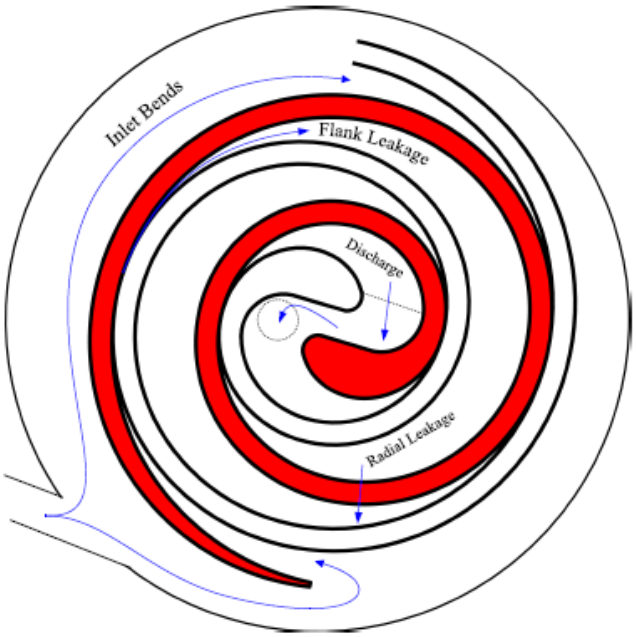

Figure 2.8. Mass flows in the scroll compressor.

Otherwise, when $\left(\frac{P_d}{P_u}\right) \geq \left(\frac{2}{k+1}\right)^{k/(k-1)}$ is true, then

$$\dot{m} = cA_f \sqrt{P_u \rho_u \frac{2k}{k-1} R_p^{2/k} - R_p^{(k+1)/k}} \tag{25}$$

c is contraction coefficient
A_f is leakage flow area between flank surfaces
P_u is upstream pressure
k is isentropic expansion coefficient
R_p is pressure ratio = $\left(\frac{P_d}{P_u}\right)$
P_d is downstream pressure

However , when $\left(\frac{P_d}{P_u}\right) < \left(\frac{2}{k+1}\right)^{k/(k-1)}$ then the choked flow equation holds.

$$\dot{m} = cA\sqrt{k\rho_u P_u \left(\frac{2}{k+1}\right)^{(k+1)/(k-1)}} \tag{26}$$

The leakage area is developed for both in-flowing and out-flowing refrigerant, and is dependent upon the leakage length. The Wang et al. [20] geometry model for leakage distances along the tips of the involutes have been specified for generic initial angles, just as the geometry for the compression volumes themselves. The formulation is given in terms of leakage length, and dependent upon the crank angle; a is the radius of the base circle that defines the geometry of the involute.

For radial outflow:

for $0 \leq \theta \leq \pi$

$$L = \int_{\varphi_e - \theta}^{\varphi_e} a\left(\varphi - \frac{\alpha_i + \alpha_o}{2}\right) d\varphi \tag{27}$$

for $\pi \leq \theta \leq 2\pi$

$$L = \frac{a}{2}\left(2\pi\left(\varphi_e - \frac{\alpha_i + \alpha_o}{2}\right) - \pi^2\right) \tag{28}$$

for $2\pi \leq \theta \leq 3\pi$

$$L_1 = \int_{\varphi_e - \pi}^{\varphi_e + 2\pi - \theta} a\left(\varphi - \frac{\alpha_i + \alpha_o}{2}\right) d\varphi \tag{29}$$

and

$$L_2 = \int_{\varphi_e + \pi - \theta}^{\varphi_e - \pi} a\left(\varphi - \frac{\alpha_i + \alpha_o}{2}\right) d\varphi \tag{30}$$

for $3\pi \leq \theta \leq \varphi_e - \frac{\pi}{2} + \theta^*$

$$L = \int_{\varphi_e + \pi - \theta}^{\varphi_e + 2\pi - \theta} a\left(\varphi - \frac{\alpha_i + \alpha_o}{2}\right) d\varphi \tag{31}$$

For radial inflow:

for $0 \leq \theta \leq \pi$

$$L = \int_{\varphi_e - \pi - \theta}^{\varphi_e - \pi} a\left(\varphi - \frac{\alpha_i + \alpha_o}{2}\right) d\varphi \tag{32}$$

for $\pi \leq \theta \leq \varphi_e - \frac{5\pi}{2} + \theta^*$

$$L = \int_{\varphi_e - \pi - \theta}^{\varphi_e - \theta} a\left(\varphi - \frac{\alpha_i + \alpha_o}{2}\right) d\varphi \tag{33}$$

for $\varphi_e - \frac{5\pi}{2} + \theta^* \leq \theta \leq \varphi_e - \frac{\pi}{2} + \theta^*$

$$L = \frac{a\pi}{2}\left(4\pi - 2\theta^* - (\alpha_i + \alpha_o)\right) \tag{34}$$

For flank outflow:

for $0 \leq \theta \leq 2\pi$

$$L = r(1 - cos\theta) + \delta_f \tag{35}$$

otherwise

$$L = \delta_f \tag{36}$$

Flank inflow is equal to outflow (except for the case, as the suction backflow term is not applicable).

A volume discretization methodology whereby existence of the volumetric elements is constant and simultaneous allows for leakage calculations at every time step. By contrast, the continuous volume evolution employed here does not allow for calculation of leakage between volume elements because of the lack of simultaneous existence of volume elements. To compensate for this lack, one must exploit the object-oriented nature of Modelica by instantiating three separate and distinct compressor volume elements.
Recalling that the suction chamber exists between orbital angles of 0 and 2π, whereat the refrigerant in the suction chamber enters the compression chamber,

and the suction chamber reopens to allow entry to the flow of suction gas. Thus, in order to model the continuous evolution of the suction chamber (and by extension the compression and discharge chambers) a second instance of the volume (refer to it as V_2) is initiated with a delay of 2π radians, and a third instance (refer to as V_3) is initiated with a delay of 4π radians. In this way we can guarantee the simultaneous existence of appropriate volume chambers (suction, compression, discharge) ensuring that the mechanism driving the leakage between adjacent chambers, the difference in refrigerant pressures, is accurately determined.

2.5.3 Thermodynamics

Once the equations for the change in the scroll volume have been developed, we can apply fluid dynamic equations to the refrigerant in the system. A continuity of mass equation defines the variation in the density of the system. Development follows:
The definition of density:

$$\rho = \frac{m}{V} \tag{37}$$

then, taking the derivative:

$$\frac{d\rho}{dt} = \frac{\left(\frac{dm}{dt}\right)V - m\left(\frac{dV}{dt}\right)}{V^2} = \frac{\left(\frac{dm}{dt}\right) - \rho\left(\frac{dV}{dt}\right)}{V} \tag{38}$$

where

$$\frac{dm}{dt} = \dot{m}_{in} - \dot{m}_{out} \tag{39}$$

The temperature equation is derived from conservation of energy.

$$\frac{dE_{cv}}{dt} = \frac{dU_{cv}}{dt} = m\left(\frac{du}{dt}\right) + u\left(\frac{dm}{dt}\right) \tag{40}$$

The energy balance for an open system:

$$\frac{dE_{cv}}{dt} = \dot{Q} + \dot{W} + \sum \dot{m}\left(h + \frac{v^2}{2} + gz\right)_{in} - \sum \dot{m}\left(h + \frac{v^2}{2} + gz\right)_{out} \tag{41}$$

Neglecting kinetic and potential energies we have:

$$\frac{dE_{cv}}{dt} = \dot{Q} + \dot{W} + \sum \dot{m}\, h_{in} - \sum \dot{m}\, h_{out} \tag{42}$$

From the definition of internal energy:

$$dU = TdS - PdV \tag{43}$$

$$dS = \left(\frac{\partial S}{\partial T}\right)_V dT + \left(\frac{\partial S}{\partial V}\right)_T dV \tag{44}$$

$$dU = T\left(\frac{\partial S}{\partial T}\right)_V dT + \left[T\left(\frac{\partial S}{\partial V}\right)_T - P\right] dV \tag{45}$$

From the definition for specific heat at constant volume

$$T\left(\frac{\partial S}{\partial T}\right)_V dT = c_v \tag{46}$$

and substituting

$$\left(\frac{\partial S}{\partial T}\right)_V = \left(\frac{\partial P}{\partial T}\right)_v \tag{47}$$

we can give an expression for change in internal energy as:

$$du = c_v dT + \left[T\left(\frac{\partial P}{\partial T}\right)_v - P\right] dv \tag{48}$$

but is more useful to describe the specific heat

$$c_v = \left(\frac{\partial h}{\partial T}\right)_v - \left(\frac{\partial P}{\partial T}\right)_v v \tag{49}$$

then taking the derivative for internal energy

$$\frac{du}{dt} = \left(\left(\frac{\partial h}{\partial T}\right)_v - \left(\frac{\partial P}{\partial T}\right)_v v\right)\frac{dT}{dt} + \left[T\left(\frac{\partial P}{\partial T}\right)_v - P\right]\frac{dv}{dt} \tag{50}$$

and again utilizing a definition for enthalpy:

$$u = h - Pv \tag{51}$$

Then, substituting:

$$\begin{gathered}\frac{dU_{cv}}{dt} = m\frac{du}{dt} + u\frac{dm}{dt} = \\ = m\left\{\left(\left(\frac{\partial h}{\partial T}\right)_v - \left(\frac{\partial P}{\partial T}\right)_v v\right)\frac{dT}{dt} + \left[T\left(\frac{\partial P}{\partial T}\right)_v - P\right]\frac{dv}{dt}\right\} + (h - Pv)\frac{dm}{dt}\end{gathered} \tag{52}$$

and the definition for energy:

$$\begin{gathered}\dot{Q} + \dot{W} + \sum \dot{m}\, h_{in} - \sum \dot{m}\, h_{out} = \\ = m\left\{\left(\left(\frac{\partial h}{\partial T}\right)_v - \left(\frac{\partial P}{\partial T}\right)_v v\right)\frac{dT}{dt} + \left[T\left(\frac{\partial P}{\partial T}\right)_v - P\right]\frac{dv}{dt}\right\} + (h - Pv)\frac{dm}{dt}\end{gathered} \tag{53}$$

or:

$$= \left[m\left(\frac{\partial h}{\partial T}\right)_v - \left(\frac{\partial P}{\partial T}\right)_v V\right]\frac{dT}{dt} + \left[T\left(\frac{\partial P}{\partial T}\right)_v - P\right]\frac{dV}{dt} + (h - Pv)\frac{dm}{dt} \tag{54}$$

Substituting a definition for work

$$\dot{W} = -P\frac{dV}{dt} \tag{55}$$

and finally we have an expression for conservation of energy that can be utilized in the program for the change in temperature.

$$\begin{gathered}\left[m\left(\frac{\partial h}{\partial T}\right)_v - \left(\frac{\partial P}{\partial T}\right)_v V\right]\frac{dT}{dt} + \left[T\left(\frac{\partial P}{\partial T}\right)_v\right]\frac{dV}{dt} + (h - Pv)\frac{dm}{dt} = \\ = \dot{Q} + \sum \dot{m}\, h_{in} - \sum \dot{m}\, h_{out}\end{gathered} \tag{56}$$

The implementation for the fluid equations is straightforward in Modelica. The acausal modeling language allows us to enter the physical equations as constructed. The continuity of mass equation is utilized by the solver for determining density while the continuity of energy equation is utilized by the solver for determining temperature. The non-density terms in the continuity of

mass equation are the mass flow term and volume terms. The continuity of energy equation requires the implementation of the real gas model to instantiate enthalpy and pressure terms.

2.5.4 Real gas equation of state model

For the development of a stand-alone compressor model, a full analysis of the equation of state with a number of state variables is not needed.
The critical elements needed to examine the compressor are temperature, pressure, enthalpy, density, specific heats c_p and c_v. The specific heat values are currently required for the establishment of the specific heat ratio $k = \frac{c_p}{c_v}$ that is utilized in the mass flow rate equation of the leakage model. As a result, the current working real gas model is the simplified virial equation of state model of Baehr and Tillner-Roth [21] and utilized by Halm [22] for R-22 and Chen [19] for R-410A. The difference between the refrigerants is only the constant coefficients and not the equations themselves. Chen [19] established the coefficients for R-410A utilizing a large number of predefined points in the vapor region for the regression, and one can begin by approximating the properties of the refrigerant by this method.
These polynomial equations of state were developed around the Helmholtz energy function with independent variables density and temperature. These equations uses nondimensional independent variables by normalizing the temperature and density with $\tau = \frac{T_c}{T}$ and $\delta = \frac{\rho}{\rho_c}$ where T_c and ρ_c respectively are critical temperature and density for the refrigerant.

From this method, the establishment of the equations of state is as follows:

$$\frac{P(\tau,\delta)v}{RT} = 1 + \delta\left(b_1 + b_2\tau^{1/2} + b_3\tau^{11/4} + b_4\tau^{12}\right) + \\ +2\delta^2\left(c_1\tau^{-1/2} + c_2\tau^{11/4}\right) + 3\delta^3(d_1\tau^{12} + d_2\tau^{15} + d_3\tau^{20}) \tag{57}$$

$$\frac{h(\tau,\delta)}{RT} = a_1^*\tau + m_0 + \sum_{i=1}^{4}\frac{m_i v_i^0\tau}{exp\left(v_i^0\tau\right) - 1} \\ + \delta\left(b_1 + \frac{3}{2}b_2\tau^{1/2} + \frac{15}{4}b_3\tau^{11/4} + 13b_4\tau^{12}\right) \tag{58}$$

$$+\delta^2\left(\frac{3}{2}c_1\tau^{-1/2}+\frac{19}{4}c_2\tau^{11/4}\right)+\delta^3(15d_1\tau^{12}+18d_2\tau^{15}+23d_3\tau^{20})$$

Determination of the specific heat at constant specific volume c_v:

$$c_v=\left(\frac{\partial h}{\partial T}\right)_v-\left(\frac{\partial P}{\partial T}\right)_v v \tag{59}$$

This requires derivatives of the previous equations (57) and (58) with respect to temperature T. It must be recalled in taking the derivative that τ as a function of temperature T:

$$\frac{dP(\tau,\delta)v}{RdT}=1+\delta\left(b_1+\frac{1}{2}b_2\tau^{1/2}-\frac{7}{4}b_3\tau^{11/4}-11b_4\tau^{12}\right)+$$
$$+2\delta^2\left(\frac{3}{2}c_1\tau^{-1/2}-\frac{7}{4}c_2\tau^{11/4}\right)+3\delta^3(-11d_1\tau^{12}-14d_2\tau^{15}-19d_3\tau^{20}) \tag{60}$$

and

$$\frac{dh(\tau,\delta)}{RdT}=m_0+\sum_{i=1}^{4}\frac{m_i{v_i^0}^2\tau^2exp(v_i^0\tau)}{\left(exp(v_i^0\tau)-1\right)^2}+ \tag{61}$$
$$+\delta\left(b_1+\frac{3}{4}b_2\tau^{1/2}-\frac{105}{16}b_3\tau^{\frac{11}{4}}+143b_4\tau^{12}\right) \tag{61}$$
$$+\delta^2\left(\frac{9}{4}c_1\tau^{-1/2}-\frac{133}{16}c_2\tau^{11/4}\right)+\delta^3(-165d_1\tau^{12}-252d_2\tau^{15}-437d_3\tau^{20})$$

The specific heat at constant pressure c_p

$$c_p=c_v-\frac{T\left(\frac{\partial P}{\partial T}\right)_v^2}{\left(\frac{\partial P}{\partial v}\right)_T} \tag{62}$$

where

$$\frac{dP(\tau,\delta)}{dv}\frac{v^2}{-RT}=1+2\delta\left(b_1+b_2\tau^{1/2}+b_3\tau^{11/4}+b_4\tau^{12}\right)+ \tag{63}$$

$$+6\delta^2\left(c_1\tau^{-1/2}+c_2\tau^{11/4}\right)+12\delta^3(d_1\tau^{12}+d_2\tau^{15}+d_3\tau^{20})$$

The virial equation of state for R-410A is an augmentation of the ideal gas equation of state, containing residual components that supplement the ideal gas component to approximate the real gas behaviour. Because the only vapor region is considered in this study, the behaviours at the saturation limits, and particularly the establishment of phase concentration in the two phase regime are not required. Were these required, a full mixture model for R-410A would be necessary.
To implement the real gas model in Modelica, it is important to determine which variables must be determined algebraically, and which may be determined via differential equations. Though equations for the determination of $\frac{\mathrm{dP}}{\mathrm{dT}}$ and $\frac{\mathrm{dh}}{\mathrm{dT}}$ can be determined and implemented into Modelica, they are to be implemented algebraically only, and cannot be written as differential equations in an attempt to determine P or h. In utilizing this real gas model, temperature and density are the state variables required for the determination of the remaining properties. It cannot be assumed that it's possible to utilize the real gas equations of state as ODE's that are solving pressure and enthalpy dynamically. While it is possible to formulate the equations this way in Modelica, it requires temperature or density to be solvable from the equation of state, which is (particularly in the case of temperature) infeasible.
This is a particularly important point to realize when implementing with Modelica, considering its underlying solver architecture.
Future modeling to particularly include incorporation into a larger system model will likely require an alternative means of refrigerant property determination.

2.5.5 Discharge model

The discharge model is essentially a subset of the overall leakage model. The two principal components of the model are a mass flow rate equation defining the flow of refrigerant through the discharge opening, and the area of the flow.
In order to define the flow area, one can begin by assuming the valve model as presented by Halm [22], with a check valve sealing the discharge to prevent backflow. The degree of valve opening is modeled as proportional to the difference between the discharge chamber pressure and the discharge pressure.
This equation is given as:

$$y=(P-P_{dis})\cdot\frac{\left(A_{port}\right)}{c_{valve}} \tag{64}$$

where y is the valve opening distance, A_{port} is the area of the discharge port, and c_{valve} is the spring constant for the valve.

The flow area is calculated as

$$A_{dis} = y\pi d \tag{65}$$

with d the port diameter.

A simple mass flow rate equation based upon a Bernoulli flow related by [9] is utilized to determine the flow

$$\dot{m} = A_{dis}\sqrt{2(P - P_{dis})\rho_u} \tag{66}$$

2.5.6 Heat transfer model

The compressor model was initially constructed utilizing parameters taken from Chen [19] and verified against experimental data from the same study. It was found that without a heat transfer model in place, the model overpredicts the discharge refrigerant temperature. A simple heat balance model was added to the compressor shell such that the heat transferred to the ambient through the shell was balanced by the heat conducted to the surface of the hermetic shell:

$$Q = hA\left(T_{surface} - T_{ambient}\right) = \frac{kA}{x}\left(T_{refrigerant} - T_{surface}\right) \tag{67}$$

The convection coefficient was developed from a cylinder in cross flow assumption from the Hilpert correlation [23]:

$$\frac{h_{air}D}{k_{air}} = Nu = C_1 * {Re_D}^{C_2} * Pr^{\frac{1}{3}} \tag{68}$$

where $C_1 = 0{,}683$ and $C_2 = 0{,}466$ for $Re_D = 40 \div 4000$.

The Reynolds' number range was chosen by referring on the experimental data, In particular the diameter of the compressor shell was fixed, ρ and μ were a function of the psychrometric chamber (only outdoor room) operating conditions, and the velocity of the air was known by referring on the chamber properties and was considerable as constant. It was found that the Re_D values reached the minimum (906) with 46°C and the maximum (1024) with 25°C.

2.5.7 On/Off State transition

The actuation of the solenoid valve, relieving the back pressure chamber to suction, and the dynamics of the leaf spring in the axial compliance mechanism all introduce delay into the system. Transitions from "on" state to "off" state and vice versa do not occur instantaneously, so the transitioning between states is currently modeled as a trapezoidal pulse train in Modelica. The rising, falling and period parameters of the wave shape are fitted with experimental values and written into the Modelica code:

Modelica.Blocks.Sources.Trapezoid dpulse(amplitude = 1, period = , rising = , falling = , width =).

The duration of any single phase is a function of the compressor load, so it is possible to define the proper wave shape for any load. For further information on the wave shape approximation, see section 4.3.

2.5.8 Power model

The current modeling only considers an approximate power model and Halm [22] suggests the development of a power relationship on the basis of a motor-mechanical efficiency where:

$$\eta_{mot-mech} = \frac{\dot{W}_{compression}}{a_1 + a_2 ln\left(\frac{P_d}{P_s}\right) + a_3 \dot{W}_{compression} + a_4 \dot{W}_{compression} ln\left(\frac{P_d}{P_s}\right)} \quad (69)$$

and

$$Power = \frac{\dot{W}_{compression}}{\eta_{motor-mechanical}} \quad (70)$$

This is essentially a fit of the compressor power with respect to compression work, and a relationship of this sort does not easily incorporate into a dynamic simulation. It is dependent only upon initial and final states a definition of compression work can be taken as:

$$\dot{W}_{compression} = \dot{m}\left(h_{d_{average}} - h_s\right) \quad (71)$$

If we do a least squares regression of the power with the data available, the values of the coefficients $a_1 \ldots a_4$ that minimize error when approximating

power can be determined. It would be possible to incorporate a detailed motor model, however at this time, this is not deemed a primary focus of this effort.
The dynamic compressor model hasn't been incorporated into the simulation testbed yet, but there's been a lot of work toward experimental validation of the simulation model.

Finally, figure 2.9 shows a summary of what was explained above: by subtracting all the losses to the electrical power input, the goal was to reach an isentropic compression work rate which was as close to reality as possible.

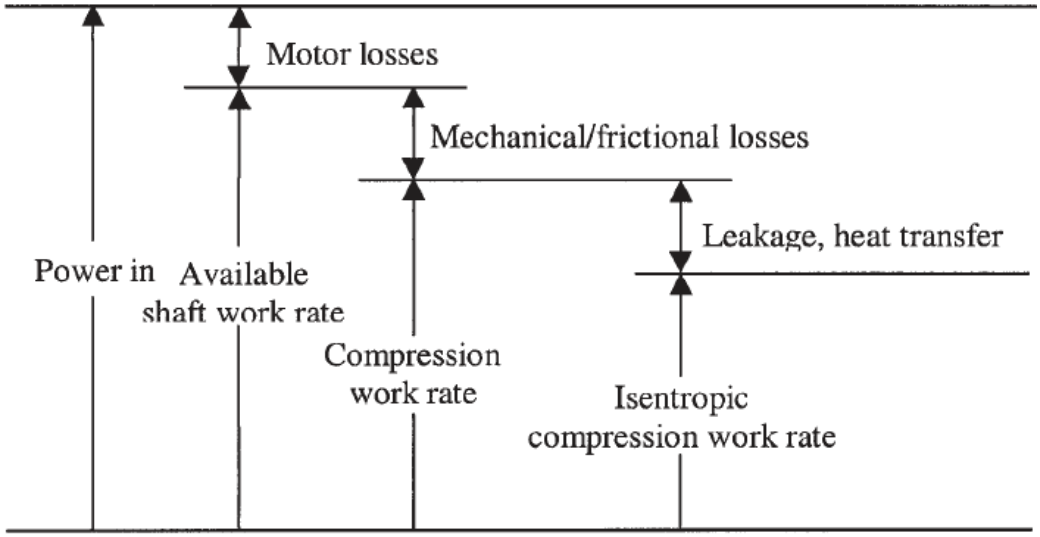

Figure 2.9. Basic energy balance for a scroll compressor.

2.5.9 Simulation Environment

The simulation environment considered in this investigation is Modelica, an object-oriented programming language that is designed for multi-domain modeling wherein a simulation may have mechanical, electrical, thermal-fluid segments etc. in the same system [24].
Unlike most programming languages, Modelica is not designed to process algorithms constructed from a series of assignment statements. Instead, it is an equation based language, and the fundamental physical equations defining the states of motion are used to develop the structure of a model.
Models are acausal, and equations are not required to be specified in terms of a single variable to be solved for. System modeling in Modelica can be developed using differential and/or algebraic equations, but is not limited to this structure.
The primary advantage of utilizing Modelica (via commercially available interface Dymola) simulation environment for development of dynamic system

models is the ability to develop system models utilizing the physical equations of motion rather than algorithms consisting of sequences of assignment statements, and allowing the solving routines to determine the variable states from the information. Additional advantages may include a more ready adaptability to whole building modeling for energy analysis of control strategies and energy optimization [25].
Modelica is gaining popularity as a modeling tool amongst HVAC practitioners for its advantages, and in a recent study [26], it was evaluated against MATLAB/Simulink [27] (including an additional MATLAB interface SimScape, a recently developed, equation-based extension to Simulink). An HVAC system was modeled and these platforms are evaluated in a comparison study of the transient, startup dynamics of simplified component models for a DX HVAC system. While the solutions evaluated similarly, the Modelica solution was found to be much more efficient in terms of computation time.

The validation of the model described in this section (2.5) is reported in section 4.4.

Chapter 3

The experimental apparatus

3.1 The experimental environment: The Oklahoma State University psychrometric chamber

The OSU Psychrometric Chamber is an environmental simulator consisting of two similar adjacent air conditioned rooms allowing test conditions such as temperature, humidity, and air flow rate to be controlled over a wide range; it is able to maintain conditions with the addition of internal thermal loading. It acts as an infinite heat source or sink by balancing the load that an HVAC unit rejects or absorbs in order to maintain a desired test condition.
The main focus of the chamber is to test unitary HVAC equipment, with one room artificially reproducing the outdoor climate conditions while the other room is employed to simulate the indoor environments and replicate indoor comfort conditions with thermal loads up to 15 tons[1] of refrigeration (53 kW). The chamber is not limited to testing unitary equipment however; each room can be operated independently in order to run a number of experiments requiring controlled ambient conditions.
The outdoor chamber simulates the outdoor weather having a design temperature range of -40°F to +130°F (-40°C to 54,4°C) and the indoor chamber replicates typical indoor environment with temperature ranging from 55°F to 100°F (12,8°C to 37,8°C). Additional specifications of the chamber are listed in table 3.1, and further details on the construction and design specifics of the chamber can be found in Cremaschi and Lee [28] and Lifferth [29].
The chamber was intentionally oversized to minimize the interference of the testing equipment with the walls and the ceiling of the chamber; it is sufficiently large to test a 15ton (53 kW) unit via its remarkable air conditioning design and capacity.

[1] Hereafter some data are first reported in I.P. units in order to justify their integer values (chosen according to ASHRAE standards, technical specifications or design values based on experience) and then converted to S.I. units.

Table 3.1. Psychrometric Chamber Specifications.

	Outdoor Chamber	**Indoor Chamber**
Dimensions	22x22x17 ft^3 (6,7x6,7x5,2 m^3)	19x22x17 ft^3 (5,8x6,7x5,2 m^3)
Temperature range	-40°F to 130°F (-40°C to 54,4°C)	55°F to 100°F (12,8°C to 37,8°C)
Relative humidity range	10% to 95%	20% to 90%
Maximum capacity of testing equipment	15 tons (53 kW) of refrigeration at -40°F (-40°C)	15 tons (53 kW) of refrigeration at 55°F (12,8°C)
Maximum weight of the testing equipment	3000 lb (1361 kg)	3000 lb (1361 kg)
Maximum air flow rate	8000 cfm (13592 m^3/h)	8000 cfm (13592 m^3/h)
Coils power	5,5 ton (19,3 kW) for each coil (double coil for each bay)	5,5 ton (19,3 kW) for each coil (single coil for each bay)
Heaters power	20 kW each (4 heaters for each bay)	20 kW each (2 heaters for each bay)
Maximum steam supply capacity of the humidifier	90 lb/h (40,9 kg/h)	90 lb/h (40,9 kg/h)
Average wall thermal transmittance	0,34 W/m^2K	0,34 W/m^2K

Uniform airflow distribution is ensured through a raised perforated floor design (see figure 3.1). Air is circulated through the conditioning loop using variable speed fans. The airflow rate can be adjusted and electro-mechanical dampers can be altered for controlling the distribution of the air to and from the under floor air plenum and ceiling return plenum. Utilizing an under floor air plenum and a ceiling return allows uniform conditions to be obtained throughout the entire room. Air flow from the conditioning loop passes through an under-floor supply plenum, and the room through perforated floor panels. In order to acquire better distribution in the supply plenum, perforated floor panels are designed to have 23%, 40% and 58% open area throughout the plenum. Roof panels with

cutouts for removable filters form the air return, with a return plenum above the chamber ceiling.

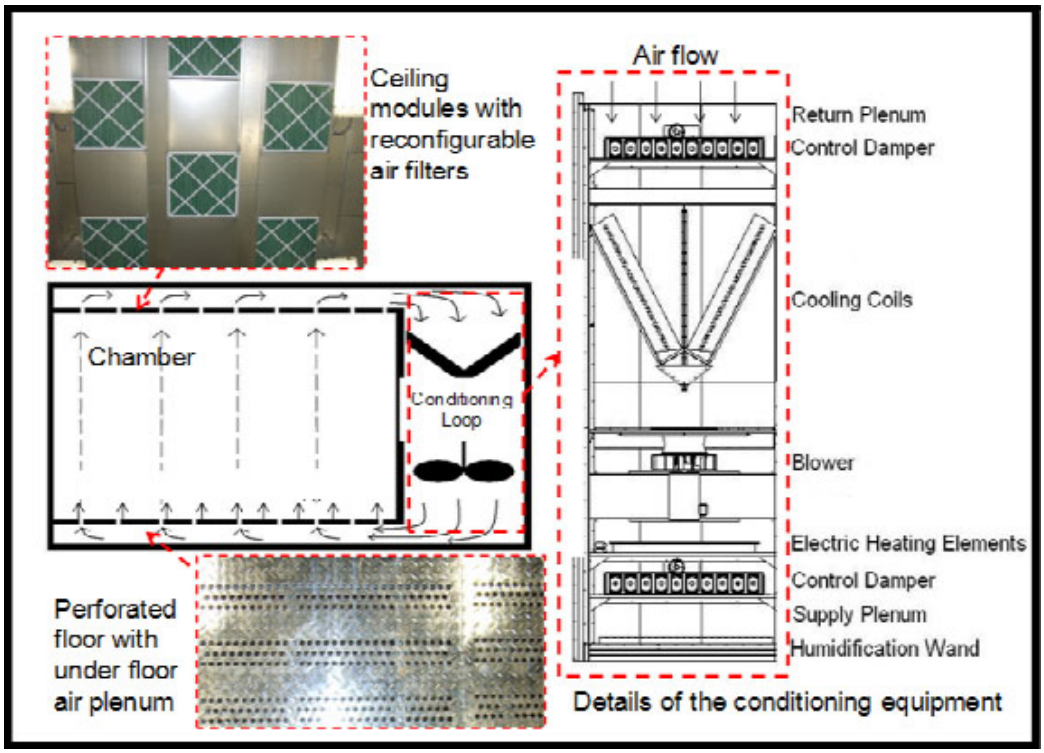

Figure 3.1. View of psychrometric chamber with details of the ceiling with reconfigurable air filters, of the perforated floor with under floor air plenum and of the chamber conditioning loop.

Uniform conditions are achieved in each room by first conditioning the air to the desired psychrometric states and then circulating it into the rooms. The first process the air encounters inside the conditioning loops is cooling and dehumidification by a set of cooling coils. The coils surface temperature and capacity are controlled by variable speed pumps, electronic mixing valves and electro-mechanical bypass valves. These parameters are adjusted so that the air is cooled and dehumidified below the desired room psychrometric state.

After being cooled and dehumidified, the air passes over electric resistance heating coils, which raise the air temperature up to the desired room temperature. The electric resistance heaters allow for precise temperature control with an almost immediate response time. Rapid fine tuning is performed to account for variation in the chamber response to a live load; that is, to any variation of the load of the unitary equipment running inside the facility during the test. The power to these heaters is controlled by a PID control algorithm

referencing the room dry bulb temperature. After passing over the electric heaters, air is passed over a steam wand where moisture is added to the air, raising the humidity to the desired state. The wand is connected to a steam generator that is also controlled by a PID control algorithm referencing the room wet blub temperature. The generator is capable of adding precise amounts of water vapor to the air. The control strategy is constructed so the cooling coils, having a large thermal inertia, are slowly changed while the heaters and steam generator are quickly adjusted to maintain desired conditions using the two PID algorithms working in parallel.

Each room has two conditioning loops and one air flow measurement apparatus, also known as code tester, as seen in figures 3.2 and 3.3. In the outdoor room, the conditioning loops and code tester are vertically arranged bays where Bay 1 and Bay 3 are conditioning loops and Bay 2 is the code tester located in between the conditioning loops. Air flow direction is downward in the conditioning bays and upward in the code tester (see figure 3.5). Each conditioning bay is equipped with air dampers, V-configured cooling coils, blowers and electric heaters. Dampers are opposite blade dampers modulating air flow, cooling coils are used to remove heat and moisture from the air stream, and centrifugal blowers with VFD controllers adjust flow rates of each conditioning loop. Electric heaters add sensible heat to air stream. As the air stream leaves the conditioning loop, a humidifier adds moisture if needed.
The Code tester (Bay 2) is equipped with air dampers, air diffusers, elliptical flow nozzles and a blower. Air dampers and blowers function the same as conditioning bays.
The diffusers located before and after elliptical nozzles constructed from perforated sheet metal having 40% free flow area in order to diffuse air stream for better static pressure measurements.
Flow nozzles are used to determine the air flow rate up to 8000 cfm (13592 m^3/h) according to ASHRAE Standards. There are seven flow nozzles installed in the code tester.

The outdoor room air is circulated through the conditioning loops as shown in figure 3.2 and 3.4.
The indoor room bays have the same arrangement as the outdoor room. The only differences between indoor and outdoor rooms are the number and size of the elliptical flow nozzles and the number of V-configured cooling coils as shown in the figures. Ten elliptical nozzles with different sizes were installed in Bay 5. Since the cooling need of the indoor room is less than the outdoor room, the number and size of cooling coils were reduced in the conditioning loops.

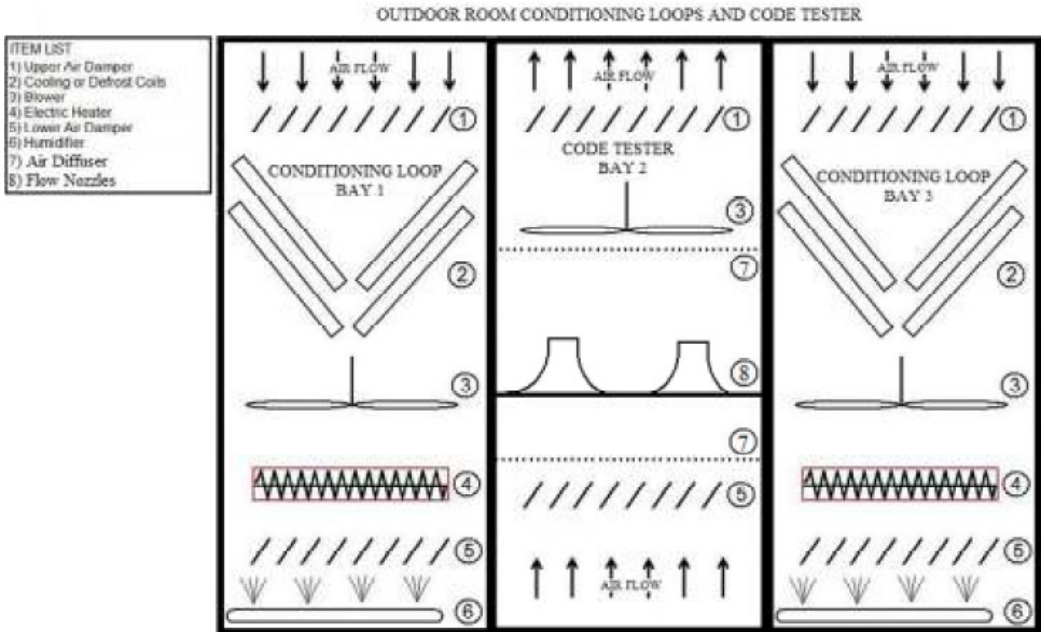

Figure 3.2. Diagram of outdoor room conditioning loops and code tester.

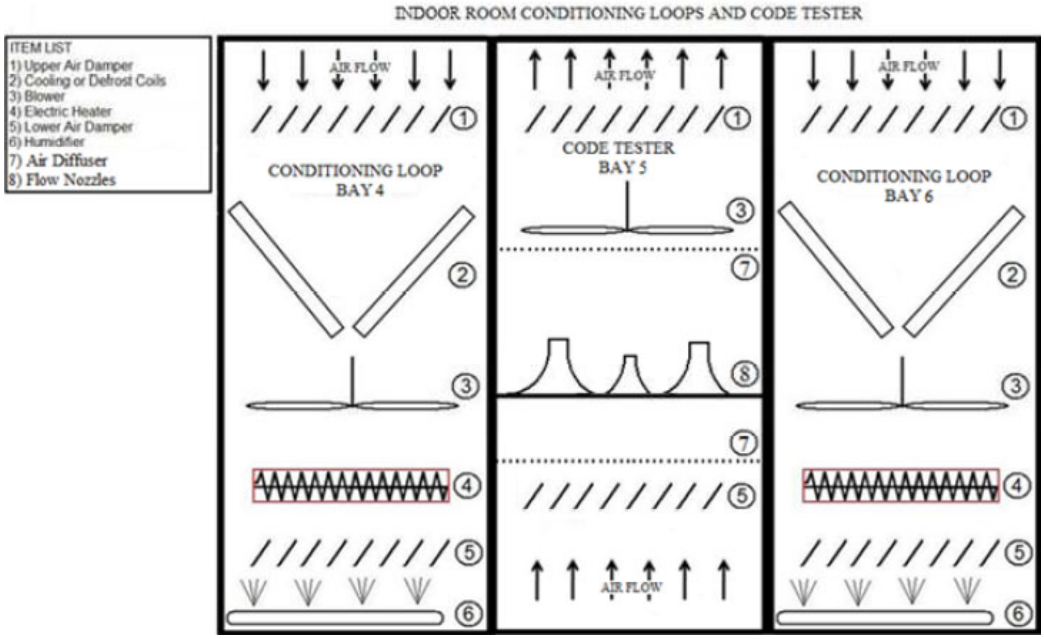

Figure 3.3. Diagram of indoor room conditioning loops and code tester.

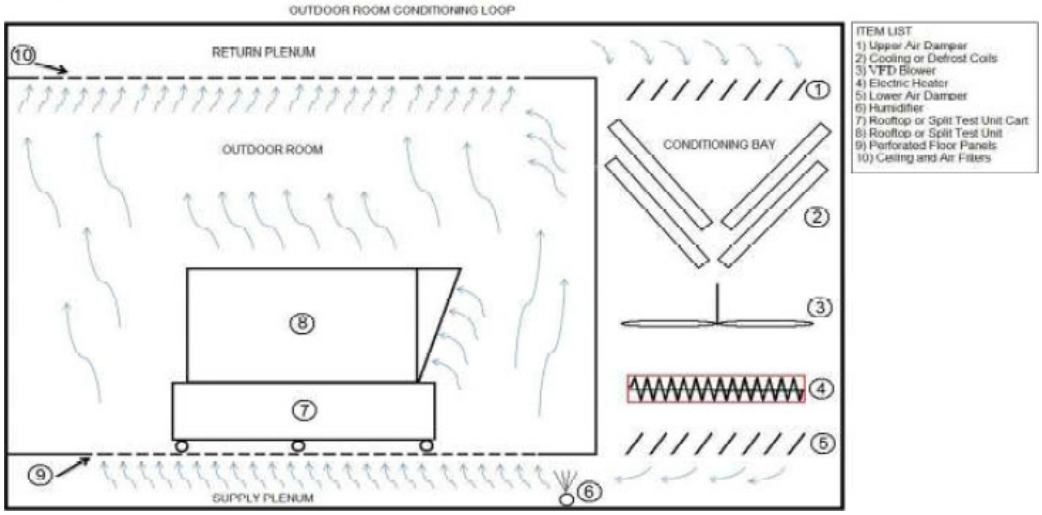

Figure 3.4. Outdoor room conditioning loop.

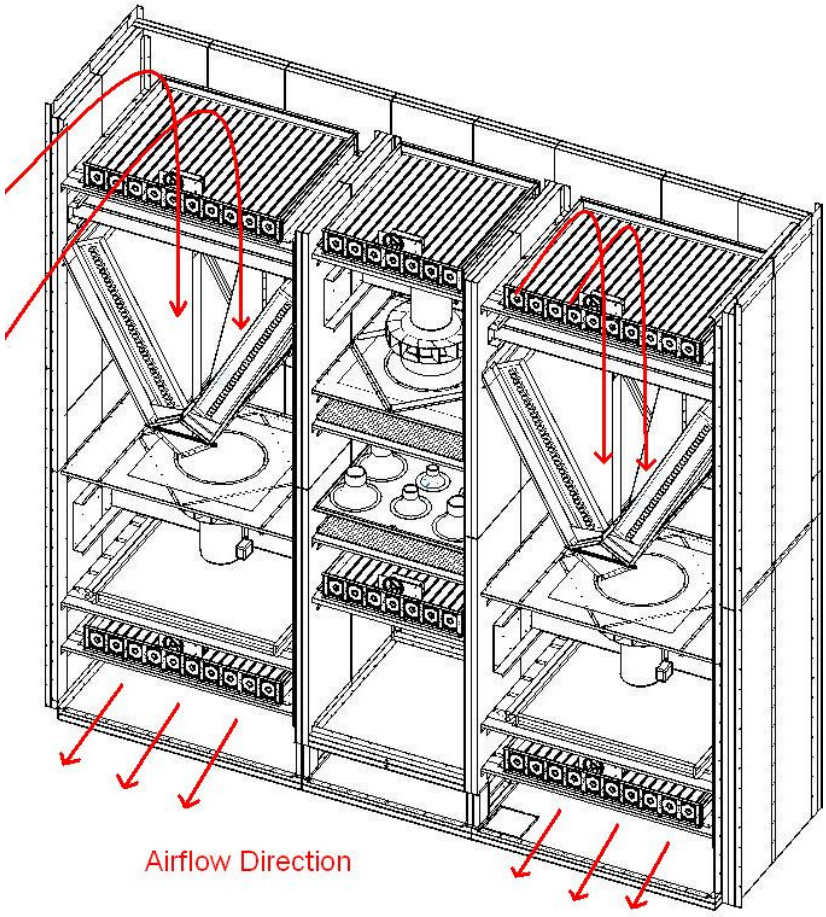

Figure 3.5. On the right and left side, the two conditioning bays. At the center, the code tester.

Before the air, which is conditioned by the unit being tested in the outdoor room, is supplied to the indoor space, it passes through an area of the chamber called the "code tester". The code tester is built in a flow nozzle bench (see figure 3.6). The flow nozzles are activated to measure different airflow rates by simply plugging certain flow nozzles to form the best configuration for the airflow measurements. More details about the design and fabrication of code tester can be found in Lifferth [29].
The pressure drop across the flow nozzles is directly measured to determine the airflow rate, while temperature and static pressure are also measured to determine density of the air. A variable speed blower and a set of precision dampers were also installed inside the code tester. The blower is used to account for the pressure losses caused by all the measuring devices located in the duct system connecting the unit being tested to the indoor room. With the variable speed blower the external static pressure experienced by the unit can be accurately controlled during the performance measurements.

Figure 3.6. Flow nozzle bench.

We report the calculation method for the volumetric air flow rate by using Equations (72) and (73) (ASHRAE 1995).

$$\dot{V} = 1096 C A_n \sqrt{p_v v'_n} \tag{72}$$

$$v'_n = \frac{29.92 v_n}{p_n(1 + \omega_n)} \tag{73}$$

where:
$\dot{V}$ is the volumetric flow rate of air through a single nozzle (cfm);
C is the coefficient of discharge for the nozzle (dimensionless);

A_n is the exit area of the nozzle (ft^2);
p_v is the pressure difference across the nozzle (in H_2O);
v'_n is the adjusted specific volume of the air at the nozzle (ft^3/lb);
v_n is the specific volume of the air as measured from wet and dry bulb temperatures;
assuming standard atmospheric conditions
p_n is the pressure at the nozzle throat (in Hg);
ω_n is the absolute humidity at the nozzle (lbs moisture/lbs dry air);

After having its properties measured in the code tester, the air is re-distributed to the indoor room through the other two conditioning bays.

The indoor and outdoor chambers are isolated from one another by insulated wall paneling, except for a single doorway. A separation door, a large 4-inch panel that fits in the doorway, has four 24 inch diameter holes that allow the supply and return air of the unit to pass through. It also isolates the indoor and outdoor room from one another so they can easily operate at different conditions.
The air temperature and pressure are measured directly at the unit supply and return locations. This is achieved with temperature sampling probes and static pressure taps secured immediately at the beginning of the duct system that connects the unit to the indoor room.
Two 24-inch ducts were chosen to minimize the pressure drop and maintain a low air velocity inside the duct. At each end of all the flexible ducts an adapter was installed. This allowed the ducts to be connected to any of the components (code tester, separation door, and unit cart), as well as insured good sealing between components and fast experimental setup time. The adapter converted the circular ducts to a flat plate with a bulb seal. It only took four bolts to attach or disconnect an adapter and flex duct from a component.

3.2 Data Acquisition System

3.2.1 Lab View

The built-in data acquisition system of the chamber was used for acquiring all the data from the sensors to the chamber computer for further processing. The details of the data acquisition system can be found in Worthington et al. [30].

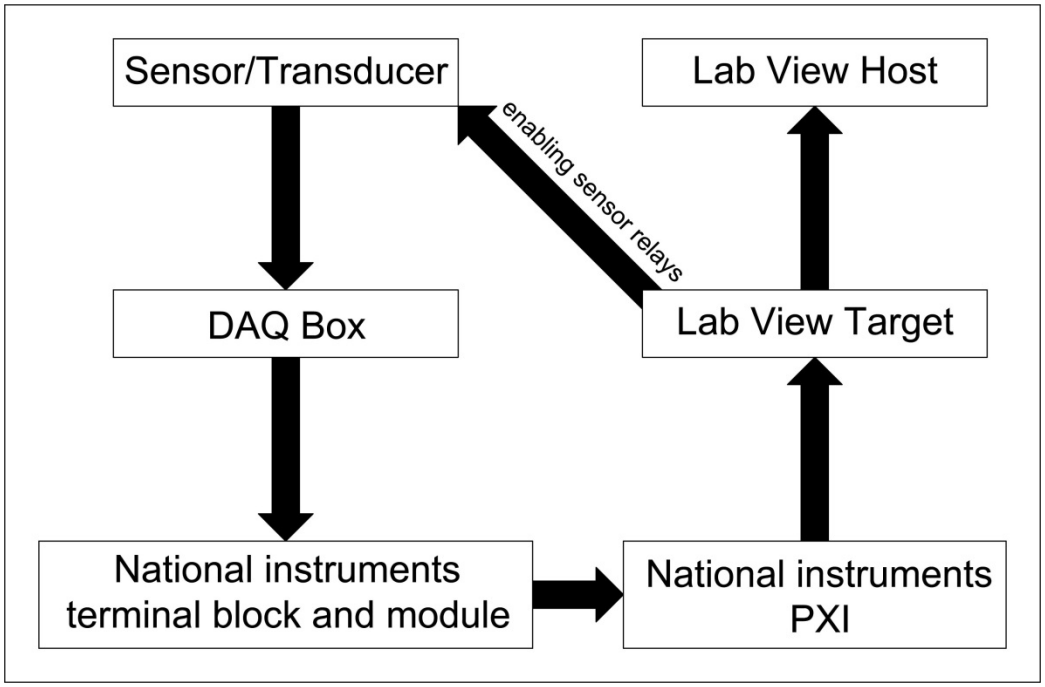

Figure 3.7. Data Flow Diagram for Lab View data acquisition system.

As shown in figure 3.7, all the sensors other than the thermocouples were powered using relays that can be turned on from the Lab View main program. Once the sensor is powered, it senses the corresponding quantity as a resistance and sends a current or voltage output through the wiring first to the DAQ box and then to the National Instruments PXI (open, PC-based platform for test, measurement, and control) via the terminal block and module. The signal is then sent to the main Lab View program named "Target". The signal is processed, converted to the variable value and then sent for further processing and monitoring to the secondary Lab View code called "Host".

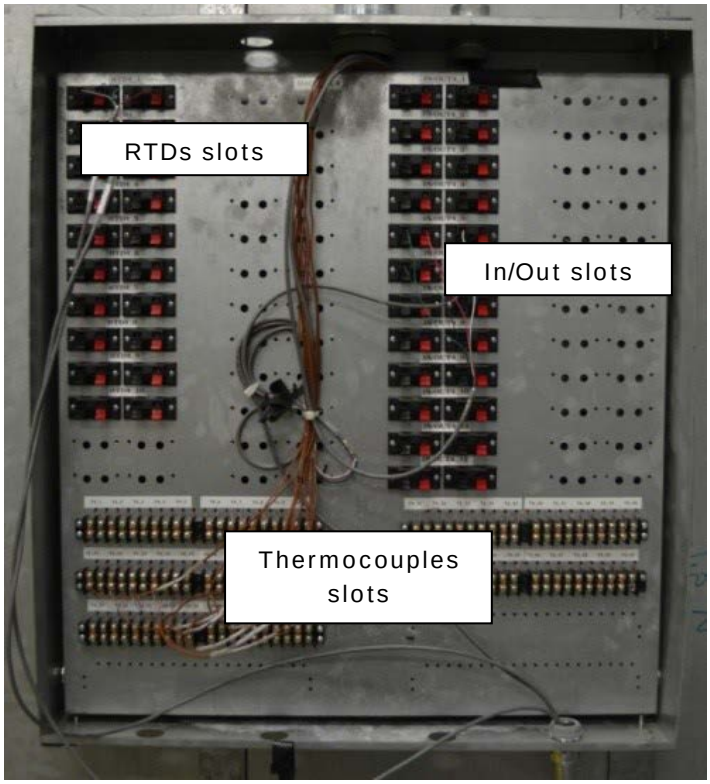

Figure 3.8. Data acquisition box: on the top left are the RTD channels, on the top right are the IN/OUT channels, at the bottom are the thermocouples channels.

The DAQ box (figure 3.8) works as a connection junction for the chamber DAQ and the sensors.
There are terminal strips for connecting the thermocouples and speaker connectors for connecting RTDs and other in/out signals (such as pressure transducers or flowmeters).
The DAQ box connects to the corresponding National Instruments terminal block and module, as shown in the figure 3.7. There are different dedicated modules for thermocouples, RTDs, relays and other input signals. All the modules are put into the slots of NI SCXI-1001 cards. There are two of them in the chamber DAQ system. The cards are connected via data cables to NI PXI-1042Q, which acts as a CPU. The Lab View program is loaded into the PXI.
When all the channels in the modules have been properly configured by automation explorer, (a program similar to an OS in a typical computer), the sensor output may be read into Lab View for further processing. Besides the two SCXIs, there are also 2 SCB-68 cards connected to the DAQ system, which can send analog or digital output signals. These are typically used for controlling variable frequency driven devices. All the channels in the DAQ system are referred to by index numbers in the order they are read by the PXI. There are

303 analog inputs (256 thermocouples, 32 high accuracy RTDs, 4 relative humidity probes, 8 differential air pressure transducers, 1 barometer, 2 watt transducers), 81 digital inputs and 192 analog outputs.
The Lab View real time software for the chamber had two main Virtual instruments (VI). The first one (Target), runs in the remote PXI while the other program (Host), runs on a typical CPU. The function of the target is to read values in all the sensors dedicated to the chamber, convert them to appropriate units, control and monitor the chamber conditioning, and ensure safe operation of the chamber equipment.
The data was processed in the Target and then sent to the Host computer for further processing. This additional processing includes things such as creating graphical user interfaces and plotting graphs dedicated to individual projects. Both the Target and Host programs were designed with user friendly graphical interfaces that make monitoring the system intuitive.

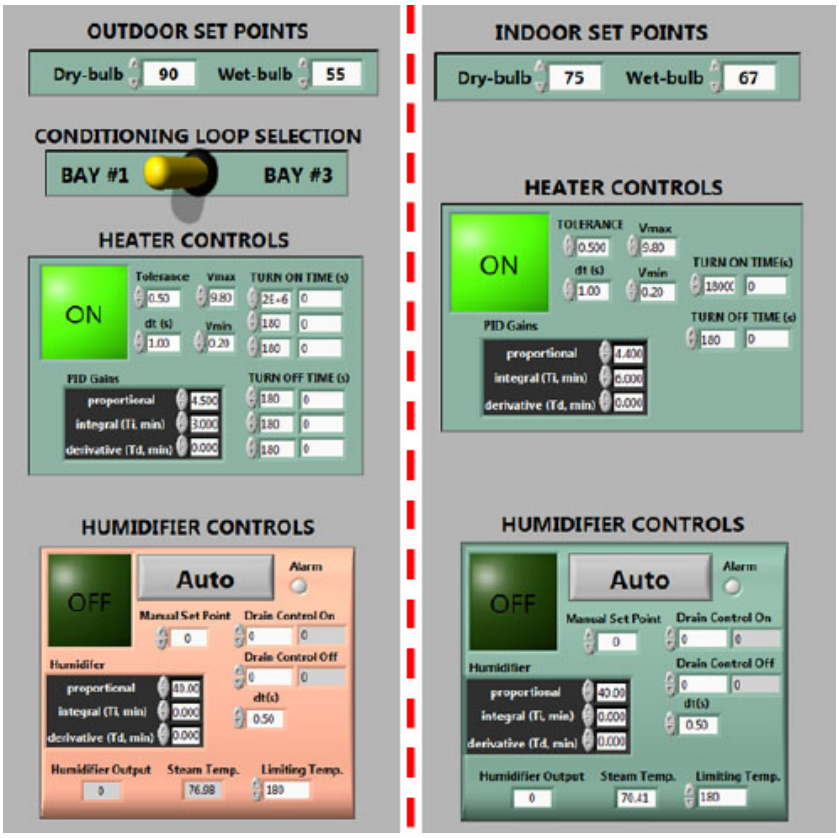

Figure 3.9. The outdoor and indoor room conditioning interfaces in the Target program.

The chamber operating conditions can be manipulated from the user interfaces. As an example, a step-function is incorporated into the Lab View program,

which allows the user to define large set point changes. The temperature step function takes any set point changes larger than 2°F (1,1°C) and steps it in increments of 2°F (1,1°C) while waiting at each incremental change one minute to insure stable control.
For both of the rooms in the chamber, the user must specify the desired dry bulb and wet bulb temperatures per the standards and turn the heater and humidifier on to let the PID controller obtain steady state and stable temperatures. The user can fine tune the proportional, integral and derivative gains of the PID controls. The PID gains used during this experimentation are listed in the table 3.2.

Table 3.2. Values for the constants in the PID controller.

	PID gains		
	Proportional	**Integral**	**Derivative**
Outdoor heater	4.5	3.0	0.0
Indoor heater	4.4	6.0	0.0
Humidifier	40.0	0.0	0.0

An additional function of the target VI is to establish the shut-off limits for the unit operation. There were cut-off limits set for high discharge pressure, low suction pressure and high unit power. If any of those limits were reached during the test, then the Lab View controls automatically shut down the unit. This was a safety procedure of the Lab View controls.

Figure 3.10 shows the code tester interface, where the user can adjust the in-house blower speed and the damper positions in order to get the desired flow rate and pressure drop across the unit.
The psychrometric condition of the code tester and the nozzle temperatures are monitored here as well.

Figure 3.11 shows the flow nozzle selection interface for a desired flow rate and the nozzle configuration for the present work. The user enters a desired value of flow rate and Lab View recommends a nozzle configuration based on the ASHRAE Standard 216. The user must still configure the nozzle bank manually: he has to close with some insulation tape the red nozzles and leave the blue ones opened.

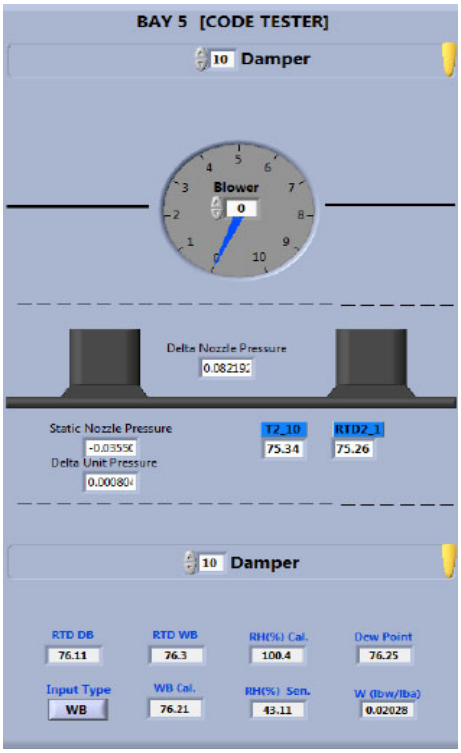

Figure 3.10. Code Tester interface.

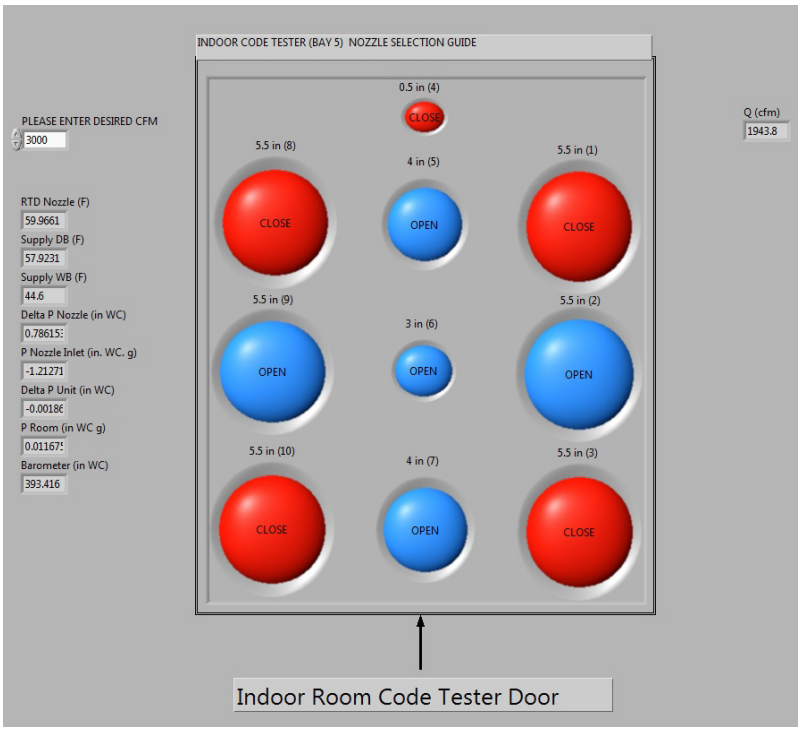

Figure 3.11. Indoor room code tester nozzle configuration.

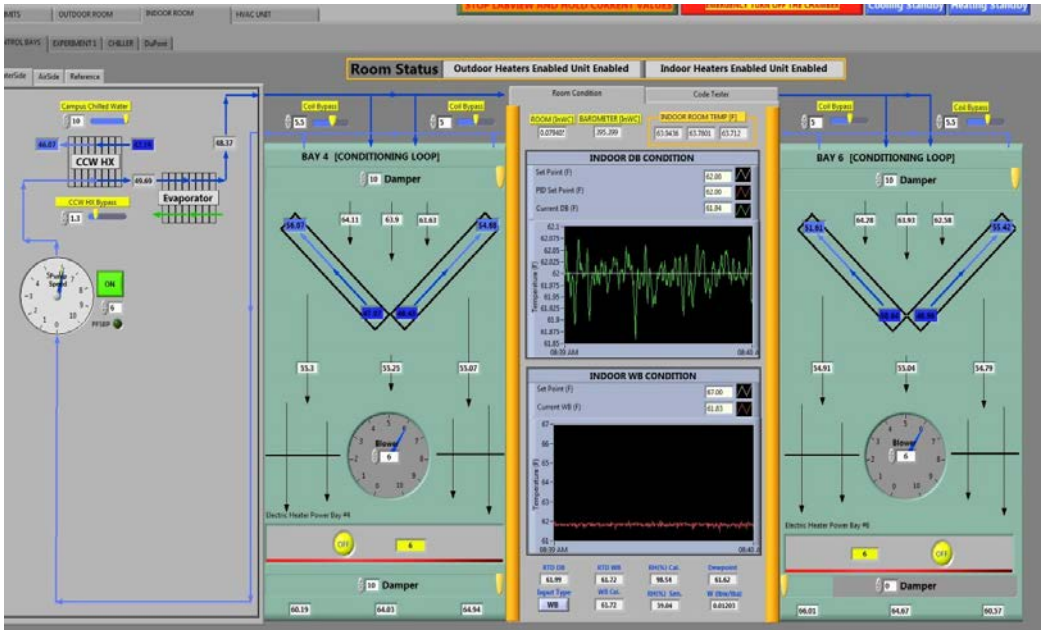

Figure 3.12. Interface for indoor room status monitoring. Temperature setpoints are established and monitored via the interface.

The data acquisition system is capable of recording data from the experimentation. The program is configured to allow up to six recording to be simultaneously collected for any or all input and/or output signals occurring inside the chamber at sampling rates as fast as one millisecond. One can see that the data file could grow quite large as there are over five hundred input and output signals to/from the chamber at any given time with room for further expansion.

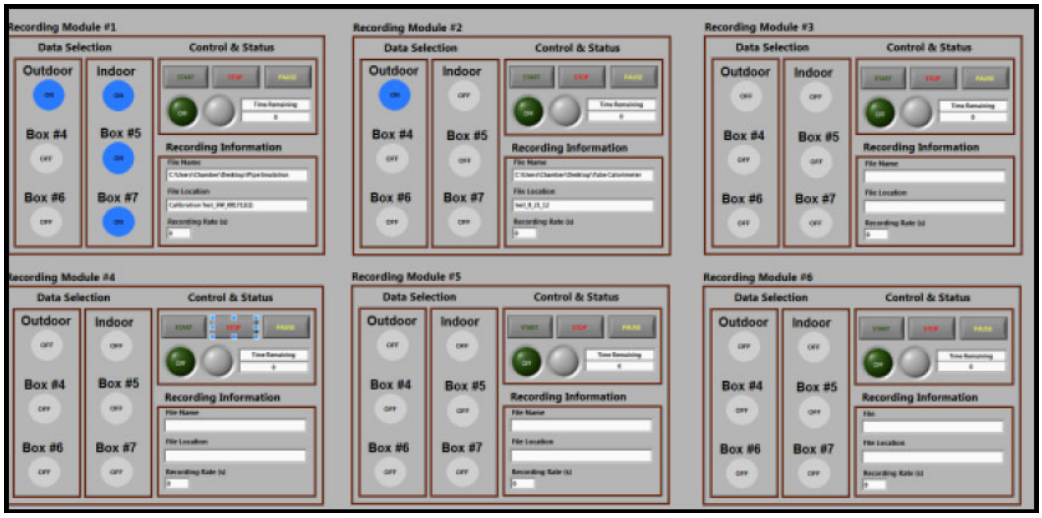

Figure 3.13. Data recording module interface.

Therefore, to help with data analysis the chamber output and input signals are sub categorized to allow the user to reduce the amount of data recorded in a file. These six sub categories are called outdoor, indoor, DAQ Box #4, DAQ Box #5, DAQ Box #6, and DAQ Box #7. The user is able to choose the sub categories desired and any signal being sent to or from the chosen selection will be recorded into a Tab delimited text file. After the system reaches steady state at required conditions, data are recorded using a recording module in the Lab View host (Figure 3.13) Users can specify the recording rate and the duration. The general procedure is to record the data for an hour at each test condition with a rate of 2 seconds for each sample. The sampling rate may be varied as long as the Lab View host CPU can store the whole amount of information.

Some of the sensors used in the experimental set-ups of the psychrometric chamber, such as the pressure transducers, need input power supply in direct current (excitation current) to produce output signals in current (4-20 mA). This power is provided by Lab View itself, which has three power supplies with different tensions (22 VDC, 5 VDC, 10 VDC)
In figure 3.14 is shown the sensor power control interface, where it is possible to switch the power channels for the sensors on or off.

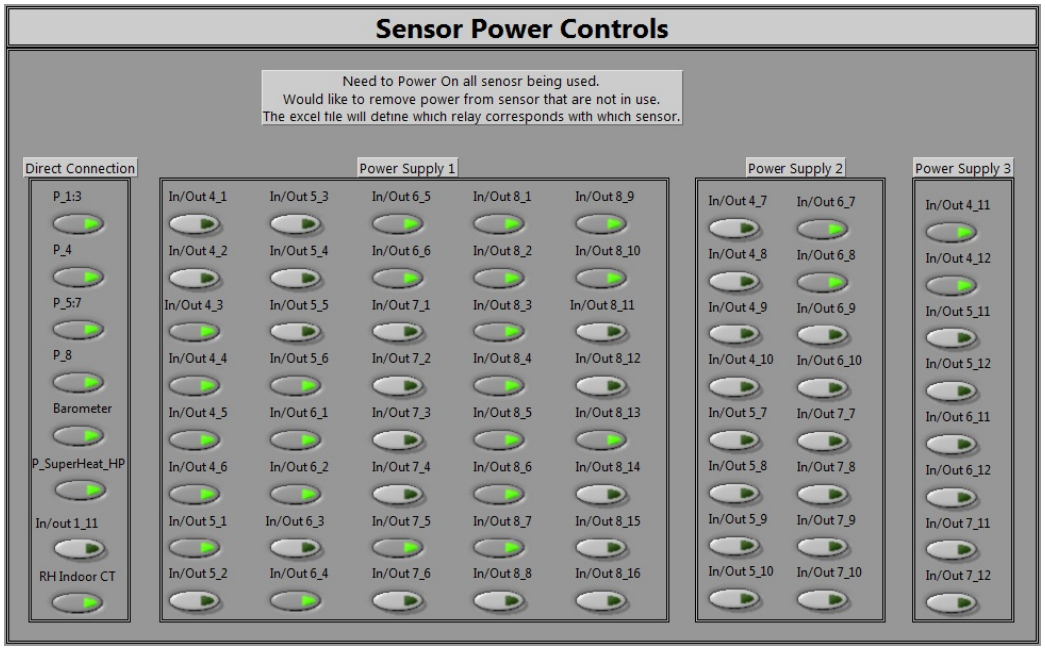

Figure 3.14. Channels that are powered by the Lab View system.

Once all the sensors are read in the Target, they are transmitted to the host computer and the secondary Lab View program is used to graphically represent the data associated with a particular project.

In table 3.3 are reported the measured variables acquired by Lab View for the first campaign of tests and the corresponding acquisition channels.

Table 3.3. The parameters monitored by Lab View for the digital scroll compressor experimentation (first campaign of tests).

Sensor #	Index #	Channel	Type
1	192	T4_7	Suction Thermocouple (Compressor 1)
2	193	T4_8	Discharge Thermocouple (Compressor 1)
3	194	T4_9	Suction Thermocouple (Compressor 2)
4	195	T4_10	Discharge Thermocouple (Compressor 2)
5	300	IN/OUT4_3	Suction Pressure (Compressor 2)
6	301	IN/OUT4_4	Discharge Pressure (Compressor 2)
7	308	IN/OUT4_11	Suction Pressure (Compressor 1)
8	309	IN/OUT4_12	Discharge Pressure (Compressor 1)
9	304	IN/OUT4_7	Discharge Mass Flow Rate (Compr. 1)
10	305	IN/OUT4_8	Discharge Density (Compressor 1)
11	306	IN/OUT4_9	Suction Density (Compressor 1)
12	307	IN/OUT4_10	Suction Mass Flow Rate (Compressor 1)
13	329	IN/OUT6_8	Unit Power Consumption

Figure 3.15 shows the scheme of the experimental set-up on the Host with textboxes, graphs and quadrants for real-time monitoring the measured values of the parameters of interest.

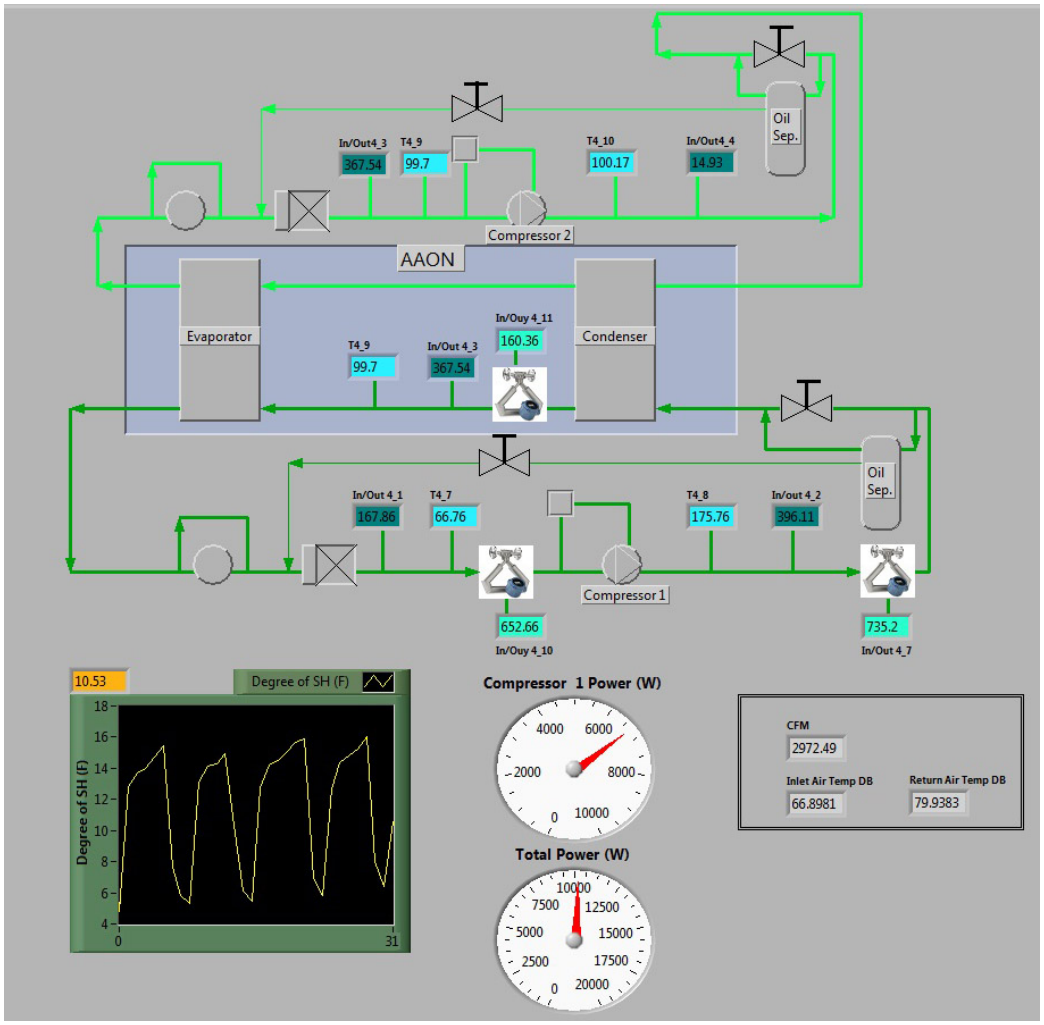

Figure 3.15. How the experimental setup looks on the Host Lab View screen.

3.2.2 JENEsys ProBuilder Console by Niagara Software

All the other parameters, such unit air pressure drop, supply and return temperatures, coil temperatures, were monitored by the unit controller software, JENEsys ProBuilder.
The JENEsys controller, mounted onto the unit, is linked by a common LAN CAT5 cable to a personal computer in the laboratory control room. The controller software, JENEsys ProBuilder, allows the remote control of the unit from the computer.

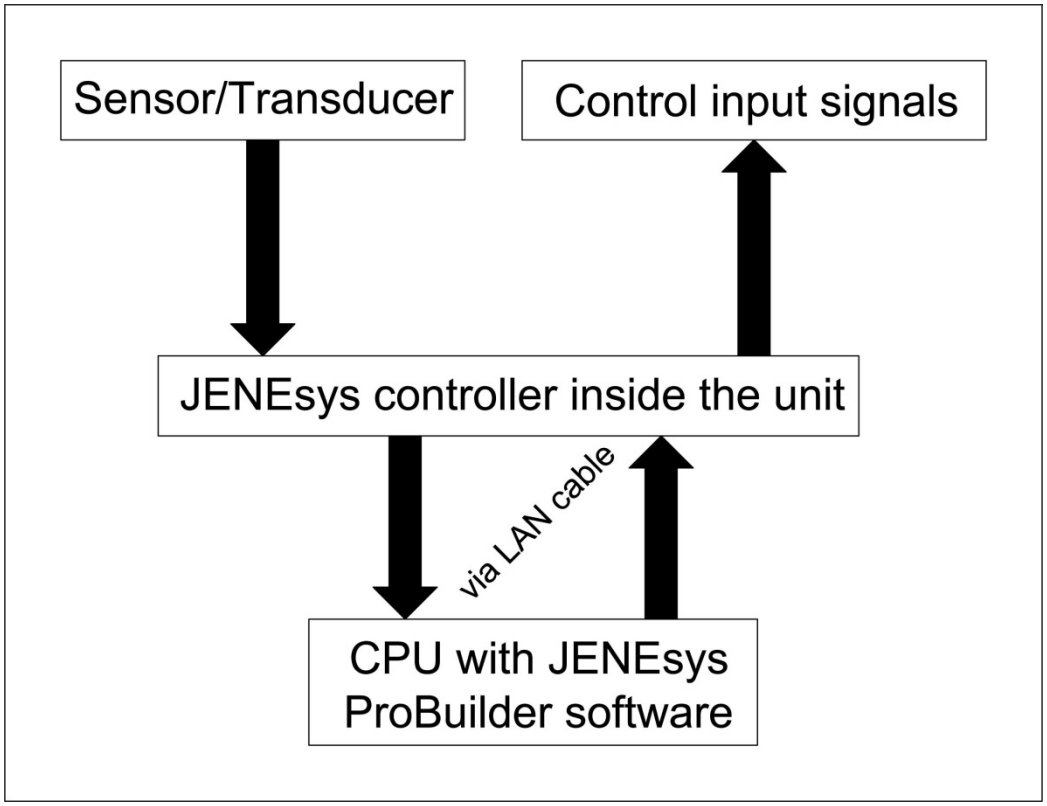

Figure 3.16. Data Flow Diagram for JENEsys controller.

As in many other control softwares, the JENEsys ProBuilder can be used through two different levels: it has its own operative system, called *Platform*, on which it is possible to set up many *Stations*, which are the programming files related to every single HVAC system the end user wants to control.
Every station needs its login information, for security purpose, and after the login the home page shows all the components installed in a friendly-user interface (figure 3.21).
While starting up the software, it is possible to check all the values reported by the sensor, in order to verify any out-of-range signal which may mean wrong wiring or communication issues.

The layout of our experimental testbed had already been designed by AAON, so we didn't need to get through the code to implement all the calibration equations and label every component in the graphical interface. This had to be done just for the Lab View side. Just in case a new measuring tool has to be installed, building an equation will simply be a matter of defining a *scale* and an *offset*.

$$\text{Scale} = \frac{(y_2 - y_1)}{(x_2 - x_1)} \tag{74}$$

$$\text{Offset} = y_1 - (scale * x_1) \tag{75}$$

Every parameter of interest can be recorded for a desired recording time and recording rate. The collected data will be stored in the controller memory until the user decides to export those data for further processing.
It's obvious and it's part of the control purpose, all the parameters of interest can be managed in a customized way to achieve the best control strategy. However, for safety purposes as well, every kind of acoustic or visual alarm can be set in case of some component's failure. For example, it was noticed that, as common sense suggests, when running the compressor at low load (25%) and high temperature difference between the two chambers, i.e. 97°F (36,1°C) in the outdoor room and 62°F (16,7°C) in the indoor room, the temperature of the supply air can't reach, by running just one compressor, the desired value to cool down the room. This results in a cooling failure that can be reported in many ways by the control software.

For what concerns the JENEsys controller, and the Lab View itself as well, it's also possible to set some *Shutoff Limits* (low and high) for each parameter of interest. This allows the control system to shut the unit down whenever some measurement seems to get out of control.
In figure 3.17 it's possible to see a screencap of some general shutoff limits about all the psychrometric chamber, and for every single project.

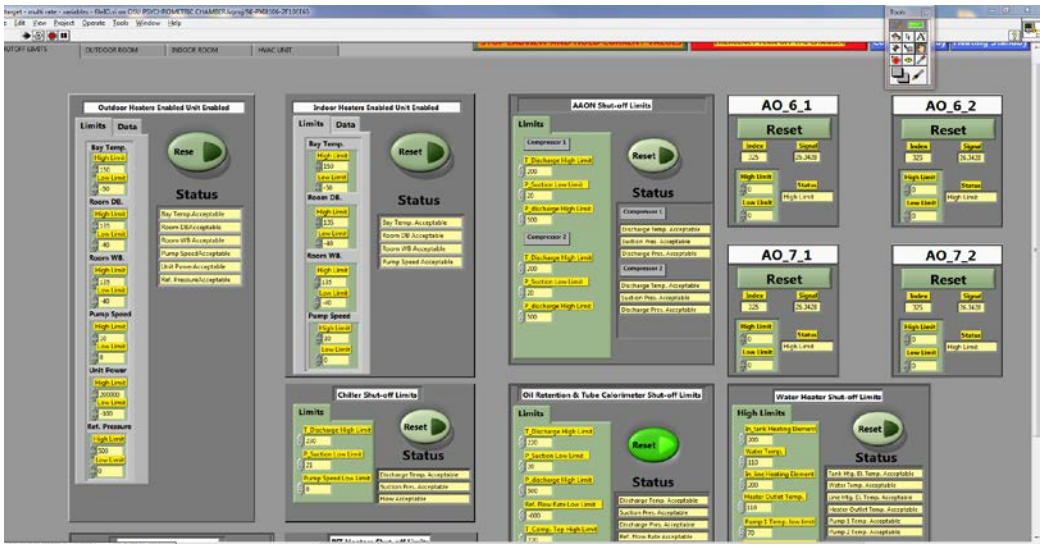

Figure 3.17. Chamber shutoff limits of the OSU Lab experiments.

It gets evident, at this point, that some issues in the operation of two different DAQ and control system can come up and generate conflictual behaviour of the unit. Thus, we chose to operate the Lab View as a simple monitoring tool,

because of its easiness to see on the same screen how both the AAON unit and the whole psychrometric chamber behave and interact (see the Target and the Host screens in figure 3.18 and the block diagram of the AAON unit in figure 3.19). The JENEsys ProBuilder software, therefore, got the only control tool from which to operate the system.

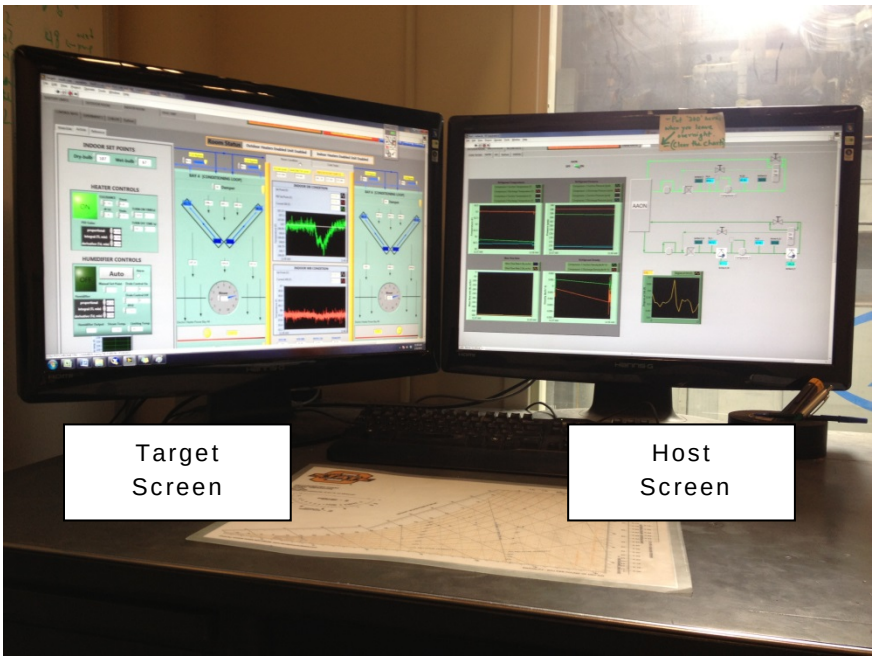

Figure 3.18. The Target and the Host screens.

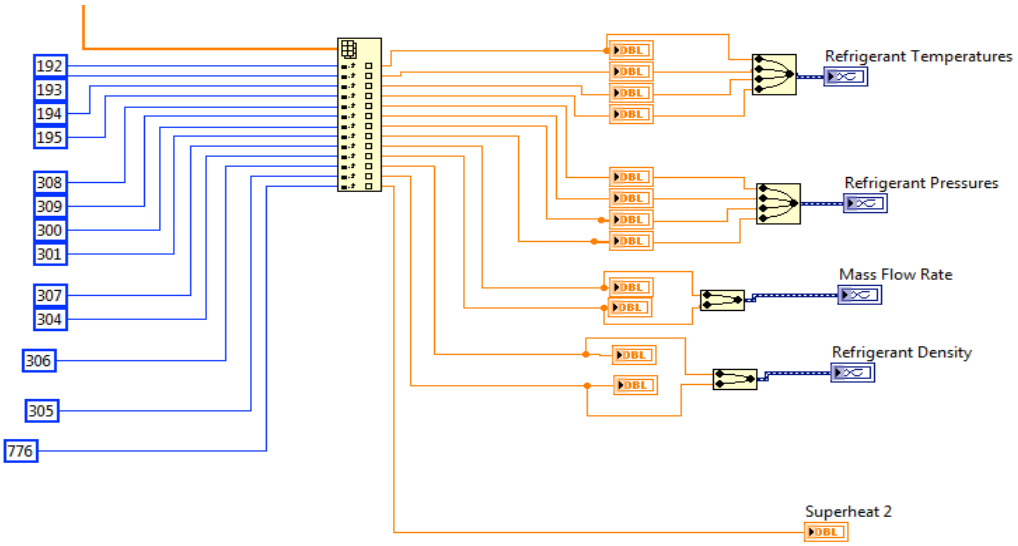

Figure 3.19. Block diagram of our experiment on Lab View.

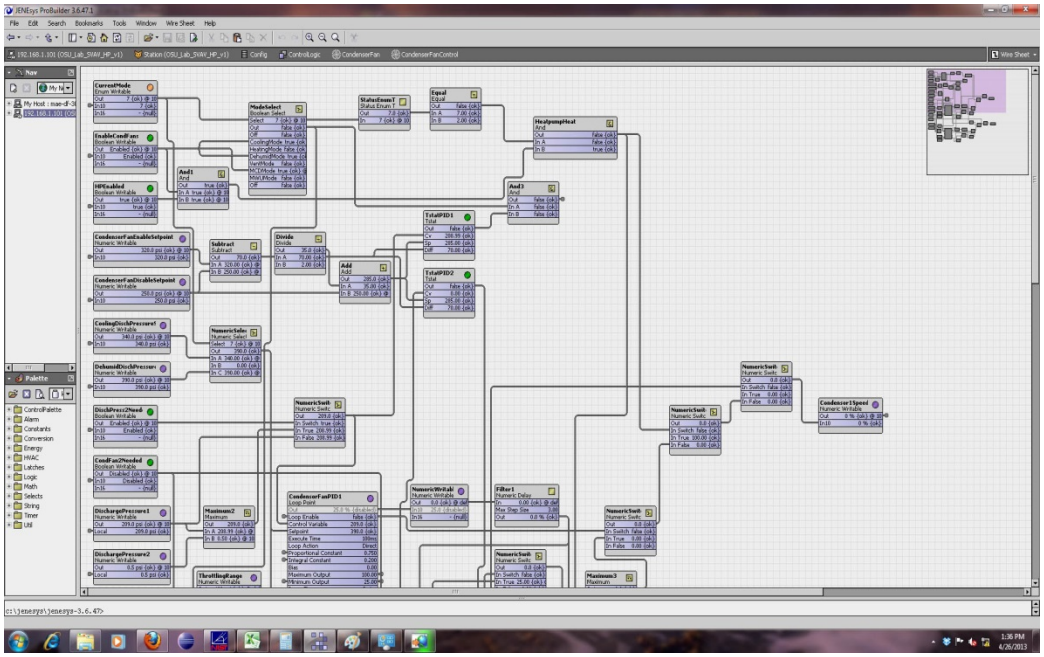

Figure 3.20. The JENEsys block diagram.

Using the JENEsys ProBuilder interface (shown in figure 3.21) is possible to set easily the fans rotating speed and the compressor load.

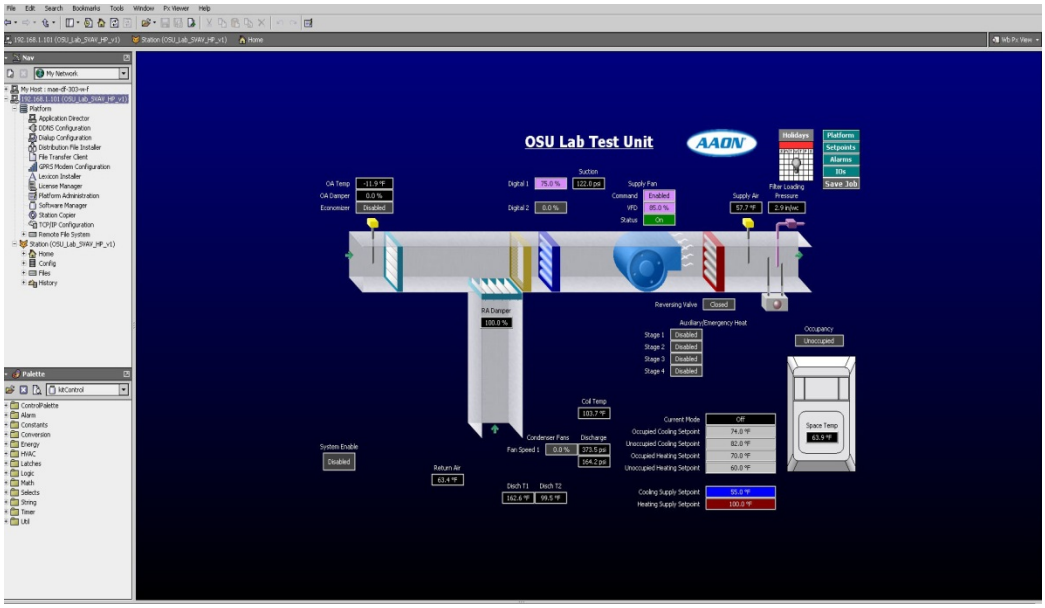

Figure 3.21. The JENEsys ProBuilder interface allows the user to set compressor position, fan airflow rates as well as other items for unit operation.

Since the first stage of tests was just compressor-focused, the supply fan speed was manually overridden and kept always at 85%, while the condenser fan control was overridden to maintain 100% airflow.
By imposing these conditions, ambient conditions varied from test to test, and the compressor was run at 100%, 75%, 50% and 25% load.
When the tests got overall-system-oriented, by focusing on the control side, the unit was operated in automatic mode.

3.3 The experimental test-bed: AAON Rooftop 15ton unit

3.3.1 Description

The air conditioning unit forming the basis for these investigations is an AAON RN-15 rooftop air-to-air heat pump. As shown in table 3.4, it has a 15ton (52,7 kW) cooling nominal capacity. The unit was originally constructed with standard, single speed scroll compressors circulating refrigerant R-410A with a four-row fin and tube evaporator. The unit was configured for nominal 3600 supply cfm (6120 m^3/h), with .92 inches of H_2O (1,75 kPa) of static pressure. A 22-inch (56 cm) direct drive supply blower is powered by a 5 hp (3,73 kW), high efficiency motor with a variable frequency drive. Two constant speed condenser fans were also installed. The unit features 80 kW of auxiliary electric heat to supplement the heat pump. The electrical power of the unit is provided by a variable transformer, which allows the voltage and power configuration (single, two, or three phase) to be adjusted. The 15ton AAON unit was placed upon an 8-wheeled cart which is designed to simulate the unit supply and return plenum, as well as housing measurement devices. The cart supply and return plenums were connected to the separation door and then to the code tester by using flexible 24-inch (61cm) diameter neoprene ducts. The unit did not feature a programmable controller, it was constructed with a simple terminal strip for external application of control. In this configuration, the unit did not satisfy the requirements of the proposed investigation.

Table 3.4. Technical specifications of the 15 ton air-to-air rooftop unit.

Total cooling capacity	52,7 kW
Operating conditions (at full load)	Entering air temperature: 27°C DB, 18,9°C WB Leaving air temperature: 10°C DB, 9,7°C WB

Supply air fan (quantity – supply voltage – phases number – nominal power)	1 – 460 VAC – 3-phase – 3,73 kW
Supply air nominal flow rate	3600 cfm (6120 m^3/h)
Condenser fans (quantity – supply voltage – phases number – nominal power)	2 – 460 VAC – 3-phase – 560 W
Condenser air nominal flow rate	1000 cfm (1700 m^3/h)
Expansion valve type – number used	Thermal - 1 for each compression stage
Evaporator coil area – material - rows	1,36 m^2 – Copper – 4
Evaporator fin type – material – density - thickness	Flat – Aluminum- 14 FPI (fins per inch) = 5,5 fins per cm – 0,2 mm
Evaporator face velocity	1,25 m/s
Number of tubes - diameter	20 - ¼"

Namely, it did not incorporate digital scroll compressors, variable speed condenser fans, or a programmable controller. In order to prepare the unit to act as an experimental testbed for control algorithms, it required a significant amount of reworking.

3.3.2 Upgrading the unit

The rooftop unit was upgraded for this research project. The two existing scroll compressors, 7,5 nominal (26,5 kW) ton Copeland scroll model ZP83KCE, were replaced with two new digital scroll compressors (7,5 nominal ton Copeland digital scroll model ZPD83KCE, see specs in section 2.4). A controller was mounted onto the unit for control algorithm testing, condenser fans motors were changed from standard, single speed motors to high efficiency motors with variable frequency drive, and new sensors and transducers were installed. Based upon a brand new electrical wiring diagram, most of the electrical wiring was remade in order to fit the new requirements. New VFD, fuse blocks, terminal blocks, power supply device, solid-state relays with their own connections were installed onto the unit (see figure 3.29).

The existing scroll compressors were removed from within the unit's compressor and controls cabinet. The new compressors were mounted on a structure

external to the unit itself, in order to accommodate the physical space required for the installation of the sensors for the experimentation (see figures 3.27, 3.32, 3.33, 3.34). The compressor mount was insulated to reduce vibration and fixed to the chamber interior walls to minimize any movement during operation. This external compressor and sensor mounting required new refrigerant piping to be mated to the original piping. The compressors were equipped with crankcase heaters, that have the aim to clear any liquid refrigerant if energized at least 24 hours before operation.

The self-contained unit, normally close-coupled, has relatively short piping lengths, and the addition of the new components external to the cabinet caused the line lengths to increase. Any new pressure losses introduced by the increase in line length and the addition of sensors (particularly the mass flow rate meters) is mitigated by an increase in the refrigerant pipe diameter by one size. Suction lines were increased from 7/8" (22 mm) outside diameter (OD) to 1.25" (32 mm) OD, and discharge line was increased from 5/8" (16 mm) OD to 7/8" (22 mm) OD. The notable increase in the line length and diameter caused the system to be charged in 20 pounds (9,1 kg) of R-410A, for each compression stage, instead of the usual 14 pounds (6,4 kg) that the manufacturer suggests. This charge was considered acceptable by running the system monitoring the refrigerant superheat and subcooling, referring to the manufacturer stated operating ranges: superheat has to be kept in the 4÷9°C range and the subcooling between 4°C and 6°C. This last range was however referred to chillers. Since the system can work as a heat pump as well, the presence of the liquid receiver allows the subcooling to be close to 3°C or less.

The liquid receiver is normally included in reversible vapor compression heat pumps to temporarily store the excess refrigerant charge occurring due to change of operation mode. The presence of a liquid receiver influences the total amount of refrigerant charged into a system, and particularly when using refrigerant mixtures, could affect the system circulation composition. The evaluation of the proper charge derives from the trivial consideration that when the quantity of refrigerant increases, the superheat decreases and the subcooling increases. This is ok when considering the composition of the refrigerant flowing through the components, but it means that the pressures of the cycle both increase: this causes an increase in the power consumption of the compressor but an increase in capacity, too. So there must be a compromise between the two needs.

The following components were added in-line for each compressor, and connected either to the DAQ system or to the unit controller (see table 3.5 for specifications and figure 3.35 for layout of the experimental set-up):

- Sight glass
- Suction line filter drier
- Suction line Coriolis mass flow meter (only for stage 1 compressor) with transmitter
- Discharge line Coriolis mass flow meter (only for stage 1 compressor) with transmitter
- Suction line thermocouple
- Discharge line thermocouple
- Suction line pressure transducer (current output)
- Suction line pressure transducer (voltage output)
- Discharge line pressure transducer (current output)
- Discharge line pressure transducer (voltage output)
- Low pressure switch (suction line)
- High pressure switch (discharge line)
- Discharge temperature switch (discharge line)
- Coalescent/Helical oil separators with needle valves
- Ball bypass valves for oil line

Before charging the system with refrigerant, all the new piping was vacuumed, charged with nitrogen and leak-checked at a 500 psi (34,5 bar) pressure, around 15% more than the pressure we recorded at the hardest operating conditions (outdoor ambient at 46°C). Due to the high number of new soldering joints and threaded fittings (flow meters, above all), a leakage which was below 0,1 psi/hour (690 Pa/hour) for 24 hours was considered acceptable. This choice was also made because the operating windows for the two stages of tests were both less than 2 weeks long, and between the two stages the refrigerant was recovered and charged again at the same amount: this allowed considering the system always operating with the proper charge, especially from the beginning to the end of the test.

The existing unit terminal strip was replaced by a JENEsys controller (see figure 3.31), linked to the control room, which collects all the following signals and allows the remote control of the unit (fans, blower, compressors, dampers, supply air temperature…):

- Air flow switch (already on unit)
- Supply air temperature sensor
- Return air temperature sensor
- Supply static pressure sensor
- Indoor room thermostat
- Heat pump coil temperature (replacing previous defrost temperature sensor)
- Variable frequency drive for new condenser fans motors

- 3-phase condenser fans motors, replacing old ones

During the start-up operations, all the wiring was double-checked and the proper verse of rotation of condenser fans, supply fan and compressor was checked.

Table 3.5. Components list, ranges and capabilities.

N.	Sensor	Component	Manufacturer + Model/Type	Nominal Range and Accuracy	# used	Description
1	Refrigerant low side and high side pressure (current 4-20 mA output)	Pressure Transducer, suction and discharge side	Setra Model 206	7 - 500 psig (50 to 3,450 kPa) ±0.65psi (4.5 kPa)	4	
	Refrigerant low side and high side pressure (voltage output)	Pressure Transducer, Suction side	MCS Model 200-F-T	0 - 200 psig (0 to 1.378 kPa) ±0.25% of span	2	
	Refrigerant low side and high side pressure (voltage output)	Pressure Transducer, Discharge side	MCS Model 667-F-T-40	0 - 667 psig (0 to 4.598 kPa) ±0.25% of span	1	
2	Refrigerant temperature, low side and high side	Inline thermocouple	Omega Model TMQSS-125G-6	.-40 to 130 °F (-40 to 54 °C) ±0.5°F (0.3°C), special limits from in-house and in-situ customized calibration with high accuracy temperature bath	4	T-Type thermocouple (Copper-Constantan)
3	Refrigerant Mass Flow Rate , Density, Temperature	Refrigerant mass flow meter, suction side	Micro Motion Model CMF050H320N QBAEZZZ Sensor S/N: 14090465	Mass Flow rate 0÷15000 lb/hr (6800 kg/hr), ±0.5% of rate, Density 312 lb/ft^3 (5000 kg/m^3), ±0.0312 lbm/ft^3 (0.5kg/m^3),	1	4-wire Model
		Refrigerant mass flow meter, discharge side	Micro Motion Model CMF050M320 NRAAEZZZ Sensor S/N: 14318717	Mass Flow rate 0÷15000 lb/hr (6800 kg/hr), ±0.5% of rate, Density 312 lb/ft^3 (5000 kg/m^3), ±0.0312 lbm/ft^3 (0.5kg/m^3),	1	9-wire Model

		Transmitter for Refrigerant mass flow meter, suction side	Micro Motion Model 2700R12BBAE ZZZ S/N: 3105115 Sensor S/N: 14090465		1	
		Transmitter for Refrigerant mass flow meter, discharge side	Micro Motion Model 2700C12BBAE ZZZ S/N: 3227885 Sensor S/N: 14318717		1	
4		JENEsys Controller	Vykon JM34-IO/16		1	Receives signals from sensors, includes Jene PC1000
		JENEsys expansion module	Vykon JM16		1	Receives signals from sensors
5		VFD	Yaskawa J1000		1	For evaporator blower, previously on unit
		VFD	Yaskawa V1000		1	For condenser fans, brand new
6		DC Power Supply 24V	Kele DCP-524		1	
7		Solid State Relay	Omron G3NA-210B		2	
8		Air Flow Switch	Cleveland Controls AFS-228-165		1	Mounted next to evaporator coil
9	Air temperature sensor	Duct Temperature Sensor (SAT-RAT)	MAMAC TE-701-B-7-C		2	Temperature of supply/return air temperature
10	Thermostat	Room temperature sensor (SPAT)	ACI Systems R38460		1	For the indoor room
11	Air temperature sensor	Supply Static Pressure Sensor	ACI Systems R17050		1	Ends with Pitot tubes
12	Coil temperature sensor	HPTS Heat pump temperature sensor	ACI Systems		1	Mounted on the condenser coil
13	Pressure switch	Low Pressure Switch	Wilspec P.N. P59910/27029	0-50 psi	2	Mounted on suction line
		High Pressure switch	Wilspec P.N. P97420	0-600 psi	2	Mounted on discharge line
14		Digital Scroll Compressor	Copeland ZPD83KCE		2	

15		Solenoid Valve	Copeland ES43-151		2	
16		Condenser Fans Variable Speed Motors	Baldor SuperE Motors	460 V, 1,4 A, 1165 Rpm	2	
17		Discharge temperature Switch	Cleveland	30-485 °F, voltage output	2	
18		Centrifugal refrigerant oil separator (Compr.2)	Henry Technologies S-5587	Max discharge 6.5 CFM, 450 psig max, Oil flow rate @ 175 PSI differential: 0.80 gal/min	1	Connections are nickel plated steel - 7/8" OD
		Coalescent Oil Separator (Compr.1)	Temprite 900 series	0.05 microns fine particals can be seperated	2	37N6, Max 650 psi, 15F10Z
19		Suction line filter drier	Sporlan C-419-S-T-HH		2	Charging port included
20		Sight glass for mass flow rate size 3/4" , O.D. 7/8"			2	Mounted on suction side for each compressor
21		Refrigerant R410A				
22		POE oil	Lubrizol Emkarate RL 32-3MAF			ISO VG 32,Synthetic mixed acid polyol ester
23		Needle Valve 3/8"	Parker 6A-V6LR-B	opens 10% per 1/2 turn; total 5.5 turns	2	Grainger Item # 1RBB1
24		Gas Line Copper Pipe	Pipe size: 1", O.D.: 1 1/4" suction, 3/4"-7/8" discharge			
25		Liquid Line Copper Pipe	Pipe size: 3/8, O.D.: 1/2"			
26		Oil line Copper Pipe	Pipe size: 1/4, O.D.: 3/8"			
27	Power consumption of the unit	AC Watt transducer	Flex-Core AGW-008E	Full scale power: 3 kW x [current trasformer ratio]; accuracy: ±0.2% Rdg, ±0.04% F.S.	1	Input: 0-5 Aac, 0-300 Vac; Output: 4-20 mA
28		Current transformer	Flex-Core 60RBT-151	Current ratio: 150:5	3	600 V class; accuracy: burden VA for 3% class = 20+1%, secondary winding resistance = 0.055 Ω (75°C)

3.3.3 Measurement tools/sensors and calibration

➢ Thermocouples

A total number of four in-line thermocouples were used to measure the suction and discharge temperatures. The values were sent to the DAQ system and used to check the operating conditions of the compressor and the refrigerant. The discharge temperature, by the way, was measured and monitored through a temperature switch, too, which was linked to the controller.

The calibration of the thermocouples was done in a temperature bath (figure 3.22) with reference to NIST (National Institute of Standards and Technology) traceable thermometer. The thermocouples were dipped in the distilled water, surrounded by a simple plastic cup in order to prevent the sensors from feeling the radiation coming from the walls of the bath. The software by National Instruments, Measurement & Automation Explorer (MAX) is used along with the NI-DAQ to record the data points at a sampling rate of 1 millisecond (1 kHz) during the calibration.

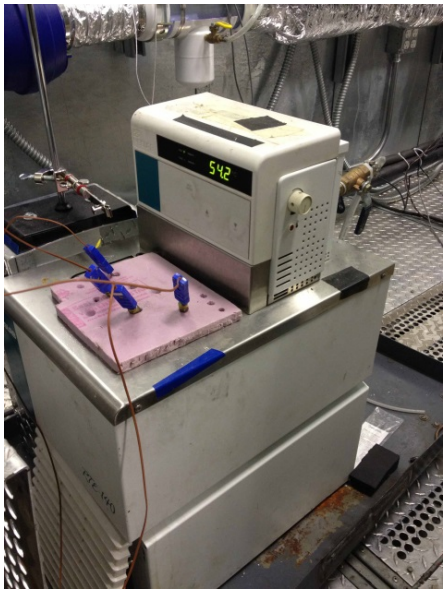

Figure 3.22. Thermostatic bath.

The operating ranges, were different between suction and discharge. For the suction side, we took five points from -20°C to 100°C, and for the discharge side we took another five points from 0°C to 200°C.

➢ Pressure transducers

A total number of four in-line pressure transducers were used to measure suction and discharge pressures. The signal, which is a 4-20 mA one, is sent to Lab View and needs the proper conversion equation (see section below). These

pressure transducers have just a measuring and monitoring purpose. They were already calibrated in factory with an accuracy of ±0.65psi (±4.5 kPa). The power is directly given from the Data Acquisition box (see figure 3.8) through a four-wire cable: two are for the power and two for the signal that is sent to the Lab View.
Same speech for the voltage-output pressure transducers, that are installed in the same position as the current-output ones but the signal is sent to the JENEsys controller and have a control purpose (but their trend can be recorded, stored and plotted through the software). See table 3.5 for any other technical specifications about these components.

- Coriolis mass flow meters

Two Coriolis mass flowmeters were mounted at the suction and discharge line. This kind of instruments was chosen because Coriolis mass flow meters are known to be good at measuring any kind of substance and, most important, they don't need a long enough straight pipe before the point of installation. This was crucial, because it was needed to deal with very little room for the installation of all the tools. The only severe disadvantage is that Coriolis mass flow meters have big pressure drops, but this issue was solved by increasing the diameter of the line.

Table 3.6. Specifications of Coriolis mass flow meter.

	Item Specification
Manufacturer	Micro Motion, Inc.
Model	(CMF050) CMF050H320NQBAEZZZ
Type	Coriolis Mass Flow and Density Meter
Transmitter	2700C12BBAEZZZ
Flow rate range	15000 lb/hr (6800 kg/hr)
Flow rate accuracy	±0.5% of the flow rate
Zero stability	0.06 lbm/hr (0.027 kg/hr)
Density range	312 lbm/ft^3 (5000 kg/m^3) or (5 g/cm^3)
Density accuracy	±0.0312 lbm/ft^3 (±0.5 kg/m^3)
Temperature range	300°F (148°C)
Temperature accuracy	±2°F (±1°C)
Output	4 to 20 mA
Acquisition sample rate	0.2 sec
Pressure rating for sensor	1500 psig (10.4 MPa)

Due to the high precision required to this kind of instrumentation, the calibration was made by the MicroMotion company and the calibration certificate was

attached. A start-up debugging was only needed, and then the operating range for mass flowrate and density to be imposed.
Differently from the pressure transducers, the flowmeters send the mass flow rate and density signals to the Lab View but get power from the chamber power line.

- Wattmeter

The power consumption of the unit was measured, too.
The wattmeter needs as inputs both the voltage and the current of each phase; for each sample the voltage is multiplied by the current at the same instant.
This was made through a box containing a wattmeter, a terminal block as a measuring point for the voltage and three current transformers in order to scale the current flowing through the wattmeter (its current range is 0÷5 A). This box was linked right after the main breaker. The power cord goes inside the box, sees its current transformed, and after the power measurement the wires go to supply the unit with power.

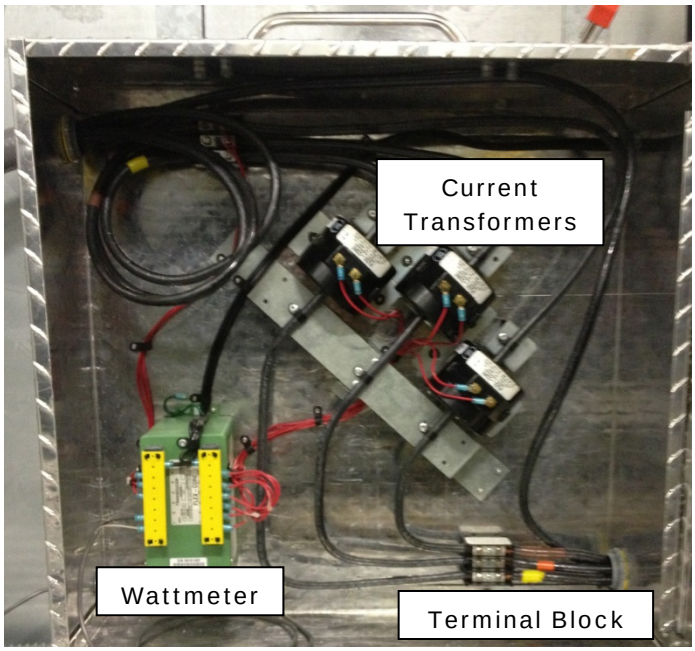

Figure 3.23. The wattmeter and the current transformers, one for each phase.

This allowed to monitor and record the unit consumption and get to the compressor power consumption with a simple procedure. While recording a test, in fact, the overall unit consumption is measured. After every test, though, the compressor was turned off and we made a final recording of at least 30 minutes in which what could be seen was the power consumption of the supply fan and the condenser fans. Thus, during the data post-processing the only compressor

power consumption was obtained by simply subtracting the supply fan/condenser fans power from the overall power consumption that were previously measured. In table 3.5 are reported the technical specifications of the devices and in figure 3.23 is how the box looks like when connected to the line.

Conversion equations

All the mA signals that run from the sensors to the Lab View have to be converted in order to get the proper measurement unit. This requires the user to link a manual reading to the Lab View reading. Below is presented an example of this process, which was made for the mass flow meters.

At the beginning of the test campaign, the mass flow rate measurement was made in just mA. A correct lbs/hr unit was obtained by writing down, for every 100% load test, a set of read values (from the flow meters displays) in a high enough number. By writing down the time of the recording these data were linked to the recorded data (current output). The more tests were run, the more accurate the equation became. In figure 3.24 and table 3.7 is the processing of the first six tests in order to get to a conversion equation.

The values that have to be determined in order to get to a conversion equation are the scale and the offset, which will be simply determined using equations 74 and 75.

Table 3.7. Performed tests and relative calibration procedure.

Test [OT-IT]	Suction avg. read value (lbs/hr)	Suction avg. Current (mA)	Disch. avg.read value (lbs/hr)	Disch. avg. current (mA)
77-67	1003,312	12,017	1002,088	11,999
82-67	1012,636	12,087	1011,280	12,068
82-80	1175,506	13,401	1175,759	13,387
87-72	1079,263	12,629	1079,141	12,610
87-82	1212,868	13,706	1212,741	13,689
97-62	979,968	11,831	980,488	11,820

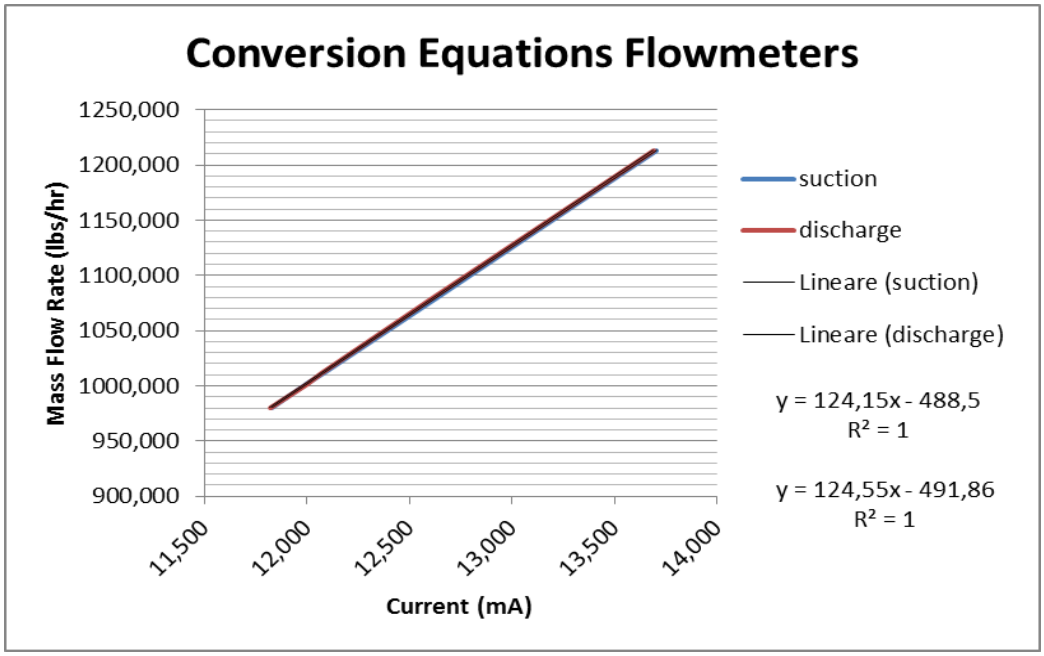

Figure 3.24. Plot of the conversion equation analysis. The calibration was made in lbs/hour.

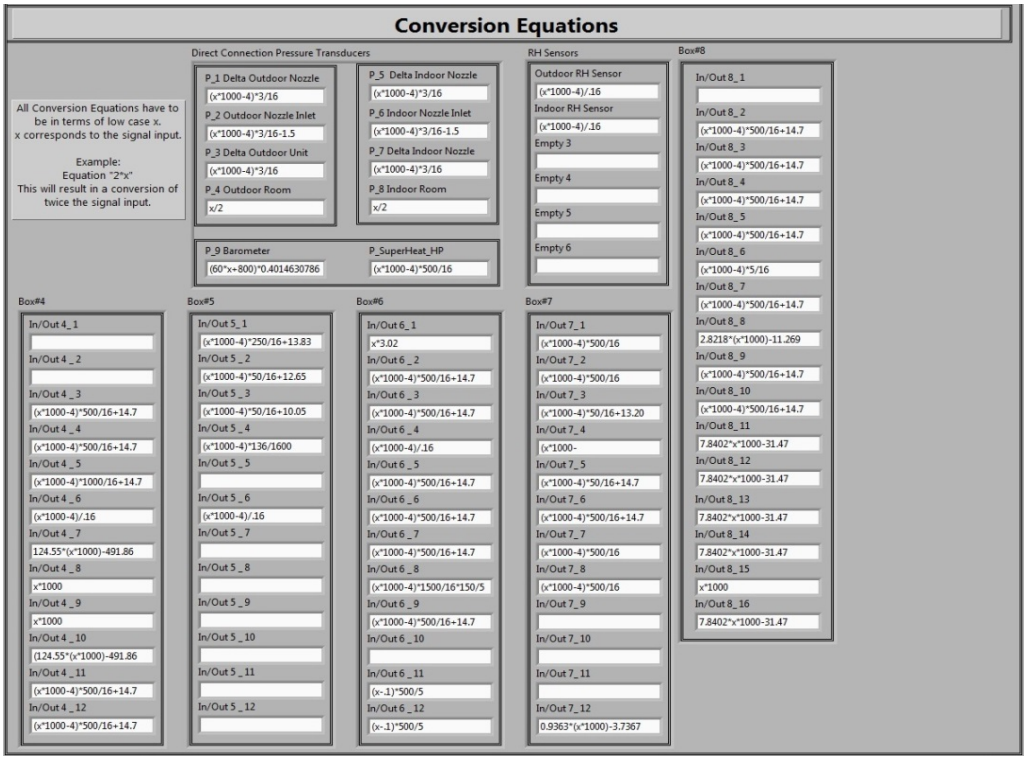

Figure 3.25. Summary of the laboratory channels in which every user can put his conversion equations for his experiments.

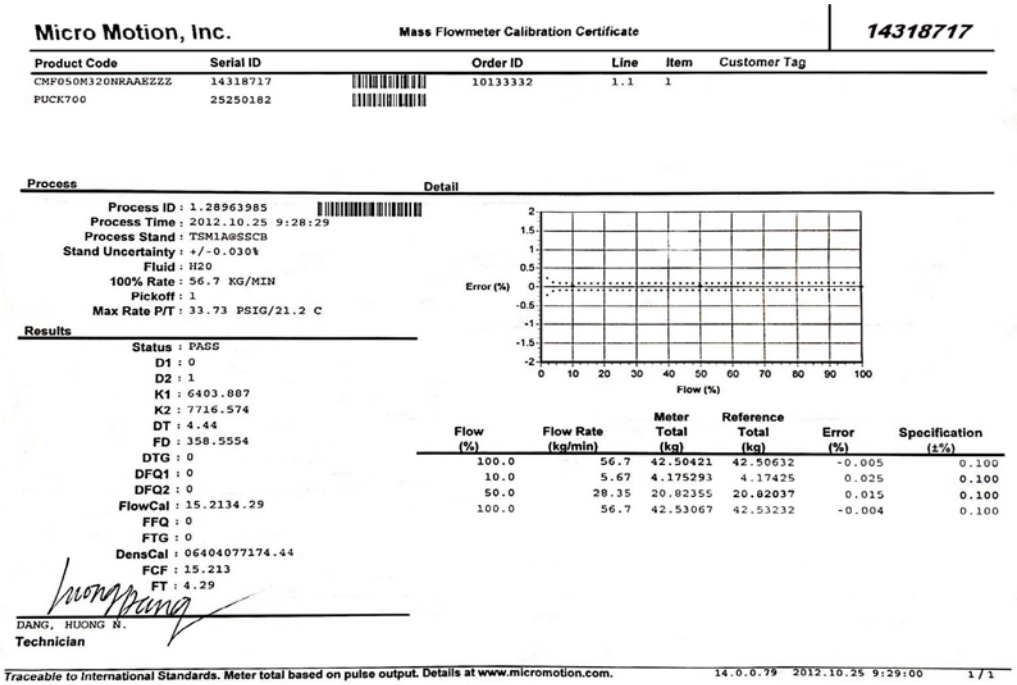

Micro Motion, Inc. — **Mass Flowmeter Calibration Certificate** — **14318717**

Product Code	Serial ID	Order ID	Line	Item	Customer Tag
CMF050M320NRAAEZZZ	14318717	10133332	1.1	1	
PUCK700	25250182				

Process

Process ID : 1.28963985
Process Time : 2012.10.25 9:28:29
Process Stand : TSM1A@SSCB
Stand Uncertainty : +/-0.030%
Fluid : H20
100% Rate : 56.7 KG/MIN
Pickoff : 1
Max Rate P/T : 33.73 PSIG/21.2 C

Results

Status : PASS
D1 : 0
D2 : 1
K1 : 6403.887
K2 : 7716.574
DT : 4.44
FD : 358.5554
DTG : 0
DFQ1 : 0
DFQ2 : 0
FlowCal : 15.2134.29
FFQ : 0
FTG : 0
DensCal : 06404077174.44
FCF : 15.213
FT : 4.29

DANG, HUONG N.
Technician

Detail

Flow (%)	Flow Rate (kg/min)	Meter Total (kg)	Reference Total (kg)	Error (%)	Specification (±%)
100.0	56.7	42.50421	42.50632	-0.005	0.100
10.0	5.67	4.175293	4.17425	0.025	0.100
50.0	28.35	20.02355	20.02037	0.015	0.100
100.0	56.7	42.53067	42.53232	-0.004	0.100

Traceable to International Standards. Meter total based on pulse output. Details at www.micromotion.com. 14.0.0.79 2012.10.25 9:29:00 1/1

Figure 3.26. Calibration certificate of the Coriolis mass flow meters.

Figure 3.26. Project progress.

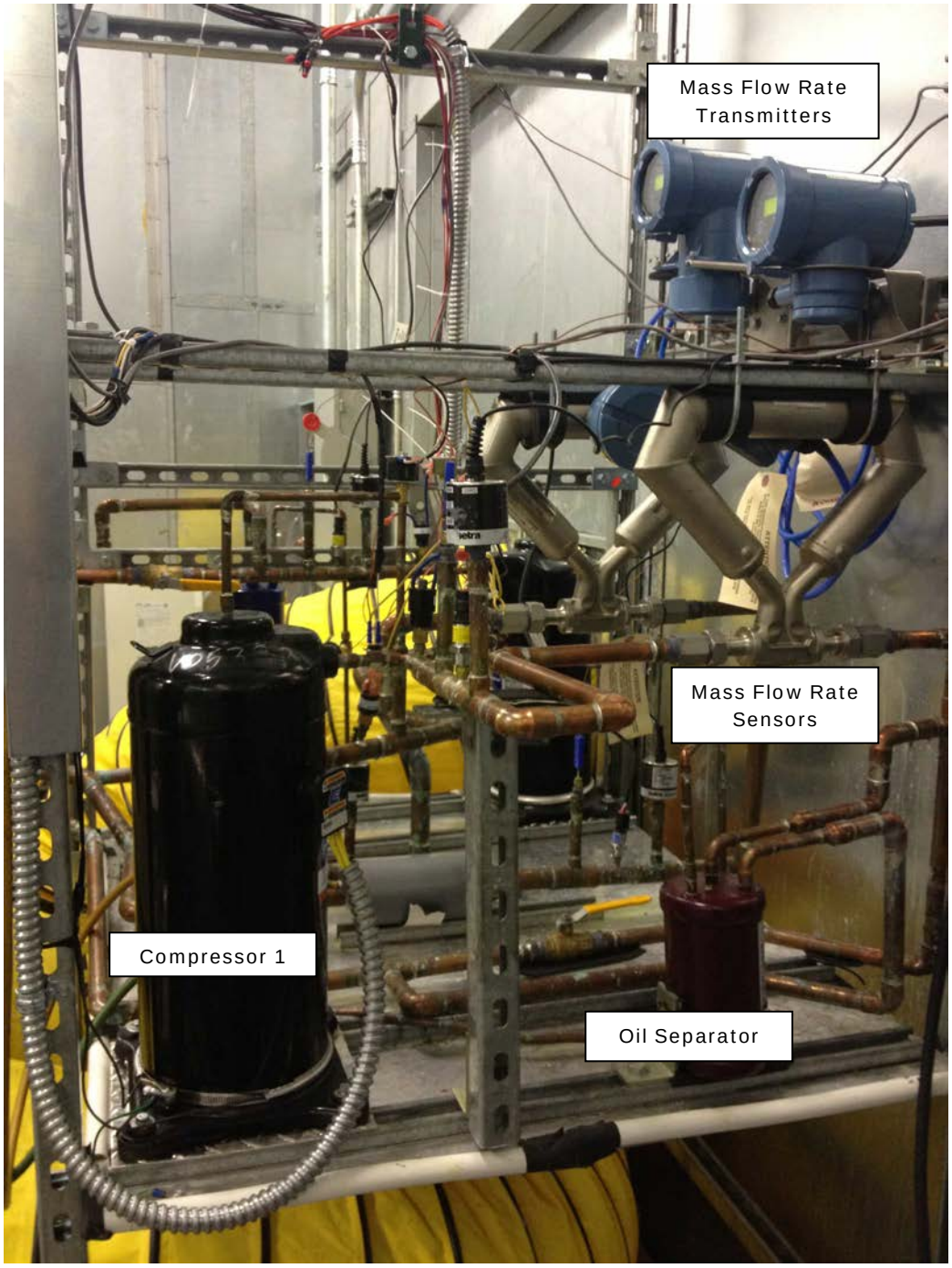

Figure 3.28. The new piping and sensors of the experimental set-up.

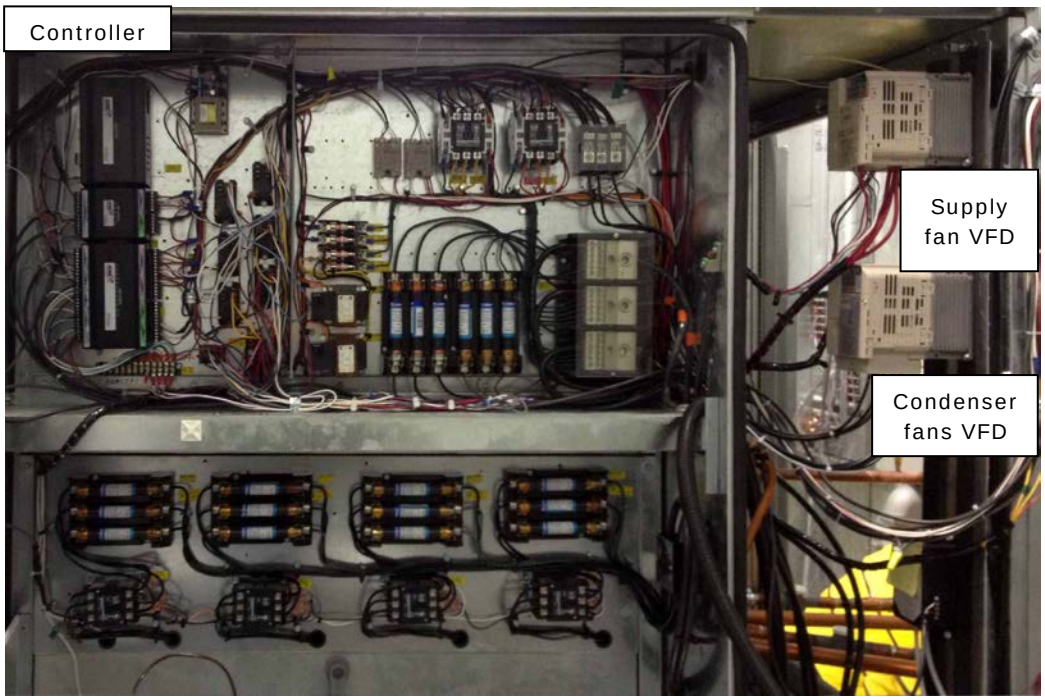

Figure 3.29. The new controller and the new wiring, relays, contactors, terminal blocks and the fans VFDs.

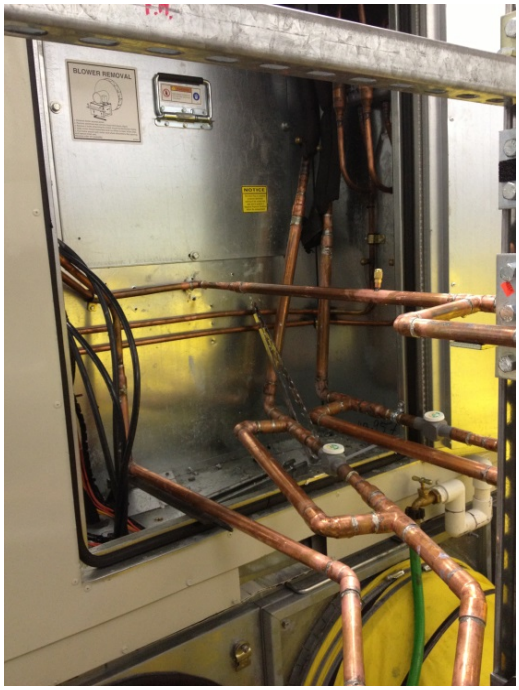

Figure 3.30. Connections from the existing piping to the new apparatus.

Figure 3.31. The new controller and wiring (magnification of fig.3.29).

Figure 3.32. View of the 15ton unit, condenser fans are running. On the back side, the experimental set-up.

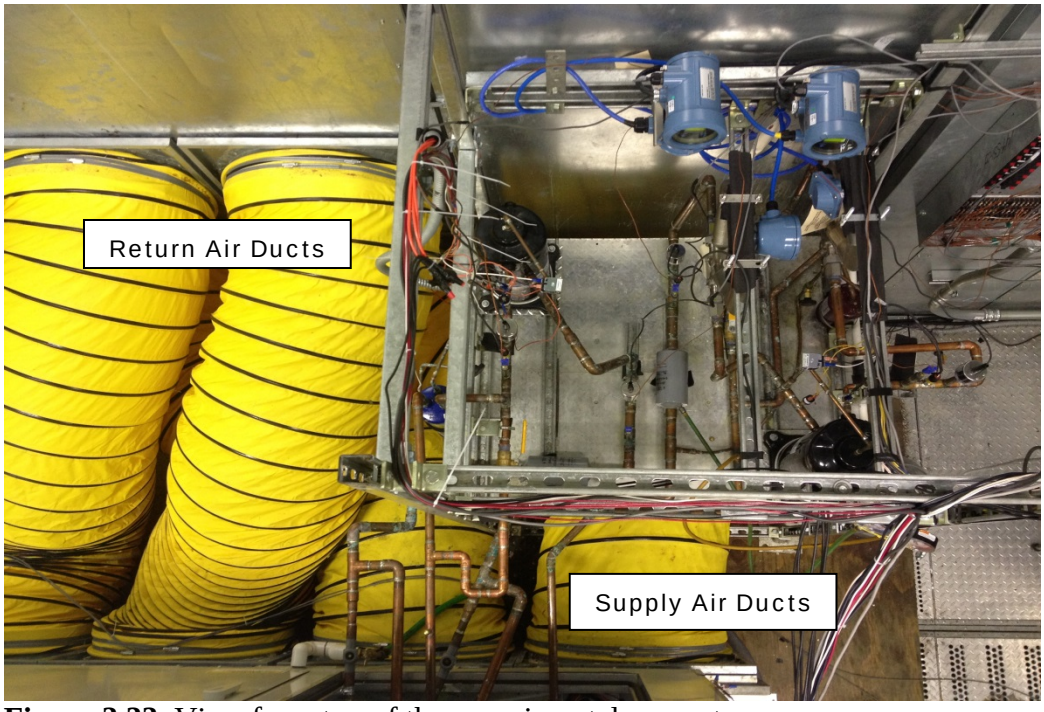

Figure 3.33. View from top of the experimental apparatus.

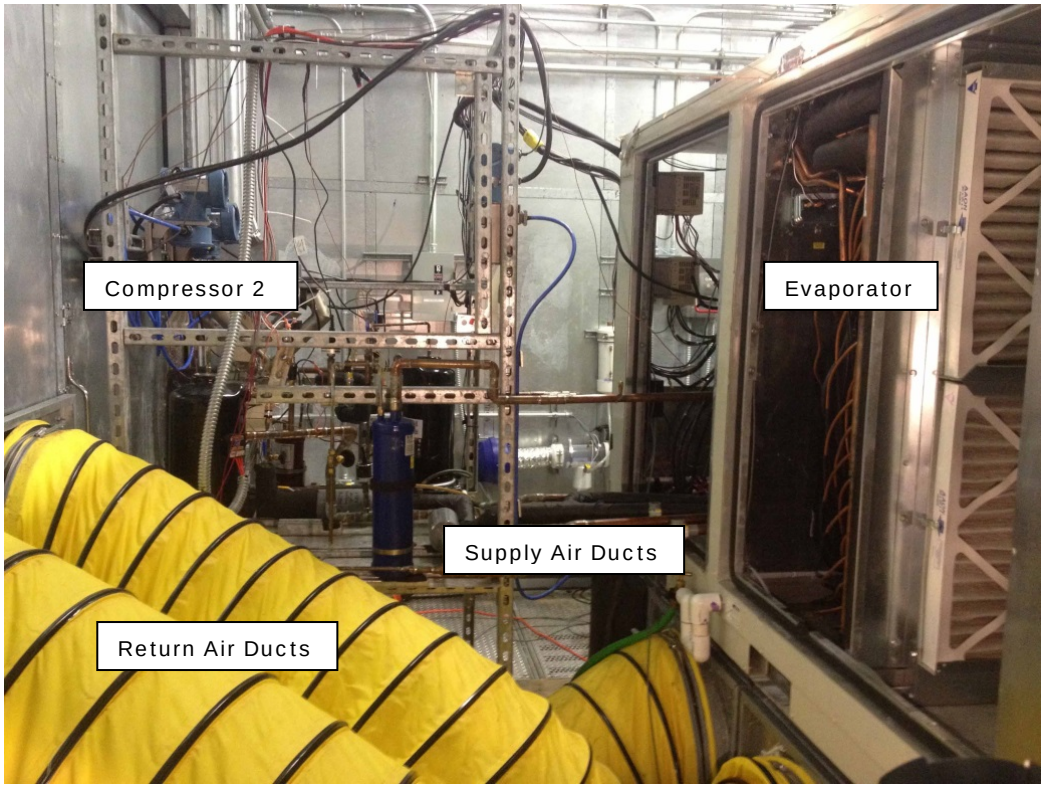

Figure 3.34. View from the back of the experimental apparatus.

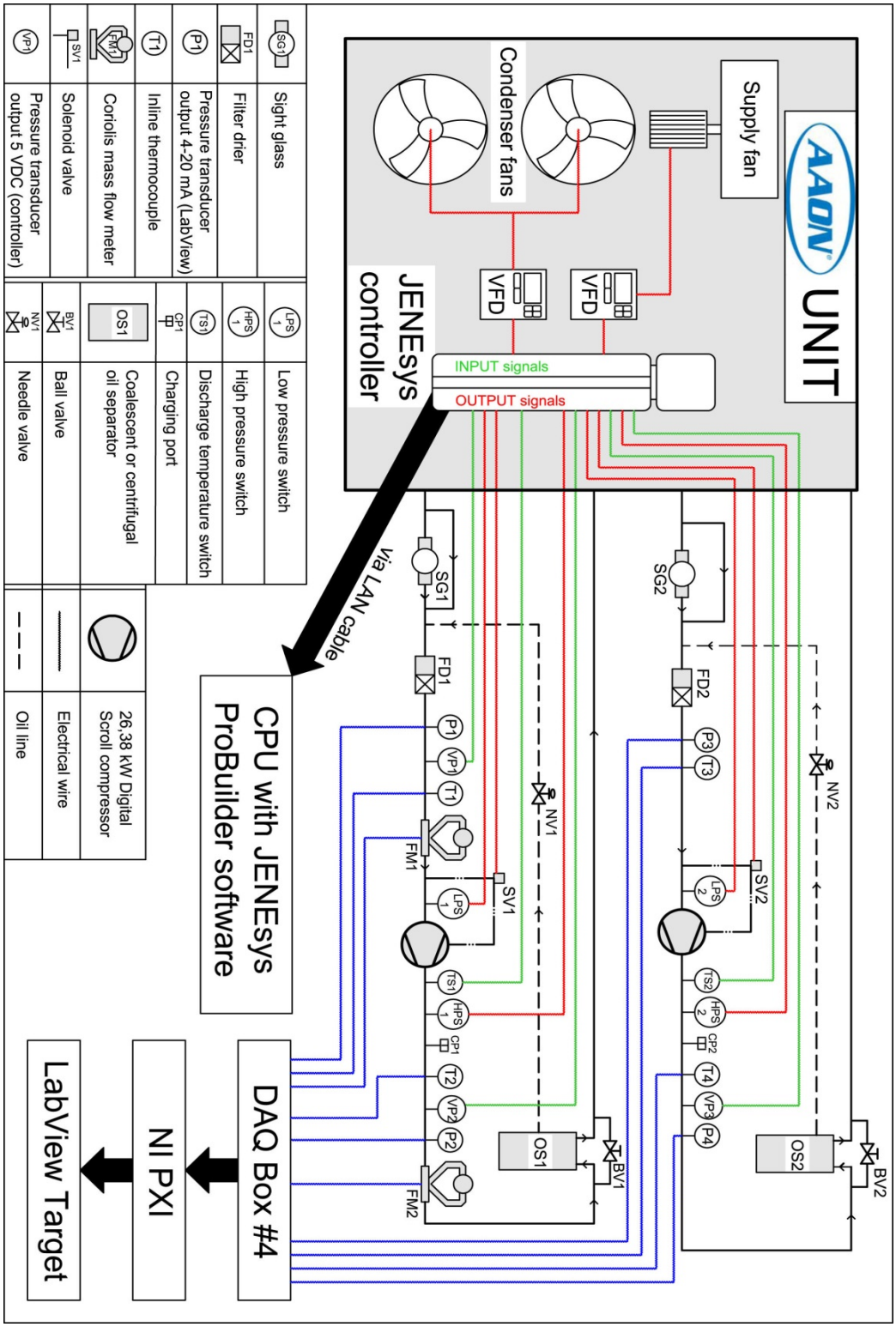

Figure 3.35. Layout of the project and DAQ/control connections.

Chapter 4

Compressor-oriented campaign of tests

4.1 Experimental methodology and results

During the first campaign of tests we investigated the digital scroll compressor. We established an operational map for the compressor that was used to validate the compressor simulation model. To prepare the psychrometric test chamber, the indoor and outdoor rooms were set to a desired ambient condition with the unit operating at steady state. Once the set point conditions were reached and maintained for 60 minutes, data recording started at a sampling rate of 2 seconds for additional 60 minutes. During this 2 hour period the dry bulbs in each room were maintained within ±0,2°F (±0,11°C) of the set points, and the indoor wet bulb was maintained within ±0,8°F (±0,44°C) of the set point. The speed of both condenser fans and evaporator blower was maintained fixed during the recording, too.
In order to prevent the unit from having too much pressure drop, the indoor room code tester fan were switched on: the resulting effect in the air ducts was the sum of the pushing action imposed by the supply fan, and the sucking action imposed by the code tester fan. This allowed to reach the desired air flow rate without an excessive pressure drop.
It has to be reported that between the unit and the code tester bay there was the need to go through another experimental apparatus of the Oklahoma State University Lab, so that the experiments could be run together at the same time (as shown in figure 4.1).

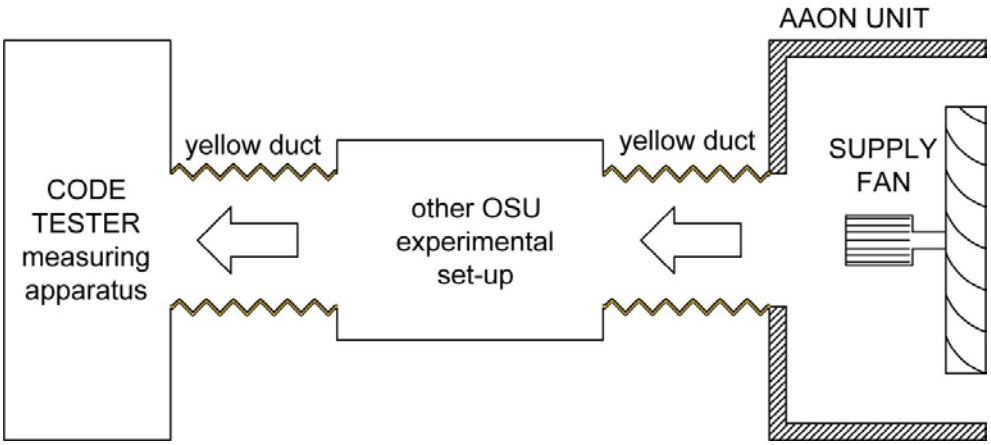

Figure 4.1. Configuration of the air side ducts.

That one, in fact, needed just the air flow that was pushed from the supply fan, and this is basically the reason why the air properties couldn't be measured from the very beginning of the test campaign. Anyway, this didn't matter because since the goal was characterizing the compressor, what was needed was just the ambient temperatures. During the second stage of tests, that apparatus was disconnected so the yellow ducts run straight from the unit to the code tester, where all the probes for the air properties measurements are.

Since the air properties measurements were unavailable at that time, the blower and code tester fan speed were set in order to have always the same air flow, which had to be high enough to ensure a good heat exchange at the evaporator.

Table 4.1. Test conditions for the compressor experiment.

OUTDOOR ROOM		**INDOOR ROOM**		**COMPRESSOR LOAD**
[°F]	**[°C]**	**[°F]**	**[°C]**	**[%]**
77,00	25,00	67,00	19,44	25-50-75-100
82,00	27,78	67,00	19,44	25-50-75-100
82,00	27,78	80,00	26,67	50-75-100
87,00	30,56	72,00	22,22	25-50-75-100
87,00	30,56	82,00	27,78	25-50-75-100
92,00	33,33	67,00	19,44	25-50-75-100
97,00	36,11	62,00	16,67	25-50-75-100
97,00	36,11	72,00	22,22	25-50-75-100
97,00	36,11	77,00	25,00	25-50-75-100
105,00	40,56	82,00	27,78	50-75-100
115,00	46,11	82,00	27,78	50-75-100

The reported percentage of compressor load corresponds to the actual on-cycle time compared to the total cycle time (15 seconds). For example, a 25% compressor load corresponds to a 3,75 seconds on-cycle time and 11,25 seconds off-cycle time.

The parameters under investigation include:

- Suction pressure
- Discharge pressure
- Suction temperature
- Discharge temperature
- Suction mass flow rate
- Discharge mass flow rate

- Suction density
- Discharge density
- Compressor electrical power

Table 4.2. Results of preliminary compressor experiment at the test conditions for varying load fractions.

Outdoor T - Indoor T [°F and (°C)]	Load [%]	Suction T [°C]	Discharge T [°C]	Suction p [bar]	Discharge p [bar]	Evap T [°C]	Cond T [°C]	Suction mass flow [kg/h]	Discharge mass flow [kg/h]	Suction density [kg/m^3]	Discharge density [kg/m^3]	Power consumption [W]
77-67 (25.00-19.44)	100	12,0	71,7	8,99	21,86	3,8	35,9	455,96	454,83	34,54	67,83	5388
	75	15,4	70,7	10,36	20,67	8,4	33,7	344,10	345,80	40,46	64,51	3986
	50	17,6	71,7	11,37	19,50	11,6	31,3	231,68	235,63	45,22	60,99	2863
	25	21,0	76,5	12,65	18,15	15,3	28,6	109,09	111,91	50,94	57,27	1666
82-67 (27.78-19.44)	100	12,2	74,7	9,09	23,15	4,2	38,2	459,92	458,79	34,94	71,55	5630
	75	15,7	74,0	10,41	21,91	8,6	36,0	342,97	344,67	40,61	68,03	4124
	50	18,3	74,8	11,52	20,72	12,0	33,7	230,55	234,50	45,72	64,51	2925
	25	21,9	79,9	12,77	19,35	15,6	31,1	107,96	111,35	51,09	60,49	1716
82-80 (27.78-26.67)	100	16,6	73,8	10,49	24,19	8,9	40,0	533,96	533,19	39,01	75,73	5969
	75	20,2	73,0	12,03	22,61	13,5	37,2	394,32	396,01	46,00	70,92	4406
	50	22,5	73,6	13,25	21,18	16,9	34,6	263,81	268,52	52,03	66,57	3128
87-72 (30.56-22.22)	100	14,5	77,7	9,71	24,93	6,3	41,3	490,38	489,32	36,79	76,90	5996
	75	18,1	76,7	11,14	23,57	10,9	38,9	365,87	367,45	43,00	72,98	4398
	50	20,7	77,3	12,32	22,25	14,4	36,6	246,22	250,19	48,47	68,98	3108
	25	24,3	82,0	13,64	20,76	18,0	33,8	117,02	120,92	54,14	64,29	1768
87-82 (30.56-27.78)	100	18,0	76,8	10,85	25,78	10,0	42,6	551,22	550,25	40,15	80,39	6302
	75	21,8	76,0	12,48	24,18	14,8	40,0	409,82	411,81	47,55	75,61	4632
	50	24,2	76,4	13,73	22,72	18,2	37,4	276,41	281,56	53,76	71,16	3287
	25	27,8	79,5	15,34	20,93	22,2	34,1	127,41	131,98	60,95	65,60	1824
92-67 (33.33-19.44)	100	13,5	82,0	9,36	26,11	5,1	43,2	470,27	469,58	35,57	79,64	6228
	75	16,6	80,9	10,62	24,73	9,3	40,9	344,30	346,07	41,22	75,81	4501
	50	19,5	81,5	11,77	23,47	12,8	38,8	233,29	236,67	46,24	72,08	3118
	25	23,6	87,5	12,99	22,04	16,2	36,2	107,08	110,22	51,25	67,37	1775
97-62 (36.11-16.67)	100	12,1	86,7	8,94	27,17	3,6	44,9	445,28	444,68	34,24	82,17	6461
	75	15,3	86,4	10,04	25,97	7,4	43,0	320,62	322,31	39,08	78,17	4658
	50	18,3	86,8	11,17	24,83	11,0	41,1	220,20	223,33	43,76	74,98	3238
	25	23,0	93,4	12,30	23,47	14,3	38,8	101,31	104,99	47,58	70,72	1727
97-72 (36.11-22.22)	100	15,6	84,6	10,04	27,52	7,4	45,4	503,67	503,04	37,65	85,60	6584
	75	18,6	83,6	11,31	26,40	11,4	43,7	367,53	369,39	43,48	81,37	4685
	50	21,7	83,9	12,59	25,15	15,1	41,6	251,23	255,40	49,10	77,26	3264
	25	26,2	90,3	13,97	23,57	18,8	38,9	111,05	114,50	54,63	71,58	1770
97-77 (36.11-25.00)	100	17,4	84,0	10,60	27,74	9,2	45,7	534,27	533,42	39,35	87,44	6797
	75	20,3	82,7	11,96	26,63	13,3	44,0	389,76	391,68	45,72	82,94	4925
	50	23,5	82,8	13,30	25,33	17,1	41,9	266,52	270,95	51,73	78,39	3437
	25	27,6	88,0	14,75	23,74	20,8	39,2	123,12	126,87	57,75	72,55	1938
105-82 (40.56-27.78)	100	22,1	88,5	11,71	28,79	12,6	47,3	584,19	583,76	42,44	95,09	7266
	75	25,1	87,1	13,23	28,11	16,9	46,3	428,98	431,51	49,76	90,57	5215
	50	27,8	87,2	14,62	27,29	20,5	45,0	288,98	294,46	56,26	85,93	3558
115-82 (46.11-27.78)	100	23,6	95,6	12,10	30,21	13,7	49,4	597,39	597,14	43,56	104,86	8196
	75	25,8	94,2	13,48	29,56	17,5	48,5	432,48	435,03	50,44	100,22	5920
	50	28,4	94,3	14,77	28,98	20,9	47,6	292,29	297,20	56,47	95,59	4096

Since the studied apparatus resulted to be different from any standard equipment that could be seen to confront our data, there was no particular expectations about the values of the parameters of interest. But since the focus on the compressor and the compressor map of the Digital Scroll Compressor was provided by Emerson, it was good to see that all the investigated parameters, in particular the compressor absorbed power and the evaporating and the condensing temperatures, were very close to the values reported in the compressor map, referring to full load operating conditions (figure 4.2). The experimentally obtained and the provided data show a max. 3% difference.

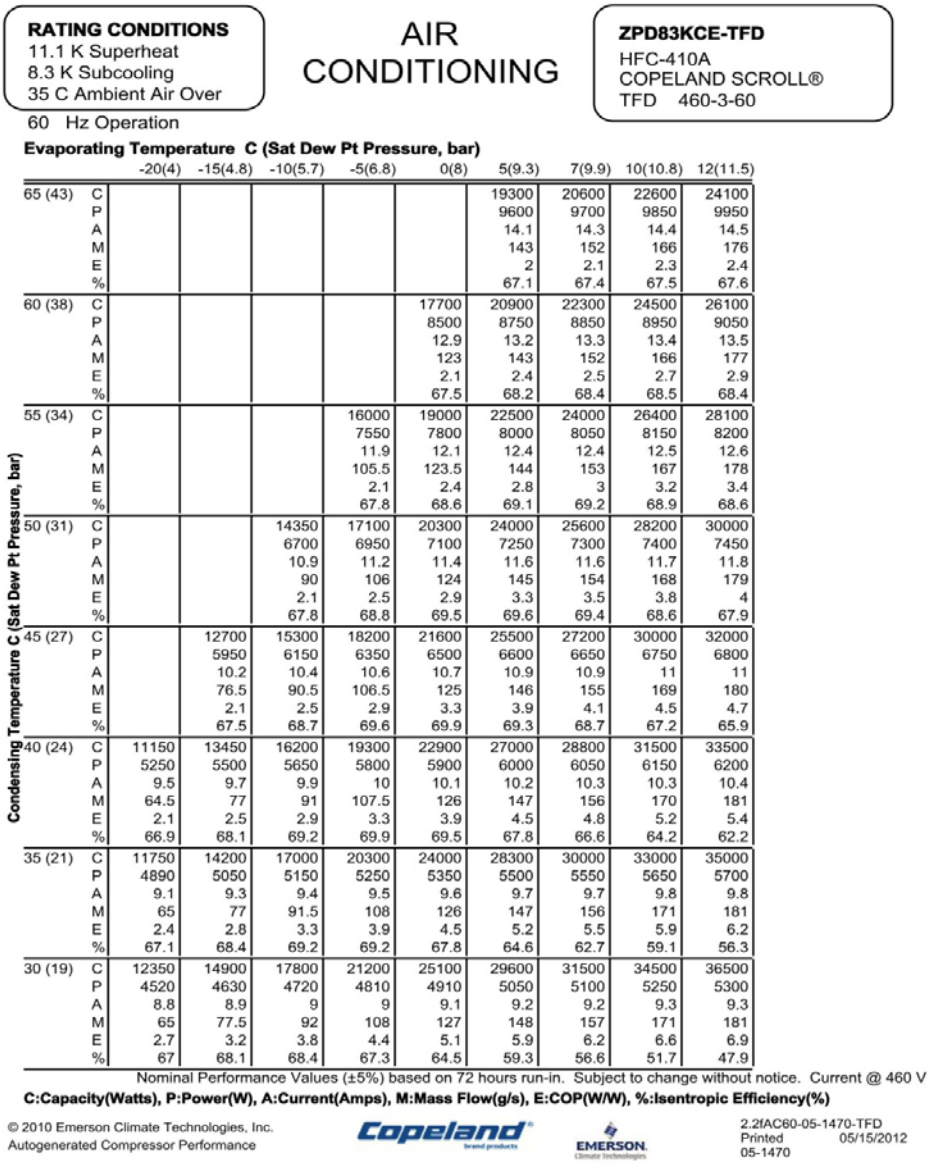

RATING CONDITIONS
11.1 K Superheat
8.3 K Subcooling
35 C Ambient Air Over
60 Hz Operation

AIR CONDITIONING

ZPD83KCE-TFD
HFC-410A
COPELAND SCROLL®
TFD 460-3-60

Evaporating Temperature C (Sat Dew Pt Pressure, bar)

Condensing Temperature C (Sat Dew Pt Pressure, bar)

		-20(4)	-15(4.8)	-10(5.7)	-5(6.8)	0(8)	5(9.3)	7(9.9)	10(10.8)	12(11.5)
65 (43)	C						19300	20600	22600	24100
	P						9600	9700	9850	9950
	A						14.1	14.3	14.4	14.5
	M						143	152	166	176
	E						2	2.1	2.3	2.4
	%						67.1	67.4	67.5	67.6
60 (38)	C					17700	20900	22300	24500	26100
	P					8500	8750	8850	8950	9050
	A					12.9	13.2	13.3	13.4	13.5
	M					123	143	152	166	177
	E					2.1	2.4	2.5	2.7	2.9
	%					67.5	68.2	68.4	68.5	68.4
55 (34)	C				16000	19000	22500	24000	26400	28100
	P				7550	7800	8000	8050	8150	8200
	A				11.9	12.1	12.4	12.4	12.5	12.6
	M				105.5	123.5	144	153	167	178
	E				2.1	2.4	2.8	3	3.2	3.4
	%				67.8	68.6	69.1	69.2	68.9	68.6
50 (31)	C			14350	17100	20300	24000	25600	28200	30000
	P			6700	6950	7100	7250	7300	7400	7450
	A			10.9	11.2	11.4	11.6	11.6	11.7	11.8
	M			90	106	124	145	154	168	179
	E			2.1	2.5	2.9	3.3	3.5	3.8	4
	%			67.8	68.8	69.5	69.6	69.4	68.6	67.9
45 (27)	C		12700	15300	18200	21600	25500	27200	30000	32000
	P		5950	6150	6350	6500	6600	6650	6750	6800
	A		10.2	10.4	10.6	10.7	10.9	10.9	11	11
	M		76.5	90.5	106.5	125	146	155	169	180
	E		2.1	2.5	2.9	3.3	3.9	4.1	4.5	4.7
	%		67.5	68.7	69.6	69.9	69.3	68.7	67.2	65.9
40 (24)	C	11150	13450	16200	19300	22900	27000	28800	31500	33500
	P	5250	5500	5650	5800	5900	6000	6050	6150	6200
	A	9.5	9.7	9.9	10	10.1	10.2	10.3	10.3	10.4
	M	64.5	77	91	107.5	126	147	156	170	181
	E	2.1	2.5	2.9	3.3	3.9	4.5	4.8	5.2	5.4
	%	66.9	68.1	69.2	69.9	69.5	67.8	66.6	64.2	62.2
35 (21)	C	11750	14200	17000	20300	24000	28300	30000	33000	35000
	P	4890	5050	5150	5250	5350	5500	5550	5650	5700
	A	9.1	9.3	9.4	9.5	9.6	9.7	9.7	9.8	9.8
	M	65	77	91.5	108	126	147	156	171	181
	E	2.4	2.8	3.3	3.9	4.5	5.2	5.5	5.9	6.2
	%	67.1	68.4	69.2	69.2	67.8	64.6	62.7	59.1	56.3
30 (19)	C	12350	14900	17800	21200	25100	29600	31500	34500	36500
	P	4520	4630	4720	4810	4910	5050	5100	5250	5300
	A	8.8	8.9	9	9	9.1	9.2	9.2	9.3	9.3
	M	65	77.5	92	108	127	148	157	171	181
	E	2.7	3.2	3.8	4.4	5.1	5.9	6.2	6.6	6.9
	%	67	68.1	68.4	67.3	64.5	59.3	56.6	51.7	47.9

Nominal Performance Values (±5%) based on 72 hours run-in. Subject to change without notice. Current @ 460 V

C:Capacity(Watts), P:Power(W), A:Current(Amps), M:Mass Flow(g/s), E:COP(W/W), %:Isentropic Efficiency(%)

Autogenerated Compressor Performance

Copeland brand products
EMERSON Climate Technologies

2.2fAC60-05-1470-TFD
Printed 05/15/2012
05-1470

Figure 4.2. Compressor Map (ZPD83KCE).

Preliminary observations demonstrated that the behavior at full load is similar to a typical scroll compressor. The parameters of interest remain stable throughout the experiment (see figure 4.3). This was expected, as the scroll unloading mechanism was not operational under fully loaded conditions.

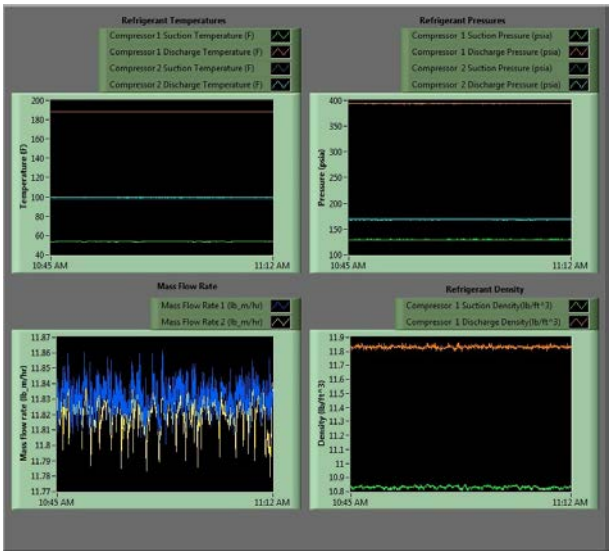

Figure 4.3. Screencap of the compressor working at full load (mass flow rate and density are still not converted, so the signal is in mA, and applicating the conversion equation it gives an average 1107 lbs/hr (503 hg/h) mass flow rate, so a 2 kg/h oscillation).

At part load the pulsing flow is evident, as seen in figure 4.4.

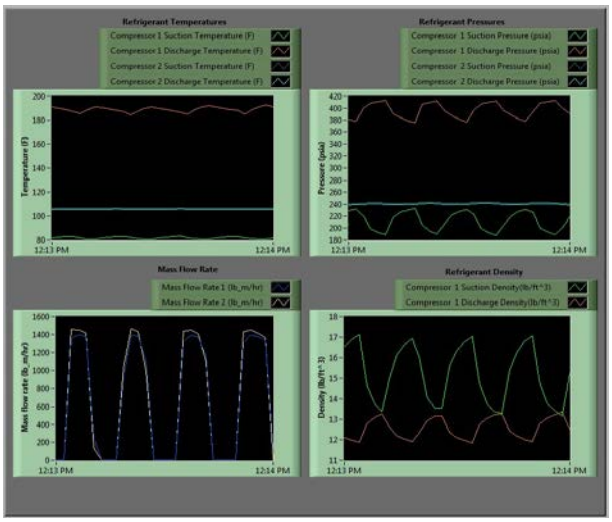

Figure 4.4. Screencap of the compressor working at 50% compressor load.

An interesting result of the experiment was that suction and discharge flow rate meters observe different mass flow rate at the same time, due to the dynamic operation of the compressor. This was a good starting point when determining the overall system capacity, efficiency, heat exchange etc. A key consideration during such pulsed flow behaviours is how to define a specific value (average) of mass flow rate, density, temperature and pressure to characterize the unit with a particular and significant COP value. Considering tab. 4.2, suction and discharge mass flow rates are very similar at any load (less than 3%) so we'll consider just one of them in the calculations and won't take any average value.

4.2 Model validation

In order to produce verifiable results in Modelica, values need to be applied to the geometric parameters, and provide test cases by specifying the inlet condition as well as the saturated condensing pressure due to its role in the modeling of the discharge valve dynamics. The model of Chen [14] details the geometry parameters as well as a number of such conditions with which to verify the model. This can be noticed when testing as simulation trial 1, wherein it was attempted to validate the model on the basis of Chen's [14] compressor geometry and experimental data.

A feature of the compressor studied by Chen is that while measurements were taken at a constant frequency of 60 Hz, the angular speed varied with the pressure ratio across the device:

$$\omega = 2\pi \left[f \left(\tan(1.13\exp(-3(f-22)) - 6.36\exp(-2)) \left(\frac{P_d}{P_s} \right) + 0{,}988 \right) \right] \quad (76)$$

where f is frequency, and this must be taken into account during the validation.

For simulation trial 1, fifteen data points are given by saturated evaporation pressure, saturated evaporation temperature, suction superheat, and the corresponding saturated condensing pressure. The measured points were taken with 10 °C suction superheat. Results are presented in table 4.3. This simulation did not include a heat transfer model.

In simulation trial 1 it can be clearly seen that while simulated mass flow rate follows closely with measured data, the simulated mass flow rate itself tracks closest to presented data when the inter-chamber leakages were not included. By this modelling, the discharge temperature is overpredicted. Because of the

overprediction, a heat transfer sub-model was added to the overall simulation to simulate the heat lost to the environment during Simulation trial 2.

Table 4.3. Results of simulation versus measured data for Simulation trial 1.

Point			Experimental Data		Simulated Data		Difference	
	P_{evap}	T_{cond}	$\dot{m}_{R410A}$	T_{DIS}	$\dot{m}_{R410A}$	T_{DIS}	$\dot{m}_{R410A}$	T_{DIS}
	bar	°C	kg/h	°C	kg/h	°C	%	°C
1	5,72	25	36,98	61,3	35,48	71,35	0,04	10,05
2		30	36,99	66,86	35,28	79,95	0,05	13,09
3		35	36,07	72,54	34,85	88,16	0,03	15,62
4		40	35,55	80,06	34,79	95,75	0,02	15,69
5		45	34,18	88,11	34,28	102,75	0,01	14,64
6	7,96	25	50,35	55,55	49,9	64,85	0,01	9,3
7		30	50,37	60,24	49,65	74,4	0,01	14,16
8		35	49,82	65,63	49,27	82,2	0,01	16,57
9		40	48,55	73,13	49,12	90,35	0,01	17,22
10		45	46,94	80,35	48,8	97,8	0,04	17,45
11	10,81	25	67,52	48,15	68,48	61,8	0,01	13,65
12		30	66,95	54,08	68,01	68,01	0,02	15,23
13		35	65,75	61,14	67,9	67,9	0,03	16,07
14		40	64,43	67,54	67,7	67,7	0,05	17,23
15		45	63,34	73,73	67,3	67,3	0,06	18,97

In Simulation trial 2 the model was then modified by altering the geometric characteristics to assumed values for the 7.5 ton digital scroll compressor and again simulated against experimental data taken during full flow conditions at 11 different points. The simple heat transfer model discussed in sub-section 2.5.6 was applied with the convection coefficient based upon the psychrometric chamber volumetric flow at 100%.

Table 4.4. Results of simulation versus measured data for Simulation trial 2.

			Experimental Data		Simulated Data		Difference		
Point	P_{SUCT}	P_{DIS}	$\dot{m}_{R410A}$	T_{DIS}	$\dot{m}_{R410A}$	T_{DIS}	$\dot{m}_{R410A}$	T_{DIS}	$\dot{W}_{compr}$
	bar	bar	kg/h	°C	kg/h	°C	%	°C	%
1	9,01	21,88	455,85	71,7	454,4	72	0,32	0,3	4,69
2	9,09	23,13	459,75	74,7	457,2	75,4	0,56	0,7	1,74

3	9,37	26,13	470,54	81,9	468,1	83,5	0,52	1,6	0,94
4	9,72	24,94	491,61	77,7	489,1	79,5	0,5	1,8	0,34
5	10,02	27,52	502,35	84,6	501,5	86	0,17	1,4	0,8
6	10,63	27,77	534,89	84,1	533,9	85,8	0,19	1,7	1,64
7	10,48	24,19	532,85	73,9	533	76,4	0,03	2,5	0,45
8	10,84	25,80	550,65	76,9	548,5	80,5	0,38	3,6	2,29
9	11,73	28,81	584,93	88,7	587,1	88,6	0,37	0,1	0,68
10	8,95	27,18	445,57	86,7	446,1	85,9	0,12	0,8	0,52
11	12,11	30,22	597,06	95,7	605,7	93,3	1,44	2,4	0,3

A close agreement in mass flow and temperature was achieved, but it can be noticed that as ambient temperature increased in point 11 the mass flow rate prediction was less precise.

It has been developed a dynamic modeling of a digital scroll compressor that incorporates scroll geometry, leakage, a real gas model and a mathematical approximation of the digital capacity mechanism. The model was verified first against previously reported data and against newly developed experimental data. With the application of a heat transfer model, it is found to track mass flow rate and temperature within acceptable tolerances. A curve fit modeling of the power was applied to avoid the requirement of modeling the motor and introducing additional unknown quantities.
It can also be noticed that all the data are simulating 100% compressor loads but for what concerns part loads different considerations need to be done: while it is easy to set inputs and outputs for nominal full load (a nominal pressure value with an associated enthalpy that is defined by the degrees of superheat at the suction state, for example) the dynamically varying suction state associated with part load operations is difficult to define. It is not well determined by a mean pressure value, as the pressure is continuously varying. Temptatively, some sort of sinusoidal variation to the pressure at suction could be applied, but this would not really be appropriate, because it doesn't reflect the actual behaviour.
What could help in characterizing the behaviour is to create a dynamic model of the full refrigeration circuit with at least condenser, evaporator, and thermal expansion valve. The first order response of the fluid in the coils should then be defined and this should give the appropriate behaviour characteristic to the suction state.

Due to an artifact of simulation requiring some time to pass in order to develop the steady state values of mass flow rate and power, it may be advantageous to develop a new technique for determining power dynamically.

The model, finally, develops the outlet state of the compressor given the inlet state, and it has been seen through the course of the experiment that the conditions change depending upon the degree of compressor unloading. As we go forward it will be important to incorporate the model into a refrigeration circuit simulation to identify the impact of the unique unloading mechanism on the other components.

4.3 The wave shape approximation: influence of the sampling rate

The sampling rate was also studied. As discussed earlier, the default sampling rate is 2 seconds. A 1 second sampling rate was applied and the experiment was conducted again. It was determined that there is no significant difference between the recorded output for data taken at 1 second intervals and for data taken at two second intervals.

Table 4.5. Percent differences between recorded data taken at 1 second and 2 second sampling intervals (at 25% compressor load).

OT-IT	25% Load	Suction T	Discharge T	Suction p	Discharge p	Suction m.f.rate	Disch. m.f.rate	Power
77-67 °F	**difference Avg**	**0,17%**	**0,73%**	**0,05%**	**0,09%**	**0,34%**	**0,29%**	**0,02%**
	difference Max	0,13%	0,30%	0,66%	0,06%	0,24%	0,50%	0,30%
	difference Min	1,07%	0,81%	0,84%	0,06%	0,00%	0,03%	0,28%
82-67 °F	**difference Avg**	**0,14%**	**0,06%**	**0,11%**	**0,09%**	**0,46%**	**0,47%**	**0,13%**
	difference Max	0,37%	0,13%	0,09%	0,16%	0,39%	0,38%	0,24%
	difference Min	0,39%	0,75%	0,45%	0,05%	0,03%	0,00%	0,14%
87-72 °F	**difference Avg**	**0,06%**	**0,19%**	**0,08%**	**0,13%**	**0,20%**	**0,09%**	**0,66%**
	difference Max	0,30%	1,13%	0,24%	0,94%	0,02%	0,27%	0,10%
	difference Min	0,28%	0,67%	2,24%	0,06%	0,03%	0,00%	0,19%
92-67 °F	**difference Avg**	**0,12%**	**0,01%**	**0,08%**	**0,11%**	**0,47%**	**0,47%**	**0,35%**
	difference Max	0,47%	0,21%	0,06%	0,01%	0,22%	0,33%	0,23%
	difference Min	0,38%	0,31%	0,23%	0,08%	0,03%	0,03%	0,58%
97-72 °F	**difference Avg**	**0,14%**	**0,44%**	**0,09%**	**0,04%**	**0,43%**	**0,42%**	**0,11%**
	difference Max	0,19%	0,35%	0,30%	0,28%	0,15%	0,22%	0,32%
	difference Min	0,05%	0,22%	2,20%	0,21%	0,00%	0,03%	0,10%

The first approximation for the loading/unloading plot was to be a square wave pulse train, but based upon what common sense would suggest, a better approximation might be a trapezoidal wave.

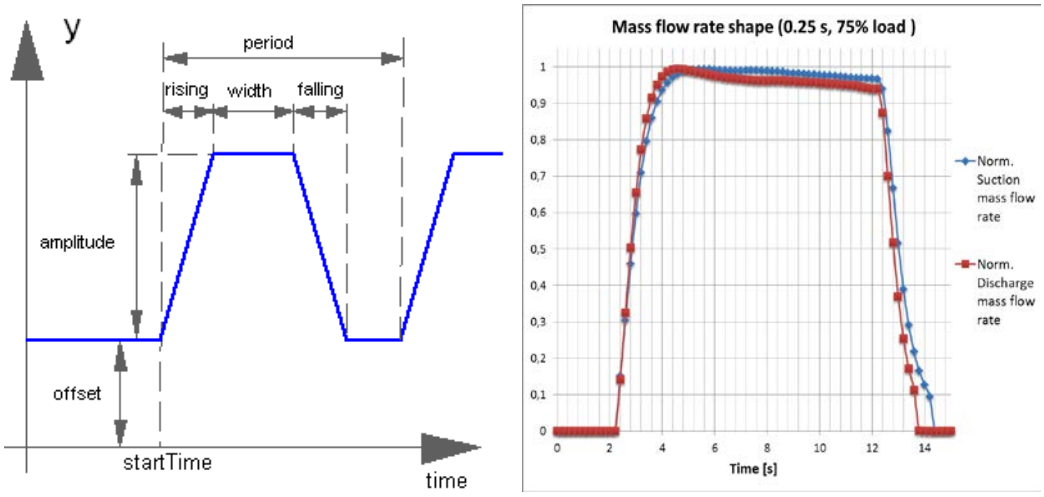

Figure 4.5. Ideal (left) and experimental (right) shape of the refrigerant mass flow rate.

Figure 4.5 shows that the trapezoidal wave is a good approximation because when the solenoid valve activates, the pressure in the back pressure chamber is relieved to suction and the leaf spring starts to dominate the back pressure. This will happen on a short time scale, but it is not instantaneous, so the rise time and falling time might be short, but for the compressor operating at 60 Hz, 1 second is a fairly long time (relatively). A higher fidelity model would attempt to get the dynamics of the process correctly, but it's not easy to determine the spring constant and the settling time for the back pressure chamber to equilibrate to suction pressure, so for now the pulse train will approximate the behaviour.
Furthermore, it's noticeable that the suction and discharge mass flow rates have the same trend, and the differences are negligible.
In order to experimentally validate this considerations, more tests at part load were run with a smaller sample rate, which decreased from 1 to 0,5 s and then 0,25 s. The mass flow rate plots below show differences in decreasing the sample rate, but the difference gets thinner from 0,5 to 0,25 s because since the target flow rate (100% load) is pretty high and it has to jump from 0 to about 500 kg/hr, it gets way difficult to show the trapezoidal wave we're expecting, but it clearly occurs.

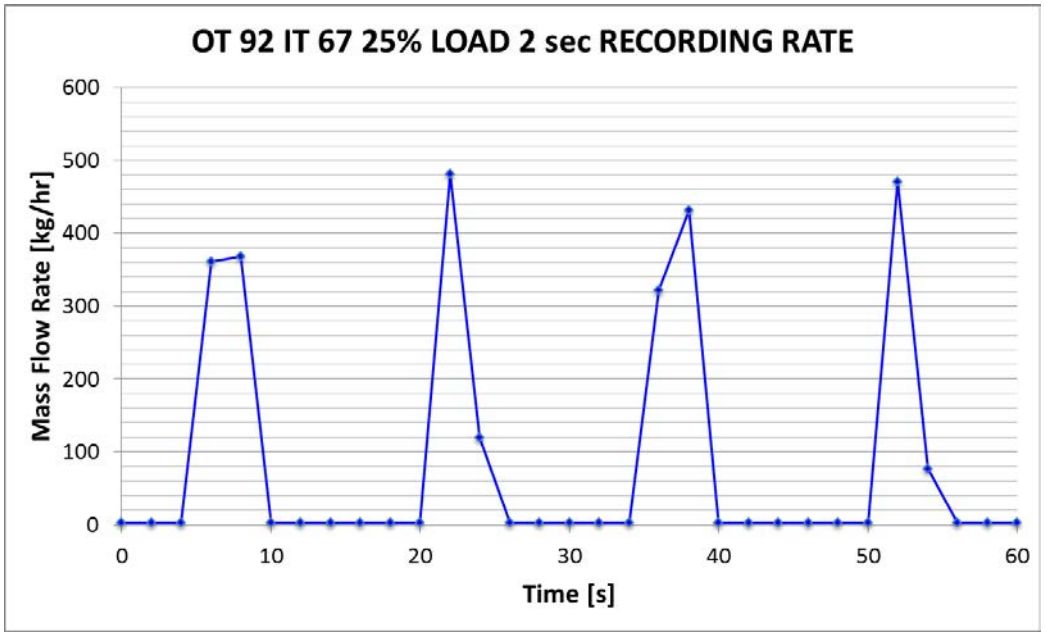

Figure 4.6. Refrigerant mass flow rate waves with 2 s sampling rate (25% load).

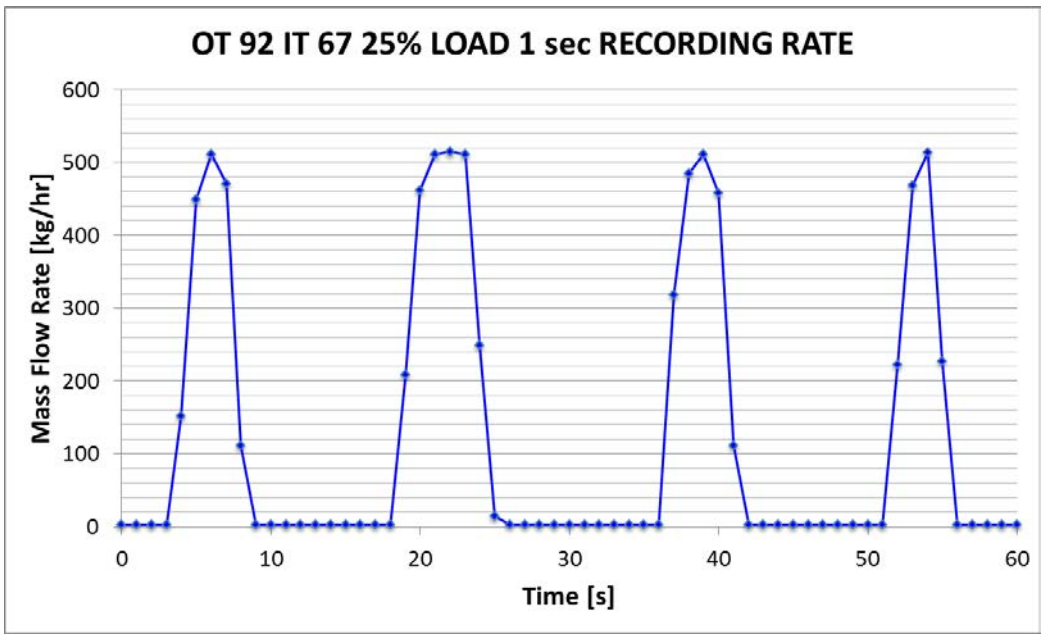

Figure 4.7. Refrigerant mass flow rate waves with 1 s sampling rate (25% load).

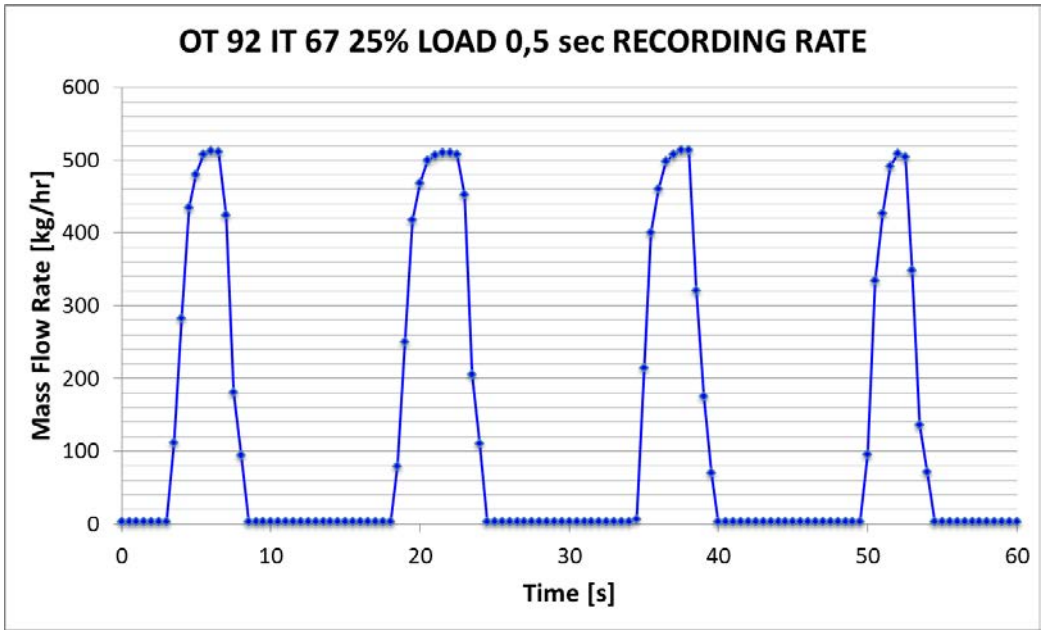

Figure 4.8. Refrigerant mass flow rate waves with 0,5 s sampling rate (25% load).

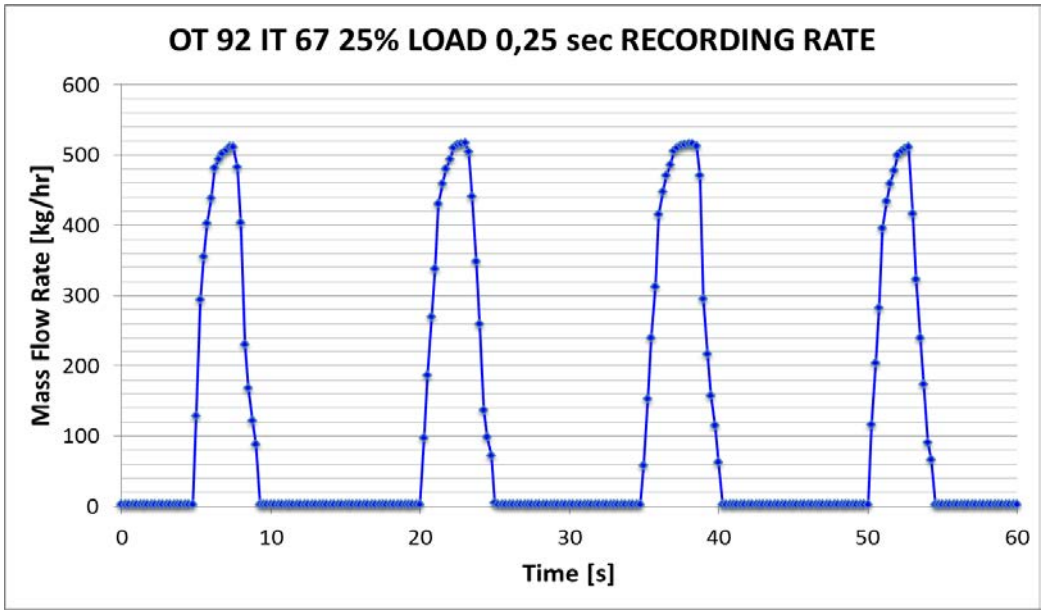

Figure 4.9. Refrigerant mass flow rate waves with 0,25 s sampling rate (25% load).

What these additional tests at lower sampling rate also showed, was that at part load the compressor hardly provides the target flow rate, in fact by the time the flow rate increases through the trapezoidal wave, the cycle time imposes it to cut

off. This is well showed when comparing the 0,25 s sampling time plots at different load, like at 25% and 75%.

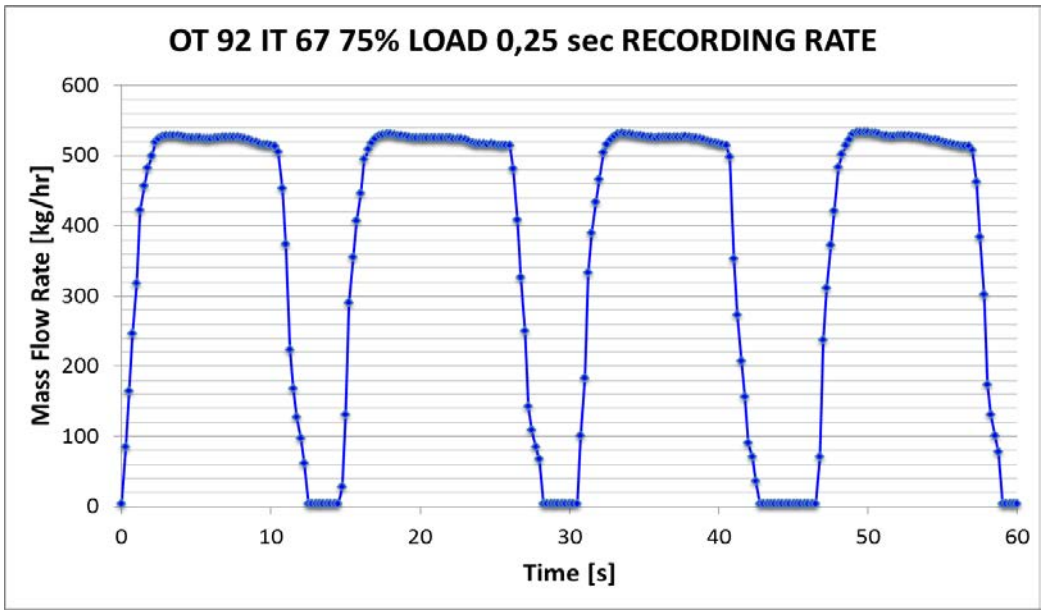

Figure 4.10. Refrigerant mass flow rate waves with 0,25 s sampling rate (75% load).

This is a pivotal consideration if one thinks about the heat transfer through the coils: what the evidences suggest and was verified in the second campaign of tests, is that when the compressor load goes below around 30%, the time when the flow rate is the regime flow rate is very little. This can be thought as a continuous attempt by the compressor to reach up the regime flow rate but by the time it tries to settle at the regime conditions of flow rate, it already has to shut off. That will surely affect the heat transfer in the coils: what has to be verified is at which load the heat transfer starts to get insufficient. At low load conditions, in fact, it's unlikely for the flow to reach turbulent conditions and the heat transfer coefficient drops down. Thus, at part load the digital scroll compressor kind of operation results inefficient, especially because in the heat pump mode it can cause many defrost cycles.
At this conditions one would rather run the compressor at higher load, like at 30%, and shutting it off when necessary.
This aroused the feeling that additional test at very low load (12%, 17,5%, 25%, 30%) could be run with a very high recording rate (0,1 s) in order to push the data acquisition capability to the limit and try to capture as well as possible the behaviour of the refrigerant and the physics inside the compressor. These tests were run during the second campaign.

When the load fraction on the compressor is reduced, the controller applies a signal to the solenoid valve to relieve the back pressure chamber for modulation. The loaded duration is closely associated with the load fraction. Figure 4.11 illustrates the behaviour of the compressor under a 25% load fraction with a cycling period of 15 seconds. During the off state a valve closes to prevent back flow, and mass flow is effectively zero. Power consumption is non-zero during this time as the motor continues to spin in the unloaded state. This confirms what was expected while running the simulation model (see figure 4.11)
Another interesting feature that was noticed is the delay between the instantiation of the on state and the reinstatement of compressor flow in the figure below, taken for a 1 s recording rate at 25% compressor load. This is well predicted by the simulation model and shows a good match with the experimental outcome.

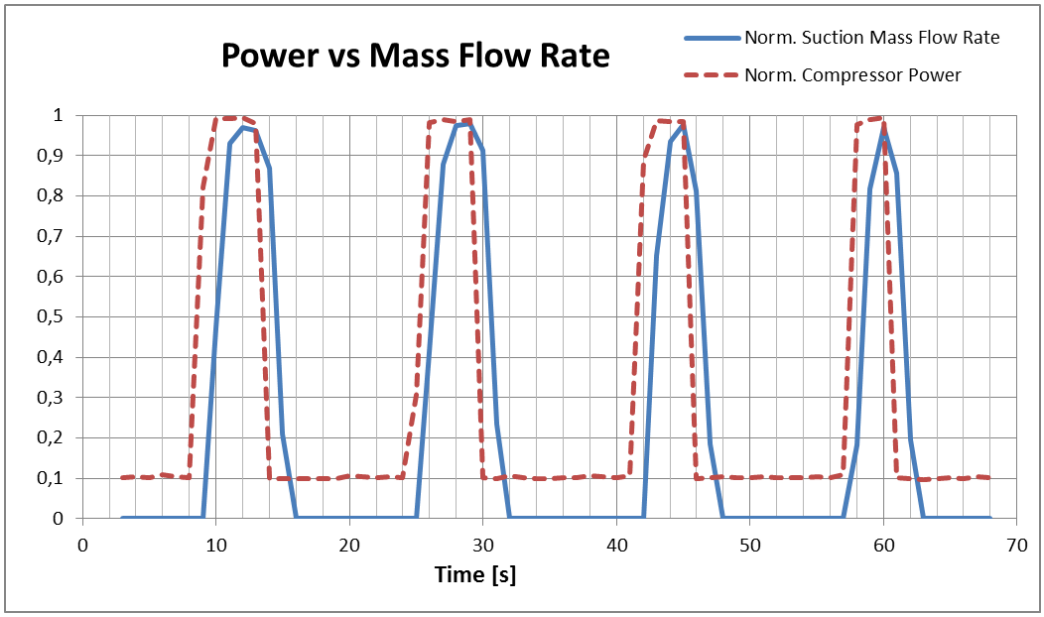

Figure 4.11. Experimentally obtained data for the digital scroll compressor at 25% load. Because of the idle cycle, the absorbed power never goes to zero.

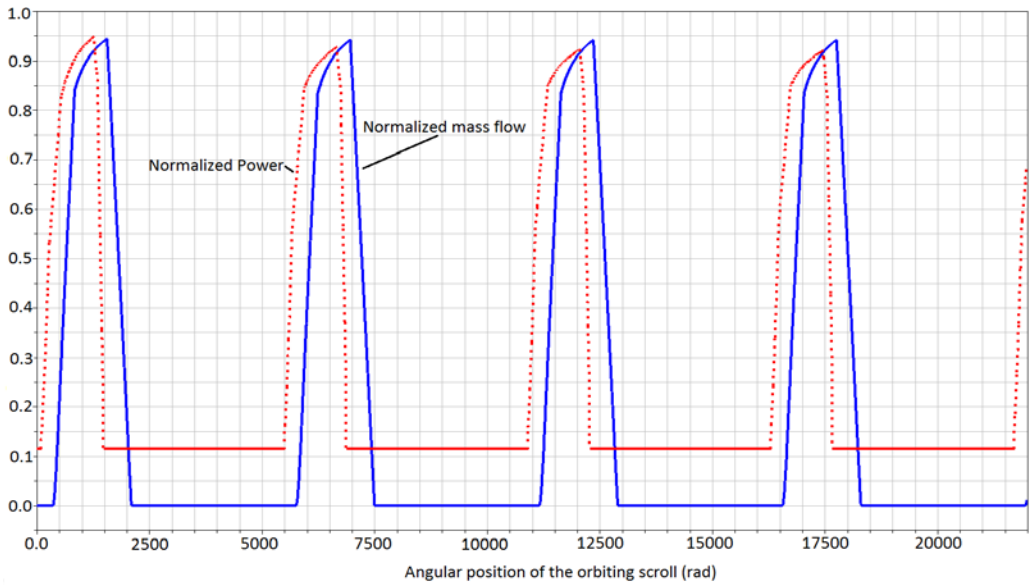

Figure 4.12. Dynamic simulation for digital scroll compressor at 25% load fraction.

Chapter 5

Unit-oriented campaign of tests

5.1 Introduction and unit upgrade

The first stage of tests was exclusively focused on the digital scroll compressor, in order to build a compressor map, to study the wave shape and to validate a simulation model.
For this reason several devices (flow meters, thermocouples and pressure transducers) were mounted only on the suction and on the discharge side, in order to observe the different behaviour of the refrigerant across the compressor, changing both the ambient conditions (evaporating temperature, condensing temperature) and the compressor load.
The second stage was focused on a more synoptic investigation, in understanding how the compressor interacts with the whole unit and its impact on the air side.

The tests that were run were:

- Unit-oriented campaign of tests, effects of the pulsing flow on the unit capacity (section 5.2);
- Low load compressor-oriented tests (section 5.3);
- Towards the transient operation: the *Step-Function Test* (section 5.4);

For the project purposes the experimental set-up was modified by equipping it with new sensors/devices in order to have further data and information about the behaviour of the unit:

- Power box for independent compressor power consumption measurement, to integrate the overall power consumption info.
- Flow meter on the liquid line.
- In-line thermocouple on the liquid line.
- In-line pressure transducer on the liquid line.
- Sampling tree for air properties at the outlet of the evaporator, air side (supply air properties).
- Sampling tree for air properties at the inlet of the evaporator, air side (return air properties).
- Surface thermocouples mounted at the top and at the bottom of the compressor shell, in order to monitor its temperatures and eventually try

to build a natural convection heat transfer model to try to get to the actual efficiency of the compressor (for future developments).
- 20 kW electric heater (step function purposes).
- Surface thermocouple to monitor the temperature increase of the air heated by the electric heater (step function purposes).

5.1.1 Power box for independent compressor power consumption measurement

For the first campaign of tests a separate power measurement of the compressor was not needed since its operation was only in steady state conditions; in fact the only overall unit power consumption measurement was used, and the compressor power intake was merely deduced by subtracting the absorbed power of the fans to the one of the unit (as already explained in sub-section 3.2.3).
On the contrary, for the step function test and above all for future developments an independent power measurement is not only advisable but also indispensable. In fact, when running the unit in transient conditions in order to determine the optimal control strategy, it's mandatory to have independent power measurements for every component, so a more analytical view was required.

Optimal control means achieving the same capacity (for some defined environmental conditions) by changing independently the fans speed and the compressor speed. The desired outcome was obviously minimizing the overall consumption, but it's needed to know the absorbed power of each component separately, in order to figure out which was the optimal arrangement in controlling the unit, how to run each component.

So a new wattmeter was put, along with a new terminal block and three new current transformers on the power line of the compressor, not in a proper "box" but directly inside the unit (as shown in figure 5.1); the signal output was connected to Lab View (not to the controller) as the other power signal.
The model of the wattmeter is the same of the one we used for the unit power estimation, but the current transformers are different (see table 5.2 for specifications).

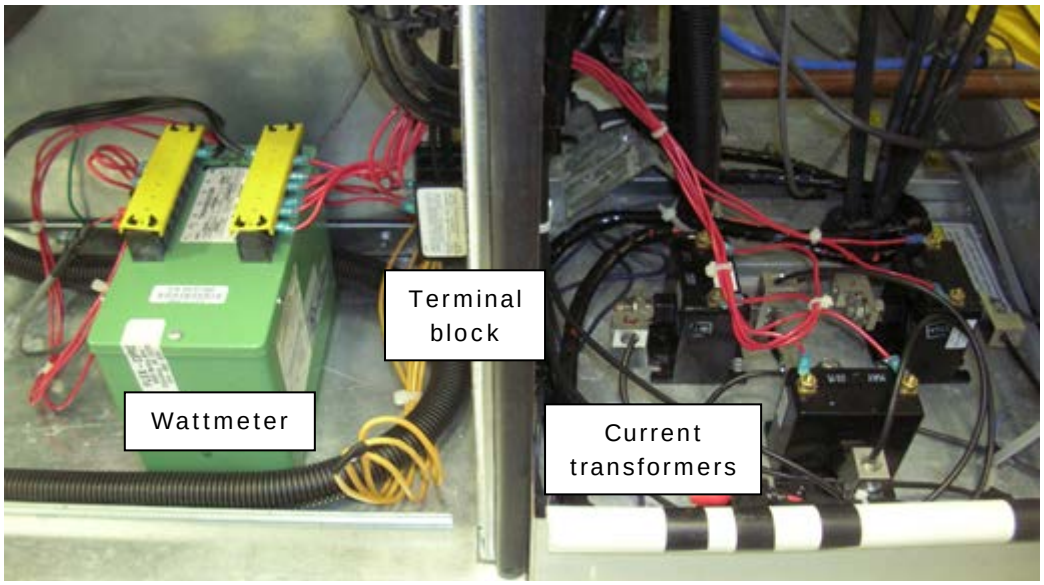

Figure 5.1. Second power measuring point for independent compressor power consumption. On the left, the wattmeter and the terminal block. On the right, the current transformers.

5.1.2 New mass flow meter, thermocouple and pressure transducer on the liquid line

As already previously mentioned, with the second stage of tests the target became the unit in its entireness; so from the point of view of the refrigerant the whole refrigeration cycle was the focus, not only the compression phase.
One of the second stage purposes was verifying and quantifying the influence of the modulation of the compressor, realized by the solenoid valve, on the refrigerant cycle, in particular on the fluid between the condenser and the evaporator.
Therefore some new sensors were needed to grasp the subcooling ΔT, pressure drop, and fluctuations, delay and inertia of the system, in terms of mass flow rate, temperature and pressure.
As shown in figure 5.2 a new Coriolis mass flow meter was mounted on the liquid line and calibrated. It was a smaller model than the one used for suction and discharge lines, but for the mass flow rate was more than adequate (see table 5.1, for specifications). The integration of the new mass flow meter to the existing two gave information about the delay with which the pulsing wave imposed by the compressor is felt by the other points of the unit.

In order to achieve sharp and complete measurements, temperature and pressure were monitored, too. New thermocouple and pressure transducers were mounted

right after the mass flowmeter, so it was possible to keep our eye on the same parameters of interest as in the first set of tests: mass flow rate, density, temperature and pressure in almost every point of the refrigeration cycle.

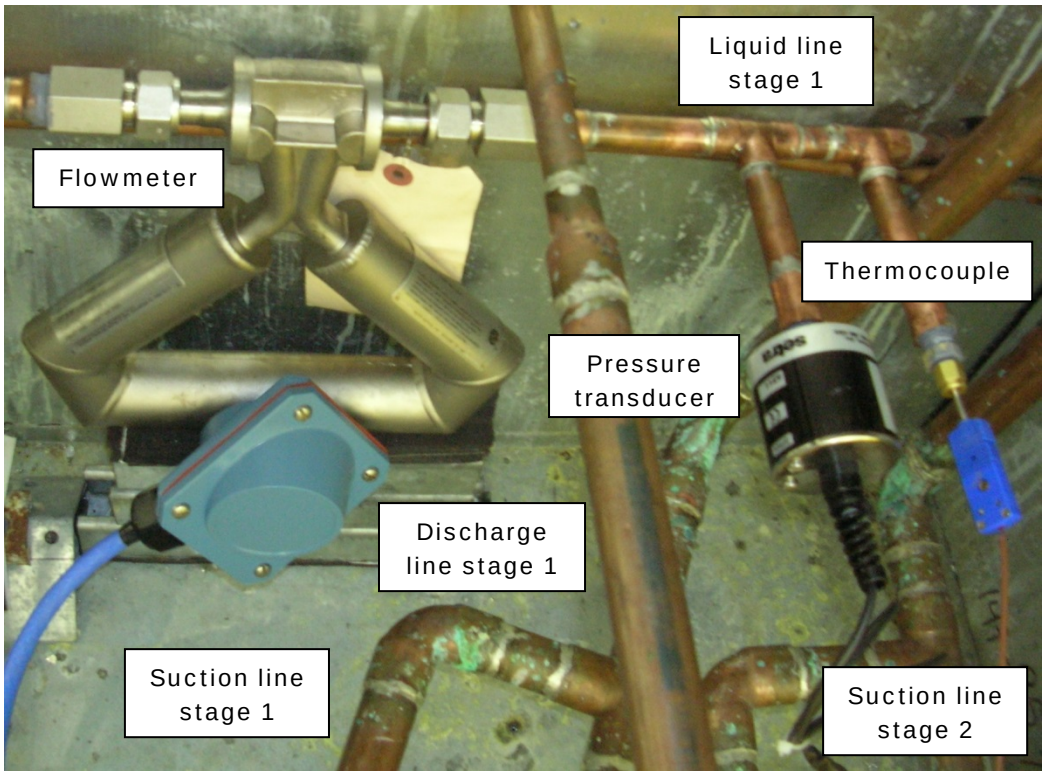

Figure 5.2. New measuring devices on the liquid line (from the left: Coriolis mass flow meter, pressure transducer and thermocouple).

Table 5.1. Specifications of Coriolis mass flow meter.

	Item Specification
Manufacturer	Micro Motion Inc.
Model	(CMF025) CMF025M319NRAAEZZZ
Type	Coriolis Mass Flow and Density Meter
Transmitter	2700C12BBAEZZZ
Flow rate range	4800 lbm/hr (2180 kg/hr)
Flow rate accuracy	±0.10% of the flow rate FS (Full Scale)
Zero stability	0.06 lbm/hr (0.027 kg/hr)
Density range	0÷312 lbm/ft^3(5000 kg/m^3) or (5 g/cm^3)
Density accuracy	±0.0312 lbm/ft^3 (±0.5 kg/m^3)
Temperature range	300°F (148°C)
Temperature accuracy	±2°F (±1°C)

Output	4 to 20 mA
Acquisition sample rate	0.2 sec
Pressure rating for sensor	1500 psig (10.4 MPa)

5.1.3 The air side measurements: the air sampling trees

Although the refrigerant side measurements were important to understand the cycle and functioning of the unit, the primary measurements used for capacity and performance (EER, Energy Efficiency Ratio) calculation were determined from the air side instrumentation.
In this way it is possible to know the influence of the modulation of the compressor not only on the refrigerant cycle, but also on the air side, so on the heat exchange that occurred to the air through the evaporator. Moreover, obviously, we needed to measure the capacity (so the effectiveness of the unit) in order to figure out the optimal strategy in controlling the unit, to maximize the capacity while minimizing the power consumption, and so maximizing the EER.
The air humidity, temperature, and pressures were measured directly at the unit supply and return locations. This was obtained with sampling probes and pressure taps secured immediately at the beginning of the duct system that connects the unit to the indoor room. With this configuration (Fig. 5.6), the pressure drop and heat transfer through the ducting system resulted to be negligible during the performance measurements.

The sampling probes (which constitute the so-called “sampling tree”) shown in figure 5.3 are designed to mechanically average the air in the duct. This was achieved by probing small samples of air at different locations in the duct cross section and mixing all the samples into one air stream.

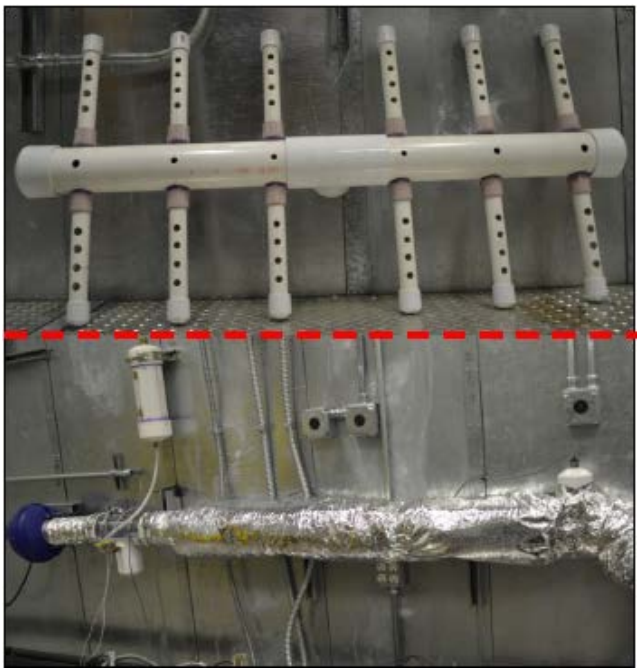

Figure 5.3. Sampling tree (top) and dry/wet bulb probe (below).

The supply sampling tree is located inside the unit, after the supply fan (figure 5.4), while the return one was mounted on the separation wall in the indoor room in front of the return air ducts (figure 5.5).
Then this mixed air streams are transferred to remote psychrometers (psychrometric devices used to measure the dry bulb and wet bulb temperatures of the air using RTDs, very accurate temperature sensors, specs shown in table 5.2), which are located in the indoor room in a fixed position (figures 5.8 and 5.9) and are each connected to the corresponding sampling tree by using a 4" (10,16 cm) silver flexible duct[2] which runs inside the yellow duct that allows the connection between the unit and the indoor room for the supply air (figure 5.7) and for the return air it runs directly inside the indoor room (figure 5.5), since there is not heat transfer because the return air temperatures are the same of the indoor ones. A negligible heat exchange from the duct to the ambient is ensured by making the silver duct stand right in the middle of the flow inside the yellow ducts, by designed hangers (figure 5.6), so that it can be considered that the same air properties inside the unit, next to the supply fan, are nearly the same measured around 3 meters away where the indoor room code tester is.
The second component installed inside the yellow duct is a small (1/4" diameter) plastic tube, that has the function of measuring the pressure difference

[2] Hereafter some data are first reported in I.P. units in order to justify their integer values (chosen according to ASHRAE standards, technical specifications or design values based on experience) and then converted to S.I. units.

across the supply and return ducts. Another end of this tube is connected to the code tester, so that it's possible to measure the static pressure difference between the supply air and the barometric pressure inside the chamber.
Having the wet bulb probes in a fixed remote position helped in preventing any damage and inconsistencies during setup of the instrumentation for the unit; thus improving the repeatability of the measurements. Another added benefit to having this setup is that the sampling probes are capable of being easily moved and modified depending on what equipment is going to be tested. Therefore, allowing for quicker setup time. For example it was needed to keep a particular sock wet on the probe in order to measure not only the temperature (dry bulb) but also the humidity (wet bulb); this could be realized easily by recharging periodically the water contained in a fixed tank (figure 5.8) mounted next to the wet bulb probe (a small plastic pipe linked the tank to the probe and it was used to moisten the sock).
Before the air, which is conditioned by the unit, is supplied to the indoor space, it passes through the code tester, which literally sucks the air coming from the unit outlet. The code tester is built in flow nozzle bench. A set of flow nozzles (figure 3.6) is activated to measure different airflow rates by simply plugging certain flow nozzles to form the best configuration for the airflow measurements. The pressure drop across the flow nozzles was directly measured to determine the airflow rate. Also inside the code tester, the air temperature and static pressure were measured so the density of the air could be calculated. Knowing the actual density of the air allowed very accurate estimation of the airflow rate. For further information about the code tester see section 3.1.
It's important to see that the air, after it has its properties measured, it's sent back to the conditioning bays and then to the chamber, so the mass flow rate balance is correct.

For this new set of tests, since the unit is designed for 6000 cfm (10194 m^3/h) but runs with only one compression stage, the decision was to supply 3000 cfm (5097 m^3/h). They were obtained by both the supply fan and the code tester fan effects. The first one pushes the air through the ducts, the second one sucks it from the unit and sends the air inside the indoor room.

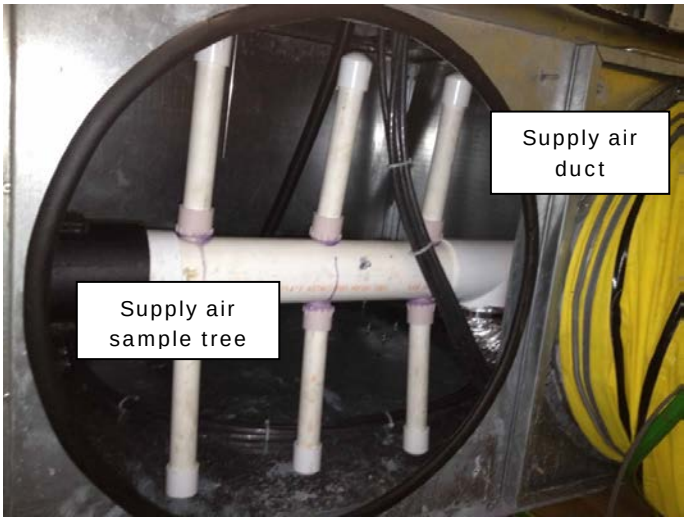

Figure 5.4. View of the supply air ducts and the sample tree.

Figure 5.5. View of the supply and return air ducts and the sample tree from inside the indoor room.

Figure 5.6. The silver duct's hanger

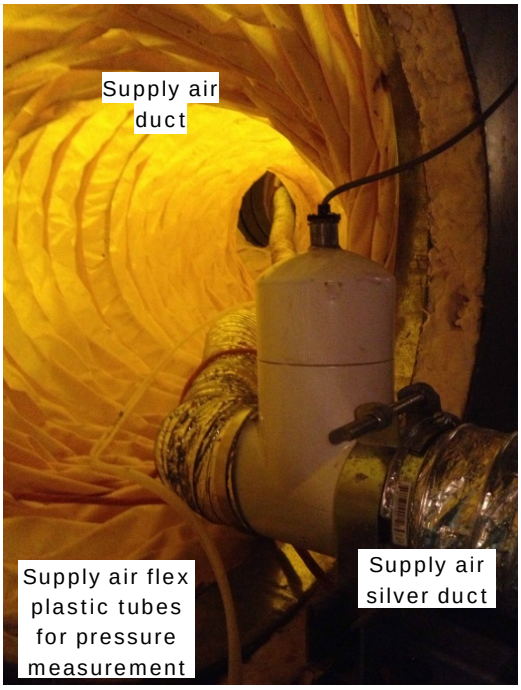

Figure 5.7. View of the yellow duct from the inside.

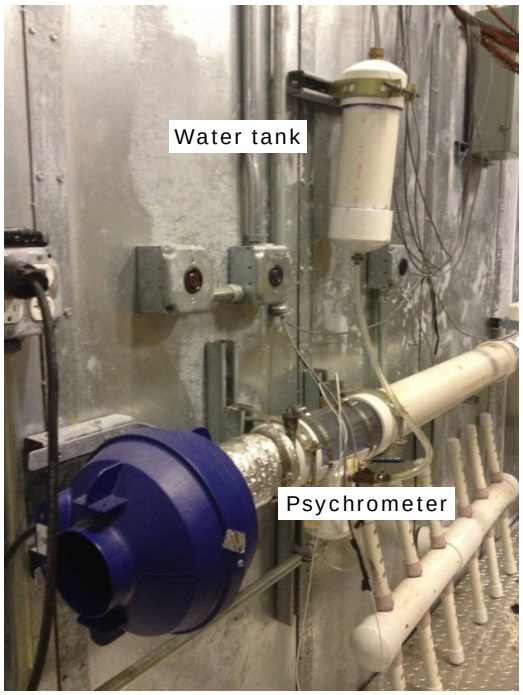

Figure 5.8. View of the indoor room psychrometer.

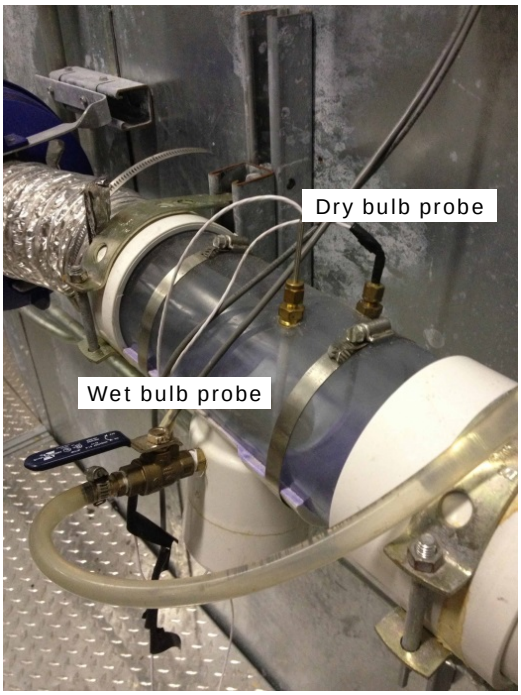

Figure 5.9. Close view of the indoor room psychrometer's probe.

Once it was made sure that both the dry bulb and wet bulb probes were connected and the socks are not dirty, the psychrometer fan was running, and the yellow ducts were not crushed, one first test, called *Calibration Test*, was run, in order to verify step by step that we were in a good shape to reach a good heat balance across the evaporator coil.

Calibration test

Before the unit was turned on, a first test with just the supply fan working was run. This is a simple way to verify that, at least at the air side, the absolute humidity *x* is constant across the coil only if the instruments are working and well calibrated. This part required a lot of time because it always happens that the wet bulb probes are not properly wet, or there are unexpected heat losses, and the RTDs are not calibrated well.
In particular, a new calibration for the code tester RTDs had to be made. These measure the supply air temperatures, and after a few tries it was found that their calibration range reached only around 55°F (12,78°C), while it was desired to work with lower supply air temperatures. A new calibration was required in order to extend the range of the old one.
The code tester nozzles configuration needed to be adjusted as well. The air flow rate that is shown on the Lab View interface (see figures 3.11 and 3.15) is a calculated value, from the pressure difference that is measured across the nozzles. After the program suggests a nozzle configuration to obtain the desired air flow rate, the user has to manually close or open the nozzles (see figure 3.6) in order to get his flow, because the Lab View will calculate the air flow rate thinking that the nozzle configuration is the one it suggested. After a couple of days we found out that the very small nozzle on the back of the plate was open while it should have been closed, so our trial tests got affected by that small nozzle.

Table 5.2. New components list, ranges and capabilities.

N.	Sensor	Component	Manufacturer + Model/Type	Nominal Range and Accuracy	# used	Description
1	Refrigerant low side and high side pressure (current 4-20 mA output)	Pressure Transducer, suction and discharge side	Setra Model 206	7 - 500 psig (50 to 3,450 kPa) ±0.65psi (4.5 kPa)	1	
2	Refrigerant temperature, low side and high side	Inline thermocouple	Omega Model TMQSS-125G-6	-40 to 130 °F (-40 to 54 °C) ±0.5°F (0.278°C)	1	T-Type thermocouple (Copper-Constantan)
3	Refrigerant Mass Flow Rate , Density, Temperature	Refrigerant mass flow meter, liquid side	Micro Motion Model CMF025M319 NRAAEZZZ Sensor S/N: 14318717	Mass Flow rate 4800 lb/hr (2180 kg/hr), ±0.10% of rate RV, Density 312 lb/ft^3 (5000 kg/m^3), ±0.0312 lbm/ft^3 (0.5kg/m^3)	1	9-wire Model
		Transmitter for Refrigerant mass flow meter, liquid side	Micro Motion Model 2700C12BBAE ZZZ S/N: 3227885 Sensor S/N: 14318717		1	
4	Power consumption of the unit	AC Watt transducer	Flex-Core AGW-008E	Full scale power: 3 kW x [current trasformer ratio]; accuracy: ±0.2% Rdg, ±0.04% F.S.	1	Input: 0-5 Aac, 0-300 Vac; Output: 4-20 mA
5		Current transformer	Flex-Core 189-050	Current ratio: 50:5	3	600 V class; accuracy: ANSI metering class 0.6
6	Chamber dry bulb and wet bulb temperature, supply and return	RTD	Omega Model PR-10	5 (-15) to 140 (60) °F (°C) Accuracy ±0,1°F (0,056 °C)	4	100 Ω at 0°C; temperature coefficient of resistance = 0.00385 Ω/Ω/°C; 6" length, 1/8" diameter
7	Chamber Barometric Pressure	Vaisala	Model PTB110	200 (50) to 442 (110) inWC (kPa) Accuracy ±0,12 inWC (0,03 kPa)	1	

5.2 Unit-oriented campaign of tests, effects of the pulsing flow on the unit capacity

5.2.1 Experimental set-up and methodology

The second kind of test were still run in steady state conditions, but since all the air side measurements were added, it was possible to evaluate the performances of the overall unit, while the first stage of tests was only compressor-oriented.
The goal during this campaign of tests was to investigate thoroughly the behaviour and the performances of the chiller, in particular the influence of the modulation of the compressor on them.
The obtained set of data will be also used, by other people who will work at this project in the next years, to develop and validate a model of the chiller which will be able to predict its performances.
The parameters under investigation are reported in the following table:

Table 5.3. Measured variables of interest for the unit-oriented campaign of tests.

Sensor #	Channel	Type
1	T4_7	Suction Thermocouple (Compressor 1)
2	T4_8	Discharge Thermocouple (Compressor 1)
3	T4_11	Liquid Thermocouple (Compressor 1)
4	T4_19	Shell top Temperature (Compressor 1)
5	T4_20	Shell bottom Temperature (Compressor 1)
6	IN/OUT5_7	Suction Pressure (Compressor 1)
7	IN/OUT5_8	Discharge Pressure (Compressor 1)
8	IN/OUT4_3	Liquid Pressure (Compressor 1)
9	IN/OUT4_9	Suction Density (Compressor 1)
10	IN/OUT4_10	Suction Mass Flow Rate (Compressor 1)
11	IN/OUT4_7	Disch. Mass Flow Rate (Compressor 1)
12	IN/OUT4_8	Discharge Density (Compressor 1)
13	IN/OUT4_11	Liquid Mass Flow Rate (Compressor 1)
14	IN/OUT4_12	Liquid Density (Compressor 1)
15	IN/OUT6_3	Compressor Power Consumption
16	IN/OUT6_8	Unit Power Consumption

17	RTD2_2	Indoor Code Tester DB RTD (Supply)
18	RTD2_3	Indoor Code Tester WB RTD (Supply)
19	RTD5_9	Indoor Wall DB RTD (Return)
20	RTD5_10	Indoor Wall WB RTD (Return)
21	ΔP_5 Indoor Nozzle	ΔP Nozzle Code Tester Indoor Room
23	ΔP_7 Indoor Unit	Δ P Unit Supply-Return
24	ΔP_8 Indoor Static	Static ΔP Unit-Chamber
25	BAROMETER	Barometric pressure
26	CFM_INDOOR	Air flow rate [cfm]

The setup for this kind of test was very time-consuming, because of the amount of the parameters of interest.
The first step consisted in preparing all the necessary hardware.
The refrigerant side was about to be ready, since all the instruments were already installed and calibrated.
For what concerns the air side, the unit to the probes that allow the measurement of the air properties had to be connected.

Unit performances test

After reaching a satisfying balance for the air side, the unit was run, in steady state conditions, in order to verify that the heat balances across the evaporator, refrigerant side and air side, agreed on similar values. A 5% difference (2011 ANSI/AHRI Standard 550/590, *Performance rating of water-chilling and heat pump water-heating packages using the vapor compression cycle*) between the two quantities was considered as acceptable. Before discussing about why reaching a good heat balance is so important, let's first make clear how to define the components, so the control volume, on which a good heat balance was built.

Considering the control volume shown below (figure 5.10) and the involved variables, the heat balance is presented below:

$$\dot{Q}_{ref} - \left(\dot{Q}_{air} + \dot{W}_{supply\ fan}\right) \cong 0 \tag{77}$$

- *Refrigerant side heat exchange*

$$\dot{Q}_{ref} = \dot{m}_{ref,suction} \cdot \left(h_{ref,OUT} - h_{ref,IN}\right) \tag{78}$$

where

$$\begin{cases} h_{ref,OUT} \cong h_{ref,suction} = f\left(T_{ref,suction}; p_{ref,suction}\right) \\ h_{ref,IN} = f\left(T_{ref,liquid}; p_{ref,liquid}\right) \end{cases} \quad (79)$$

- *Air side heat exchange*

$$\dot{Q}_{air} = \dot{Q}_{air,SENS} + \dot{Q}_{air,LAT} = \dot{V}_{air} \cdot \rho_{air} \cdot \left(h_{air,IN} - h_{air,OUT}\right) \quad (80)$$

where

$$\begin{cases} h_{air,IN} = f\left(T_{DB,IN}; T_{WB,IN}\right) \\ h_{air,OUT} = f\left(T_{DB,IN}; T_{WB,IN}\right) \end{cases} \quad (81)$$

$$\begin{cases} \dot{Q}_{air,SENS} = \dot{V}_{air} \cdot \rho_{air} \cdot c_{p_{air}} \cdot \left(T_{DB,IN} - T_{DB,OUT}\right) \\ \dot{Q}_{air,LAT} = \dot{V}_{air} \cdot \rho_{air} \cdot \Delta h_{EVAP} \cdot \left(x_{air,IN} - x_{air,OUT}\right) \end{cases} \quad (82)$$

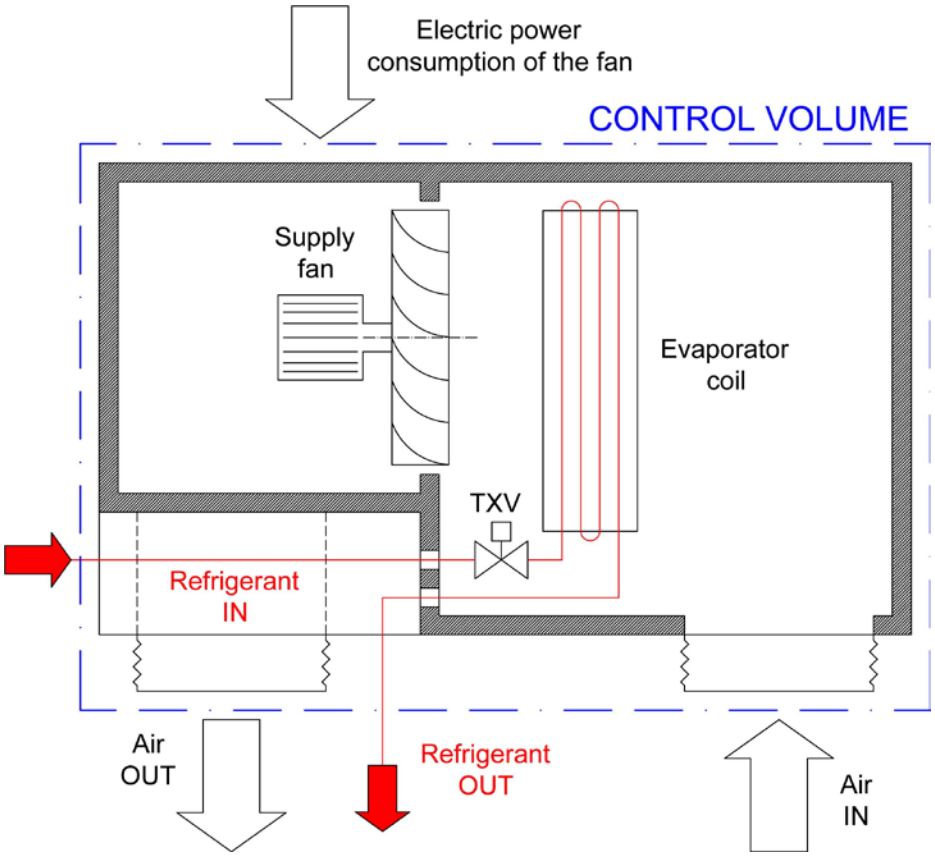

Figure 5.10. Control volume for heat balance evaluation.

It is extremely hard to reach a satisfying heat balance.
It needs to be considered that on the refrigerant side, obviously, any little error/perturbation in the temperature or pressure measurements corresponds to a small variation on the refrigerant enthalpy. So, besides the fact that from the constructive point of view it is nearly impossible to put both thermocouples and pressure transducers right before and right after the evaporator coil, and besides the fact that it could be way better if the whole copper line was insulated in order to reduce the heat transfer to the ambient, we weren't much concerned by the uncertainty in our refrigerant side measurements because they wouldn't have been much affected, anyways.
The air side, though, is much more complicated to be set. We were expecting from the theory, and found out during this long lasting balance-adjustment process, that even a 0,5°F (0,28°C) variation for the dry bulb temperatures could affect badly the measurement in the heat transfer, because the air properties change a lot; for the wet bulb temperatures that situation is even worsened: a 0,2°F (0,11°C) deviation is enough to increase or decrease significantly the heat balance.
So basically every day inspections inside the psychrometers were needed to be done, to check if the probes were damaged or dirty or dry.
Furthermore, it has to be considered that the first stage of tests required a "short" time to reach the steady-state conditions, around one hour, because we were only monitoring and interested in the dry bulb temperature, which is pretty fast to get stable. Now, in the second stage, it was necessary to reach stable conditions for the wet bulb, too. This required the use of the chamber humidifier, and it was found out that a much longer time to reach the wet bulb stable conditions than the dry bulb was needed, sometimes even one hour more than the dry bulb.

To prepare the psychrometric test chamber, the indoor and outdoor rooms were set to a desired ambient condition with the unit operating at steady state, in manual mode. Once the set point conditions were reached and maintained for 60 minutes, data recording started at a sampling rate of 1 second for additional 30 minutes. During this period the dry bulbs in each room were maintained within ±0.2°F (±0.11°C) of the set points, and the indoor wet bulb was maintained within the same range, too. The speed of both condenser fans and evaporator blower was maintained fixed during the recording, too.

The ambient outdoor temperature varied from 80°F (26,67°C) to 105°F (40,56°C) capturing the unit real life service exposure. The indoor conditions were altered to investigate the unit thermal energy characteristics when subjected to different internal loads and different sensible to latent heat capacity factors with respect to the one at design conditions, but always moving around the AHRI standard for air conditioning applications, which is 80°F (26,67°C)

dry bulb temperature and 67°F (19,44°C) wet bulb temperature.

Furthermore, it was necessary to make sure that during the whole period of testing all the parameters that have effects on the chamber operation are in the expected ranges. Otherwise, the shutoff limits previously set will shut off the interested component. For example, when the compressor discharge temperature goes above a certain value, usually 200°F (93,33°C), this causes many actions by the Lab View, both primary and secondary (it depends on the relation between the parameters in the block diagram). One among the primary safety is that the compressor is immediately turned off when the discharge temperature rises up too much. However, since we were operating the unit from the PC with the JENEsys software that has its own safeties, we disabled this kind of primary shutoff limit. Anyway, it was found out that this shutoff limit had an effect on the Indoor Room Code Tester: when passing the limit, the blower of the code tester automatically turns off, and this means that the air flow rate decreases, and the heat exchange performances changes so we lose the steady state conditions. When this happened, the test was discarded and repeated again in order to have a good recording at steady-state conditions.

Two other important parameters that had to be constantly monitored where the pressure differences across the code tester and across the unit itself.
Since the air flow rate is calculated through a Lab View code that has the pressures as an input, we had to make sure that the ΔP across the nozzle was remaining constantly below 3 inH_2O (746 Pa), otherwise we would have lost some accuracy of the measurement and some components might break with such high ΔP.
In a similar way, if a too high ΔP between supply and return air across the unit had been found, that might have meant that something was going wrong.

In the following table, the ambient conditions at which the tests were run are reported.

Table 5.4. Test conditions for the unit experiment (chamber temperature setpoints).

OUTDOOR ROOM		INDOOR ROOM				COMPRESSOR LOAD
Dry Bulb Temp.		Dry Bulb Temp.		Wet Bulb Temp.		[%]
[°F]	[°C]	[°F]	[°C]	[°F]	[°C]	
85	29,44	80	26,67	67	19,44	25-50-75-90-100
90	32,22	80	26,67	67	19,44	25-50-75-100
97	36,11	80	26,67	67	19,44	25-50-75-100
80	26,67	70	22,22	59	15,00	25-50-75-100
105	40,56	82	27,78	69	20,56	25-50-75-100

5.2.2 Results and performance analysis

Table 5.5. Refrigerant side and air side measured quantities.

Test (Outdoor Temperature - Indoor Temperature)	OT 29.44°C - IT 26.67°C					OT 32.22°C - IT 26.67°C					OT 36.11°C - IT 26.67°C					OT 26.67°C - IT 21.11°C					OT 40.56°C - IT 27.78°C				
Compressor load	**100%**	**90%**	**75%**	**50%**	**25%**	**100%**	**75%**	**50%**	**25%**		**100%**	**75%**	**50%**	**25%**		**100%**	**75%**	**50%**	**25%**		**100%**	**75%**	**50%**	**25%**	
Suction TC [°C]	14,28	15,59	17,33	20,67	24,92	14,26	17,28	20,81	25,79		14,57	18,19	21,80	26,53		9,92	13,44	16,50	20,48		15,93	19,65	23,05	26,76	
Discharge TC [°C]	76,19	75,17	74,73	75,06	78,76	79,13	77,53	77,48	82,31		83,43	81,86	81,81	85,39		73,28	72,34	72,63	75,87		89,01	87,80	87,61	90,00	
Liquid TC [°C]	36,65	35,73	34,65	33,15	31,29	39,26	37,17	35,80	33,90		43,04	41,08	39,70	37,81		33,03	31,33	30,18	28,33		47,46	45,50	44,11	42,32	
Suction P [bar]	9,72	10,36	11,06	12,50	14,16	9,74	11,11	12,59	14,37		9,90	11,40	12,90	14,67		8,52	9,85	11,09	12,58		10,25	11,76	13,10	14,45	
Discharge P [bar]	25,21	24,52	23,58	22,17	20,61	26,54	24,92	23,61	21,91		28,78	27,09	25,71	24,06		22,86	21,66	20,54	19,18		31,55	29,77	28,29	26,50	
Liquid P [bar]	23,44	22,88	22,12	21,04	19,96	24,84	23,54	22,49	21,29		27,13	25,78	24,69	23,48		21,32	20,35	19,52	18,57		29,92	28,50	27,45	26,25	
Suction Mass Flow Rate [kg/h]	507,78	456,18	378,42	258,70	129,96	508,91	375,63	269,64	129,04		518,46	386,09	272,17	140,42		446,17	337,62	240,78	122,05		533,29	394,83	278,06	140,76	
Discharge Mass Flow Rate [kg/h]	506,42	453,52	378,99	261,50	133,42	507,68	376,13	272,42	132,24		517,29	387,61	276,50	144,66		444,97	338,85	244,38	125,75		532,40	396,41	281,43	143,85	
Liquid Mass Flow Rate [kg/h]	505,64	440,57	355,71	236,96	136,90	506,81	360,23	243,90	130,55		516,35	369,98	259,50	144,50		437,73	305,54	221,58	119,25		523,92	370,00	263,56	126,97	
Suction Density [kg/m^3]	184,86	194,07	204,48	225,55	248,51	185,13	205,14	225,99	249,99		187,66	208,56	229,23	253,11		173,09	191,35	208,27	229,24		191,11	211,75	230,73	248,97	
Discharge Density [kg/m^3]	191,12	188,05	183,42	176,32	168,16	197,25	189,85	183,40	173,64		207,87	200,03	193,31	183,73		178,76	173,27	167,93	161,50		220,78	212,19	205,00	195,39	
Liquid Density [kg/m^3]	263,77	263,26	255,98	252,78	208,76	260,62	257,40	247,02	205,60		255,83	248,56	233,42	207,43		258,81	248,76	242,61	198,91		234,22	233,64	238,28	238,57	
Compressor Power [W]	6076,6	5363,6	4445,8	3157,7	1918,0	6330,5	4599,0	3345,0	1964,5		6791,9	4920,4	3521,9	2152,0		5520,2	4107,4	3016,2	1869,3		7352,0	5333,4	3800,0	2232,7	
Unit Power [W]	9647,2	8931,2	8015,9	6726,4	5506,6	9886,4	8138,6	6890,1	5514,8		10316,3	8450,5	7069,5	5718,0		9150,8	7755,8	6681,8	5543,0		10827,4	8836,8	7298,9	5723,4	
Supply fan Power [W]	1829,6	1829,6	1829,6	1829,6	1829,6	1831,6	1831,6	1831,6	1831,6		1837,0	1837,0	1837,0	1837,0		1890,5	1890,5	1890,5	1890,5		1840,2	1840,2	1840,2	1840,2	
Indoor Code Tester DB RTD (Supply) [°C]	17,18	17,76	18,72	20,95	24,11	17,40	18,75	21,23	24,62		18,00	19,35	21,67	24,96		12,29	13,73	16,06	19,19		19,05	20,72	22,92	25,20	
Indoor Code Tester WB RTD (Supply) [°C]	15,00	15,55	16,35	18,39	21,18	15,08	16,03	18,71	21,53		15,50	16,51	17,45	18,55		10,23	11,28	12,65	14,27		16,29	17,65	19,25	20,87	
Indoor Wall DB RTD (Return) [°C]	26,67	26,66	26,66	26,68	26,67	26,67	26,68	26,67	26,67		26,68	26,67	26,67	26,66		21,11	21,12	21,14	21,07		27,78	27,78	27,80	27,71	
Indoor Wall WB RTD (Return) [°C]	19,41	19,45	19,55	20,36	21,93	19,27	19,12	20,64	22,22		19,47	19,43	19,39	19,36		14,89	14,86	15,22	15,49		20,18	20,42	21,07	21,63	
DeltaP_5 Indoor Nozzle [Pa]	451,29	450,80	449,71	448,09	446,45	448,30	448,05	446,55	444,37		453,74	454,60	454,46	455,66		465,06	466,75	466,46	463,48		435,55	438,65	435,18	431,00	
DeltaP_6 Indoor Duct [Pa]	95,77	95,41	95,36	96,12	98,79	92,93	93,86	95,12	96,26		99,89	102,28	104,84	111,14		105,43	108,99	110,61	110,64		76,35	81,62	79,49	77,58	
DeltaP_7 Indoor Unit [Pa]	538,15	537,24	536,67	535,95	536,99	536,12	536,64	535,68	532,80		535,36	538,46	540,10	537,98		550,23	555,95	556,60	554,62		539,16	542,33	539,85	533,23	
DeltaP_8 Indoor Static [Pa]	0,03	-0,01	-0,01	-0,01	-0,01	-0,01	-0,01	-0,01	-0,01		0,00	0,00	0,00	0,00		-0,01	-0,01	-0,01	-0,01		-0,01	-0,01	-0,01	-0,01	
BAROMETER [kPa]	97,79	97,76	97,73	97,69	97,65	97,60	97,65	97,70	97,71		97,94	97,87	97,86	97,79		97,87	97,88	97,90	97,89		97,87	97,87	97,87	97,90	
Air flow rate [m^3/min]	84,1	84,1	84,2	84,4	84,7	83,9	84,1	84,3	84,6		84,4	84,7	85,0	85,6		84,5	84,9	85,2	85,4		82,8	83,4	83,4	83,3	

Table 5.6. Refrigerant side and air side calculated quantities.

Test (Outdoor Temperature - Indoor Temperature)	OT 29.44°C - IT 26.67°C					OT 32.22°C - IT 26.67°C					OT 36.11°C - IT 26.67°C					OT 26.67°C - IT 21.11°C					OT 40.56°C - IT 27.78°C				
Compressor load	100%	90%	75%	50%	25%	100%	75%	50%	25%		100%	75%	50%	25%		100%	75%	50%	25%		100%	75%	50%	25%	
REFRIGERANT SIDE																									
Suction enthalpy [kJ/kg]	432,43	432,22	432,34	432,41	433,20	432,36	432,15	432,36	433,71		432,27	432,43	432,73	433,85		430,87	431,17	431,29	431,99		432,87	433,17	433,69	434,71	
Discharge enthalpy [kJ/kg]	474,09	473,88	474,74	477,18	483,51	475,69	476,11	477,93	485,79		477,74	478,23	480,09	486,51		474,11	474,79	476,72	482,23		480,86	481,79	483,55	488,74	
Liquid enthalpy [kJ/kg]	260,23	258,61	256,68	254,05	250,79	265,00	261,21	258,77	255,40		272,07	268,42	265,89	262,42		253,81	250,84	248,86	245,67		280,68	276,84	274,17	270,79	
Evap T [°C]	6,24	8,33	10,54	14,78	19,19	6,29	10,69	15,01	19,74		6,84	11,59	15,86	20,48		1,97	6,66	10,64	14,98		7,99	12,64	16,42	19,93	
Cond T [°C]	41,59	40,45	38,84	36,32	33,41	43,74	41,12	38,89	35,86		47,20	44,62	42,42	39,67		37,57	35,39	33,28	30,59		51,19	48,66	46,47	43,69	
href,IN,evap [kJ/kg]	260,23	258,61	256,68	254,05	250,79	265,00	261,21	258,77	255,40		272,07	268,42	265,89	262,42		253,81	250,84	248,86	245,67		280,68	276,84	274,17	270,79	
href,OUT,evap [kJ/kg]	432,43	432,22	432,34	432,41	433,20	432,36	432,15	432,36	433,71		432,27	432,43	432,73	433,85		430,87	431,17	431,29	431,99		432,87	433,17	433,69	434,71	
mdot,ref [kg/h]	507,8	456,2	378,4	258,7	130,0	508,9	375,6	269,6	129,0		518,5	386,1	272,2	140,4		446,2	337,6	240,8	122,1		533,3	394,8	278,1	140,8	
Q_ref [kW]	**24,288**	**22,000**	**18,465**	**12,817**	**6,585**	**23,658**	**17,836**	**13,002**	**6,391**		**23,070**	**17,589**	**12,614**	**6,686**		**21,943**	**16,912**	**12,201**	**6,317**		**22,545**	**17,145**	**12,321**	**6,409**	
AIR SIDE																									
Tair,DB,IN (return) [°C]	26,67	26,66	26,66	26,68	26,67	26,67	26,68	26,67	26,67		26,68	26,67	26,67	26,66		21,11	21,12	21,14	21,07		27,78	27,78	27,80	27,71	
Tair,WB,IN (return) [°C]	19,41	19,45	19,55	20,36	21,93	19,27	19,12	20,64	22,22		19,47	19,43	19,39	19,36		14,89	14,86	15,22	15,49		20,18	20,42	21,07	21,63	
Tair,DB,OUT (supply) [°C]	17,18	17,76	18,72	20,95	24,11	17,40	18,75	21,23	24,62		18,00	19,35	21,67	24,96		12,29	13,73	16,06	19,19		19,05	20,72	22,92	25,20	
Tair,WB,OUT (supply) [°C]	15,00	15,55	16,35	18,39	21,18	15,08	16,03	18,71	21,53		15,50	16,51	17,45	18,55		10,23	11,28	12,65	14,27		16,29	17,65	19,25	20,87	
RH_{IN} [%]	50,91	51,24	51,77	56,58	66,43	50,09	49,16	58,33	68,32		51,25	51,04	50,81	50,69		51,43	51,18	53,54	55,91		50,10	51,42	55,09	58,87	
RH_{OUT} [%]	79,75	79,81	78,99	78,62	77,31	78,64	75,96	79,15	76,43		77,69	75,36	66,37	54,39		77,84	75,04	68,02	58,75		75,88	74,39	71,27	68,15	
W_{IN} [g_{DA}/kg_{dryair}]	11,18	11,24	11,36	12,45	14,66	11,00	10,79	12,84	15,09		11,26	11,21	11,16	11,12		8,04	8,00	8,39	8,73		11,75	12,07	12,96	13,80	
W_{OUT} [g_{DA}/kg_{dryair}]	9,79	10,17	10,69	12,25	14,66	9,78	10,30	12,56	14,95		10,04	10,61	10,78	10,78		6,93	7,35	7,75	8,16		10,48	11,42	12,53	13,77	
h_{IN} [kJ/kg]	55,24	55,38	55,69	58,50	64,13	54,77	54,26	59,46	65,20		55,45	55,31	55,18	55,08		41,56	41,48	42,48	43,27		57,83	58,65	60,94	62,99	
h_{OUT} [kJ/kg]	41,99	43,53	45,85	52,10	61,47	42,19	44,89	53,10	62,74		43,38	46,29	49,10	52,46		29,78	32,29	35,66	39,91		45,65	49,74	54,83	60,32	
$\rho_{air,IN}$ [kg/m^3]	1,1700	1,1700	1,1699	1,1691	1,1676	1,1701	1,1702	1,1688	1,1673		1,1699	1,1699	1,1700	1,1700		1,1943	1,1943	1,1939	1,1940		1,1653	1,1650	1,1644	1,1641	
$\rho_{air,OUT}$ [kg/m^3]	1,2092	1,2065	1,2022	1,1920	1,1776	1,2083	1,2023	1,1906	1,1754		1,2056	1,1996	1,1901	1,1770		1,2320	1,2255	1,2154	1,2020		1,2010	1,1935	1,1839	1,1740	
mdot,air [kg/s]	1,69	1,69	1,69	1,68	1,66	1,69	1,68	1,67	1,66		1,69	1,69	1,69	1,68		1,74	1,73	1,73	1,71		1,66	1,66	1,65	1,63	
c_p [kJ/kgK]	1,005	1,005	1,005	1,005	1,005	1,005	1,005	1,005	1,005		1,005	1,005	1,005	1,005		1,005	1,005	1,005	1,005		1,005	1,005	1,005	1,005	
delta h evap [kJ/kg]	2501,0	2501,0	2501,0	2501,0	2501,0	2501,0	2501,0	2501,0	2501,0		2501,0	2501,0	2501,0	2501,0		2501,0	2501,0	2501,0	2501,0		2501,0	2501,0	2501,0	2501,0	
Q_sens [W]	16,157	15,126	13,459	9,653	4,275	15,757	13,417	9,135	3,403		14,779	12,451	8,481	2,878		15,389	12,881	8,816	3,223		14,557	11,774	8,075	4,122	
Q_lat [W]	5,891	4,533	2,827	0,839	0,000	5,156	2,064	1,171	0,580		5,159	2,540	1,602	1,427		4,832	2,820	2,762	2,438		5,267	2,703	1,763	0,116	
SHR [%]	**73,3%**	**76,9%**	**82,6%**	**92,0%**	**100,0%**	**75,3%**	**86,7%**	**88,6%**	**85,4%**		**74,1%**	**83,1%**	**84,1%**	**66,8%**		**76,1%**	**82,0%**	**76,1%**	**56,9%**		**73,4%**	**81,3%**	**82,1%**	**97,3%**	
Q_tot [W] =Q_s+Q_l	22,047	19,659	16,286	10,492	4,275	20,913	15,481	10,306	3,984		19,938	14,991	10,083	4,305		20,221	15,701	11,578	5,661		19,825	14,477	9,838	4,239	
Q_tot [kW]	**22,457**	**20,052**	**16,602**	**10,730**	**4,418**	**21,268**	**15,794**	**10,644**	**4,085**		**20,448**	**15,267**	**10,249**	**4,403**		**20,461**	**15,950**	**11,769**	**5,743**		**20,205**	**14,780**	**10,063**	**4,353**	

First of all, before any investigation about performance and trends, it was necessary to be sure about the reliability of the collected data, above all the heat transfer rate exchanged on both the refrigerant and the air side. So the preliminary step was examining the **heat balance percent error**, defined as:

$$\Delta HB[\%] = \frac{HB}{\dot{Q}_{AVERAGE\ \ evaporator}} = \frac{\dot{Q}_{ref} - \left(\dot{Q}_{air} + \dot{W}_{supply\ fan}\right)}{\left(\frac{\dot{Q}_{ref} + \left(\dot{Q}_{air} + \dot{W}_{supply\ fan}\right)}{2}\right)} \cong 0 \quad (83)$$

and verifying that it is lower than a conventional maximum value; a 5% difference was considered as acceptable (see sub-section 5.3.1).
Some of the tests illustrated below (a representative sample was chosen) were run three times to double check the consistency of our measurements, thus it was possible to make correct statements about values with a real physical meaning, not random misleading values which may lead to flawed conclusions.

Table 5.7. Heat balance across the evaporator, compressor EER, overall unit EER and involved thermal/electric powers.

Test (Outdoor T - Indoor T)	Compressor load	Q_refrigerant [kW]	Q_air [kW]	Supply fan Power [kW]	Compressor Power [kW]	Q_ref - (Q_air + W_blower) [kW]	HEAT BALANCE percent error	Compressor EER	Unit EER
OT 29.44°C - IT 26.67°C	100%	24,288	22,457	1,830	6,077	0,002	0,01%	3,70	2,33
	90%	22,000	20,052	1,830	5,364	0,118	0,54%	3,74	2,25
	75%	18,465	16,602	1,830	4,446	0,033	0,18%	3,73	2,07
	50%	12,817	10,730	1,830	3,158	0,257	2,03%	3,40	1,60
	25%	6,585	4,418	1,830	1,918	0,338	5,26%	2,30	0,80
OT 32.22°C - IT 26.67°C	100%	23,658	21,268	1,832	6,330	0,558	2,39%	3,36	2,16
	75%	17,836	15,794	1,832	4,599	0,210	1,19%	3,43	1,94
	50%	13,002	10,644	1,832	3,345	0,526	4,13%	3,18	1,54
	25%	6,391	4,085	1,832	1,964	0,474	7,71%	2,08	0,74
OT 36.11°C - IT 26.67°C	100%	23,070	20,448	1,837	6,792	0,785	3,46%	3,01	1,98
	75%	17,589	15,267	1,837	4,920	0,486	2,80%	3,10	1,81
	50%	12,614	10,249	1,837	3,522	0,527	4,27%	2,91	1,45
	25%	6,686	4,403	1,837	2,152	0,446	6,91%	2,05	0,77
OT 26.67°C - IT 21.11°C	100%	21,943	20,461	1,890	5,520	-0,408	-1,84%	3,71	2,24
	75%	16,912	15,950	1,890	4,107	-0,929	-5,34%	3,88	2,06
	50%	12,201	11,769	1,890	3,016	-1,458	-11,27%	3,90	1,76
	25%	6,317	5,743	1,890	1,869	-1,316	-18,87%	3,07	1,04
OT 40.56°C - IT 27.78°C	100%	22,545	20,205	1,840	7,352	0,499	2,24%	2,75	1,87
	75%	17,145	14,780	1,840	5,333	0,525	3,11%	2,77	1,67
	50%	12,321	10,063	1,840	3,800	0,417	3,45%	2,65	1,38
	25%	6,409	4,353	1,840	2,233	0,216	3,42%	1,95	0,76

The equations from (77) to (82) defined in sub-section 5.3.1 were applied, and all the power values reported in table 5.7 were calculated; in the same table there's an estimation of the $\Delta HB[\%]$ applying equation (83).

The last test run (OT 40,56°C – IT 27,78°C) has a satisfying heat balance, the error is around 3%, always under 4%; a similar situation for the first test (OT 29,44°C – IT 26,67°C) is observable, with a more-than-negligible error for compressor loads above 50% and an error around 5% (still tolerable) for 25% load.
The other two tests with different outdoor temperature (32,22°C and 36,11°C) but the same indoor temperature (26,67°C) show a trend that is comparable to the previous one, but the error at 25% load is much higher than the other $\Delta HB[\%]$ at higher loads.
The reason for that could be due to the presence of the oil flowing in the system; the amount of oil affects the fluid properties of R410A and obviously the higher is the percent quantity the higher is the deviation of the emulsion properties from the R410A ones. When evaluating the enthalpies of the refrigerant to estimate the $\dot{Q}_{ref}$, the *RefProp* software was used assuming that the fluid in the circuit is only R410A. This simplification introduced inaccuracy to the calculations: a small negligible error if the load is high, because the mass flow rate is significant and more than sufficient to guarantee a continuous circulation of the oil, but a no more slight error if the load is low, because the intense modulation of the mass flow does not prevent the formation of a film of oil on the walls of the coils. Therefore $\dot{Q}_{ref}$ was overestimated for the low loads and that is at least one of the reasons why $\Delta HB[\%]$ became high at 25% compressor load (for further analysis see table 5.12)

The test conducted at OT 26,67°C and IT 21,11°C shows a completely different trend. The $\Delta HB[\%]$ is always positive for the other tests, while with this combination of outdoor/indoor temperatures negative values were found (but the absolute ones show the same tendency of the other tests in increasing when the load decreases).
The cause is imputable to a higher heat exchange efficiency across the evaporator due to an inferior average temperature of the coil (return air is colder, so the evaporating temperature is lower too).
Because of this, although the sensible heat is lower, a significant latent heat is observable, and so a higher dehumidification and lower SHR, sensible heat ratio, defined as

$$SHR = \frac{\dot{Q}_{air,SENS}}{\dot{Q}_{air}} = \frac{\dot{V}_{air} \cdot \rho_{air} \cdot c_{p_{air}} \cdot \left(T_{DB,RETURN} - T_{DB,SUPPLY}\right)}{\dot{V}_{air} \cdot \rho_{air} \cdot \left(h_{air,RETURN} - h_{air,SUPPLY}\right)} \quad (84)$$

as shown in table 5.6, antepenult row.

The effect of the higher heat exchange efficiency for this test is clearly noticeable in table 5.8, when we consider the actual percentage of $\dot{Q}_{air}$ at 50% and 25% loads.
First of all the *actual percentage* and the *percent difference* of a quantity for a particular test and compressor load were defined as (where $c.l.\%$ means compressor load and Q is the examined quantity)

$$A.P.of\ Q\ [c.l.\%] = \frac{Q\ [c.l.\%]}{Q\ [100\%]} \tag{85}$$

$$P.D.of\ Q\ [c.l.\%] = \frac{A.P.of\ Q\ [c.l.\%] - c.l.\%}{c.l.\%} \tag{86}$$

Table 5.8. Actual percentage and percent difference against "ideal" percentage for $\dot{Q}_{ref}$, $\dot{Q}_{air}$, $\dot{W}_{compr}$, $\dot{m}_{ref,suction}$.

Test (Outdoor T - Indoor T)	Compressor load	Actual PERCENTAGE of Qref [%]	Percent DIFFERENCE on Qref [%]	Actual PERCENTAGE of Qair [%]	Percent DIFFERENCE on Qair [%]	Actual PERCENTAGE of compr power [%]	Percent DIFFERENCE on compr power [%]	Actual PERCENTAGE of suction mass flow rate [%]	Percent DIFFERENCE on suction mass flow rate [%]
OT 29.44°C - IT 26.67°C	**100%**	**100,00%**	0,00%	**100,00%**	0,00%	**100,00%**	0,00%	**100,00%**	0,00%
	90%	**90,58%**	0,64%	**89,29%**	-0,78%	**88,27%**	-1,93%	**89,84%**	-0,18%
	75%	**76,02%**	1,37%	**73,93%**	-1,43%	**73,16%**	-2,45%	**74,52%**	-0,63%
	50%	**52,77%**	5,54%	**47,78%**	-4,43%	**51,96%**	3,93%	**50,95%**	1,89%
	25%	**27,11%**	8,45%	**19,67%**	-21,31%	**31,56%**	26,25%	**25,59%**	2,38%
OT 32.22°C - IT 26.67°C	**100%**	**100,00%**	0,00%	**100,00%**	0,00%	**100,00%**	0,00%	**100,00%**	0,00%
	75%	**75,39%**	0,52%	**74,26%**	-0,99%	**72,65%**	-3,13%	**73,81%**	-1,59%
	50%	**54,96%**	9,92%	**50,05%**	0,10%	**52,84%**	5,68%	**52,98%**	5,97%
	25%	**27,02%**	8,06%	**19,21%**	-23,16%	**31,03%**	24,13%	**25,36%**	1,42%
OT 36.11°C - IT 26.67°C	**100%**	**100,00%**	0,00%	**100,00%**	0,00%	**100,00%**	0,00%	**100,00%**	0,00%
	75%	**76,24%**	1,66%	**74,66%**	-0,45%	**72,45%**	-3,41%	**74,47%**	-0,71%
	50%	**54,68%**	9,35%	**50,12%**	0,25%	**51,85%**	3,71%	**52,50%**	4,99%
	25%	**28,98%**	15,93%	**21,53%**	-13,87%	**31,69%**	26,74%	**27,08%**	8,33%
OT 26.67°C - IT 21.11°C	**100%**	**100,00%**	0,00%	**100,00%**	0,00%	**100,00%**	0,00%	**100,00%**	0,00%
	75%	**77,07%**	2,76%	**77,96%**	3,94%	**74,41%**	-0,79%	**75,67%**	0,89%
	50%	**55,60%**	11,21%	**57,52%**	15,04%	**54,64%**	9,28%	**53,97%**	7,93%
	25%	**28,79%**	15,15%	**28,07%**	12,27%	**33,86%**	35,45%	**27,36%**	9,42%
OT 40.56°C - IT 27.78°C	**100%**	**100,00%**	0,00%	**100,00%**	0,00%	**100,00%**	0,00%	**100,00%**	0,00%
	75%	**76,05%**	1,40%	**73,15%**	-2,46%	**72,54%**	-3,28%	**74,04%**	-1,28%
	50%	**54,65%**	9,30%	**49,81%**	-0,39%	**51,69%**	3,37%	**52,14%**	4,28%
	25%	**28,43%**	13,71%	**21,54%**	-13,82%	**30,37%**	21,48%	**26,39%**	5,58%

The table illustrates values of $A.P.$ for $\dot{m}_{ref,suction}$ which are quite comparable with the corresponding compressor loads ($P.D.$ always below 10% even at 25% load) but there is a significant deviation from the "ideal" load for $\dot{Q}_{ref}$ and above all $\dot{Q}_{air}$.

For every test $A.P.$ of $\dot{Q}_{ref}$ is similar to the corresponding compressor load if this load is 75% or above, but below that value the $A.P.$ of $\dot{Q}_{ref}$ is considerably higher than the ideal load. One of the reasons is, as already said previously, the larger presence of oil in the coil at low load.

More interesting is the $A.P.$ of $\dot{Q}_{air}$.
Except for the test run at the lowest indoor temperature, the $A.P.$ of $\dot{Q}_{air}$ is quite similar or a bit lower than the corresponding compressor load and at 25% load the $A.P.$ of $\dot{Q}_{air}$ is around 19÷21%, showing the mediocre heat exchange at very low load. The test conducted at OT 26,67°C and IT 21,11°C shows completely different values: due to the higher heat exchange efficiency the $A.P.$ of $\dot{Q}_{air}$ is much higher than the compressor load (in fact the $P.D.$ values for this test are positive), even at compressor low load. This is another approach to explain the negative values assumed by the $\Delta HB[\%]$.

The last quantity reported in table 5.8 to be studied is the $\dot{W}_{compr}$: at 75% compressor load the $A.P.$ of $\dot{W}_{compr}$ is lightly lower than 75%, at 50% it is lightly higher, and at 25% it is significantly higher, over 30%, showing at low load a very poor efficiency.

The tests were run at just five different indoor/outdoor temperatures, nevertheless it is possible to investigate unit and compressor performances (at least trends and behaviours) taking into consideration several variables and conditions.
A preliminary evaluation is considering the **overall unit EER**, defined as:

$$EER_{unit} = \frac{\dot{Q}_{air}}{\dot{W}_{unit}} = \frac{\dot{V}_{air} \cdot \rho_{air} \cdot \left(h_{air,RETURN} - h_{air,SUPPLY}\right)}{\dot{W}_{compr} + \dot{W}_{supply\ fan} + \dot{W}_{condenser\ fans}} \qquad (87)$$

The EER_{unit} was expected to drop if the compressor load decreases, due to the constriction of the refrigerant cycle: the mass flow rate through the system and the pressure ratio become lower, so there's a reduction of the power absorbed by the compressor (figure 5.12), but there's also a reduction of the heat exchange across the evaporator (so of the cooling capacity), more significant than the one of the electric power. The inclination of the cooling capacity curve (figure 5.13) is steeper than the one of the compressor power. The power absorbed by the fans is almost the same, variations are negligible, so we can evaluate only the compressor power trend. Therefore applying the equation reported above one can predict a downward trend for the EER_{unit} in decreasing the compressor load, as shown in figure 5.11.

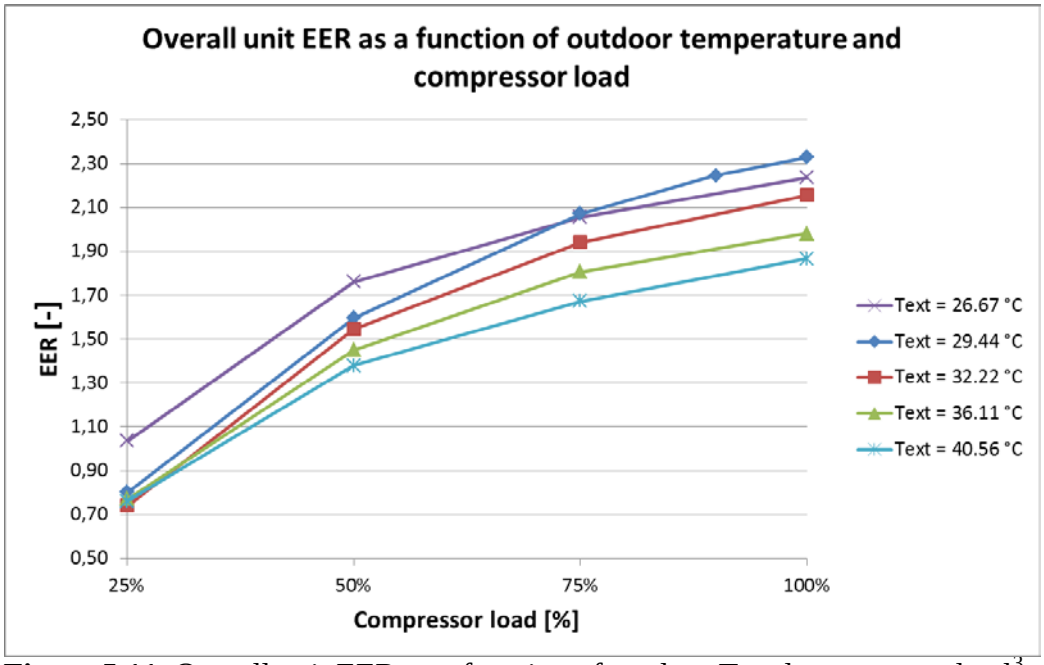

Figure 5.11. Overall unit EER as a function of outdoor T and compressor load[3] .

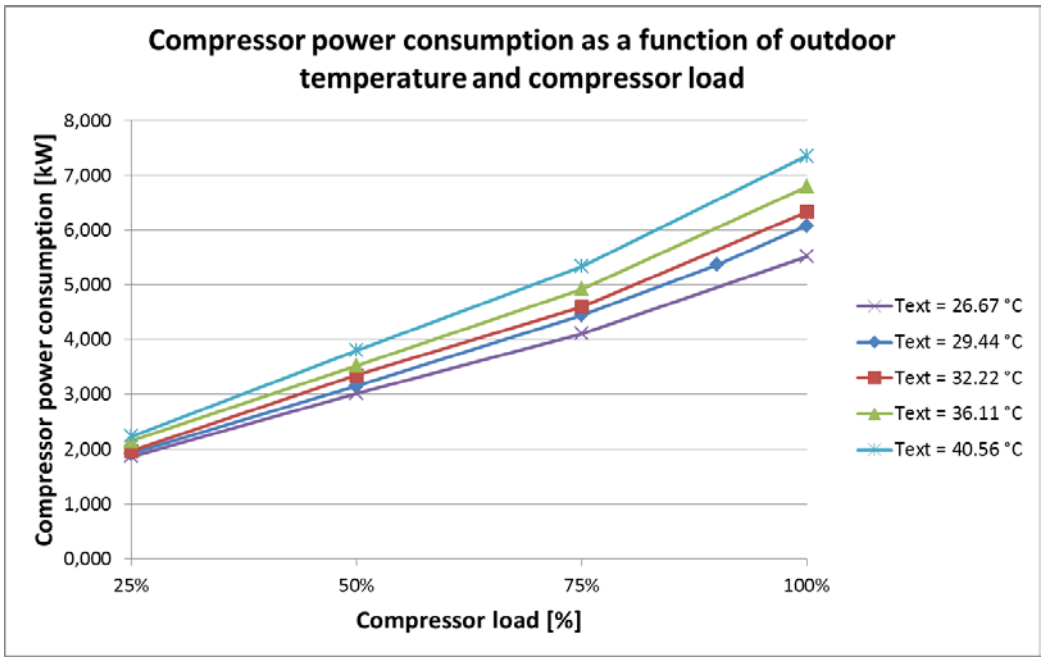

Figure 5.12. Compressor power consumption as a function of outdoor T and compressor load.

[3] The "T_{ext}=26,67°C" discordant trend is explained in the sub-section

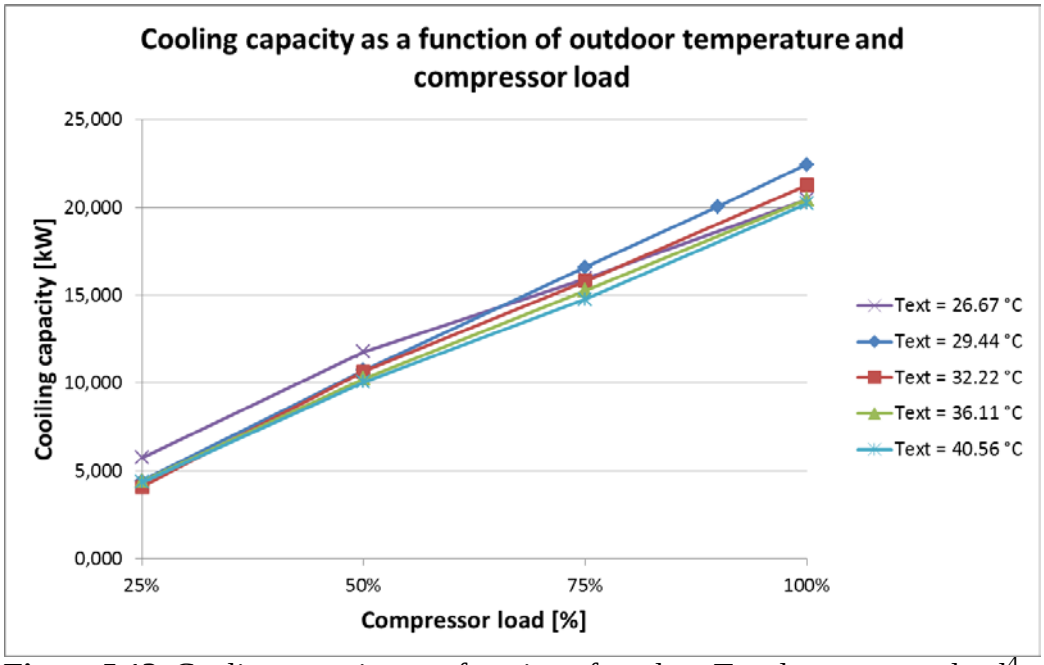

Figure 5.13. Cooling capacity as a function of outdoor T and compressor load[4].

Other evident consideration is about the **role played by the outdoor temperature**. The higher is the external temperature, the higher is the pressure ratio of the cycle; if one makes a comparison among tests with different outdoor temperatures, keeping the same compressor load, there are two opposite behaviours to be noticed: if the T_{ext} increases the compressor power (so the unit power) increases as well while the cooling capacity reduces, so it can be easily presumed that the EER_{unit} decreases.

The **influence of the indoor temperature** needs to be considered as well.
Three of these tests were run with the same indoor temperature (26,67°C) and another test (OT 40,56°C) was run with IT equal to 27,78°C, only one degree higher, so it can be assumed that the results of these four tests suitable for comparison, taking into consideration the effect of OT on EER_{unit}.

The test run at OT 26,67°C and IT 21,11°C needed different evaluation.
By observing figure 5.11 and 5.14, the EER_{unit} trend recorded in this test is similar to the other ones at 25% and 50% compressor load, but at 75% (and even more so at 100%) there is an attenuation of the upward trend, that is enough to cause a lower EER_{unit} than the corresponding one of the test run at OT 29,44°C and IT 26,67°C. The reason is simple and is shown in figure 5.12 and 5.13: the power trend as a function of compressor load is almost the same of the other

[4] The "T_{ext}=26,67°C" discordant trend is explained in this sub-section

ones but the cooling capacity trend is less sloped at high load (figure 5.13 shows this cooling capacity reaching almost the same values of the ones of the two tests run at the highest outdoor temperatures).
Therefore the cause has to be searched in the refrigerant cycle.
If the OT and IT are lower the heat exchanged by the refrigerant across the evaporator, defined as

$$\dot{Q}_{ref}\{\downarrow\} = \dot{m}_{ref,suction}\{\downarrow\} \cdot \left(h_{ref,OUT} - h_{ref,IN}\right)\{\uparrow\} \qquad (88)$$

is slightly lower, since the reduction of refrigerant mass flow rate is slightly higher than the Δh_{ref} raise; nevertheless there's a higher heat exchange efficiency across the evaporator due to an inferior average temperature of the coil.
This is the reason why $\dot{Q}_{air}$ of the test run at OT 26,67°C and IT 21,11°C, at full compressor load, became very similar to the ones of the two tests run at the highest outdoor temperatures, even if its $\dot{Q}_{ref}$ was lower.

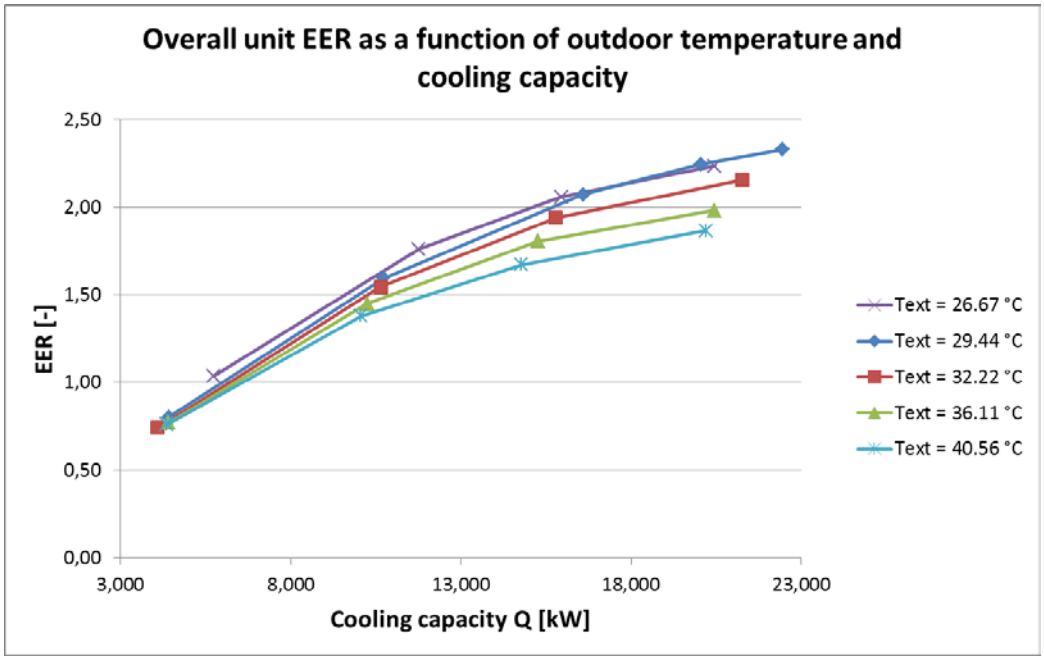

Figure 5.14. Overall unit EER as a function of outdoor T and cooling capacity.

Condensing and evaporating temperatures are obviously related to the outdoor and indoor ones.
Figure 5.15 displays the influence of T_{cond} and T_{evap} on EER_{unit}: it was estimated that the maximum efficiency for the overall unit is reachable with T_{cond} around 40°C and T_{evap} around 5°C.

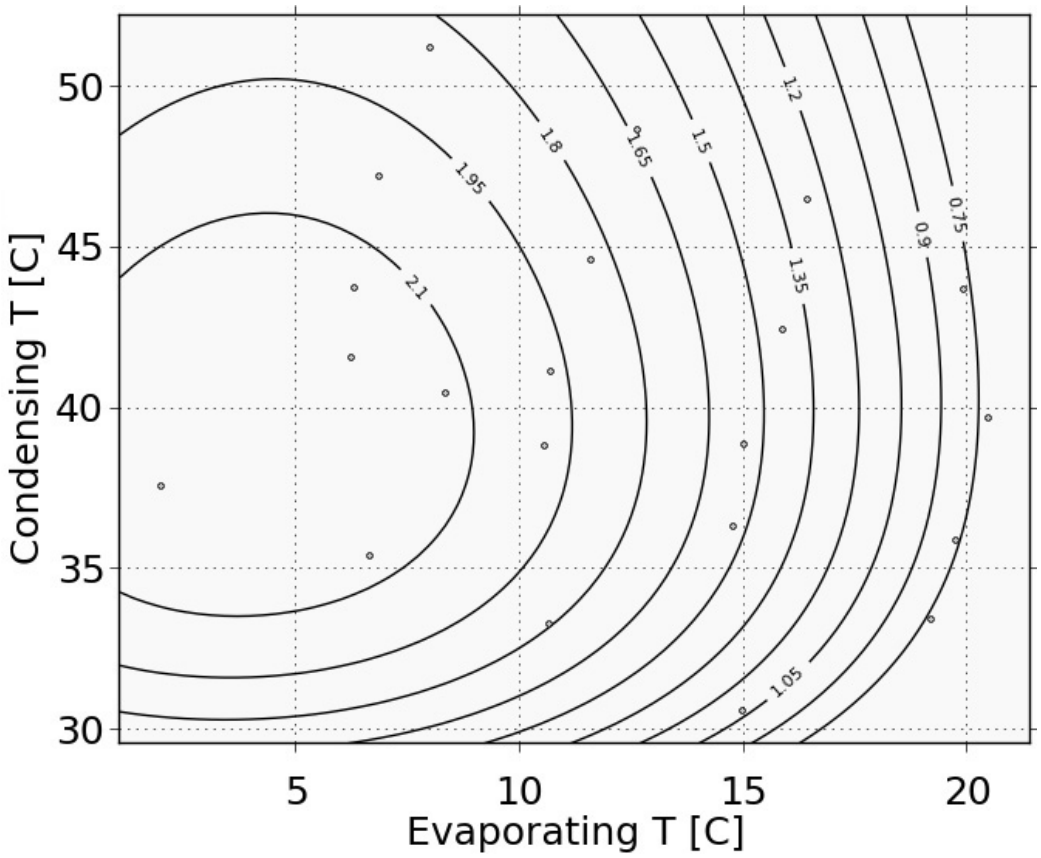

Figure 5.15. Unit map which shows the EER_{unit} for each test (with iso-efficiency curves) as a function of condensing and evaporating T [°C].

Taking into consideration the **compressor EER**, defined as

$$EER_{compr} = \frac{\dot{Q}_{air}}{\dot{W}_{compr}} \tag{89}$$

the same considerations about the cooling capacity and the compressor power can be made, but the EER_{compr} trend is different.
The EER_{unit} has a monotonic ascending trend while increasing the compressor load, on the contrary the EER_{compr} (as shown in figure 5.16 and 5.17 presents an inflection point around 75÷90% load, apart from the EER_{compr} calculated for the test run at OT 26,67°C and IT 21,11°C which has the inflection point around 50% load.
Without the constant contribution of the fans power, the EER_{compr} shows that the compressor works better at loads around 50÷75%. This can be observed

from table 5.8 looking at the actual percentage of the compressor power (it is always above the ideal percentage apart from the 75÷90% load).

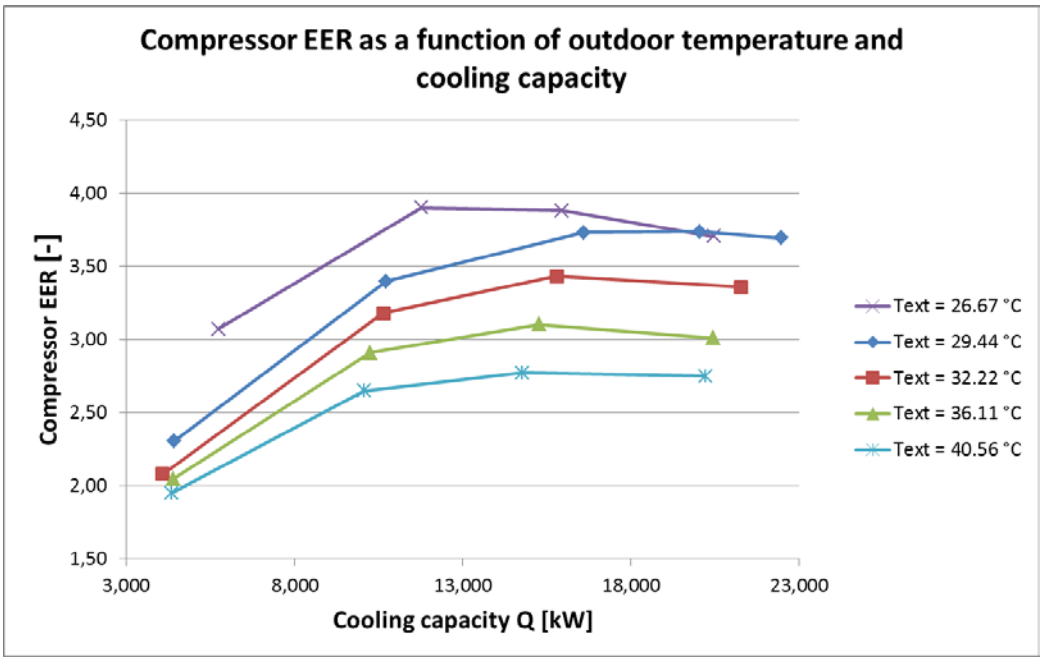

Figure 5.16. Compressor EER as a function of outdoor T and cooling capacity.

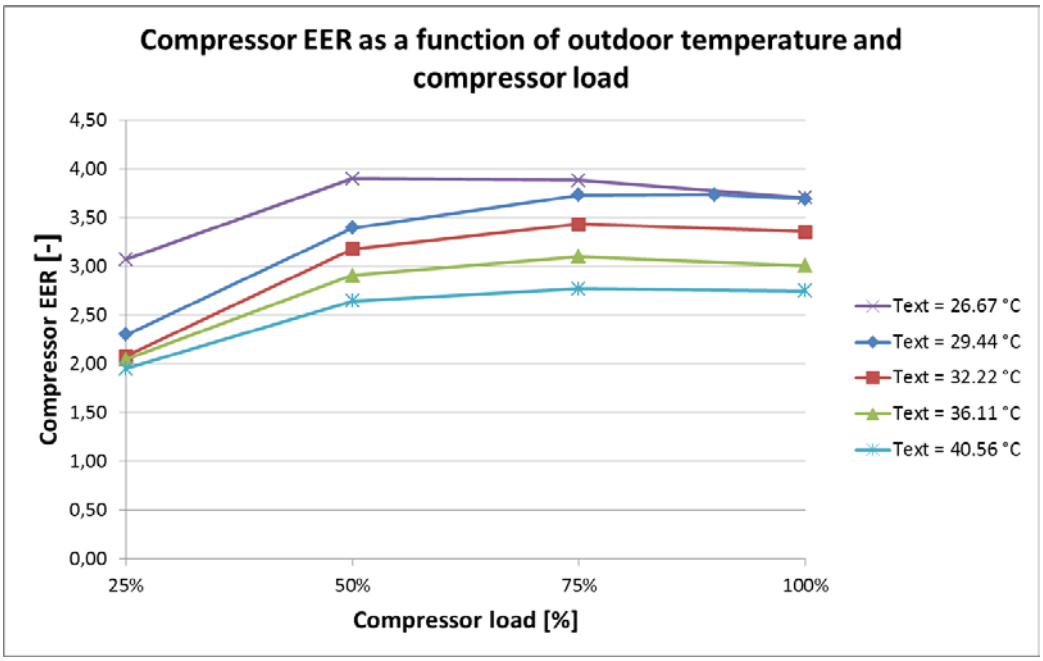

Figure 5.17. Compressor EER as a function of outdoor T and compressor load.

Below is reported the psychrometric chart with the points reached by the air during the test conducted at OT 36,11°C and IT 26,67°C while varying the compressor load. The figure below is a quick and easy way to understand the influence of the load on the air side psychrometric transformation. For example, it is possible to note that, as expectable, at low load the dehumidification (in absolute terms) is lower than at higher load.

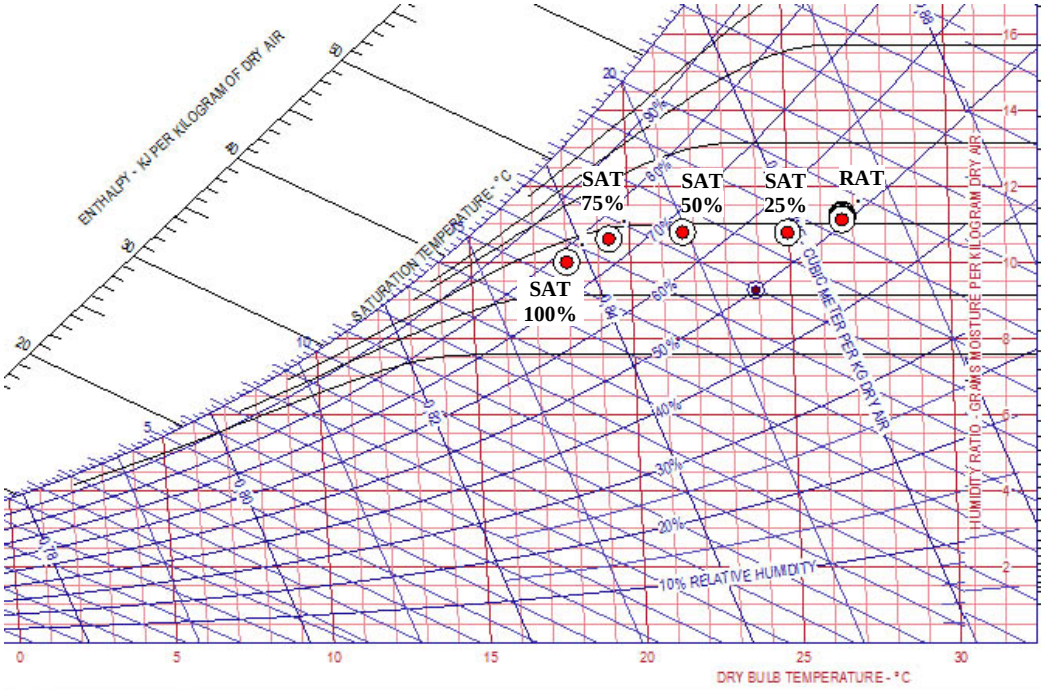

Figure 5.18. Air thermo-hygrometric transformation varying the compressor load, test conducted at OT 36,11°C and IT 26,67°C.

5.2.3 Uncertainty Propagation Analysis

The refrigerant or air properties measured using any of the instruments have uncertainty; this uncertainty is further reflected when mining up the points from the lookup table and magnified when building any other calculated value by the proper formulas. This sub-section illustrates the method used to get the error propagated from the pressure, temperature and flow rate readings to all the other calculated parameters of interest. When building the heat balance, the result will be written by showing an average value and a confidence interval, that shows how reliable our measurements were.

Recalling from the theory that the main causes of a population of measurements can be a lot, but most of them are:

- Incorrect measurement procedure;
- Inaccurate measurement tool;
- The measured object or property changes during the measurement;
- Incorrect model (intrinsic uncertainty of the measured object).

For what concerns our HVAC application, the model is obviously correct because the user is not dealing, for example, with quantum mechanics properties, and it is assumed that the position of the measurement tools is not affecting the properties of the substances. In a similar way it was made sure that all the tools were in the correct position and they were neither moving nor vibrating, so they weren't likely to measure wrongly.
What couldn't be ignored or neglected was the accuracy of the tools, but first of all it was made sure that possible systematic and stochastic errors could be decreased as much as possible.
First, since all the measurements were displayed on the Lab View screen, it was known there could be some components of error that were due to the effects of the impedance of the wires, but they could be considered as negligible since the wiring was short enough and contained in the suggested ranges. Plus, it has to be enlightened that the wires of the flow meters were of a shielded kind, so any external possible cause of interaction with the Sensor+Cable+Transmitter system was excluded and the signal was considered as reliable; same consideration applies for the cables which connect the flow meter transmitter, pressure transducers and RTDs to Lab View PXI.
Plus, it can also be assumed that the sampling rate of the Lab View system (0,2 seconds) was fast enough not to miss any kind of information about the parameters of interest.
Finally, the systematic sources of error were reduced by doing an accurate calibration: this could allow to simplify the uncertainty propagation calculation

by assuming that the only uncertainty to consider was the one that was only due to the measurement tools' accuracy.
To summarize, the correct way to build an extended, combined uncertainty should include both the accuracy of the tools and all the other sources of errors, and moreover it should also include a statistical analysis that allow the user to provide the correct shape of the measure, with its confidence interval.
Though, it was assumed that all the sources of error were reduced enough to be considerable as negligible, and the uncertainty propagation analysis was only built on the accuracy of the tools, that was provided along with its calculation method in the technical specs of the components.

In table 5.9 is reported a summary of the information about the instrumentation, which was found in the technical specifications. The info about the accuracy of the single instrument (which could be given as an absolute or relative value) allows to start up an uncertainty propagation analysis using the software EES. The final outcome will say how confident one can be on the results that were found when building the heat balance.

Table 5.9. Summary of the measured properties and accuracy of instruments.

Item #	Measurement	Sensor	Absolute Uncertainty (technical spec.)	Relative Uncertainty (technical spec.)
1	**Air, Refrigerant Temperatures**	Thermocouple	±0,278°C	-
2	**Air Temperature**	RTD	±0,056°C	-
3	**Refrigerant Pressure**	Pressure Transducer	±0,045 bar	-
4	**Refrigerant Mass Flow Rate**	Coriolis Mass Flow Meter	-	±0,5% (R.V.)
5	**Air Volumetric Flow Rate**	Pressure Taps Across Nozzles[5]	-	±0,03% (R.V.)
6	**Compressor Absorbed Electrical Power**	Wattmeter	±36 W (0,04%F.S. where F.S. = 90000 W)	-
7	**Overall Unit Absorbed Electrical Power**	Wattmeter	±12 W (0,04%F.S. where F.S. = 30000 W)	-

[5] see section 3.1 for specs about the calculation method.

Below is the table containing all the outputs of the uncertainty calculation made by the software EES. Given the measured properties and their uncertainties, the software makes the analysis by compounding them in the formulas.
The propagation law of uncertainty (for non-correlated variables) used is:

$$U_{combined,y} = \sqrt{\sum_{i=1}^{N} \left(\frac{\partial f}{\partial x_i} U_{x_i} \right)^2} \tag{91}$$

where N is the number of variables x_i that influence, with their uncertainties U_{x_i}, the combined uncertainty of the calculated quantity under examination (f is the formula which involves the variables x_i to calculate the quantity y)

Table 5.10. Uncertainty propagation analysis, results.

Test (Outdoor T - Indoor T)	Compressor Load	Q_refrigerant [kW]	Q_air [kW]	HEAT BALANCE percent error [%]	Unit EER
OT 29.44°C - IT 26.67°C	100%	24,288±0,148	22,457±0,782	**0,01±3,32**	2,33±0,08
	90%	21,999±0,134	20,052±0,724	**0,54±3,41**	2,25±0,08
	75%	18,465±0,112	16,602±0,647	**0,18±3,60**	2,07±0,08
	50%	12,817±0,078	10,730±0,542	**2,03±4,42**	1,60±0,08
	25%	6,585±0,040	4,418±0,493	**5,26±7,99**	0,80±0,09
OT 32.22°C - IT 26.67°C	100%	23,658±0,146	21,268±0,752	**2,39±3,35**	2,16±0,08
	75%	17,836±0,110	15,794±0,624	**1,19±3,64**	1,94±0,07
	50%	13,002±0,080	10,644±0,544	**4,13±4,46**	1,54±0,08
	25%	6,391±0,039	4,085±0,494	**8,73±8,45**	0,74±0,09
OT 36.11°C - IT 26.67°C	100%	23,070±0,146	20,448±0,734	**3,46±3,37**	1,98±0,07
	75%	17,589±0,110	15,267±0,617	**2,80±3,71**	1,81±0,07
	50%	12,614±0,0789	10,249±0,522	**4,27±4,43**	1,45±0,07
	25%	6,686±0,042	4,403±0,451	**6,91±7,35**	0,77±0,08
OT 26.67°C - IT 21.11°C	100%	21,943±0,132	20,461±0,704	**-1,84±3,24**	2,24±0,08
	75%	16,912±0,101	15,950±0,594	**-5,34±3,42**	2,06±0,08
	50%	12,201±0,073	11,769±0,508	**-11,27±3,79**	1,76±0,08
	25%	6,317±0,038	5,743±0,413	**-18,87±5,46**	1,04±0,07
OT 40.56°C - IT 27.78°C	100%	22,545±0,148	20,205±0,730	**2,24±3,42**	1,87±0,07
	75%	17,145±0,111	14,780±0,613	**3,11±3,80**	1,67±0,07
	50%	12,321±0,080	10,063±0,535	**3,45±4,60**	1,38±0,07
	25%	6,409±0,041	4,353±0,477	**3,42±7,85**	0,75±0,08

It can be seen from the table that there was the highest uncertainties on the air side, because as it'll be shown there was a high inaccuracy in measuring the wet bulb temperature. Actually, this measurement was not inaccurate when measuring in steady-state conditions, but in general when the compressor load decreases and the refrigerant mass flow rate pulses, the air temperature should pulse as well. The wet bulb probe was not as fast as it was needed, though, so it was possible to notice slow-frequency fluctuations and average values quite well, but not the fast fluctuations imposed by the refrigerant side.
This led to consider that it was not possible to expect a sharp heat balance, because even if the average values were mostly far below the 5% limit, the range of the uncertainty got relatively big when summing up all the uncertainties. Given also the high uncertainty due to the wet bulb temperatures measurements, that is the cause of very high variations in the air enthalpy even with a very low variation in the wet bulb temperature itself, it was clear why even with very satisfying average heat balance values, the uncertainty range was pretty broad and there wasn't much it could be done about that, because it's related to the measuring tool.

Another important consideration is about the influence of each measurement uncertainty on the combined uncertainty of a calculated value (*sensitivity analysis* of measurements towards error propagation)
In the following table are reported the percent weight of each quantity on the uncertainty of the main calculated values for the test conducted at OT 40,56°C and IT 27,78°C.
As it can be noticed from the table 5.11, $\dot{Q}_{ref}$ is influenced mainly by the refrigerant mass flow rate, while the other significant variables are the inlet and outlet temperatures (considering the evaporator), in particular the inlet one is much more important than the suction one; there is no noteworthy difference about the percent weights if the compressor load varies and it can be also observed a next-to-nothing influence of the refrigerant pressure (in particular the liquid side pressure).
On the contrary, the compressor load affects the percent weights for $\dot{Q}_{air}$; if the load is high the influence of the air flow rate is relevant too, while the weights of the inlet and outlet wet bulb temperatures, even if they are far from negligible, are lower. This situation is overturned for low compressor loads. Even if the RTDs which measured the air dry bulb temperatures are the same of the ones used to measure the air wet bulb temperatures, so with the same accuracy, their influences are trifling.
Similar inferences for $\Delta HB[\%]$ and EER_{unit} can be made since the refrigerant side and the electric powers have no significant influence on those two quantities. This is another explanation (besides the oil stagnation, see sub-section 5.2.2) why the heat balance verification is more critical for low load; in

fact, if the load is low, possible errors, although small ones, in measuring the wet bulb temperatures have more-than-relevant consequences on the heat balance.

Table 5.11. Percent weight, calculated by EES software, of each measured variable on the combined uncertainty of $\dot{Q}_{ref}$, $\dot{Q}_{air}$, $\Delta HB[\%]$ and EER_{unit}.

OT 40,56°C IT 27,78°C	**25% compressor load**	**100% compressor load**
$\dot{\mathbf{Q}}_{\mathbf{ref}}$	$\begin{cases} \dot{m}_{ref,suction} = 62{,}24\% \\ T_{ref,suction} = 11{,}62\% \\ p_{ref,suction} = 1{,}33\% \\ T_{ref,liquid} = 24{,}82\% \end{cases}$	$\begin{cases} \dot{m}_{ref,suction} = 58{,}25\% \\ T_{ref,suction} = 10{,}11\% \\ p_{ref,suction} = 1{,}49\% \\ T_{ref,liquid} = 30{,}15\% \end{cases}$
$\dot{\mathbf{Q}}_{\mathbf{air}}$	$\begin{cases} \dot{V}_{air} = 7{,}21\% \\ T_{DB,return} = T_{DB,supply} = 0{,}00\% \\ T_{WB,return} = 47{,}74\% \\ T_{WB,supply} = 45{,}04\% \end{cases}$	$\begin{cases} \dot{V}_{air} = 67{,}11\% \\ T_{DB,return} = T_{DB,supply} = 0{,}00\% \\ T_{WB,return} = 18{,}82\% \\ T_{WB,supply} = 14{,}06\% \end{cases}$
$\Delta\mathbf{HB}[\%]$	$\begin{cases} \dot{W}_{blower} = 0{,}56\% \\ \dot{V}_{air} = 7{,}12\% \\ T_{DB,return} = T_{DB,supply} = 0{,}00\% \\ T_{WB,return} = 47{,}16\% \\ T_{WB,supply} = 44{,}49\% \\ \dot{m}_{ref,suction} = 0{,}41\% \\ T_{ref,suction} = 0{,}08\% \\ T_{ref,liquid} = 0{,}16\% \end{cases}$	$\begin{cases} \dot{W}_{blower} = 0{,}23\% \\ \dot{V}_{air} = 64{,}50\% \\ T_{DB,return} = T_{DB,supply} = 0{,}00\% \\ T_{WB,return} = 18{,}09\% \\ T_{WB,supply} = 13{,}51\% \\ \dot{m}_{ref,suction} = 2{,}14\% \\ T_{ref,suction} = 0{,}37\% \\ T_{ref,liquid} = 1{,}11\% \end{cases}$
$\mathbf{EER}_{\mathbf{unit}}$	$\begin{cases} \dot{V}_{air} = 7{,}19\% \\ T_{DB,return} = T_{DB,supply} = 0{,}00\% \\ T_{WB,return} = 47{,}59\% \\ T_{WB,supply} = 44{,}90\% \\ \dot{W}_{unit} = 0{,}32\% \end{cases}$	$\begin{cases} \dot{V}_{air} = 66{,}57\% \\ T_{DB,return} = T_{DB,supply} = 0{,}00\% \\ T_{WB,return} = 18{,}67\% \\ T_{WB,supply} = 13{,}94\% \\ \dot{W}_{unit} = 0{,}82\% \end{cases}$

5.2.4 Influence of the pulsing flow on the refrigerant side

With the new sensors mounted on the liquid line, between the condenser and the TXV, it is possible to observe and somehow quantify the inertia and the delay of the system. As explained in the low-load section (5.3) it was not possible to study meticulously the liquid behaviour at low load because of the too low subcooling (figure 5.37), below 1°C, that doesn't prevent the mass flow rate measurement from being affected by the presence of some bubbles of vapour.
With load above 50% the subcooling is sufficient to measure properly the mass flow rate on the liquid line (above 1°C); the test conducted at OT 36,11°C and IT 26,67°C with 75% load was chosen to investigate the liquid behaviour.
Observing figure 5.19, which reports the mass flow rates of the suction and liquid line, some considerations can be made.
The distance between the compressor and the liquid line, in terms of piping, is long enough to cause several phenomena that make the two wave shapes (shown in figure 5.19) different.
First of all it is possible to verify the presence of an expected **delay** of the mass flow rate in the liquid line, due to the inertia of the system. Since the curves are not only shifted in time but they have different shapes (the reason for this difference is explained later on), it is needed to define a conventional and reasonable way to calculate the delay. This was defined as the time difference between the instant when the suction mass flow rate finishes its off-cycle (the last zero value, point A in figure 5.20) and the instant when the liquid mass flow rate reaches the corresponding cycle minimum value (point B in figure 5.20). The delay at 75% load was estimated for all the tests and was found an average value of 0,518 s.

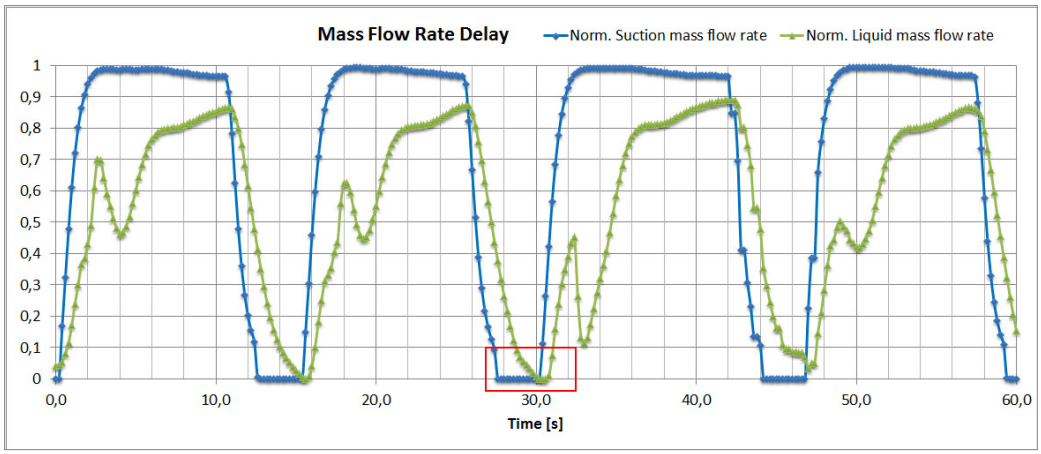

Figure 5.19. Normalized suction and liquid mass flow rate, OT 36,11°C-IT 26,67°C test, 75% load, 1 minute of recording at 0,2 s sampling rate.

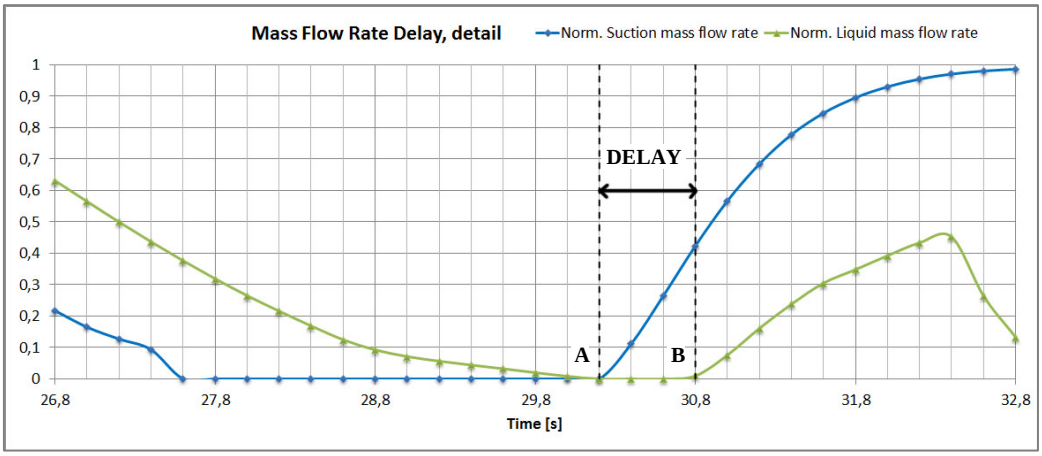

Figure 5.20. Magnified detail of the delay in the plot of normalized suction and liquid mass flow rate (see Figure.5.19)

Because of the reduced subcooling, it is hard to estimate a proper value of the delay for loads below 75% (see figures 5.33, 5.34, 5.35), so it is not possible to understand if the delay is influenced by the load percentage, yet; there will be the opportunity to study if the user should intervene on the unit substituting the existing TXV with a an electronic expansion valve (EXV) in order to grant a higher subcooling for the unit even for low loads thanks to the lower inertia and to the possibility of remote control by the user.
It is also possible to define a pressure delay between the discharge and liquid lines (see figure 5.21). Using the same calculation approach described previously, the pressure delay was calculated and a value of 0,546 s was found, pretty the same of the mass flow rate delay; after all, the pressure trend is the cause of the mass flow rate one, so it is only an experimental confirm of that.

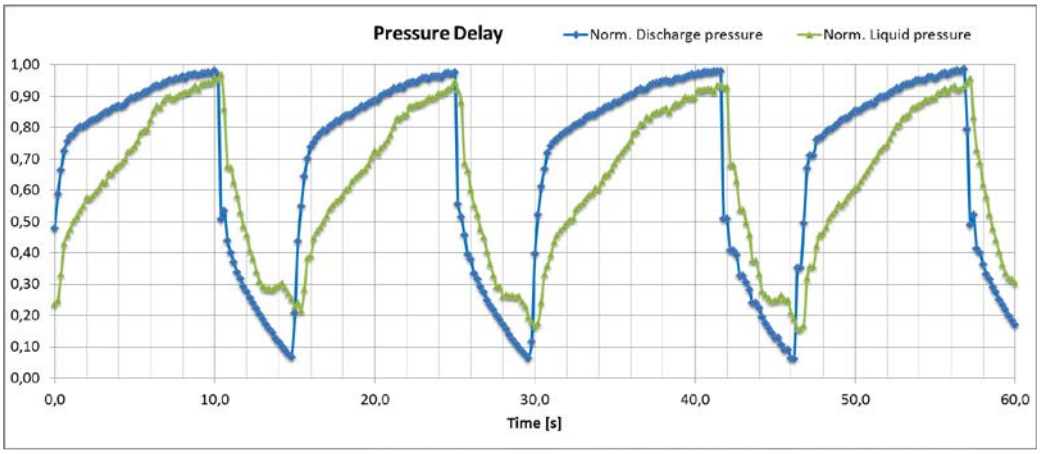

Figure 5.21 Normalized discharge and liquid pressure, OT 36,11°C-IT 26,67°C test, 75% load, 1 minute of recording at 0,2 s sampling rate.

By observing figure 5.19, in addition to the delay, a peak of mass flow rate for the liquid line is noticeable before achieving the real maximum values of the on-cycle. This characteristic profile can be found in all cycles and it is always delineated by several sampled values, therefore it is not an uncertainty or some bad working conditions of the Coriolis mass flow meter (as it happened for low loads) but it is certainly a physical phenomenon. Taking into consideration the outline of this phenomenon and the dynamic behaviour of the refrigerant (even if the tests were conducted in steady-state conditions) introduced by the modulation of the compressor, the best hypothesis is that the system is affected by a sort of slight **fluid hammer**. This occurrence (also called "hydraulic shock") is generally a pressure surge or wave caused when a fluid (usually a liquid but sometimes also a gas) in motion is forced to stop or change direction suddenly. The fluid hammer commonly occurs when a valve closes abruptly at an extremity of a pipeline system, and a pressure wave propagates in the pipe. If the pipe is suddenly closed at the outlet (downstream), the mass of fluid before the closure is still moving forward with some velocity, building up a high pressure and shock waves.
This is what happens in the liquid line; the trend of the "liquid" pressure shown in figure 5.22 is pivotal to understand the fluid hammer. When the solenoid valve lifts up the fixed scroll, the suction pressure increases while the discharge pressure and consequently the pressure in the liquid line reduces. The mass flow rate flowing through the compressor suddenly decreases from the maximum value to zero, and this has to occur as well for the liquid line. But, because of this abrupt shutting, a small backward wave pressure causes an interruption of the pressure drop in the liquid line followed by a small peak; this phenomenon, combined with the inertia of the system, makes the liquid mass flow rate drop less steep during the off-cycle; at the beginning of the on-cycle, as reaction of the system, the pressure increases less steeply causing a reduction of the mass flow rate.
Comparing the curves in figure 5.22 it is possible to notice that the relative minimum value of the liquid mass flow rate is achieved when the pressure gradient reaches the lowest value of the on-cycle rise (this is illustrated in the figure with dashed vertical lines); after that instant the pressure growth is more vertical and as consequence the mass flow rate increases again.

In this case the pipeline is not so long and also the velocity of the fluid is very low, so the kinetic energy is small enough to consider this event negligible in terms of safety of the pipes.

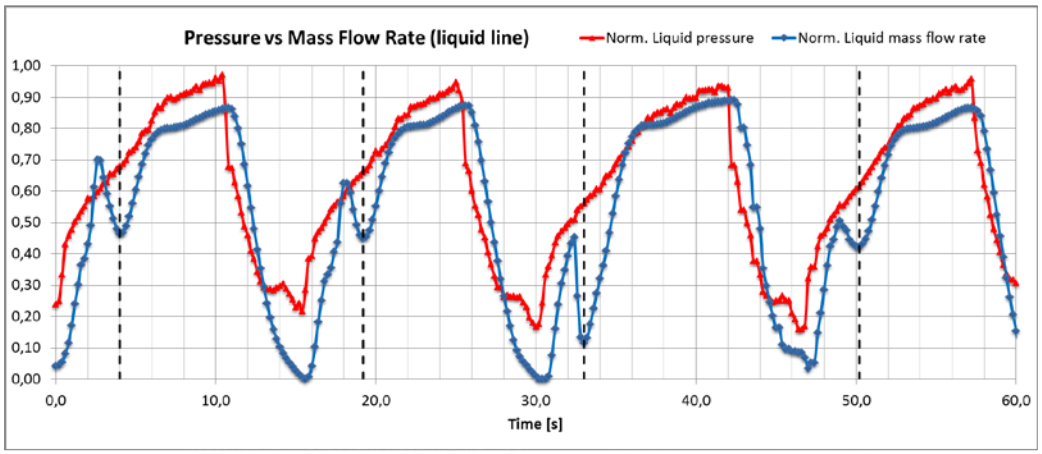

Figure 5.22. Normalized liquid pressure and mass flow rate, OT 36,11°C-IT 26,67°C test, 75% load, 1 minute of recording at 0,2 s sampling rate. Pressure range 24,08÷26,81 bar, mass flow rate F.S. 558 kg/h.

5.2.5 Influence of the pulsing flow on the air side

Once satisfying heat balances were reached, so the data collected were considered to be reliable, it was time to go deeper with the analysis and first of all one of the first aspects that are crucial in declaring that this system is more or less efficient than the other two which it is compared with was investigated: heat pumps with either fixed speed compressors or variable speed compressors. This aspect is an investigation on how the pulsing flow affects the air side heat exchange, and if there is any performance gain or loss.

First of all, a baseline was established: the behaviour of the system at 100% compressor load. This is considerable as a conventional scroll compressor's operation and allows to see first how we kept the system working in steady-state conditions, while the psychrometric chamber's controls and the unit itself were continuously trying to make self-adjustments to stabilize the indoor and outdoor temperature.
A representative test was chosen and it was the one run with 97°F (36,11°C) outdoor temperature, 80°F (26,67°C) indoor dry bulb temperature and 67°F (19,44°C) indoor wet bulb temperature.
As a first plot we looked at the way the supply and return air temperatures change in steady state conditions (figure 5.23). The sample rate for all the graphs of this section is 1 second.

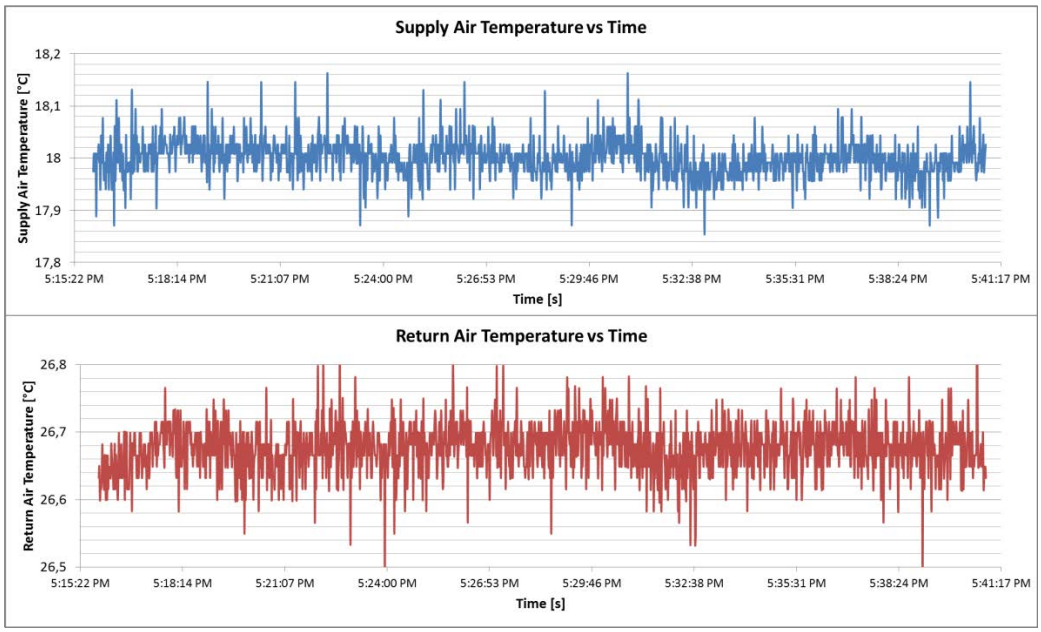

Figure 5.23. Supply air temperature (above) and return air temperature (below) fluctuations at compressor full load (30 min).

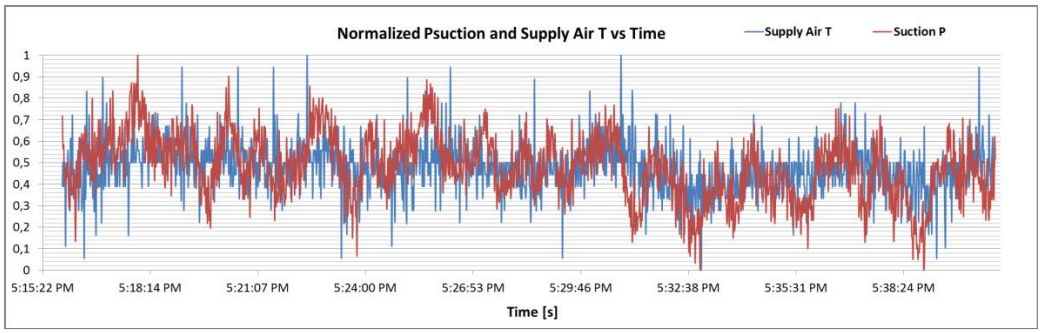

Figure 5.24. Normalized suction pressure and normalized supply air temperature fluctuations at compressor full load (30 min). Pressure range 9,86÷9,95 bar, temperature range 17,85÷18,16°C.

Table 5.12. Statistical analysis of the collected data of suction pressure and supply air temperature

	% Variation min vs max	Average	Std. Deviation
Suction P	0,84%	9,9 bar	0,012 bar
Supply Air T	0,86%	18°C	0,033°C

Supply and return air temperature curves are very flat, in a very tight window between 0,1 and 0,2°C, which could be considered as a measurement

uncertainty. In fact, as reported in the table above, both suction pressure and air temperature have almost every number very close to the average value, and some of them can be considered as simple outliers. It can be said that there is no fluctuation in any parameters of interest at all, when investigating in a 100% compressor load test.

Things change when the compressor load decreases: the supply air temperature starts to fluctuate and the amplitude of these fluctuations gets from around 0,2°C at 100%, to 0,44°C at 75%, to 0,61°C at 50%, to 0,78°C at 25% compressor load. As an example, figure 5.25 shows the air temperature fluctuations for the test at 50% when the wave shapes of the mass flow rates are understandable because the *on* and the *off* compressor times have the same duration (7,5 seconds on a 15 seconds total cycle time).

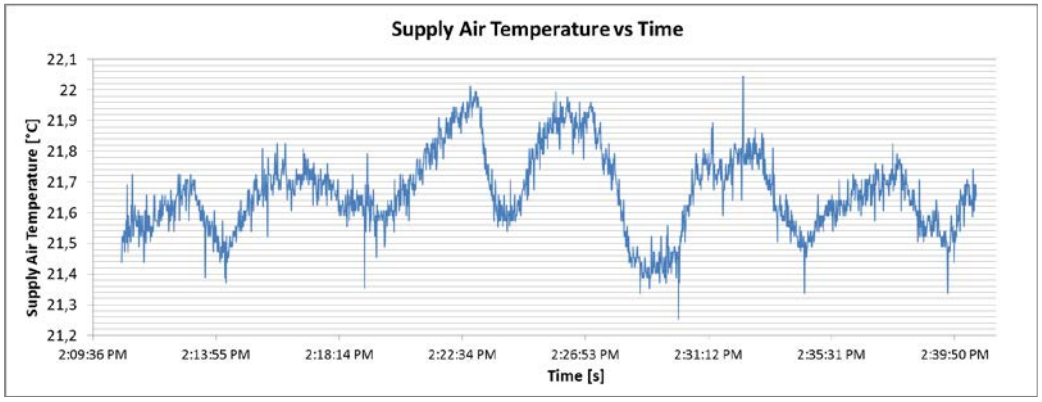

Figure 5.25. Supply air temperature fluctuations at compressor 50% load (30 min).

We expected a fluctuation of the supply air temperature as a reaction of the air side to the refrigerant pulsing flow. This should show a very quick response in the air side, as the compressor cycles in few seconds, but it was never noticed any fast change on the air side, as reported in the plot of the supply air temperature in relation to the refrigerant mass flow rate (figure 5.26).
The air temperature fluctuations seem to be casual and not directly related to the quicker pulsing flow.

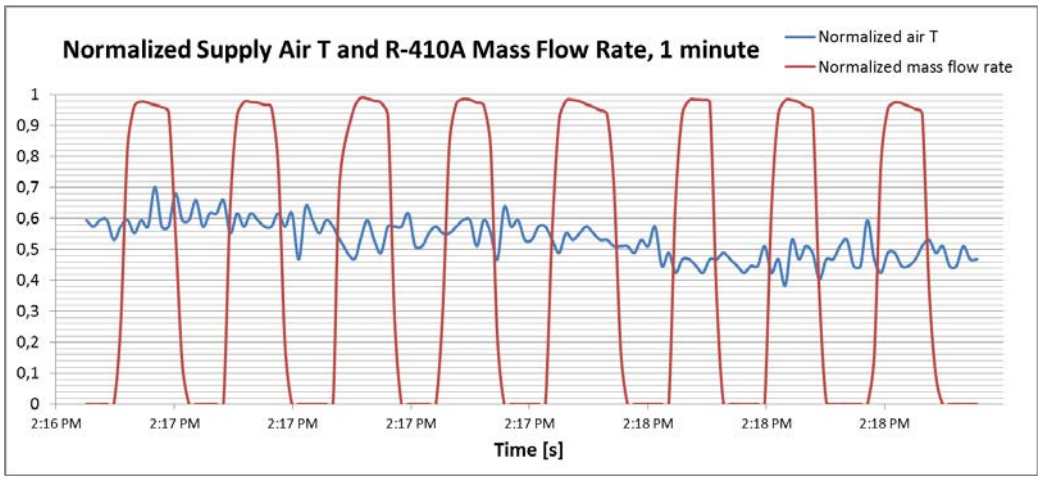

Figure 5.26. Normalized supply air T and refrigerant mass flow rate fluctuations at compressor 50% load (1 min). Temperature range 21,66÷22,05°C, mass flow rate F.S: 594,74 kg/h.

First reasons we thought for reaching a shape like the one in figure 5.25, were:

- A continuous adjustment in the indoor and outdoor temperature due to the pulsing nature of the flow: this would justify the long shape of the wave because it would reflect the slow nature of the psychrometric chamber in adjusting a set point. This has not happened, because both the indoor and outdoor room temperatures plots were very flat. Only the supply air temperature changed (see figure 5.27).

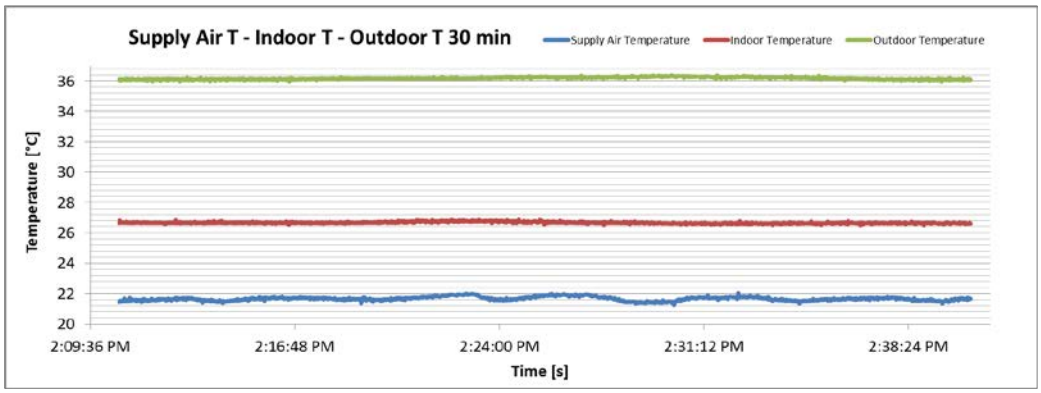

Figure 5.27. Supply air T, indoor and outdoor T trends at compressor 50% load (30 min).

- One other possible reason of the air side fluctuation can be an outcome of the action of the TXV on the refrigerant flow. Since it's a mechanical component, its dynamics is very slow and the goal of an investigation of a TXV

action could be seen by plotting the superheat of the vapor coming out from the evaporator coil (see figure 5.28): if its shape follows a mirror image of the supply air temperature, then it would be possible to say that it's because of an action of the TXV that the air temperature fluctuates.
This is due to the fact that during operation, when the mass flow rate increases because of the on-cycle, the evaporating pressure decreases and the condensing pressure increases, so even though the Δh_{evap} decreases because of the backward shape of the saturation curve in p-h diagram, and the superheat increases for the same reason, the capacity increases because the mass flow rate rises more than the Δh_{evap} reduces. That causes the air temperature to decrease.
By plotting the superheat vs supply air temperature shape, there wasn't any evidence of any effect though. At part load, the average superheat fluctuates in its range with a profile similar to the one of the air, but as we can see in the figure below the oscillations seem to be delayed than the ones of the air, so, in other words, it looks like there is no apparent causal relation between the superheat fluctuations and the air side ones.

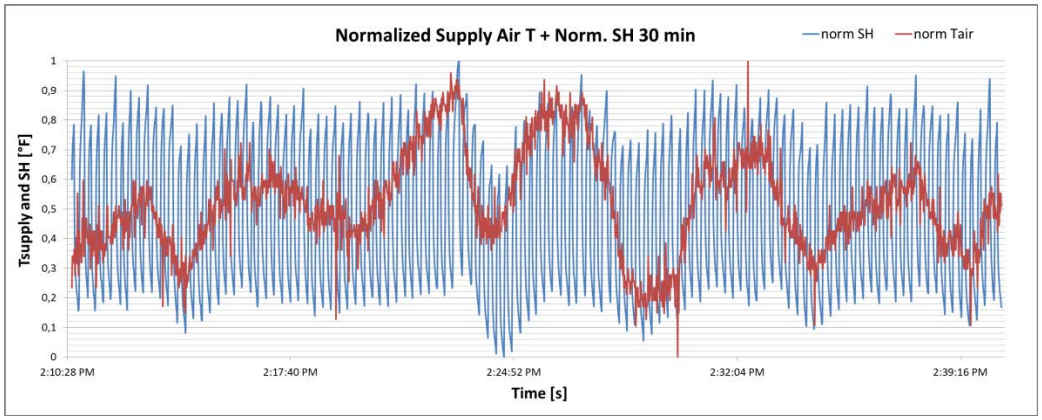

Figure 5.28. Normalized supply air T and normalized superheat fluctuations at compressor 50% load (30 min). Temperature range 21,66÷22,05°C, SH range 1,47÷10,75°C.

Then we decided to plot the compressor cycling and the air temperature and noticed that it was getting hard to define our operation as a proper steady state one. In fact, the compressor cycling causes the air side fluctuations we discussed above, and the interesting thing is that it seems that the compressor sometimes makes **longer** and sometimes **shorter on-cycles**, during the same test, even though the speed we manually set should be always 50%. As reported in figure 5.29, apparently when the air temperature increases too much, the compressor starts a longer on-cycle (circled in figure 5.29) in order to reduce it, as if there was a control or a set point on the air temperature, which we didn't set at all during these tests, though.

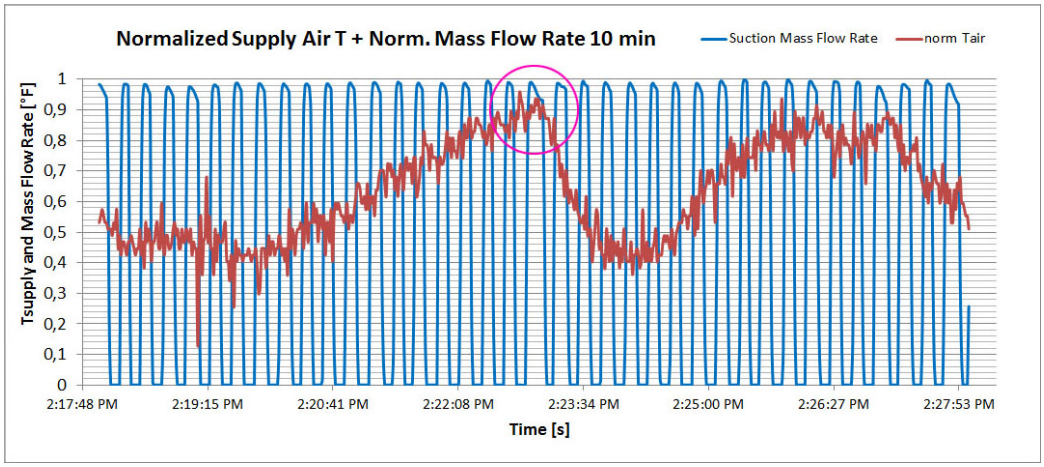

Figure 5.29. Detail of the magnitude of the cycles in normalized supply air T and normalized mass flow rate fluctuations at compressor 50% load (10 min). Temperature range 21,66÷22,05°C, mass flow rate F.S. 594,74 kg/h.

So possible reasons can be related to:

- Refrigerant migration
- Superior control of the heat pump over the compressor
- Self-control logic of the compressor

The first option, which anyway is already reported in some literature [8], is that sometimes there is some charge migration inside the line. This is just a mass transfer and it's due to the fact that the inlet temperature in the heat exchanger keeps pretty stable, but the mass flow rate doesn't, because of the pulsing flow, so the average density of the flow changes. If one could virtually weigh the coils and calculate the average refrigerant mass contained at different cycles he could observe slightly different values. The heat exchange conditions keep varying and some refrigerant mass migrates from one part of the line to the other, even though the presence of the liquid receiver dampens everything. If there is no further control logic in the heat pump, that makes the compressor's on-cycle last longer, it could be just a matter of the compressor self-adjusting its operating conditions, as sometimes it struggles a little bit more to suck refrigerant because some of it got accumulated in the circuit.

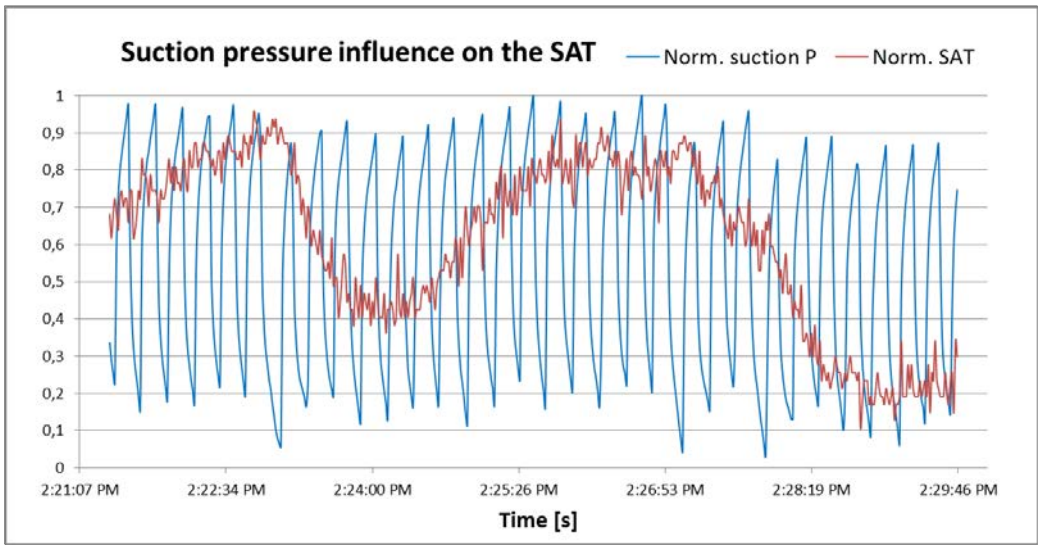

Figure 5.30. Suction pressure influence on the supply air T at compressor 50% load (10 min). Temperature range 21,66÷22,05°C, pressure range 11,13÷14,69 bar.

When the suction pressure increases too much (figure 5.30), that could be because there is too much refrigerant accumulated at the suction side. In figure 5.31 the air temperature fluctuations are related to the suction, discharge and liquid pressures very much, and they are also delayed a little bit in time, which could be expected from the very beginning. It can be seen on the envelope built on the minimum suction pressures and maximum discharge and liquid pressures.

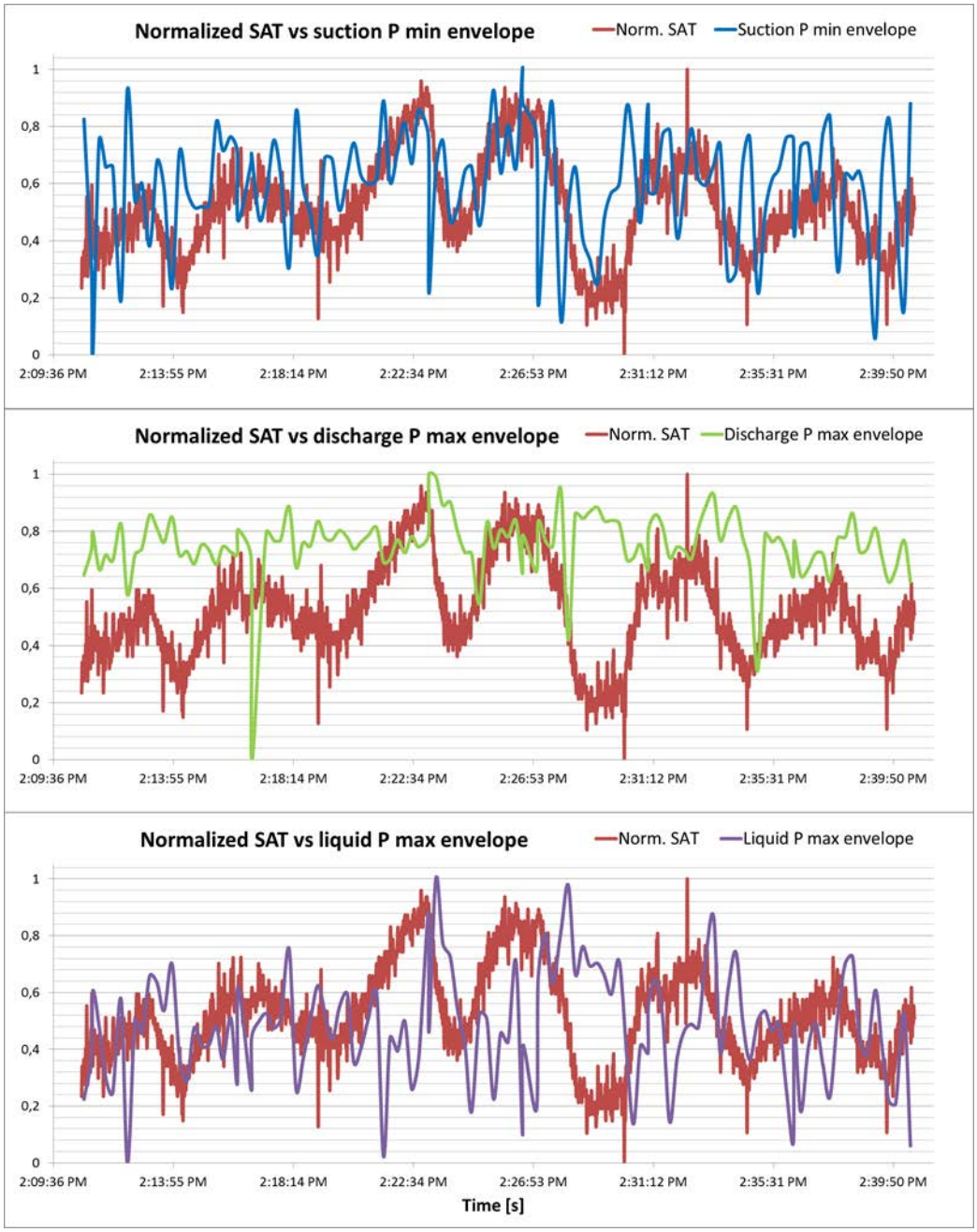

Figure 5.31. Normalized SAT and the envelopes of suction min pressure (top graph), discharge max pressure (middle graph) and liquid max pressure (bottom graph) at compressor 50% load (10 min). Temperature range 21,66÷22,05°C, suction pressure range 11,13÷14,69 bar, discharge pressure range 23,88÷28,57 bar, liquid pressure range 24,08÷26,39 bar.

The second option is suggested by making the consideration that, in addition to just a signal coming from the controller (so the phenomenon is due to the overall heat pump control logic and not to the compressor's) defining the frequency of the mating/unmating of the scrolls, there are some auxiliary control loops that have to check suction and discharge pressure and make sure things are within tolerance, because there is common logic for shutdown at high pressure and maybe avoidance of two phase state at suction. Further information cannot be reported due to confidentiality agreements with AAON, Inc.

The third option is especially noticeable while operating at low load conditions. First of all, the compressor built-in control logic prevented us to operate at 10% load, because its minimum operating speed is 12%. Secondly, sometimes it was noticed that the compressor makes one or more longer on-cycles, because it seems that there are some monitored parameters that make it self-preserve itself, for example when there is lack of oil: it is in the line and if the load is too low it is possible that it's not pushed strongly enough during the short on-cycle in order to go back to the compressor. So it feels that there is a lack of lubrication and decides that some cycles have to last longer. So this logic comes straight from the compressor. This can be seen in figure 5.32, an example of the compressor self-adjusting its speed at very low load.
So, in a similar way as the first option, the compressor could make some small self-adjustments in order to reach stable operating conditions.

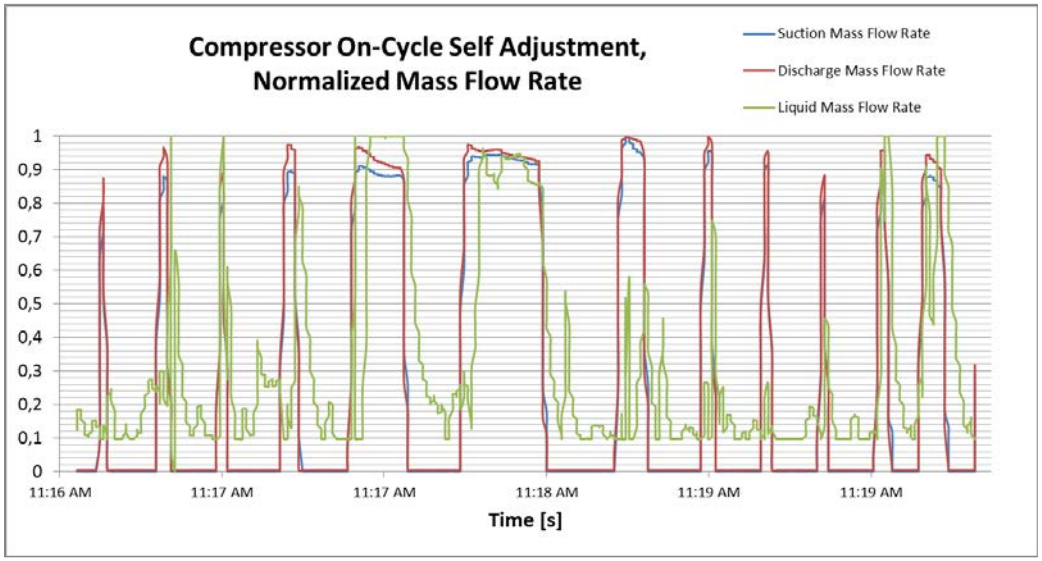

Figure 5.32. Normalized mass flow rate fluctuations at compressor 12% load (4 min). The 12% load suddenly becomes close to a 50% and 75% load wave shape.

What makes the first option stronger is the fact that we didn't notice any of these behaviours at 100% compressor load, and this makes us believe that any operating condition that is not 100% is hard to be defined as steady-state.

What is pretty simple to do to verify what we assume which could be one of the possible future developments of the project, would be mounting a sight glass on the liquid receiver, so that it would be possible to see how the refrigerant charge moves and migrates from one part of the circuit to the other.
Another optimal development of the apparatus, that would work both for this kind of test and obviously for the low load compressor tests, would be building at least a thermocouple grid to be put on the evaporator coil, to punctually monitor the coil temperatures and see if there is any change in the heat exchange, if any part of the coil is favorited or affected by the pulsing flow.
We haven't had the chance to install this instrumentation, so we could just investigate on the common parameters like supply and return air temperatures and build the energy balances that are the key of proving if what we measured made sense or not. The evidence of the previous pictures is that, as expected, a deep analysis of the development of the air side heat exchange was not possible because of the weak instrumentation. Nevertheless, it was possible to show, as it's evident in figure 5.29, that the supply air dry bulb temperature tended to fluctuate with a bigger amplitude the more the compressor load was decreased but, as it will be discussed later, at some point it began hard to identify if the room temperature was kept stable by the chiller (this means it had enough cooling capacity) or by the chamber itself (this means the compressor load was too low to provide enough cooling).

5.3 *Low load* compressor-oriented tests

5.3.1 Experimental setup and methodology

As previously reported, the first kind of new test that became interesting to be run was to operate the system, still with just one compressor, at very low load.
A set of tests at the same ambient conditions of the first ones were run, with the compressor running at 12%, 17,5% and 30% with a very high recording rate, 0,1 seconds. It wasn't possible to decrease the compressor load lower than 12% because of a limitation of the compressor itself (auto-protection mode). The tests were made maintaining the same methodology as the previous tests: still with the goal of running the system at steady state conditions, the indoor and outdoor rooms were set to a desired ambient. Once the set point conditions were reached and maintained for 60 minutes, data recording started at a sampling rate of 0.2 seconds for additional 10 minutes. This recording time is not long but it was chosen for the following reasons: preventing the DAQ system to crash because of a too large amount of data was desireable, and since the conditions were more than stationary, it was proved that there wasn't any tangible difference between longer or shorter recording times, as long as it would be possible to get enough cycles of the compressor.
Both the DAQ system and the Coriolis mass flow meters came up to be the time limitating factors in this investigation. In fact, their sample time is 0.2 seconds. It was known that from the technical specs of both components and we verified that by starting a recording with a 0.1 sample rate: simply, every value we had was repeated twice.
So if there was the need to go deeper in the analysis of the behavior of the system, in order to understand all the dynamic phenomena that are ruled by the pulsing flow, some radical changes would need to be applied to the DAQ system and to the flow meters.
During the recording period the dry bulbs in each room were maintained within ±0.2°F (±0.1°C) of the set points, and the indoor wet bulb was maintained within ±0.2°F (±0.1°C) of the set point. This setup made sure that the average values to be calculated, especially for what concerns the air properties (temperature, above all) would be contained in the ±0.1°C range, and this assumptions could allow to make the collected data more reliable.
The speed of both condenser fans and evaporator blower was kept fixed during the recording, too.

The new instrumentation that was installed allowed to capture much more information on both air side and refrigerant side of the apparatus.

5.3.2 Results

The new Coriolis mass flow meter allowed to collect data about the mass flow rate and the density of the refrigerant, while the new thermocouple and the new pressure transducer that were put right after the mass flow meter gave a good overview on the refrigerant properties right before the TXV.

What had to be shown with this third flow meter was that the pulsing flow imposed by the compressor, causes a measurable and possibly predictable delay in the development of the flow through the whole line, in this case after the condenser coil. We were also interested in looking for a sort of damping of the mass flow rate and other properties, and trying to quantify them.
The problems related to these kind of measurements were due to the nature of the mass flow meter itself: as any other flow meter, it suffers while measuring two-phase flow, with bubbles or generally slag flow. It is immediately possible to be linked to potential problems at low load, when the average flow rate is so low that the condensation phase is truncated and the flow that reaches the flow meter is not liquid (that would require a certain amount of subcooling), but two-phase already. This should actually ensure more condensation, but the ultimate effect of the decreasing mass flow rate is that the cooling cycle squeezes itself so crosses the saturation curve in the two-phase zone. One last reason could be that the mass flow rate fluctuation is not steady-state or continuous, like in compressor equipped with inverter, so some phenomena can suffer this unsteadiness. Many test at low load were conducted to try to avoid this problem, that obviously grows when the compressor load decreases. Satisfying results were found only with a 75% compressor load. In the plots it's possible to see how late and how damped the flow rate reaches the flow meter in the liquid line. In figures 5.33, 5.34, 5.35 it is shown how difficult the measurement of a liquid mass flow rate becomes as the compressor load decreases, and this behaviour is obviously independent from the outdoor/indoor temperatures, since it's proper of the compressor itself. The air side measurements are not reported in the 1-minute plots, since such fast dynamics doesn't affect the air properties in this shot time.

It is also possible to notice what was one of the expectations of the observations: some delay in the mass flow rate compared to suction and discharge. However, it's not possible to determine the entity of this delay because of the bad measurements of the two-phase flow. This kind of investigation was done in sub-section 5.2.4), with higher compressor loads and so with better measurements.

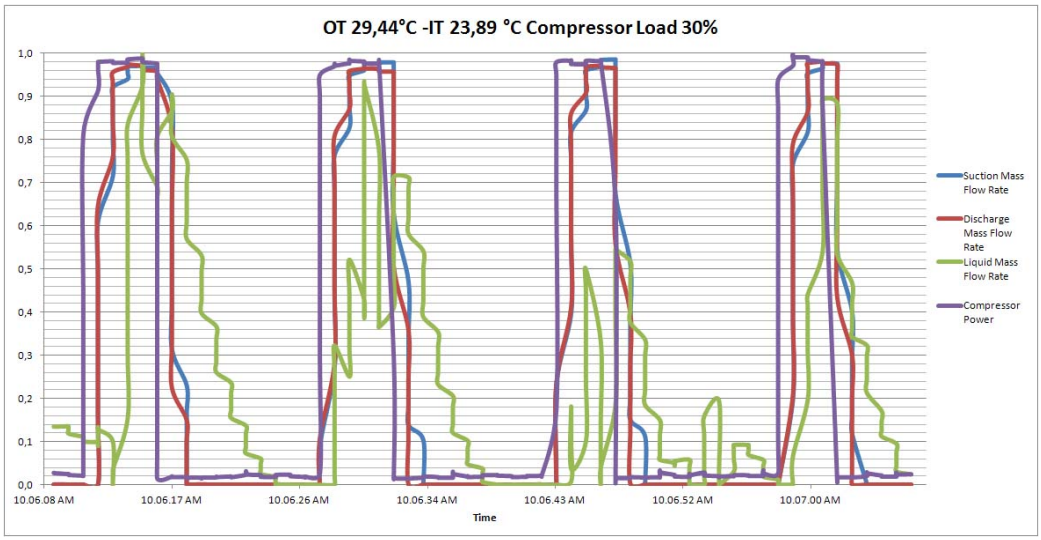

Figure 5.33. Compressor power and suction, discharge and "liquid" mass flow rate fluctuations at 30% compressor load (1 minute). Power F.S.: 6141W, Mass flow rate F.S. 584 kg/h.

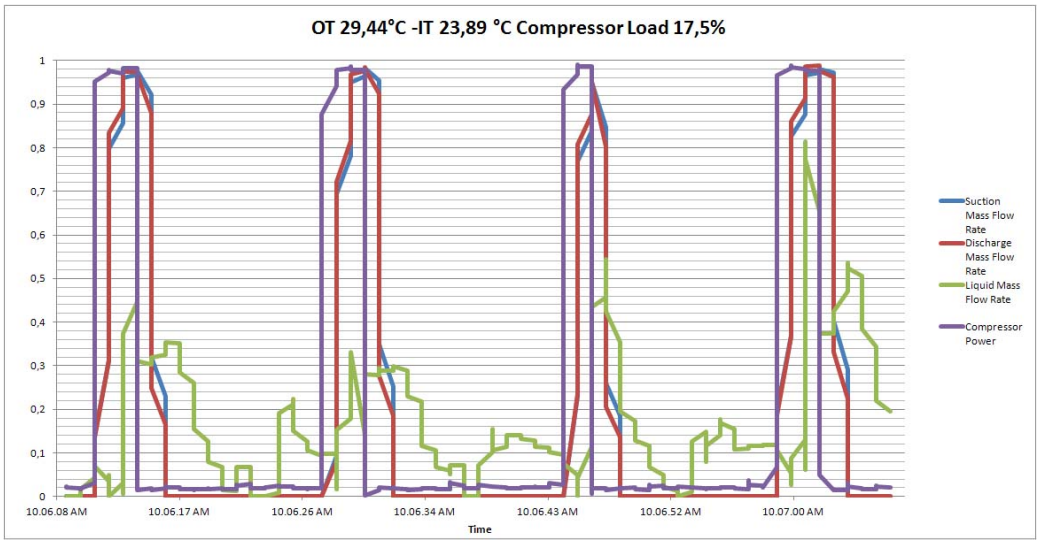

Figure 5.34. Compressor power and suction, discharge and "liquid" mass flow rate fluctuations at 17,5% compressor load (1 minute). Power F.S.: 6175 W, Mass flow rate F.S.: 572 kg/h.

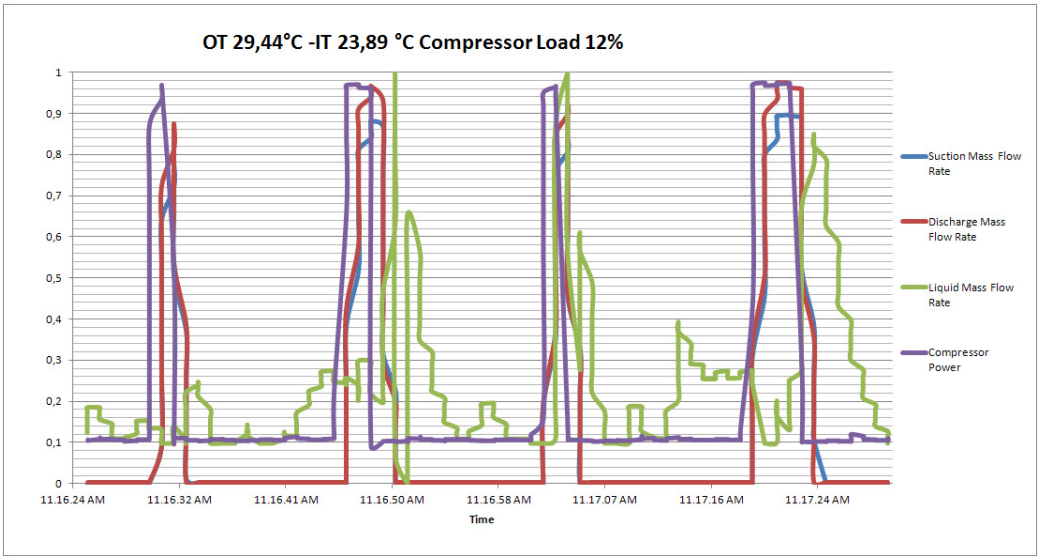

Figure 5.35. Compressor power and suction, discharge and "liquid" mass flow rate fluctuations at 12% compressor load (1 minute). Power F.S.: 6247 W, Mass flow rate F.S.: 581 kg/h.

It's also shown how the cooling cycle evolves while running at lower loads than 100%: the discharge pressure, at lower loads, decreases as the load decreases. As shown in the p-h diagram (figure 5.36), the condensing temperature decreases and so does the pressure.

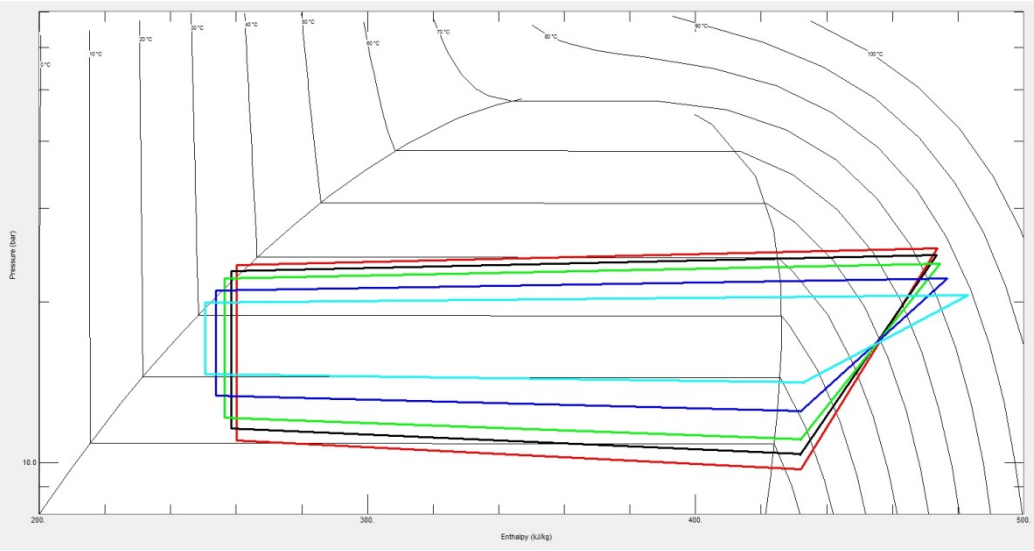

Figure 5.36. Refrigerant cycle shape modifications due to different compressor load (100-90-75-50-25%) observed in the steady-state test performed at OT 29,44°C and IT 26,67°C. Red: 100% load; light blue: 25% load.

This means that when below a load that depends on the indoor and outdoor conditions, there isn't enough subcooling through the condenser anymore (figure 5.37).

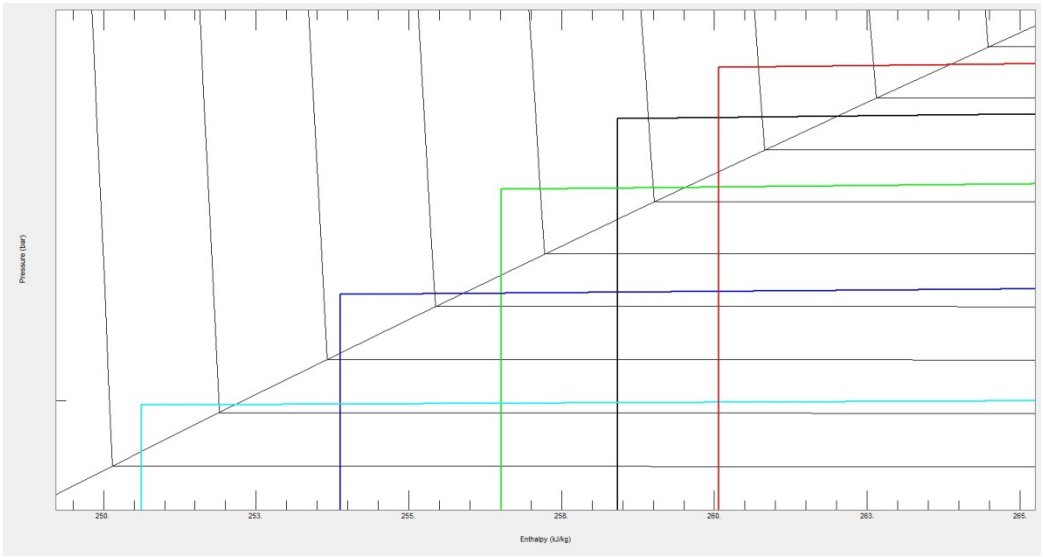

Figure 5.37. Magnified detail of figure 5.36 which shows the $\Delta T_{subcooling}$ decreasing while reducing the compressor load (the pseudo-vertical lines in the diagram are isotherms with one-degree step).

Plus, it needs to be considered that we could install the flow meter way far from the condenser coil, around 1,2 m after, because there wasn't the needed room. This caused a further pressure drop that brought the flow closer to being two-phase. So, as the flow meter accuracy decreases, the data tend to be more unreliable the lower the compressor load is. Better considerations about the liquid refrigerant behaviour are reported in sub-section 5.2.4.

Even though this set of tests was still thought as compressor-oriented, the measurement tools that were installed to measure the air properties allowed to make a preliminary investigation on the main point that the research on digital scroll compressors is on: how does the heat exchange work in the coils when a pulsing flow is imposed on the refrigerant side?
In the following charts (figures 5.38 and 5.39) it's shown how the low load affects the air side performances: first it needs to be considered that very often, especially when the temperature difference between indoor and outdoor room increases, the compressor cannot provide enough cooling capacity, so the room provides that. Anyway, the dry bulb air temperature fluctuates a lot, and it does more when the load decreases.

Secondly, the more the load decreases, the more the mass flow rates shapes become irregular, as if the compressor tried to reach the refrigerant nominal mass flow rate but doesn't manage to.

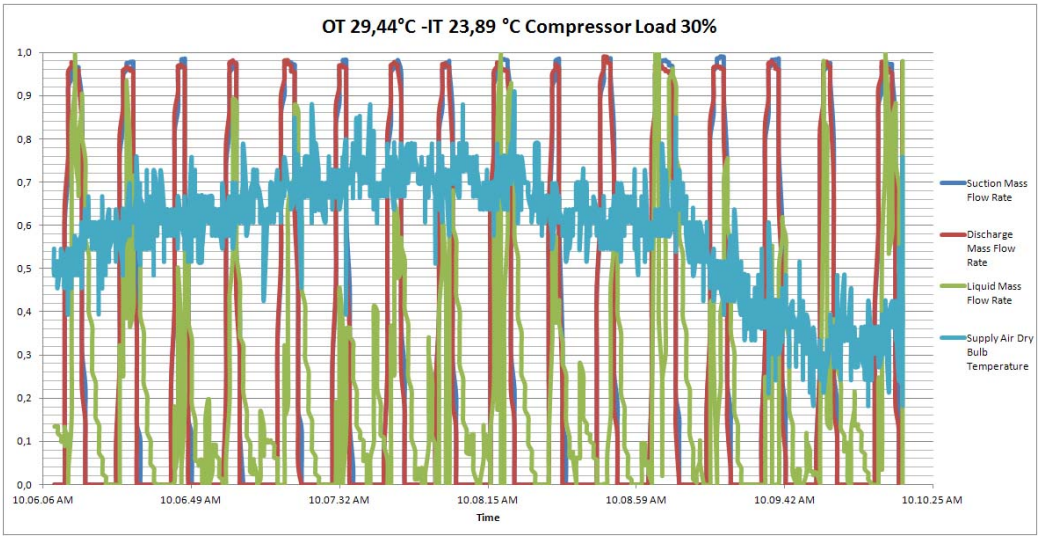

Figure 5.38. Refrigerant mass flow rate waves against supply air fluctuation (30% load, test conducted at OT 29,44°C and IT 26,67°C, 4-minute plot). Mass flow rate F.S. 554 kg/h, SAT range 20,84°C÷21,4°C

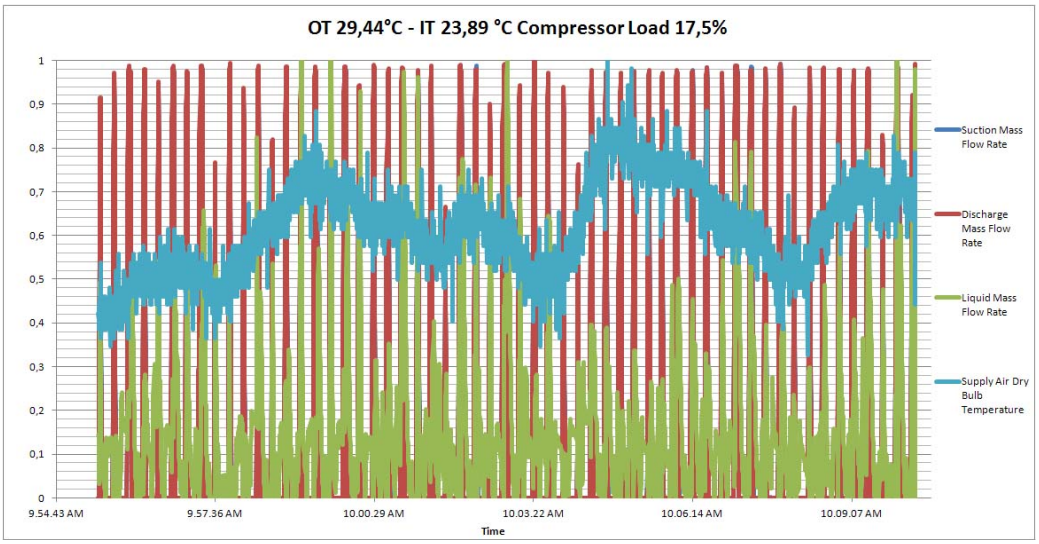

Figure 5.39. Refrigerant mass flow rate waves against supply air fluctuation (17,5% load, test conducted at OT 29,44°C and IT 26,67°C, 4-minute plot). Mass flow rate F.S. 541 kg/h, SAT range 22,12°C÷23,00°C

5.3.3 Conclusions

To summarize, it's evident how unstable the plots of the mass flow rates at very low load are, especially the liquid mass flow rate. The collected data allow us to prove that there is a delay in the development of the pulsing flow, from before to after the condenser, and it is possible to make hypothesis on the time delay. But the absolute values of the mass flow rate that are measured by the liquid line mass flow meter are not reliable. A better way to verify the delay is to analyze higher compressor load tests, when enough subcooling of the refrigerant is reached and so the liquid line mass flow meter doesn't have to deal with two-phase flow.

It's also evident that for many cycles of the compressor, when running at loads usually below 25%, it tries to reach the nominal mass flow rate (the one at 100% for the corresponding ambient conditions), but the impulse is so small that it doesn't get to this condition.
Heat exchange is affected in this condition, efficiency decreases, so one feels it's possible to say that if the required capacity is very low, it could be more efficient to run the compressor at around 30% for some time and turn it off for some time.

5.4 Towards the transient operation: the *Step-function* test

Another interesting feature that became interesting to study was to determine the settling time of the unit after implementing a step function in the ambient conditions. This will be very helpful for the simulation purposes and it was run by imposing a certain room temperature and measuring the transient between the moment the new condition was imposed and the time the unit takes to reach stable conditions. It's not trivial to look for a good way to achieve this goal: any of the main components of the unit (Evaporator, Condenser, Compressor, TXV) has its own dynamics, that have to be related to the chamber dynamics. So a great effort is required in the modeling in determining both the single time constants and the overall unit one. Plus, it is proved that the unit behaviour affects the chamber operation, that will react with cooling, heating or humidification to any change in the ambient conditions. So it was necessary to look for a way to restrict this interaction as much as possible, in order to isolate the unit behaviour.

5.4.1 Experimental setup

The way we thought we could obtain a step function that could have an immediate effect on the unit was to install a 20 kW electric on-off heater right before the evaporator coil, on the return air side. This could allow to have an immediate increase in the return air temperature that simulates, for example a sudden overcrowding in the indoor room. So, by acting on the control in order to keep a constant supply air temperature, the goal was to get an idea of the way the unit reacts to this, in terms of magnitude and time constant of the fluctuation. In figure 5.40 it's shown what was expected:

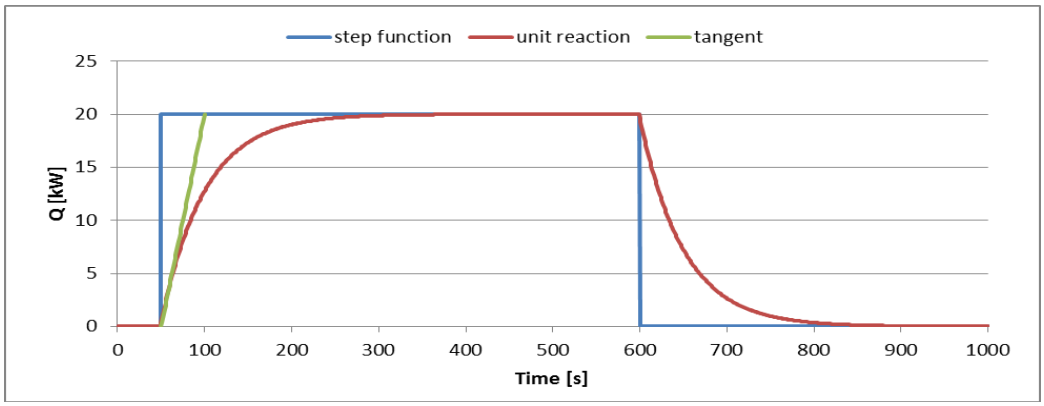

Figure 5.40. Simplified representation of the two transients due to switching on and off a step function

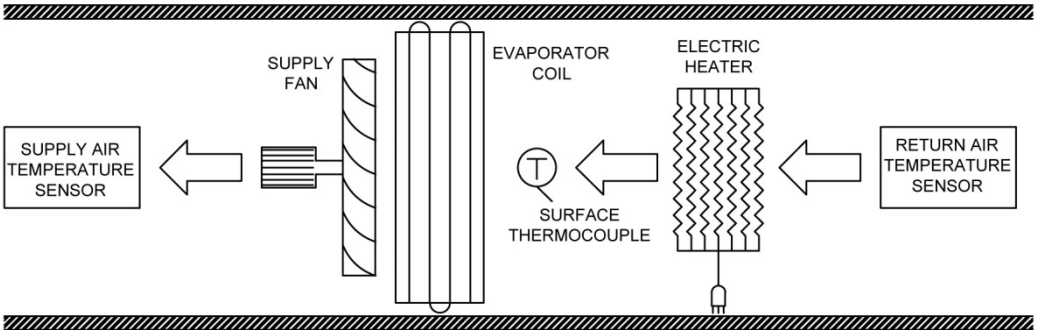

Figure 5.41. Air side scheme for the step-function test.

Figure 5.42. Evaporator coil and unit electric heater (left) and magnified image of the electric heater (right).

It was necessary to use an electric heater of the same kind that is installed in the conditioning bays of the chamber. It has a 460 V voltage input so it required a three phase plug and a very thick power chord. That was run from the plug to the heater, as shown in figure 5.42, and it was secured to the unit by some chains that could prevent it from shaking and causing any kind of electric arc.
The only possible safety was a surface thermocouple that ran from the DAQ box to the wall next to the evaporator coil. It was run by to the ceiling to a couple of inches next to the filters, in a way that it could be shielded as much as possible from the radiation delivered by the heater, so that our temperature measurements could be reliable.

By building a simple heat balance, it was possible to calculate the predicted/expected temperature that the air could get to, and by monitoring its temperature it could be possible to intervene in case it went too high (above 80°C).

$$\dot{Q}_{air} = \dot{V}_{air} \cdot \rho_{air} \cdot c_{p_{air}} \left(\bar{T} - T_{air,return}\right) \tag{92}$$

where:

- $\dot{Q}_{air}$ is the 20 kW input we put in the system,
- $\dot{V}_{air}$ is the air flow rate,
- ρ_{air} is the return air density,
- $T_{air,return}$ is the return air temperature, which is known as it is the indoor room temperature and it's measured by the Return Air Temperature sensor which is put inside the unit but before the electric heater,
- $\bar{T}$ is the unknown expected new temperature, when switching the heater on, which is simulating the sudden increase so it is seen by the unit as a "fake" return air temperature, while the indoor room still remains at the desired setpoint.

So the expected air temperature should have been, more or less, around 34°C, considering the indoor temperature at which the test was conducted (21,11°C)

5.4.2 Experimental procedures and choices

What's been most complicated and challenging throughout this project was to deal with the continuous interaction between the chamber and the unit. The big size of the unit caused its dynamics to affect a lot the chamber's ones. That's the reason why it took always around one hour to obtain stable conditions of the indoor/outdoor room temperatures.
In this case, there was the chance to choose how to design the test. The options for the control purposes were:

1. put the heat source in the indoor ambient, and rely on the fact that the unit dynamics should anyway be faster than the chamber's ones, so that by trying to keep an indoor ambient temperature as constant as possible the unit would change its operating conditions and reach new stability with the 20 kW more of heat input.
2. Put the heat source right before the evaporator coil and control the supply air temperature. By choosing this option the room would never see any temperature change, so the chamber dynamics should stay as reduced as possible and the analysis should be easier.

The second option was chosen, but well aware that it's impossible to delete any chamber/unit interaction: by controlling the supply air temperature, in fact, the unit sees the heater's kick right away and so the temperature increase. But by the time that the compressor changes its speed to face this new condition, and in order to keep the supply air temperature low as before, a certain amount of warmer air will be pushed inside the indoor room.
This was previously in equilibrium, and had not seen the heater switching on, because it's inside the unit. Nevertheless, the warm air coming from the unit causes the equilibrium to break, and the contemporary increase of the cooling imposed by the bays' coils and the decrease of the heat imposed by the bays' heaters. All this means that the unit will never be isolated, there will always be a period of time in which the chamber itself tries to face the new heat input imposed by the heater, together with the unit which, in a faster way, tries to keep a constant supply air temperature.
Plus, this could lead to a result in which the new stable conditions (so the unit performances) are obtained with a little help/harm of the chamber, and not just an output of the unit's dynamic operation.
The results will suggest exactly this impression. In order to have reliable data, the user should act on the chambers' controls in advance, before switching the heater on, so that any kind of fluctuations can be damped, but these conclusions will be discussed later on.

5.4.3 Performances and results

It was decided to conduct the test at these temperatures: OT 26,67°C, IT 21,11°C.
This choice was dictated by several considerations. First of all it was one of the same test of this last campaign, so it was possible to use the collected information to somehow predict the heat exchange across the evaporator; secondly, among the tests that run in April, it had the lowest indoor temperature, so the high heat exchange efficiency could be exploited to absorb the heater power input with the minimum burden for the refrigerant cycle and therefore for the compressor.
Since the automatic control strategy was not implemented yet (the purpose for this experiment was to discover how the unit reacted to an abrupt power input, so this test was just propaedeutic for the optimal control) it was necessary to act on the unit manually, overriding the compressor load (at fixed fans speed) in order to control the supply air temperature.

Transient after heater ignition

Before kicking the heater on, stable conditions with the compressor at 25% load were reached; that load was chosen in order to have the maximum possibility of modulation. Actually one can consider the collected data of the performance test and can observe that it is very difficult for the unit to absorb all the power input; as shown in table 5.7, the $\dot{Q}_{air}$ at 25% load was around 6 kW, while at 100% it was about 20 kW, so the cycle could absorb 14 kW exploiting full modulation. Consequently a 20 kW sudden input was a great challenge for the unit, even at full load.

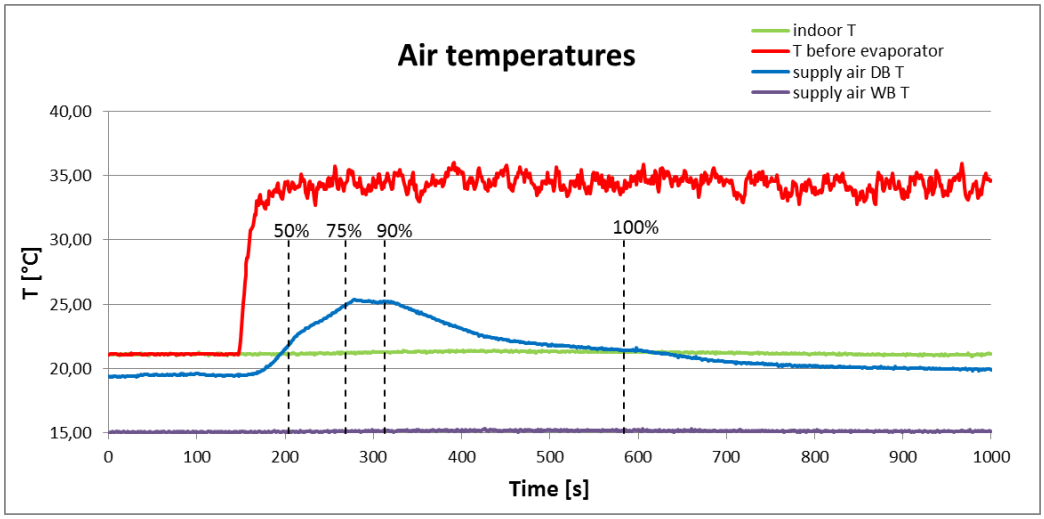

Figure 5.43. Return T (IT and T before evaporator) and supply T (DB and WB) variations after heater ignition (at 147 s).

As shown in figure 5.43 the heater ignition generated a good approximation of a step function, so the choice of the second option described in the previous section was appropriate. Even though the indoor temperature (green curve) remained pretty stable at the desired setpoint (small variations will be investigated later on), the unit saw a return air flow investing the evaporator coil as a "fake" temperature which had the shape illustrated in the figure above. After switching the heater on it could be observed an abrupt and steep increase of the **supply air temperature (SAT)**, the control variable that to be brought back to the original value. After one minute the load was risen to 50% (204 s), but the upward trend, less steep with the new load, still remained too vertical, so it was increased again to 75% after just 1 minute (268 s); thanks to the new compressor modulation the trend became quite horizontal, with a SAT of 25°C (an increase of about 6°C in 100 s!). It was necessary to lower this temperature, so we changed again the compressor load first to 90% (313 s) and then to full load (584 s).

It could be noticed that although the expected difficulty of the unit in absorbing such great power input, the SAT went back to the pre-ignition value after around 15 minutes; it is very likely that, as already said and taking into consideration the duration of the transient, the indoor room "helped" the unit in setting the indoor temperature (return air temperature, RAT) by taking upon part of the heater power.

This collateral effect can be seen in the graph below. As displayed in figure 3.2 and 3.5 and explained in section 3.1, the air of the indoor room, together with the air leaving the code tester, is processed by the bays: firstly the air goes through the coils (in which cold water circulates) for cooling and then pass through electric heaters for re-heating. The coils are manually regulated while the electric heaters are controlled automatically by a PID algorithm.
The green curve represents the temperature of the air before the bays' coil (BCT), the blue one is the temperature of the air after the bays' coil (ACT) and the red one is the temperature of the air reheated by the heaters (AHT). Before kicking the unit heater on the AHT was around 0,4°C higher than the BCT; after that it is possible to note an increase of the BCT due to the increase of the supply air temperature (the trend shape is similar) and it is also observable that the ACT has the same trend of the BCT, simply shifted down by about 4°C. The cause lies in the fact that, as previously said, the control of the water flowing inside the coil is manual, so nothing was changed during the transient. On the contrary the bays' heaters are controlled automatically, so when the PID controller measured the indoor temperature rise acted on the bays' heater reducing their electric power. In fact figure 5.44 shows that the AHT became approximately the same of the BCT at 300 s and at 500 s it further reduced settling below the BCT by around 0,2°C.

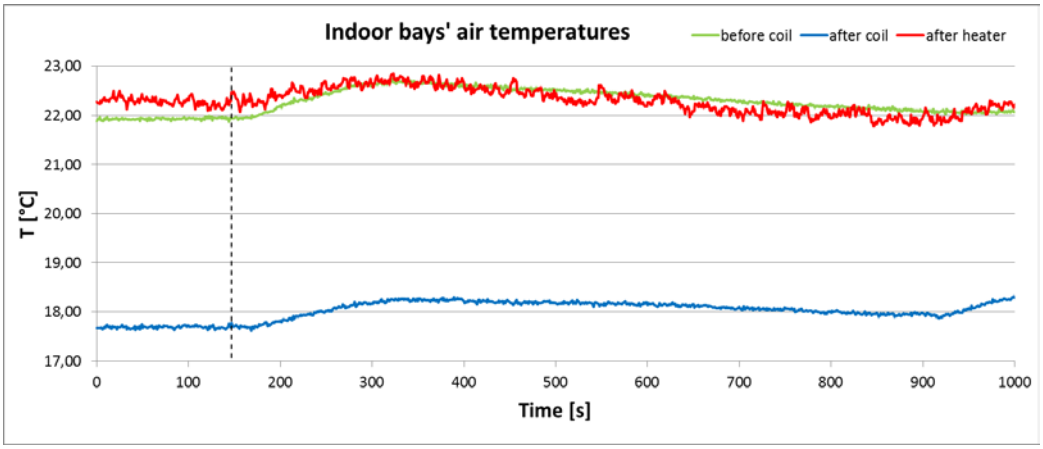

Figure 5.44. Indoor bays' air temperatures (before the cooling coil, after the cooling coil and after the chamber electric heater) variations after heater ignition (at 147 s).

Therefore this explains the small but not removable influence of the chamber on the transient after heater ignition (and analogously on the one after heater shutdown, exposed later on).

Now we have to discuss the transient of **outdoor and indoor temperatures**.

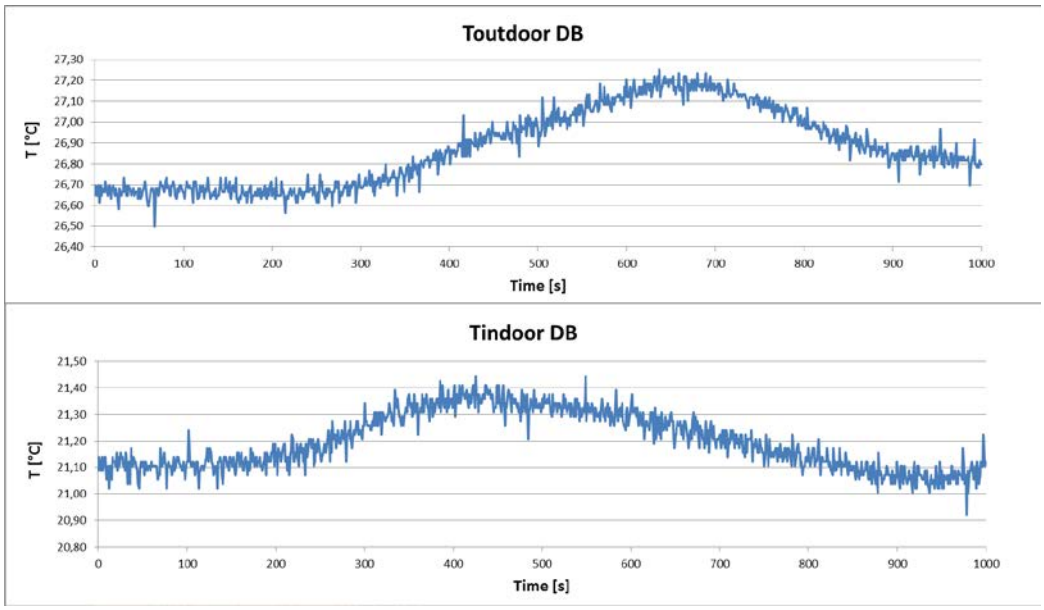

Figure 5.45. Outdoor T and indoor T variations after heater ignition (at 147 s)

As shown in the graph above the indoor T underwent an overshooting of 0,3°C (against 6°C for the SAT) and after 15 minutes it went back to the imposed setpoint, with the small but not removable intervention of the chamber. Anyway, if the purpose in this experiment is not the preservation of the exact setpoint but the safeguarding of the comfort indoor conditions, it is possible to consider definitely negligible an oscillation with an amplitude that was lower than 0,5°C.
On the other hand, for what concerns the outdoor temperature, its increase was due to the increase of the refrigerant mass flow rate and of the discharge pressure, therefore of the condensing temperature: the temperature of the condensing coil became higher and it caused, together with the intensification of the circulating mass flow, an increase in the temperature of the air moved by the condenser fans. If the chamber had been large enough not to be affected by the unit's dynamics that wouldn't have been a problem. So the experimental approaches for the two chambers were opposite: for the indoor room we needed to minimize the reaction of the chamber's bays (the unit was wanted to be the only conditioning apparatus) while for the outdoor room it was needed to use the chamber itself to minimize the overshooting of outdoor temperature as soon as possible (we registered a maximum amplitude of about 0,5°C).

Transient after heater shutdown

To complete the analysis, it was necessary to know how the unit would respond to a sudden reduction of the power input. Thus, after reaching stable conditions with the heater on, it was turned off and, as predicted, a specular trend for all the variables was obtained.

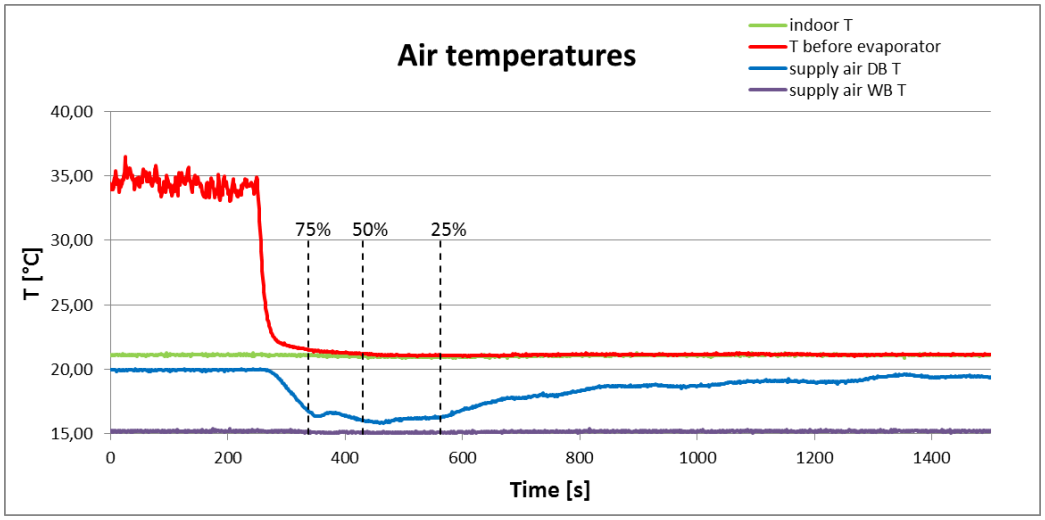

Figure 5.46. Return T (IT and T before evaporator) and supply T (DB and WB) variations after heater shutdown (at 251 s).

Actually the curves were not properly symmetrical.
By analyzing the SAT in figure 5.46 it can be seen that there's an undershooting with a lower amplitude than the one of the overshooting in the previous case (4°C against 6°C, see figure 5.43) and a more jagged, irregular shape of the line (switching the heater on, despite the manual control, a quite smooth profile was achieved).
The changes in the compressor load were more drastic in the final outcome if compared to the previous case. After one minute and a half (at 338 s) we reduced the load to 75% and we noticed an interruption of the descending trend with a slight increase of temperature followed again by a downward inclination but less steep. At 430 s the load was set at 50% and the reaction of the unit produced a change in the SAT trend close to a horizontal one, so after two minutes (at 562 s) the load was changedfor the last time by reducing it to 25%. After that adjustment the trend became softly ascending until stable conditions were reached after 10 minutes again.

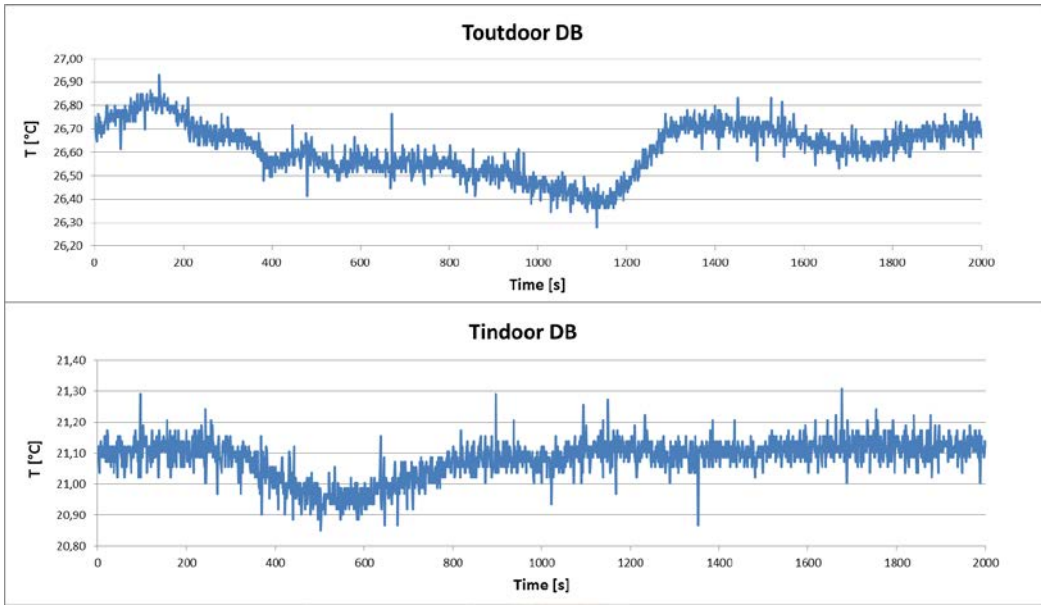

Figure 5.47. Outdoor T and indoor T variations after heater shutdown (at 251 s)

From figure 5.47 it's clear how the IT reached stability at 1100 s, so roughly 13 minutes after the heater shutdown. There is a slightly different behaviour for the outdoor temperature. After observing the room response from the heater ignition transient, it was tried to heat the room just a bit (0,1°C) before the heater shutdown to limit the following undershooting; it was a good idea, in fact that deviation from the average value was around 0,3°C (against 0,5°C in the other transient). But the stability in this case was achieved at 1400 s, five minutes after the IT.

Even in this transient there was a reaction of the chamber and probably this intervention allowed the unit to limit the undershooting of the SAT to only 4°C and, more important, to dampen the variations of the indoor temperature more efficaciously (only 0,15°C of maximum deviation from the average value, against 0,3°C of the previous transient). The reason why that action was more incisive in this transient is imputable to how the chamber controls its own temperature. As already mentioned, there are two thermal control facilities: bays' coils in which cold water flows (to low the air temperature) and bays' proportional electric heaters for re-heating. It is evident that intervening on the air with an electric device is faster, so heating the air is faster than cooling it. In this transient, after shutting down the unit heater, the air temperature decreased suddenly but the bays' heaters, in a different way from the coils, reduced their own electric power automatically and very quickly, dampening decisively the SAT and IT drop. This reaction for the purposes of the experiment is convenient regarding the outdoor chamber but it is deleterious for the indoor room since the bays' heaters are controlled automatically without any possibility of manual

regulation, so it is as if we had two conditioning facilities for our indoor environment, partially thwarting our efforts.

5.4.4 Conclusions and future developments

As already pointed out in the previous section, this test was propaedeutic for the development and experimental application of an optimal control strategy for the unit in cooling mode. So the purposes were:

a) Checking if the heater can generate a good approximation of a 20 kW step function for the evaporator coil, in order to simulate an abrupt overcrowding of the indoor environment;
b) Observing how the unit reacts to such a power input, if it is able to absorb that and, if so, how much time it needs to reach stability;
c) Observing the chambers' reaction to the two transients, in particular in the indoor room, and analyzing how much this interference affects the variables of interest.

With the collected data it can be now affirmed that it is possible to use an electric heater to study a step function transient, a rough time constant for the unit is known and the presence of a chambers' unwanted involvement was verified and proved.
This involvement is small but enough to affect somehow the test.
Therefore if someone else has to continue this project and to develop a control strategy he will have to quantify exactly the influence of the chamber, in order to calculate how many seconds before the transient starts and how intensely he has to intervene to anticipate and remove the chambers' noise.

Chapter 6

Conclusions and future developments

The tests run in the first campaign, after all the hardware (soldering and wiring most of all) was made, allowed to get confident with the behaviour of the chiller, which was not designed for being equipped with digital scroll compressor. All the measurement tools that were installed helped in monitoring and collecting information on the unit operation. The simulation model written for standard scroll compressors was improved and developed with the help of the experimental data and it was partially validated with a good match between the simulated and experimental outcomes.

In the second campaign of tests the air side measurements' quality was proved by building a heat balance across the evaporator coil. Refrigerant side and air side measurements agree and match with a slight but improvable difference of around a 5% of error: there was a much lower error in some tests, and some other tests showed worse agreement. Many investigations were made on the possible reasons, by studying any single effect with which the pulsing flow imposed by the digital scroll compressor may affect the measurements.
Investigations were made on the inertia of the system influenced by the modulation of the compressor, verifying the presence of about 0,5 seconds delay and the possible presence of fluid hammer for the refrigerant mass flow rate in the liquid line between the condenser and the TXV.
The supply air temperature is strongly affected by the system's dynamics, and this is probably due more to a non-steady state operation that causes migration of mass of refrigerant through the line, rather than an affection coming from the pulsing nature of the flow, because the pulsing mass flow rate comes with a much higher frequency than what the physics of the system show.
This behaviour shows that the unit is working cyclical mode, but it's not possible to define it as a steady-state operation. More sophisticated tools might be needed to be installed for further analysis. For example, it could be good to install a thermocouple grid right next to the evaporator coil, to punctually monitor the coil temperatures and see if there is any change in the heat exchange, or if any part of the coil is favorited or affected by the pulsing flow.

It also needs to be pointed out that the existing TXV came up to be to slow if compared to the system inertia. Due to its mechanical and inertial issues, it could help the outcomes of this project if an electronic expansion valve (EXV) was mounted, because of its higher reaction speed and the chances of tuning it offers.

In the second campaign the compressor-oriented tests of the first stage were supplemented by low-load tests, in order to study the functioning of the compressor and the unit in this condition: heat exchange is affected and efficiency decreases, so it is possible to say that if the required capacity is very low, it could be more efficient to run the compressor at around 30% for some time and turn it off for some time.
In order to evaluate the compressor efficiency, that showed lack of information, the next advisable step would be installing inside the compressor some proper devices that allow the user to acquire more knowledge about the internal causes that increase the efficiency this much, more than the intercooling explanation should realistically do.

A step-function test was also run as propaedeutic for the development and experimental application of an optimal control strategy for the unit in cooling mode and dynamic condition.
With the collected data we can now affirm that it is possible to use an electric heater to study a step function transient, we know a rough time constant for the unit and we verified the presence of a chambers' unwanted involvement.
This involvement is small but still strong enough to affect the test somehow.
When developing this aspect of the project, it will be necessary to determine how strong and with what timing to intervene on the chamber controls.

To summarize, all the improvements of the existing apparatus should allow the user to go deeper in the analysis of the operating conditions caused by the pulsing nature of the flow. In particular, for what concerns the modeling side, an optimal model of the compressor, TXV and heat exchangers characteristics and operating conditions needs to be developed. On the experimental side, the air side measurements are required to be more accurate, since it was evident that a slight error on the air properties badly affects the heat balance evaluation.

The most practical ultimate aspect of the project should be a comparison of the performances of the same system equipped with the different known kinds of compressors, in order to understand where a benefits-costs analysis leads the user.
Nevertheless, studying the nature of this kind of physics pushes the measurement tools' capability to the limit, so it feels the knowledge of the digital scroll compressor's dynamics is surprisingly interesting, regardless its immediate application in the marketed products.

Nomenclature

a	base circle radius that defines the geometry of the involute [m]
a_i	regression coefficient
A	area [m^2]
b_i	regression coefficient [-]
c_i	regression coefficient [-]
C_p	specific heat at constant pressure [J/kgK]
C_v	specific heat at constant volume [J/kgK]
C_{valve}	valve coefficient [N/m]
d_i	regression coefficient [-]
E	energy [W]
f	frequency [Hz]
g	acceleration due to gravity [m/s^2]
h	scroll height [m]
h	specific enthalpy [J/kg]
h	convection coefficient [W/m^2K]
k	conductivity [W/mK]
k	specific heat ratio [W/m^2K]
L_{io}	length along the inner involute of orbiting scroll [m]
L_{if}	length along the inner involute of the fixed scroll [m]
L_{of}	length along the outer involute of the fixed scroll [m]
L_{oo}	length along the outer involute of the orbiting scroll [m]
$\dot{m}$	mass flow rate [kg/s]
m_i	regression coefficient [-]
Nu	Nusselt number [-]
P	pressure [Pa]
P_d	downstream pressure [Pa]
P_u	upstream pressure [Pa]
Pr	Prandtl number [-]
$\dot{Q}$	rate of heat transfer [W]
r_b	base radius of involute circle [m]
r_o	offset distance [m]
Re	Reynolds number [-]
R	gas constant [J/mol*K]
S	entropy [J/kgK]
T	temperature [K]
T_m	critical temperature [K]
u	specific internal energy [J/kg]
U	internal energy [J]

v_i^0	regression coefficient [-]
ν	specific volume [m^3/kg]
V	volume [m^3]
V_{ci}	compression chamber volume [m^3]
V_{di}	discharge chamber volume [m^3]
V_{si}	suction chamber volume [m^3]
$\dot{W}$	work rate [W]
x	thickness [m]
z	altitude [m]
δ	normalized density [-]
θ	crank angle [rad]
v	velocity [m/s]
ρ	density [kg/m^3]
ρ_m	critical density [kg/m^3]
τ	normalized temperature [-]
φ	involute angle [rad]
φ_e	ending angle of the involute [rad]
φ_k	k-th angle of conjugacy [rad]
φ_{os}	starting angle of outer involute [rad]
ω	angular speed [rad]

References

[1] Liu S.-J., Krstic M., 2012. Stochastic Averaging and Stochastic Extremum Seeking

[2] Ariyur K., Krstic M., 2003. Real-time optimization by Extremum Seeking Control

[3] Chen, Y., Halm, N., Groll, E., and Braun, J.2002. Mathematical modeling of scroll compressors- part 1: compression process modeling, International Journal of Refrigeration 25: 731-750.

[4] Nieter, J., Barito, T. 1990. Dynamics of Compliance Mechanisms in Scroll Compressors, Part 1: Axial Compliance, Proceedings of the 1990 International Compressor Engineering Conference (Purdue):308-316.

[5] Zhang, W., and Zhang C. 2011. Transient modeling of an air conditioner with rapid cycling compressor and multi-indoor units, Energy conversion and management 52: 1-7.

[6] Huang, H., Li, Q., Yuan, D., Qin, Z., and Zhang, Z. 2008. An experimental study on variable air volume operation of ducted air-conditioning with digital scroll compressor and conventional scroll compressor, Applied Thermal Engineering 28: 761-766.

[7] Poort M.J. and Bullard C.W. 2006. Applications and control of air conditioning systems using rapid cycling to modulate capacity, International Journal of Refrigeration 29: 683–691.

[8] Ilic, S.M., Bullard, C. W., Hrnjak, P. S., 2001. Effect of shorter compressor On/off cycle times on A/C system performance.

[9] Hu , S., Yang, R., 2004, Development and testing of a multi-type air conditioner without using AC inverters.

[10] Tu, Q., Dong, K., Zou, D., Lin, Y., 2011, Experimental study on a multi-split air conditioner with digital scroll compressor.

[11] Joppolo, C. M., Molinaroli, L., Digital Scroll Compressors for summer air-conditioning: performance analysis of an autonomous air conditioner and comparisons with fixed and variable speed compressors.

[12] Morishita, E. et al., 1984, Scroll Compressor Analytical Model, Proceedings of the 1984 International Compressor Engineering Conference (Purdue): 487-495.

[13] Caillat, J., Ni, S., and Daniels M. 1988. A computer model for scroll compressors, Proceedings of the 1988 International Compressor Engineering Conference (Purdue): 47-55.

[14] Chen, Y., Braun, J., Groll, E. 2004. Modeling of Hermetic Scroll Compressors: Model Development, HVAC&R Research 10(2): 129-152.

[15] Winady, E., Saavedra, C., Lebrun, J. 2002. Experimental analysis and simplified modelling of a hermetic scroll refrigeration compressor, Applied Thermal Engineering 22: 107-120.
[16] Duprez, M., Dumont, E., and Frere, M. 2007. Modelling of reciprocating and scroll compressors, International Journal of Refrigeration 30: 873-886.
[17] Duprez, M., Dumont, E., Frere, M. 2010. Modelling of scroll compressors - Improvements,International Journal of Refrigeration 33: 721-728.
[18] Wu, G., Wu, K. 2004. Design and Application Research on Digital Scroll Compressor in Air Conditioning System, Proceedings of the 2004 International Compressor Engineering Conference (Purdue): 1-8.
[19] Chen, Y. 2002. Mathematical Modeling of Scroll Compressors. PHD Thesis Purdue
[20] Wang, B., Li, X., and Shi, W. 2005. A general geometrical model of scroll compressors based on discretional initial angles of involute, International Journal of Refrigeration 28: 958-966.
[21] Baehr H.D. and Tillner-Roth R. 1995. Thermodynamische EigenSchaften umweltver-traeglicher Kaeltemittel, Springer Verlag, Berlin.
[22] Halm N. 1997. Mathematical Modeling of Scroll Compressors. MS Thesis Purdue
[23] Incropera F, Dewitt D. Introduction to Heat Transfer 3rd Ed, Wiley, 1996.
[24] Fritzson P. Principles of object-oriented modeling and simulation with Modelica 2.1, Wiley-IEEE press 2004.
[25] Wetter, M. 2009. Modelica-based Modeling and Simulation to support Research and Development in Building Energy and Control Systems, LBNL Technical Report 2740E.
[26] Qiao H., Aute V., Radermacher R. 2012 Comparison of Equation-Based and Non-Equation-Based Approaches for Transient Modeling of a Vapor Compression Cycle, Proceedings of the 2012 International Compressor Engineering Conference (Purdue).
[27] www.mathworks.com
[28] Cremaschi, L., Lee, E. 2008. Design and heat transfer analysis of a new psychrometric environmental chamber for heat pump and refrigeration systems testing. ASHRAE Transactions 114 (2): 619- 631
[29] Lifferth S.O. 2009. Design and Construction of a New Psychrometric Chamber. MS Thesis Oklahoma State University
[30] Worthington, K., Cremaschi., L., and Aslan, O., 2011, A new experimental low temperature facility to measure comprehensive performance rating of unitary equipment and systems operating at design and off-design conditions